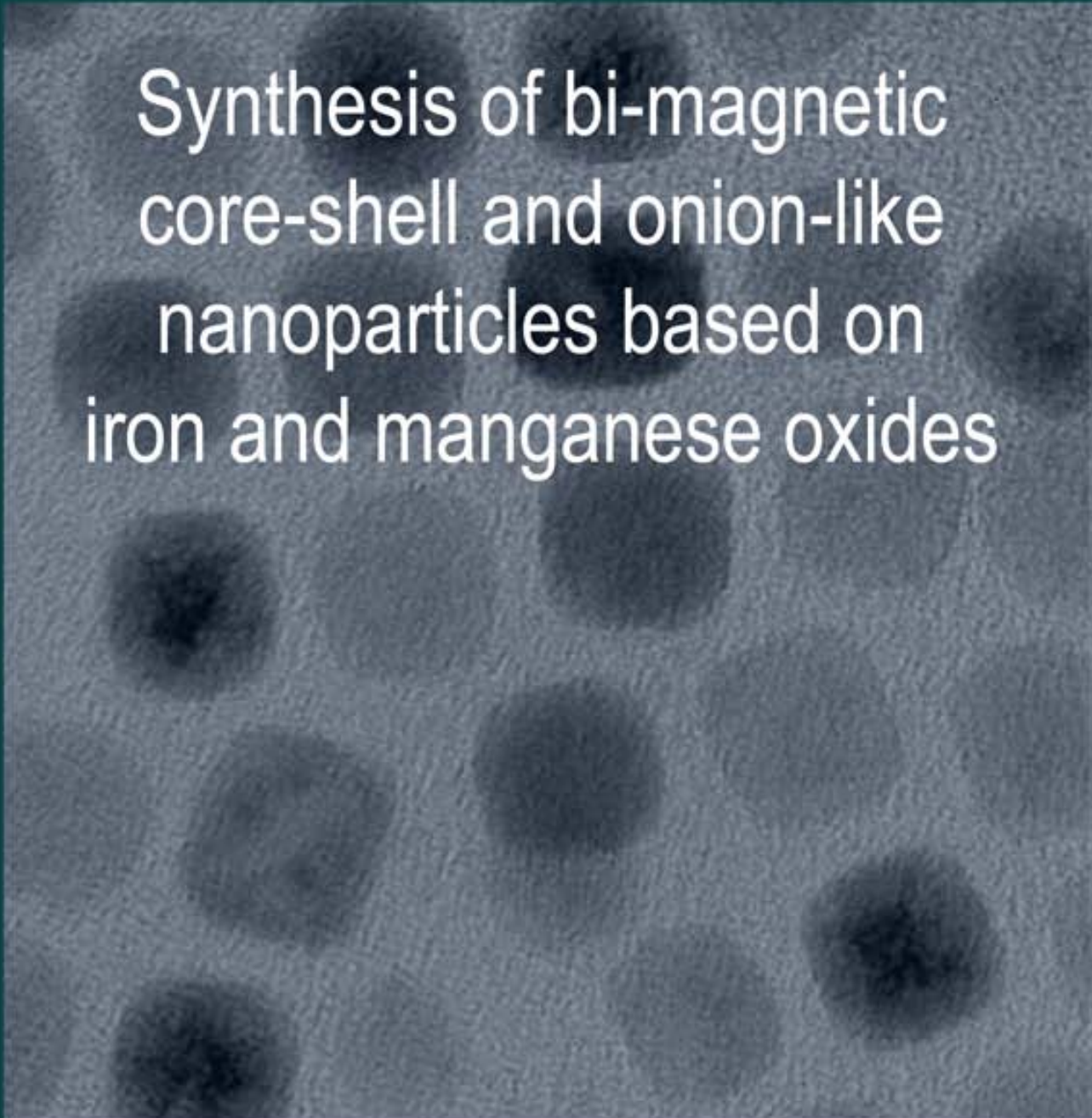


UAB

Universitat Autònoma
de Barcelona



Institut Català
de Nanotecnologia

A grayscale transmission electron micrograph (TEM) showing numerous dark, roughly spherical nanoparticles of varying sizes and some internal structure, scattered across a lighter, textured background.

Synthesis of bi-magnetic core-shell and onion-like nanoparticles based on iron and manganese oxides

Doctoral Thesis presented by **Alberto López Ortega**
and supervised by Josep Nogués Sanmiquel

Institut Català de Nanotecnologia (ICN-CIN2) and
Universitat Autònoma de Barcelona (UAB)
Bellaterra, July 2012

El Dr. Josep Nogués Sanmiquel investigador ICREA de l'*Institut Català de Nanotecnologia (ICN-CIN2)* i professor associat del *Departament de Física* de la *Universitat Autònoma de Barcelona (UAB)*, director de la tesi doctoral realitzada per l'Alberto López Ortega i que porta per títol **Synthesis of bi-magnetic core|shell and onion-like nanoparticles based on iron and manganese oxides**,

FA CONSTAR:

Que l'aportació del doctorand al treball que es presenta ha estat fonamental tant pel que fa al disseny experimental com pel que fa a l'obtenció de les mostres, la realització dels experiments, l'anàlisi de les dades i la discussió i elaboració dels resultats presentats.

I perquè així consti, a petició de la interessada i als efectes oportuns, ho signa a:

Bellaterra, el de de

ALBERTO LÓPEZ ORTEGA

JOSEP NOGUÉS SANMIQUEL



Synthesis of bi-magnetic core-shell and onion-like nanoparticles based on iron and manganese oxides

Doctoral thesis presented by

Alberto López Ortega

and supervised by

Dr. Josep Nogués Sanmiquel

Institut Català de Nanotecnologia (ICN-CIN2)
and Universitat Autònoma de Barcelona (UAB)
Bellaterra, July 2012



Abstract

This thesis deals with the synthesis and magnetic and structural characterization of two different systems based in polymagnetic nanoparticles with core|shell (CS) and onion-like architectures. The first system is formed by a double inverted core-MnO|shell-Mn₃O₄ (γ -Mn₂O₃) where core and shell display an antiferromagnetic (AFM) and ferrimagnetic (FiM) behavior, respectively. It is defined as structurally inverted since the AFM is placed in the core and the FiM in the shell (in contrast to conventional ferromagnetic(FM)/AFM CS systems); in addition, it is, also, magnetically inverted because the Néel temperature of the AFM is larger than the Curie temperature of the FiM (contrarily to standard exchange bias systems). MnO|Mn₃O₄ (γ -Mn₂O₃) CS nanoparticles have been synthesized through the controlled shell passivation of pre-made MnO nanoparticles. This procedure allows reaching a good control over the final core size and shell thickness. It was confirmed that the passivated shell composition depends on the nanoparticle size, where the larger nanoparticles presenting mainly Mn₃O₄. However, when the size diminishes, the density of defects in the MnO core increases and consequently γ -Mn₂O₃ is the more stable shell phase. Besides, small AFM MnO cores can induce a magnetic proximity effect to the FiM γ -Mn₂O₃ shell, maintaining its magnetic order well above its Curie temperature, T_C . Moreover, surface effects in the MnO core can also lead an increase of the Néel temperature of the AFM. Further, given the AFM/FiM exchange coupling the system exhibits large coercivities and loop shifts along the field axis, i.e., exchange bias. The second type of system comprises the synthesis of CS and onion-like nanoparticles based in manganese and iron oxides. Two different iron oxide nanoparticles (FeO|Fe₃O₄, AFM|FiM, CS and single phase FiM Fe₃O₄) have been used as seeds for the posterior manganese oxide deposition. From iron oxide CS seeds two different onion-like nanoparticles (three-components FeO|Fe₃O₄|Mn₃O₄ and four-components FeO|Fe₃O₄|MnO|Mn₃O₄) have been synthesized. The temperature dependence of the magnetization of these onion nanoparticles exhibits several magnetic transitions, in concordance with the presence of diverse magnetic phases. In addition, single phase iron oxide seeds were employed to deposit a manganese thin shells at high temperatures forcing a manganese-iron interdiffusion to form the final Mn_xFe_{3-x}O₄|Fe_xMn_{3-x}O₄ CS nanoparticles with a graded interphase. The structural results show that the (111) planes of the manganese oxide grow epitaxially onto the (111) planes of the truncated faces of the initial cubic iron oxide seeds. Finally, the CS Mn_xFe_{3-x}O₄|Fe_xMn_{3-x}O₄ nanoparticle, formed by soft-FiM|hard-FiM structure with a graded interphase composition, shows a strong exchange coupling between the hard and soft FiM phases.



Resum

Aquesta tesi engloba la síntesi i la caracterització estructural i magnètica de dos tipus de nanopartícules polymagnètiques: estructures nucli-escorça (core|shell, CS) i tipus ceba (onion-like). El primer sistema està format per un nucli-MnO|escorça-Mn₃O₄ (γ -Mn₂O₃) amb doble inversió, on el nucli i l'escorça mostren un comportament AFM i FiM, respectivament. Es defineix com estructuralment inversa ja que l'AFM es localitza al nucli i el FiM a l'escorça; a més, també es troba magnèticament invertida, és a dir, la temperatura de Néel de l'AFM presenta valors més elevats que la temperatura de Curie del FiM. Les nanopartícules nucli-escorça de MnO|Mn₃O₄ (γ -Mn₂O₃) s'han obtingut a través de la passivació controlada de l'escorça de nanopartícules de MnO prèviament sintetitzades. Aquest procés permet controlar tant la grandària del nucli com el gruix de l'escorça. Es va confirmar que la composició de l'escorça un cop passivada depèn de la grandària inicial de les nanopartícules; conseqüentment, les nanopartícules més grans estan formades principalment per Mn₃O₄. No obstant, a mesura que es disminueix la grandària, la densitat de defectes augmenta obtenint, d'aquesta manera, una escorça més estable formada per la fase γ -Mn₂O₃. D'altra banda, nuclis AFM de MnO relativament petits poden induir un efecte magnètic de proximitat (magnetic proximity effects) a l'escorça de FiM γ -Mn₂O₃ tot mantenint el seu ordre magnètic molt per sobre de la seva temperatura de Curie, T_C ; a més, aquest sistema presenta un augment de la temperatura de Néel de l'AFM. El segon sistema es basa en la síntesi de nanopartícules d'òxid de manganès i ferro del tipus nucli-escorça i ceba. Nanopartícules de dos òxids de ferro diferents (FeO|Fe₃O₄ CS i Fe₃O₄ monofàsica) s'han utilitzat com a llavors per a la posterior deposició d'òxid de manganès. A partir de les llavors nucli-escorça d'òxid de ferro s'han sintetitzat dos tipus de nanopartícules ceba (tres-components FeO|Fe₃O₄|Mn₃O₄ i quatre-components FeO|Fe₃O₄|MnO|Mn₃O₄). D'altra banda, nanopartícules d'òxid de ferro monofàsiques han estat utilitzades com a llavors per a dipositar una capa fina de manganès al seu voltant amb l'objectiu d'incentivar l'interdifusió del manganès-ferro i formar nanopartícules nucli-escorça de Mn_xFe_{3-x}O₄|Fe_xMn_{3-x}O₄ amb una interfase graduada. S'ha observat que l'òxid de manganès creix epitaxialment en els plans (111) sobre les cares truncades del llavors cúbiques d'oxid de ferro. Finalment, nanopartícules nucli-escorça de Mn_xFe_{3-x}O₄|Fe_xMn_{3-x}O₄ formades per una estructura tou-FiM/dur-FiM amb una composició gradual a l'interfase demostren un bon l'acoblament magnètic entre ambdues, tova i dura, fases FiM.

*El pasado ha pasado y por el nada hay que hacer
el presente es un fracaso y el futuro no se ve.*

I. Expósito, J.M. Suárez, P. Galán

Symbols and acronyms

| | | | |
|---------------------------------------|---|-----------------------------|---|
| A | exchange stiffness | R | gas constant |
| AC | alternating current | RCP | right-hand circular polarization |
| ACMS | ACSusceptibility & DCMagnetization Option | RLP | left-hand circular polarization |
| acac | acetylacetonate | RT | room temperature |
| AEM | analytical electron microscopy | RSO | reciprocating sample option |
| AFM | antiferromagnetic | r | radius |
| b | neutron-nuclear form factor | r | distance from beam and electron |
| (BH)_{max} | magnetic maximum energy product | rpm | revolutions per minute |
| C | concentration | \bar{s} | spin quantum number |
| CCD | charge-coupled device | S | supersaturation parameter |
| CS | core shell | [S] | surfactant concentration |
| c | speed of light | SEM | scanning electron microscopy |
| cgs | centimeter-gram-second system of units | SMD | single magnetic domain |
| D | diffusion coefficient | SPM | superparamagnetism |
| DBE | dibenzyl ether | SQUID | superconducting quantum interference device |
| DC | direct current | T | Temperature |
| d | diameter | TEM | transmission electron microscopy |
| d_(hkl) | interplanar distance | TEY | total electron yield |
| E | energy | TFY | total fluorescence yield |
| EELS | electron energy loss spectroscopy | TM | transition metals |
| EtOH | ethanol | Torr | pressure units |
| EPR | electron paramagnetic resonance | T_B | blocking temperature |
| ESR | electron spin resonance | T_C | Curie temperature |
| EXAFS | extended X-ray absorption fine structure | T_d | tetrahedral |
| emu | electromagnetic units | T_N | Néel temperature |
| eV | electronvolt | t | time |
| F_(hkl) | structure factor | t_{shell} | shell thickness |
| FC | field cool | V | volume |
| FFT | fast fourier transform | Vf | pseudo-Voigt function |
| FiM | ferrimagnetic | V_M | molar volume |
| FM | ferromagnetic | XANES | X-ray absorption near edge structure |
| FORC | first-order reversal curve | XAS | X-ray absorption spectroscopy |
| FWHM | full width at half maximum | XMCD | X-ray magnetic circular polarization |
| f | atomic form factor | XRD | X-ray diffraction |
| G | Gibbs free energy | xg | centrifugal force expressed in units of gravity |
| Gf | gaussian function | ZFC | zero-field cool |
| g | gram | | |
| g_e | g-factor or gyromagnetic constant | Å | angstrom |
| H | magnetic field | α | diffracted phase |
| HDD | 1,2-hexadecanediol | γ | surface free energy per unit area |
| HOMO | highest occupied molecular orbital | η | variable proportion between Gf and Lf functions |
| Hz | Hertz | θ | diffraction angle |
| H_{ex} | exchange force | λ | wavelength of light |
| ħ | Planck constant | μ_B | Bohr magneton |
| I | intensity | μ_N | nuclear magneton |
| H(Δ2θ) | diffraction peak shape function | μ_s | diffraction linear attenuation coefficient |
| HR-TEM | high resolution TEM images | μ₀ | vacuum permeability |
| (hkl) | family of lattice planes | ν | electromagnetic radiation frequency |
| J_{ex}, J_{ij} | interatomic exchange constant | σ, σ² | particle size distribution |
| \bar{j} | total angular quantum momentum number | φ₀ | magnetic flux quantum |
| K | Kelvin | φ_{mon} | monomer flux |
| K-edge | absorption edge of 1s level | χ | magnetic susceptibility |
| K_e | experimental diffraction constant | | |
| K_{(hkl)α} | diffraction constant for (hkl) family | | |
| k_B | Boltzman constant | | |
| L-edge | absorption edge of 2s2p level | | |
| Lf | lorentzian function | | |
| \vec{l} | orbital angular momentum | | |
| M | magnetization | | |
| [M] | metal precursor concentration | | |
| MC | Monte Carlo method | | |
| MGOe | mega Gauss Oersted | | |
| MPMS | magnetic property measurement system | | |
| m_e | electron mass | | |
| m_S | degenerated spin quantum level | | |
| OA | oleylamine | | |
| Ol | oleate | | |
| Oe | Oersted | | |
| ODE | 1-octadecene | | |
| OIOH | oleic acid | | |
| O_h | octahedral | | |
| PM | paramagnetic | | |
| PPMS | physical property measurement system | | |



Agradecimientos

En primer lugar es de obligada mención que todo este trabajo jamás hubiera podido llevarse a cabo sin la colaboración de muchas personas. Desde el ámbito científico mi director de tesis, jefes de grupo y departamento y los diferentes colaboradores que han sumado su conocimiento en la publicación de los artículos aquí presentados. Sin embargo estos últimos cuatro años han transcurrido también, gracias, a toda esa gente que ha estado a mi lado, cada uno a su manera han resultado, en suma, de una enorme ayuda. A todos ellos quiero expresarles mi más sincera gratitud.

A mi director de tesis, Dr. Josep Nogués, quiero agradecerle toda la confianza depositada en mi, todo su estímulo en mi labor investigadora, las discusiones científicas mantenidas y la dedicación con la que ha dirigido y ha coordinado, entre muchas otras cosas, este trabajo de investigación. Por otro lado cabe mencionar todo el apoyo que me ha brindado a la hora de entrar dentro de este extraño mundo de científicos.

Igualmente quiero agradecer a la Dra. Maria Dolors Baró y al Dr. Santiago Suriñach por la especial dedicación con la cual me han atendido y ayudado en el desarrollo de esta tesis doctoral.

Quiero, muy especialmente, recordar a todos los compañeros y compañeras con los que he dedicado y compartido mi tiempo de trabajo; su inestimable ayuda y compañía han logrado crear esos casi imperceptibles pequeños momentos que sin duda son los responsables de que nuestro mundo siga girando. Un fuerte abrazo a los compañeros del grupo de Magnetic Nanostructures del Institut Català de Nanotecnologia y al grupo de Física de Materials II de la Universitat Autònoma de Barcelona.

Para terminar, agradecer a mis amigos por sus palabras, por soportarme y conseguir demostrarme que todavía hay gente con la cual vale la pena compartir la vida. Agradecer a mi familia todo su apoyo, especialmente la risa del pequeño Joel, coetáneo a este trabajo; al tan enormemente pequeño Murdock por sus maullidos y mordiscos; y finalmente, las últimas líneas están dedicadas a esa persona que es mi par en esta vida, ella que ha estado, ahí, en mis mejores y peores momentos ayudandome y brindandome lo mas bonito de su alma y, ante todo, la sonrisa que es capaz de dibujarme cada mañana. Muchas gracias Alba.



List of Publications

Publications presented in this thesis

- I **Magnetic proximity effect in antiferromagnetic/ferrimagnetic core/shell nanoparticles.** I. V. Golosovsky, G. Salazar-Alvarez, A. López-ortega, M. A. González, J. Sort, M. Estrader, S. Suriñach, M. D. Baró, J. Nogués. *Physical Review Letters*, *102*, 247201, (2009)
- II **Size dependent passivation shell and magnetic properties in antiferromagnetic/ ferrimagnetic, core/shell, MnO nanoparticles.** A. López-Ortega, D. Tobia, E. Winkler, I. V. Golosovsky, G. Salazar-Alvarez, S. Estradé, M. Estrader, J. Sort, M. A. González, S. Suriñach, J. Arbiol, F. Peiró, R. D. Zysler, M. D. Baró, J. Nogués. *Journal of the American Chemical Society*, *132*, 9398-9407, (2010).
- III **Two-, Three-, and Four-Component Magnetic Multilayer Onion Nanoparticles Based on Iron Oxides and Manganese Oxides.** G. Salazar-Alvarez, H. Lidbaum, A. López-Ortega, M. Estrader, K. Leifer, J. Sort, S. Suriñach, M. D. Baró, and J. Nogués. *Journal of the American Chemical Society*, *133*, 16738-16741, (2011).
- IV **Strongly exchange coupled inverse ferrimagnetic soft|hard, $Mn_xFe_{3-x}O_4|Fe_xMn_{3-x}O_4$, core|shell heterostructured nanoparticles.** A. López-Ortega, M. Estrader, G. Salazar-Alvarez, S. Estradé, I. V. Golosovsky, R. K. Dumas, D. J. Keavney, M. Vasilakaki, K. N. Trohidou, J. Sort, F. Peiró, S. Suriñach, M. D. Baró, and J. Nogués. *Nanoscale*, DOI:10.1039/C2NR30986F, (2012).

Other publications

- I **Synthesis of compositionally graded Nanocast NiO/NiCo₂O₄/Co₃O₄ mesoporous composites with tunable magnetic properties.** M. Cabo, E. Pellicer, E. Rossinyol, M. Estrader, A. López-Ortega, J. Nogués, O. Castell, S. Suriñach, M. D. Baró. *Journal of Materials Chemistry*, *20*, 7021-7028, (2010).
- II **Magnetic measurements as a sensitive tool for studying dehydrogenation processes in hydrogen storage materials.** E. Menéndez, S. Garroni, A. López-Ortega, M. Estrader, M. O. Liedke, J. Fassbender, P. Solsona, S. Suriñach, M. D. Baró and J. Nogués. *Journal of Physical Chemistry C*, *114*, 16818-16822, (2010).
- III **Role of the oxygen partial pressure in the formation of composite Co-CoO nanoparticles by reactive aggregation.** J. A. De Toro, J. P. Andrés, J. A. González, J. M. Riveiro, M. Estrader, A. López-Ortega, J. Nogués. *Journal of Nanoparticle Research*, *13*, 4583-4590, (2011).
- IV **Distinguishing the core from the shell in MnO_x/MnO_y and FeO_x/MnO_x core/shell nanoparticles through quantitative electron energy loss spectroscopy (EELS) analysis.** S. Estradé, Ll. Yedra, A. López-Ortega, M. Estrader, G. Salazar-Alvarez, M. D. Baró, J. Nogués, F. Peiró. *Micron*, *43*, 30-36, (2012).
- V **3D ordered nanocomposite mesoporous Fe_xCo_{3-x}O₄@Co₃O₄ multifunctional heterostructured materials.** E. Pellicer, M. Cabo, A. López-Ortega, M. Estrader, L. Yedra, S. Estradé, F. Peiró, Z. Saghi, P. Midgley, E. Rossinyol, I. V. Golosovsky, A. Mayoral, J. D. Prades, S. Suriñach, M. D. Baró, J. Sort and J. Nogués. *submitted*, (2012).
- VI **Resolving material-specific structures within Fe₃O₄| γ -Mn₂O₃ core|shell nanoparticles using anomalous small-angle x-ray scattering (ASAXS).** K. L. Krycka, J. A. Borchers, G. Salazar-Alvarez, A. López-Ortega, M. Estrader, S. Estradé, J. Sort, F. Peiró, M. D. Baró, C. C. Kao, and J. Nogués. *submitted*, (2012).
- VII **Hard x-ray RIXS-MCD as a novel magnetic probe for the investigation of core-shell nanoparticles.** A. Juhin, A. López-Ortega, M. Sikora, M. Estrader, S. Estradé, F. Peiró, M. D. Baró, P. Sainctavit, P. Glatzel and J. Nogués *submitted*, (2012).
- VIII **EEL spectroscopic tomography: towards a new dimension in nanomaterials analysis.** Ll. Yedra, A. Eljarrat, R. Arenal, F. de la Peña, E. Pellicer, M. Cabo, A. López-Ortega, M. Estrader, M. D. Baró, S. Estradé and F. Peiró *submitted*, (2012).



Contents

| | |
|---|-----------|
| Abstract | vii |
| Resum | ix |
| Symbols and acronyms | xiii |
| Agradecimientos | xv |
| List of Publications | xvii |
| 1 Introduction to nanostructures | 1 |
| 1.1 Quasi-Zero dimensional structures: Nanoparticles | 3 |
| 1.1.1 Nanoparticles synthesis | 3 |
| 1.1.2 Nanoparticles applications | 5 |
| 1.1.3 Magnetic nanoparticles | 6 |
| 2 Introduction to magnetic nanoparticles | 7 |
| 2.1 Magnetic materials | 7 |
| 2.2 Magnetic properties of nanoparticles | 12 |
| 2.2.1 Single magnetic domain, SMD | 13 |
| 2.2.2 Superparamagnetism, SPM | 13 |
| 2.2.3 Surface effects | 15 |
| 2.2.4 Inter-particle interaction effects | 16 |
| 2.3 Exchange-spring magnets | 17 |
| 2.4 Exchange bias | 20 |
| 3 Core Shell (CS) magnetic nanoparticles | 25 |
| 3.1 FM(FiM) AFM exchange-coupled CS nanoparticles | 26 |
| 3.2 Hard-FM(FiM) Soft-FM(FiM) exchange-coupled CS nanoparticles | 28 |
| 4 Experimental Techniques | 33 |
| 4.1 Transmission electron microscopy, TEM | 33 |
| 4.1.1 Image mode in TEM | 35 |
| 4.1.2 Electron energy loss spectroscopy, EELS | 36 |
| 4.2 Diffraction analysis techniques | 37 |
| 4.2.1 Bragg's law | 38 |
| 4.2.2 Intensity of diffraction peaks | 38 |
| 4.2.3 Peak shape function | 39 |
| 4.2.4 Rietveld refinement | 40 |
| 4.2.5 Powder X-ray diffraction, XRD | 40 |
| 4.2.6 Neutron diffraction | 42 |
| 4.3 Magnetometric measurements | 44 |
| 4.3.1 First-order reversal curve, FORC | 46 |
| 4.4 Electron spin resonance, ESR | 48 |
| 4.5 X-ray Absorbption spectroscopy, XAS | 49 |
| 4.5.1 X-ray Magnetic circular dichroism, XMCD | 52 |

| | | |
|----------|---|------------|
| 4.6 | Monte Carlo, MC, simulations | 53 |
| 5 | Synthetic aspects and parameters | 57 |
| 5.1 | Nucleation and growth theory | 57 |
| 5.1.1 | Nucleation | 57 |
| 5.1.2 | Growth | 59 |
| 5.1.3 | Separating the Nucleation and Growth processes | 60 |
| 5.2 | Synthesis of manganese and iron oxide nanoparticles | 60 |
| 5.2.1 | Products used in the synthesis | 61 |
| 5.2.2 | Synthesis of the core-MnO shell-Mn ₃ O ₄ (γ -Mn ₂ O ₃) system | 61 |
| 5.2.3 | Synthesis of core-FeO shell-Fe ₃ O ₄ and Fe ₃ O ₄ systems | 64 |
| 5.2.4 | Seed-growth synthesis of core-iron oxides shell-manganese oxides systems | 67 |
| 6 | Articles | 71 |
| 6.1 | AFM FiM MnO-core Mn ₃ O ₄ (γ -Mn ₂ O ₃)-shell nanoparticles | 71 |
| 6.1.1 | Article #1: Magnetic proximity effect features in antiferromagnetic/ferrimagnetic core-shell nanoparticles | 73 |
| 6.1.2 | Article #2: Size-dependent passivation shell and magnetic properties in antiferromagnetic/ferrimagnetic core/shell MnO nanoparticles | 81 |
| 6.2 | Soft-FiM hard-FiM Fe ₃ O ₄ -core Mn ₃ O ₄ -shell nanoparticles | 97 |
| 6.2.1 | Article #3: Two-, three-, and four-component magnetic multilayer onion nanoparticles based on iron oxides and manganese oxides | 99 |
| 6.2.2 | Article #4: Strongly exchange coupled inverse ferrimagnetic soft hard, Mn _x Fe _{3-x} O ₄ Fe _x Mn _{3-x} O ₄ , core shell heterostructured nanoparticles | 115 |
| 7 | Conclusions | 131 |
| | Future work | 132 |
| | Bibliography | 134 |





Chapter 1

Introduction to nanostructures

Nowadays, terms as nanoscience and nanotechnology have become household words for the vast majority of society since they are, in part, responsible for the current scientific and technological revolution. The prefix nano, which defines the working scale, is derived from the Greek word *dwarf* (nanos), giving a clear indication of the reduced dimension involved in these systems. The placement of nano in the metric scale to $1\text{ nm} = 10^{-9}\text{ m}$ (i.e., one million times smaller than 1 mm), makes it clear that these dimensions are impossible to distinguish for the naked eye. Specifically, nanoscience can be defined as the study of the fundamental principles of structures with at least one dimension roughly between 1 and 100 nanometers. These dimensions are 1/1000 smaller than structures resolvable by the naked eye but still 1000 times larger than an atom. These structures are known as nanostructures and can be considered as a bridge between atomic and bulk dimensions. Thus, it's important to understand that *the nanoscale is not just small, it is a special kind of small* [1]. Then, nanotechnology is delimited as the methods, techniques and applications of these nanostructures.

The word nanotechnology was first introduced by Naori Taniguchi in 1974. [2] But it was, in fact, at the end of the 60's when Richard Feynman first presented to the scientific community the enormous perspective of this field. Envisioning the power of controlling things on a small scale was the aim of science and technology for the following years. From the early 80's to nowadays nanotechnology and nanoscience have been developing to overcome the established technical limits. Following the scientific developments, nanotechnology applications are turning into useful and common tools for all mankind.

During the 80's the first main works in nanotechnology were developed. The discovery of the scanning tunneling microscope (STM) in 1982 [3], which was awarded the first Nobel prize in the nanotechnology field (1986), and buckminsterfullerene, 1986 [4] (Nobel prize in 1996) showed to the scientific community the enormous interest of this new emerging field, nanotechnology. However, during the 90's and even more in the new millennium the developments in this field made it grow faster than any other scientific field in the history. New materials, novel technical characterizations and their wide range of applications have made nanotechnology leap to the top of science and technology research. Due to these new perspectives a great number of research groups all over the world are focusing their work into the nanoscience and nanotechnology.

The enormous interest generated by nanoscale research is reflected in the huge increase of the investment aimed at this field. Tacking as example the US National Nanotechnology Initiative (NNI), the budget provided by U.S. government for 2012 has reached \$2.1 billion. Comparing to the the budget for 2005, \$500 million, the funding efforts have increased more than 1000 times in only five years and the cumulative NNI investment since fiscal year 2001, including the 2012 request, now totals over \$16.5 billion. [5, 6]

Nanoscience and nanotechnology is, nowadays, broadly used in virtually all the fundamental and applied sciences. Areas such as physics [7, 8], chemistry, [9] biology, [10] and medicine [11] are developing the nanoscale as a cardinal tool in their research. Well established applications can be found in fundamental physics, materials science and medicine as examples of their importance.

The unique properties and the improved performances of nanomaterials are determined, principally, by their size. Dimensions below 100 nm in size can be considered as a *lost dimension* and, therefore, nanostructures are defined as a bulk material which has lost one, two or three of its dimensions. Then, nanostructure materials can be schematized as a function of their dimensionality (D). The main types of nanocrystalline materials as regards to their dimensionality are: [12]

- Quasi Zero-dimensional (0D): nanoparticles, clusters and quantum dots with none of their three dimensions larger than 100 nm.
- One-dimensional (1D): nanowires and nanotubes, with two dimensions in the nanoscale.
- Two-dimensional (2D): thin films and multilayers, with only one dimension in the nanoscale.
- Three-dimensional (3D): mesoporous structures and 3D arrays of nanoparticles.

The size reduction in nanostructured materials can dramatically alter the fundamental well-established physical and chemical properties exhibited by the same materials in their bulk form. The changes in properties displayed as the size is reduced have several origins. Firstly, given their small size thermodynamic effects can alter the properties. For example, superparamagnetism appears because the reduction in size make the magnetic energy of the particle comparable to the thermal energy of the system. [13,14]

Another source from physico-chemical changes in nanostructures arises from the commensurability of the nanoscaled dimensions with the characteristic physico-chemical length scales, such as electron mean free path, domain wall width, diffusion length or superconducting coherence length. [15]

A part from finite size effects, nanostructures can vary their bulk properties due to other effects which arise directly from the size reduction. There are basically two types of size-dependent effects: smoothly scalable ones which are related to the fraction of atoms at the surface, and quantum effects which show discontinuous behavior due to completion of shells in systems with delocalized electrons.

One reason for the change in the physical and chemical properties of nanostructures as their size decreases is the increased fraction of the surface atoms, which often differ from those of the bulk of the material (coordination number, symmetry of the local environment, etc.). From the energy stand-point, a decrease in the particle size results in an increase in the fraction of the surface energy in its chemical potential. In fact, the main example of this effect are nanoparticles. In contrast with the other related nanostructures, nanoparticles, present large surface effects due to their quasi zero-dimensionality. [15,16]

In the last 30 years many new properties for nanoscale materials have been theoretically and experimentally proven. Some representative examples of these are:

Lower melting point or phase transition temperature, appreciably reduced lattice constants, which are related to a huge fraction of surface atoms in the total amount of atoms; the mechanical properties of nanomaterials may reach the theoretical strength, which are often one or two orders of magnitude larger than the ones observed in bulk form; optical properties can be significantly different from bulk crystals, e.g. the optical absorption peak of a semiconductor nanoparticle shifts to shorter wavelength, due to an increased band gap and the color of metallic nanoparticles may change with their sizes due to surface plasmon resonances; the electrical conductivity decreases with reduced dimensions due to increased surface scattering, although electrical conductivity of nanomaterials could also be enhanced appreciably, due to the improved structural ordering in microstructures; magnetic properties of nanostructured materials are distinctly different from those of bulk materials, where, for example, surface effects can increase/reduce the anisotropy of the system; self-purification is an intrinsic thermodynamic property of nanostructures and nanomaterials, where heat treatment increases the diffusion of impurities, intrinsic structural defects and dislocations, allowing to easily push them to the surface; the increased perfection of the crystals could have appreciable impact on the chemical and physical properties, for example, chemical stability would be enhanced. [15]

1.1 Quasi-Zero dimensional structures: Nanoparticles

A nanoparticle is a quasi-zero-dimensional (0D) nano-object in which all characteristic linear dimensions are of the same order of magnitude (not more than 100 nm). Because of this very small size scale, nanoparticles possess an immense surface area per unit volume, i.e., a huge number of atoms are located on the surface and near surface layers, and they have the ability to exhibit quantum effects. Importantly, the resulting unique properties of nanoparticles cannot be anticipated from a simple extrapolation of the properties of bulk materials. Nanoparticles exist with great chemical diversity in the form of metals, metal alloys, metal oxides, multi-metallic oxides, other non-oxide compounds and organic based materials (such as, polymers, carbon and organometallic compounds). They also exhibit great morphological diversity with shapes such as spheres, cylinders, disks, platelets, hollow spheres, tubes, and so on. Moreover, they can be found free standing (as powder) or in very diverse environments (solid foams, aerosols; gel, ferrofluids; solid sol, nanocomposites). Currently, the unique physical and chemical properties of nanoparticles are under intensive research. [17]

1.1.1 Nanoparticles synthesis

Nanoparticles can be generated via a number of different synthetic routes based on gas, liquid or solid phase approaches. These different synthetic routes can be divided in two main groups: physical and chemical approaches. Both approaches can be carried out in either gas, liquid, supercritical fluids, solid state, or in vacuum. In most of cases, one is interested in the ability to control: i) particle size ii) particle shape iii) size distribution iv) particle composition and/or v) degree of particle agglomeration.

Some examples of these methods are, for example, physical approaches: flame pyrolysis, high temperature evaporation, plasma synthesis, microwave irradiation, physical deposition synthesis or mechanical processes of size reduction including grinding, milling and mechanical alloying and for chemical approaches: chemical vapor deposition synthesis or liquid phase methods, also known as wet chemistry routes, in which chemical reactions in solvents lead to the formation of colloids and molecular self-assembly.

Physical methods allow the production of a broad range of different materials and usually large amounts of product, due to their large reaction yield. However, these methods present some drawbacks because often size, shape and size dispersion cannot be well controlled. However, wet chemistry methods can frequently give better control than physical ones, in terms of homogeneous sizes, uniform shapes and small size dispersions. Interestingly, these methods allow obtaining an extremely narrow size distribution, which is commonly called monodispersity (i.e. below 10%). Another interesting advantage to create nanoparticles using wet chemistry methods is the use of organic molecules, surfactants, which are anchored at the surface. These surfactants are useful to stabilize colloidal solutions and to avoid nanoparticle agglomeration, also surfactants can reduce the surface roughness [18] and control the nanoparticle size. [19, 20] On the other hand the main drawback presented by this synthetic routes is their small yield, typically providing amounts of products in the range of the milligrams.

The main methods to synthesize inorganic nanoparticles through wet chemistry routes are: precipitation; hydrothermal; hydride reduction; micellar or microemulsion; thermolysis (organometallic decomposition); photolysis and sonolysis; sol-gel and polyol. [21–25]

Precipitation is one of the oldest techniques for the synthesis of nanoparticles. In precipitation reactions, the metal precursors are dissolved in a common solvent (such as water) and a precipitating agent is added to form an insoluble solid. In most cases, a further reduction step is required, in solution, after synthesis. Many nanoparticles can be synthesized using these classical aqueous precipitation reactions to yield nanoparticles that often have broad size distribution and irregular morphology. The major advantage of precipitation reactions is that large quantities of particles can be synthesized. However, it is difficult to tailor the particle size since only kinetic factors are available to control growth. [26–28]

Hydride reduction of metal salts using sodium borohydride can form very uniform spherical nanoparticles. The chemistry of the reduction can be very complex, however the reduction of iron, cobalt and nickel has been explained in detail by Klabunde et al. [29] Although metal boride formation is a stable reaction, it can be eliminated with careful control of atmosphere and water content in the reaction.

For this reason, the reactions are typically carried out in non-aqueous media. Some examples of the nanoparticles obtained through this method are metal [30] and metal alloy [31, 32] nanoparticles.

Hydrothermal reactions are aqueous reactions carried out using autoclaves or high pressure reactors where the pressure can be over 10^5 Tor at temperatures above 200°C . Water acts as a reactant at these supercritical conditions, accelerating the kinetics of the hydrolysis reactions. At increased temperatures, the solubility of most ionic species increases and, with the lower viscosity of water, exhibits greater mobility. Size and morphological control in hydrothermal reactions is achieved by controlling time and temperature. The reaction conditions of precursor material and pH have an impact on the phase purity of the nanoparticles. [33–35]

Micelle synthetic routes use surfactant molecules which in solution spontaneously form spherical aggregates called micelles or microemulsions. The micelle aggregates have sizes of 1-10 nm in diameter, while microemulsions contain aggregates that are 10-100 nm in diameter. [21] Direct micelles have the hydrophilic portion of the surfactant on the outside of the aggregate exposed to polar solvent, while reverse or inverse micelles have the hydrophobic portion on the outside exposed to a non-polar solvent. In the case of reverse micelles formed in hydrocarbons, water can be readily solubilized forming a water pool where size is characterized by a water/surfactant ratio. In this fashion, the water pools within micelles impose kinetic and thermodynamic constraints on particle formation resulting in restricted nano-reactors. Many of the reactions carried out in micelles are very similar to those performed in bulk aqueous reactions, but with the added morphological controls afforded by the surfactant system. [36–38] Notably, this approach have been extensively used to synthesize polymeric (organic compounds) nanoparticles. [39]

Thermolysis (or thermal decomposition) is one of the simplest methods to prepare nanoparticles and is based on the decomposition of organometallic precursors. The relatively low decomposition temperature of organometallic compounds is a distinct advantage over other processing techniques. The decomposition temperature controls the nanoparticle growth. Since size and morphology have an effect on the properties of the nanoparticles, control of these properties is a primary goal. In many cases, polymers, organic capping agents or structural hosts are used to limit the size of the nanoparticle. The polymers and capping agents are generally used to sterically protect the particles so that they do not coalesce. The general scheme of the organometallic route can be described as two representative synthetic procedures. The first is that pyrolysis of organometallic reagents is initiated by their rapid injection into a hot high boiling point solvent, providing temporally discrete homogeneous nucleation and permitting controlled growth of particles. The second is that reagents including organometallic compounds are mixed at low temperature and the resulting solution is slowly heated in controlled manner to generate nuclei. The particle growth occurs by the further addition of resultants, or particle size is increased by aging at high temperature by Oswald ripening. The growth of particles can be stopped by the rapid decrease of reaction temperature. [40–42] Through the careful control of reaction conditions such as time, temperature and the concentration of reagents and stabilizing surfactants, uniformity of the particle size distribution can be achieved. A typical example of this synthetic procedure is the preparation of CdSe. [43]

Similar procedures to thermolysis are the sonolysis and photolysis, which use sound (ultrasound or acoustic waves) and light, respectively, to decompose the organic precursor instead of heat as in the case of thermolysis. Although these methods have been less developed than thermolysis, a broad range of different nanoparticles have been produced by these approaches. [44–48]

Sol-gel processing can be used to prepare a variety of materials, including glasses, powders, films, fibres, and monoliths. Traditionally, the sol-gel process involves hydrolysis and condensation of metal alkoxides. Metal alkoxides are good precursors because they readily undergo hydrolysis, i.e., the hydrolysis step replaces an alkoxide with a hydroxide group from water and a free alcohol is formed. Once hydrolysis has occurred the sol can react further and a condensation reaction (polymerization in some cases) occurs. Factors that need to be considered in a sol-gel process are solvent type, temperature, precursors, catalysts, pH, additives and mechanical agitation. [49] These factors can influence the kinetics, growth, and hydrolysis and condensation reactions. Because these reactions are usually carried out at room temperature, further heat treatments need to be performed to achieve the final crystalline

state. This usually causes the aggregation of the produced nanoparticles and often avoid the formation of uniform-sized particles. Therefore, it is very difficult to obtain monodisperse nanoparticles through hydrolytic sol-gel route. However, monodispersed nanoparticles can still be prepared by a modified hydrolytic sol-gel route, where the hydrolysis, condensation and crystallization occur in a high boiling point solvent under the protection of surfactant. [49–51] The non-hydrolytic sol-gel approach for the preparation of metal oxides and multi-metallic oxides was established in the early 90s, although it recently became a new route for the synthesis uniform-sized nanoparticles. [52–54]

The polyol method, in which the polyol acts as solvent, reducing agent, and surfactant, is a suitable method for preparing nanophase and micrometer size particles with well defined shapes and controlled particle sizes. By this method, precursor compounds such as oxides, nitrates, and acetates are either dissolved or suspended in a diol, such as ethylene glycol or diethylene glycol. The reaction mixture is then heated to reflux at, roughly, 185 °C. During the reaction, the metal precursors become solubilized in the diol, form an intermediate, and then are reduced to form metal nuclei, which form metal particles. [55,56] By modifying the polyol method with the addition of water to act more like a sol-gel reaction (forced hydrolysis), oxides can also be prepared. [57,58]

1.1.2 Nanoparticles applications

Nanoparticles, as a part of the nanoscale revolution, have become an important tool for a wide range of applications. The main three new effects emerging from small scale: finite size, surface and quantum effects has lead the scientific community to use these novel properties to produce a broad range of new applications. In fact, limitations to certain applications induced by the properties of bulk materials have been overcome by the use of nanoparticles and nanostructured materials, in very diverse fields as electronics, [59] optics, [60] chemical [61] and mechanical [62].

One of the most active fields of nanoparticle application is in diverse biomedical fields. Interestingly, the fact that nanoparticles exist in the same size domain as proteins makes nanomaterials suitable for bio tagging or labelling. However, size is just one of many necessary characteristics of nanoparticles, which in itself is rarely sufficient for biological tagging. In order to interact with biological targets, a biological or molecular coating or layer acting as a bioinorganic interface should be attached to the nanoparticle. Examples of biological coatings may include antibodies, biopolymers like collagen, [63] or monolayers of small molecules that make the nanoparticles biocompatible. [64] Some applications of nanomaterials in biology or medicine are: fluorescent biological labels, drug and gene delivery, bio detection of pathogens, detection of proteins, probing of DNA structure, tumor destruction via heating (hyperthermia), MRI contrast enhancement, and so on. [10,11,65–67]

Some other more general applications of the nanoparticle can be classified as a function of their area of interest:

Chemical: Chemical catalysis benefits especially from nanoparticles, due to the extremely large surface to volume ratio. The application potential of nanoparticles in catalysis ranges from fuel cell to catalytic converters [68,69] and photocatalytic devices. [70,71] Catalysis is also important for the production of chemicals. [72,73]

Optical: Nanoparticles can be engineered and used for anti-reflection coatings, [74] producing specific refractive index for surfaces, [75] or also providing light based sensors. [76–78]

Magnetic: Nanoparticles have the potential to increase the density of various storage media, [79,80] magnetic separation, [81] highly sensitive biosensing, [82,83], and also can improve the detail and contrast of MRI images. [84]

Thermal: Specifically engineered particles could improve the transfer of heat from collectors of solar energy to their storage tanks. [85] They could also enhance the coolant system currently used by transformers in these types of processes. [86]

Mechanical: Nanoparticles could provide improved wear and tear resistance for almost any mechanical device. [87] They could also give these devices previously unseen anti-corrosion abilities, [88] as well as creating entirely new composites and structural materials that are both lighter and stronger than those we use today.

Electronic: Because of their tiny size, nanoparticles are inherently poised to aid in the production of high performance delicate electronics. [89] Moreover, nanoparticle electronics can create digital displays that are more electricity-efficient, less expensive to produce, brighter in color, and also larger. [90–92]

Energy: Nanoparticle batteries would be longer-lasting and have a higher energy density than those we use today. [93] Metal nanoparticle clusters could also have revolutionary applications for hydrogen storage; they could also produce extremely efficient fuel cells by acting as electrocatalysts for these devices. [94, 95] Nanoparticles may also pave the way for practical and renewable energy; they have already demonstrated an ability to improve solar panel efficiency many times over. Not only that, but when nanoparticles are used as catalysts in combustion engines, they have shown properties that render the engine more efficient and therefore more economic. [96]

1.1.3 Magnetic nanoparticles

Magnetic nanoparticles are an important family within the 0D materials. These nanoparticles are usually composed by magnetic transition metals (iron, nickel, cobalt and manganese) and rare-earth elements (samarium, lanthanum, niobium,...) and can be found as metal, metallic alloys, oxides, other related ceramic compounds (nitrides, borides, etc..) and organometallic nanoparticles based in magnetic elements. Their structure is essentially crystalline, although can also present some amorphous parts and in most some cases amorphous nanoparticles can, also, present magnetism.

The fundamental motivation for the study of magnetic nanoparticles is the dramatic change in magnetic properties that occurs when the material is reduced to the nanoscale, particularly, when the critical length that governs the physical properties of the system (e.g., domain wall width) is comparable to the size of the nanoparticles.

From this point of view, three main effects ascribed to the reduction in size are the responsible for the new properties of magnetic nanoparticles. These effects are: finite size, surface effect (large surface-to-volume ratio) and interparticle interaction. Probably, single magnetic domain (SMD) [97, 98] particles and their related superparamagnetic (SPM) behavior [13, 14, 98] are the most known effects ascribed to magnetic nanoparticles and are a direct consequence of the finite size of these particles. On the other hand, it has been demonstrated that surface effects [14, 99–102] in nanoparticles and interparticle interaction (dipole-dipole, exchange,...) [103, 104] play an important role in the final magnetic properties of the system leading some effects such as high field irreversibility, high saturation field, extra anisotropy contributions or shifted loops after field cooling. These properties will be discussed in more detail in Chapter 2.

The magnetic properties of nanoparticles are determined by many factors, where the key parameters are the chemical composition, the type crystal structure, the particle size and shape, the morphology (for structurally inhomogeneous particles), the interaction of the particle with the surrounding matrix and the neighboring particles. Thus, by changing the nanoparticle size, shape, composition and structure, one can control to a certain extent the magnetic characteristics of the material based on them.

Given the novel properties of magnetic nanoparticles and the fine control of the characteristic parameters during the synthesis, their range of applications has been broadened during the last decade. Industrial applications of magnetic nanoparticles cover a broad spectrum of different areas from medical applications to their use as permanent magnets in motors. Some examples of these applications are: magnetic seals in motors, [105] magnetic inks, [106] magnetic recording media, [79, 80] magnetic separation, [81] magnetic resonance amplification [107] and biomedical applications such as magnetic resonance contrast media (MRI), [84] highly sensitive biosensing, [82, 83] drug delivery, [108] and hyperthermia. [109, 110]

Chapter 2

Introduction to magnetic nanoparticles

2.1 Magnetic materials

Magnetic materials are defined as materials which present a response in the presence of an external magnetic field. This magnetic response lies in the motion of the electrons. Since electrons are charged objects, $1.602 \cdot 10^{-19}$ Coloumbs, their movement produces a magnetic field as predicted by the electromagnetic theory. Then electrons can show two different magnetic momentums: i) electron shows an angular momentum or orbital magnetic dipole moment, ($l_{electron}$), which is related to its spatial movement in an specific electronic orbital around the atomic nucleus and ii) electron spin, ($s_{electron}$), which describes an effect, which can be interpreted as a revolution of the electron around its own axis. Although materials are composed of an enormous number of atoms, with large quantity of electrons in them, only a few of these electrons can be considered as magnetic. The magnetic moment of the atom can be assumed as the vector sum of all its electronic moments. Thus, taking into account the Pauli's exclusion principle, which states that the maximum number of electrons placed in an orbital state can be only two and their spins must be antiparallel aligned, the spin vector sum can give to results i) the magnetic moments of all the electrons are so oriented that they cancel each other out, and the atom as a whole has no net magnetic moment and ii) the cancelation of electronic moments is only partial and the atom is left with a net magnetic moment. Then, we define as a magnetic material as the one that has unpaired electrons in their atomic or molecular orbital, impeding the cancelation of the magnetic moment created by the movement of the spins. In fact, only the HOMO, highest occupied molecular orbital, can present unpaired electrons and for elements with their HOMO in the d-level and f-level the maximum number of unpaired electron per atom can be 5 and 7, respectively. Even if each magnetic atom generates a magnetic moment, if these moments are disposed at random, the net effect of the vector sum will be zero and the material will have not net moment. However, the magnetic moment of each atom that forms a magnetic material can interact with the magnetic moment of the other atoms in the structure. The field generated by the interactions between atomic magnetic moments is equivalent to that of an imaginary magnetic field called the molecular field. The physical origin of the molecular field arises from quantum-mechanical exchange forces, H_{ex} . Exchange force, an entirely non-classical force, depends on the relative orientation of the spins of the two interacting atoms. Then we define an exchange integral or inter-atomic exchange interactions, J_{ex} , proportional to the exchange energy, E_{ex} , between two spins. If J_{ex} is positive, E_{ex} is a minimum when the spins are parallel and a maximum when they are antiparallel. If J_{ex} is negative, the lowest energy state results from antiparallel alinement. This sign and strength of the exchange interactions give rise to different types of magnetic materials. [111]

We can classify magnetic materials basically into five different magnetic behaviors: diamagnetism, paramagnetism (PM), ferromagnetism (FM), antiferromagnetism (AFM) and ferrimagnetism (FiM). [111,112] This sorting takes into account different conditions such as the presence of unpaired electrons, their exchange energy and the sign of the exchange integral.

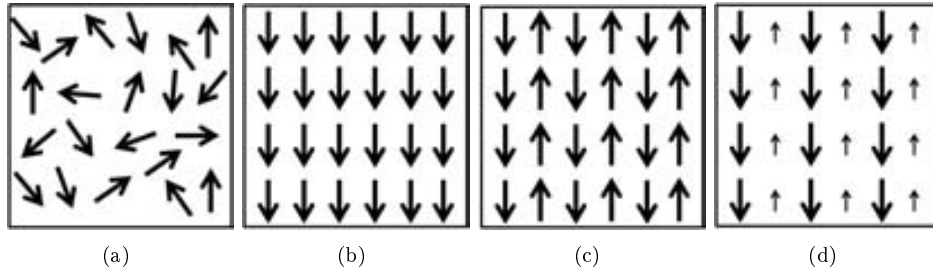


Figure 2.1: Spin order in magnetic materials: (a) paramagnetism (PM), (b) ferromagnetism (FM), (c) antiferromagnetism (AFM) and (d) ferrimagnetism (FiM)

Diamagnetic materials present closed-shell electronic structures, i.e., no unpaired electrons are present. Diamagnetic materials do not present atomic magnetic moment since the vector sum of all electron magnetic moments in each atom is canceled. However, the orbital electron motion is always present and it can create a weak magnetic signal in opposite direction of the magnetic field applied, according with Lenz's law (see figure 2.2(a)).

In contrast to diamagnetic materials, the atoms in **paramagnetic**, PM, materials have unpaired electrons and, consequently they present a net atomic magnetic moment allowing the possibility of a net magnetism in the solid. Although the atoms in the solid are structurally ordered in a crystal lattice, the magnetic moments of each atom are oriented randomly (see figure 2.1(a)) without an effective exchange energy between neighboring atoms. Therefore, the random orientation of the atomic moments leads to a zero net magnetic moment in the solid. However, when a magnetic field is applied all of the atomic moments can be aligned, which results in a macroscopic magnetic moment different from zero. The induced magnetism is rather weak and increases linearly with field, although it tends to saturate for very high fields (see figure 2.2(a)). The susceptibility, δ , which indicates the degree of magnetization of a material in response to an applied magnetic field ($\delta = M/H$), is inversely proportional to the temperature, i.e., the Curie's law (see equation 2.1), where C is a specific constant of each material. Namely, when the temperature increases δ decreases, indicating that the global magnetization is reduced because of the increased fluctuation of the magnetic moments due to the thermal agitation and, thus, the magnetic moments are more difficult to align with the field.

$$\delta = \frac{C}{T} \quad (2.1)$$

Similarly to paramagnetic materials, **Ferromagnetic** (FM), **antiferromagnetic** (AFM) and **ferrimagnetic** (FiM) solids have unpaired electrons. However, in contrast to paramagnetic materials, in FM and AFM materials the atoms, placed in a crystal lattice, present a strong exchange interaction, H_{ex} . This exchange coupling makes that the magnetic moment of each atom is coupled to the neighboring atomic moments. In this case, these materials exhibit a long-range ordering phenomenon at the atomic level which causes the unpaired electron spins to line up parallel/antiparallel with each other. The Curie law is no longer valid for these materials and they exhibit a non-linear dependence of $1/\delta$ with temperature.

The Pauli exclusion principle leads to the Heisenberg model of magnetic exchange, where inter-atomic exchange interactions, H_{ex} , can be described phenomenologically according to the Hamiltonian (see equation 2.2):

$$H_{ex} = -2 \sum_{i < j} J_{ij} s_i \cdot s_j \quad (2.2)$$

Here s_i and s_j are atomic spins at different neighboring sites. The value of the exchange coefficient or exchange constant, J_{ij} , is strongly related to the electronic overlap of the two atoms and thus the

inter-nuclear distance.

Positive values of J_{ij} lead the ferromagnetism (FM) where the neighboring magnetic moments are coupled parallel (see figure 2.1(b)). Ferromagnetic materials present a hysteretic response for magnetization ($M = \delta H$) in front of the applied field (see figure 2.2(a)), when the magnetic applied field is sufficiently high the magnetic moments can be aligned in the direction of the magnetic field and the magnetization saturates (M_S), the magnetic moment at zero applied field does not become zero but a finite value, known as remanent magnetization (M_R). In order to obtain zero magnetization an additional magnetic field is needed, named coercivity (H_C) (see figure 2.2(b)). When the temperature of the material overcome a limit known as Curie Temperature (T_C), the thermal energy is higher than the exchange interaction between neighboring atoms and the spins can rotate independently and randomly, and the ferromagnetic solid becomes paramagnetic, losing M_R and H_C . Above this temperature a the Curie-Weiss law is followed (see equation 2.3): [111]

$$\delta = \frac{C}{T - T_C} \quad (2.3)$$

where in contrast to the Curie law now the Curie Temperature (T_C) enters in the temperature dependence.

In contrast with ferromagnetic materials, antiferromagnetic (AFM) and ferrimagnetic (FiM) systems present negative values of J_{ij} , which result in an antiparallel coupling of the neighboring magnetic moments. Louis Néel defined the AFM coupling in an atomic ordered solid as two different magnetic subcells A and B, inside in a crystallographic cell, where each of sublattices has their respective spins aligned parallel (ferromagnetically) and the subcells are aligned antiparallel between them (see figure 2.1(c)). [113] In analogy with ferromagnetism when the temperature reaches an specific limit the system becomes paramagnetic and the Curie-Weiss law is followed. In this case, the transition temperature is known as Néel temperature (T_N). [113] This antiparallel coupling gives the AFM materials a zero net magnetic moment at zero field. The magnetization of the AFM materials has a weak linear dependence of magnetization as function of the applied field. In contrast, in FiM materials the magnetic moments in the two sublattices are different and thus they are no longer compensated leading to a net magnetic moment in the solid (see figure 2.1(d)). Then, their magnetic characteristics are similar to FM materials, i.e., they present M_S , M_R and H_C (see figure 2.2(b)). Although strictly speaking the transition temperature of FiM should be denoted a Néel temperature (T_N), for analogy with FM materials T_C is usually used.

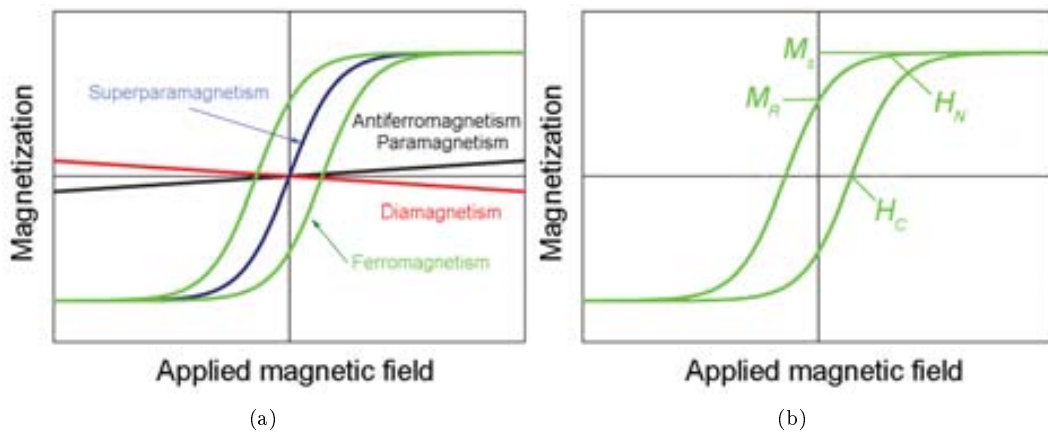


Figure 2.2: (a) Magnetic behavior for different magnetic materials in front an applied magnetic field, (b) hysteresis loop for a FM and FiM materials.

The wide variety of FM (FiM) materials existent can be further classified in a broad sense as soft or hard magnets. Hard magnets are also called permanent magnets. These require a large magnetic field to demagnetize (and magnetize). Generally hard magnets have a large remanence and coercivity and a relatively small saturation magnetization ($H_C > 1000$ Oe). Typical soft magnets, however, are easily magnetized and demagnetized, they have a small coercive field, large saturation magnetization and generally a small remanent magnetization. Soft and hard magnets have different applications depending on the characteristics required. Importantly, the intrinsic parameters responsible for the hardness or softness of the FM structure are the magnetic anisotropy, K , and the magnetostatic energy, E_m , respectively. For large values of the magnetic anisotropy, K , a larger energy is needed to rotate all the magnetic moments leading, thus, to a large H_C . In contrast, low values of magnetic anisotropy, K , makes the rotation of the moments easier, thus leading to a small H_C .

Magnetic anisotropy, K , refers to the dependence of the magnetic properties in a FM, AFM or FiM materials on the measuring direction. In the absence of an applied magnetic field, a magnetically isotropic material has no preferential direction for its magnetic moment while a magnetically anisotropic material will align its moments along a specific direction, denoted as the easy axis. An easy axis is an energetically favorable direction of spontaneous magnetization that is determined by the magnetic anisotropy. Magnetic anisotropy can be induced by different intrinsic and extrinsic parameters. Thus, there exist different kinds of magnetic anisotropies: crystal anisotropy, formally called magnetocrystalline anisotropy, shape anisotropy, stress anisotropy, induced anisotropy (which can be induced by magnetic annealing, plastic deformation and irradiation) and exchange anisotropy. [111, 112]

However, magnetocrystalline anisotropy, which is induced by the specific ions in the material and their crystallographic structure, is often the main contribution to the final magnetic anisotropy. Magnetocrystalline anisotropy is related to the spin-orbit interaction, which couples the spins moments to a preferred crystallographic axis which is defined by the electron spin orbital location.

The simplest form of magnetocrystalline anisotropy is uniaxial, where there is only one easy magnetic direction. In absence of an applied magnetic field the magnetic moments of the solid tend to align to this easy axis, and an extra energy is required to move them towards other crystallographic direction. The energy required for this rotation is called the magnetocrystalline anisotropy energy (E_A). The analytical expression of E_A can be rather complex, although for uniaxial systems E_A depends only on a single angle θ , where θ is defined as the angle of the magnetization respect the easy axis. For more complex systems it is possible to express the anisotropy energy as a series of powers of $\sin^2(\theta)$:

$$E_A = K_{u0} + K_{u1}\sin^2(\theta) + K_{u2}\sin^4(\theta) + \quad (2.4)$$

Interestingly, other, higher order, anisotropies, like cubic anisotropy, can present, at the same time, several equivalent easy axes. [111, 112] In the specific case of spherical nanoparticles with volume V , they can often be modeled as uniaxial in character, neglecting higher order terms, and represented in their simplest form as:

$$E_A = KV\sin^2(\theta) \quad (2.5)$$

In magnetic materials maintaining all the spins parallel to each other throughout the material would be energetically very costly due to the large magnetostatic energy it generates. The magnetostatic energy is defined as the energy stored due to the interaction of the magnetic field created by the magnetization in some part of the solids on other parts of the same solid. As can be depicted in figure 2.3(a) a uniformly magnetized specimen has a large magnetostatic energy associated with it. This is the result of the presence of magnetic free poles at the surface of the specimen generating a demagnetizing field, which appears in the opposite direction of the magnetization of the solid. To reduce the overall energy the magnetic moments in the material tend to distribute themselves in **magnetic domains**. A magnetic domain describes a region within a magnetic material which has uniform magnetization, where the magnetic moments maintain their collinearity. Magnetic domains, first proposed by Weiss, [111] were

defined in order to explain the fact that ferromagnetic materials with spontaneous magnetization could exist in a demagnetized state. The magnetization within the domain is saturated and will always lie in the easy direction of magnetization when there is no externally applied field. Magnetic domains exist in order to reduce the magnetostatic energy, E_m , of the system. The break up of the magnetization into two domains, as illustrated in figure 2.20(b), reduces the magnetostatic energy by half. In fact if the magnet breaks down into N domains then the magnetostatic energy is reduced by a factor of $1/N$, therefore figure 2.20(c) has a quarter of the magnetostatic energy of figure 2.20(a). Figure 2.20(d) shows a closure domain structure where the magnetostatic energy is zero, however, this is only possible for certain types of materials.

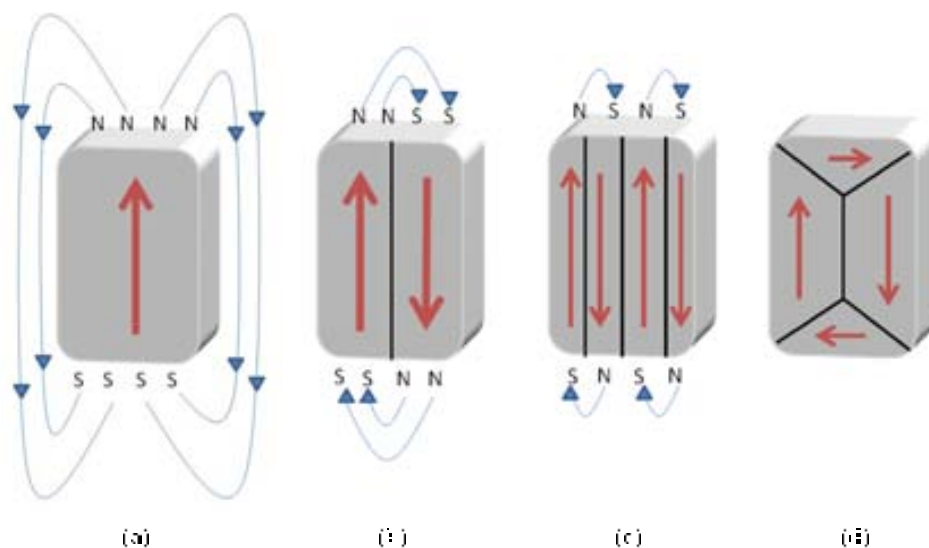


Figure 2.2: Schematic illustration of the break up of the magnetization into domains: (a) single domain, (b) two domains, (c) four domains and (d) closure domains. The red and blue rows show the magnetization inside the material and the demagnetizing field, respectively.

Following the example proposed above, the division into domains only continues while the reduction in magnetostatic energy is greater than the energy required to form the **domain walls**. The energy associated a domain wall is proportional to its area. The schematic representation of the 180° domain wall in figure 2.4 illustrates that the dipole moments of the atoms within the wall are not pointing in the easy direction of magnetization, thus they are in a higher energy state. In addition, the magnetic moments within the wall are not at 180° to each other, hence the exchange energy is higher inside the domain wall than in the domain. Therefore, the domain wall energy is an intrinsic property of a material which depends on different factors like the magnetocrystalline anisotropy or the strength of the exchange interaction between neighboring atoms. The thickness of the wall will also vary in relation to these parameters, since a strong magnetocrystalline anisotropy will favor a narrow wall, whereas a strong exchange interaction will favor a wider wall.

A global minimum energy can therefore be achieved by the balance between the magnetostatic energy and the domain wall energy, resulting in a specific number of domains within a specimen. This number of domains will depend on the size and shape of the sample (which will affect the magnetostatic energy)

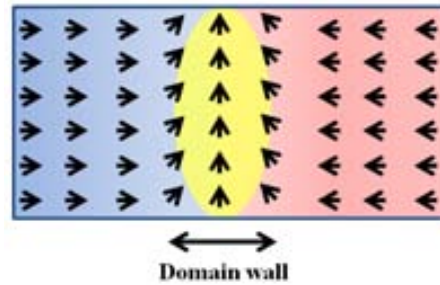


Figure 2.4: Schematic representation of a 180° domain wall

and the intrinsic magnetic properties of the material (which will affect the magnetostatic energy and the domain wall energy).

The main implication of the domains is that although there is large magnetization within individual domains, in the absence of external magnetic fields, these domains are arranged to reduce the magnetostatic energy and therefore to minimize the magnetization (see figure 2.5(a)). Thus, the net magnetization of ferromagnetic materials in response to an external magnetic field may actually occur more by the growth of the domains parallel to the applied field at the expense of other domains rather than the reorientation of the domains (see figures 2.5(b) and 2.5(c)). The effect of external magnetic fields is to cause the domain boundaries to shift in favor of those domains which are parallel to the applied field. [111, 112, 114]

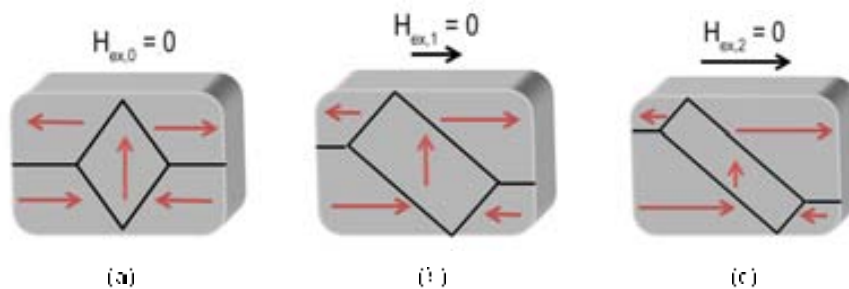


Figure 2.5: Schematic diagram of the domain wall procedure from (a) an equilibrium state, $\mathbf{H}_{ex,0} = 0$, (b) $\mathbf{H}_{ex,1} \neq 0$ and (c) $\mathbf{H}_{ex,2} > \mathbf{H}_{ex,1}$

2.2 Magnetic properties of nanoparticles

Magnetic properties of nanoparticles are strongly linked with their reduced size and, therefore, to their large surface-to-volume ratio. However, their magnetic properties cannot be linked only to a single size effect since they arise from the combination of many different causes, such as: size distribution, finite-size effects, surface effects and interparticle interactions.

Specifically, finite-size effects dominate the magnetic behavior of individual particles, increasing their relevance as the particle size decreases. The most studied finite-size effects are the single domain limit, SME, and the superparamagnetic behavior, SPM. Also, when the particle size decrease the number of atoms located at the particle surface increase. Under this conditions some magnetic surface effects can appear such as surface anisotropy, atomic disorder, spin frustration and core-surface (extra) exchange anisotropy. [66, 115, 116]

2.2.1 Single magnetic domain, SMD

As described above, magnetic domains in bulk ferromagnetic solids appear to minimize the internal magnetic energy, which includes the magnetostatic, exchange and anisotropy energies as well as the domain wall contributions. As the particle size decreases toward some critical particle radius, r_{sd} , the formation of domain walls becomes energetically unfavorable and the particles can only have one domain. Namely, the domain wall energy necessary to divide itself into magnetic domains, is larger than the magnetostatic energy to remain as a single magnetic domain (single-domain), or monodomain. These particles are usually called single domain.

For spherical particle the critical radius, r_{sd} , can be expressed as in equation 2.6. [117]

$$r_{sd} = \frac{9E_w}{\mu_0 M_S^2} \quad (2.6)$$

where E_w is the total domain wall energy per units of area and μ_0 is the vacuum permeability.

In a practical sense, particles with radius below r_{sd} limit are considered SMD since thermodynamically they cannot support the formation of a domain wall. For typical magnetic materials the dimensional limit is in the range of 20 - 800 nm, depending on the spontaneous magnetization and on the anisotropy and exchange energies. [117]

Importantly, in single-domain particles, changes in the magnetization can no longer occur through domain wall motion and instead require the rotation of spins, resulting in larger coercivities. [98]

There are various models to illustrate the magnetization reversal of single-domain particles. The Stoner and Wohlfarth (SW) model [118] describes the magnetization curves of a single-domain particle with a uniaxial anisotropy either as a result of particle shape or from the magnetocrystalline anisotropy. The main assumption of the model is the coherent rotation of the magnetization of the particle. The equilibrium direction of the particle magnetization vector is determined by the easy anisotropy axis and the direction of the applied field. When a magnetic field H is applied at an angle π to the easy axis of the uniaxial anisotropy of the particle, the magnetization vector then lies under an angle θ relative to the easy axis (see figure 2.6(a)). The free energy density of the system may be written in terms of anisotropy energy density as:

$$E_B = KV \sin^2(\theta) + HM \cos(\pi - \theta) \quad (2.7)$$

where the first term, $KV \sin^2 \theta$, refers to the magnetic anisotropy (see equation 2.5) and the second term, $HM \cos(\pi - \theta)$, represents the Zeeman term.

As illustrated in figure 2.6(b) in the absence of external perturbations, $H = 0$, two equilibrium states can be found, for $\theta = 0$ and π . The energy barrier of the system, $\theta = \pi/2$, is equal to KV , where K and V are the magnetic anisotropy and the volume of the particle. [14]

Then we can define the energy necessary to overcome the spin fluctuation in a monodomain particle with uniaxial anisotropy as KV .

2.2.2 Superparamagnetism, SPM

Since the magnetic energy of a single domain particle with uniaxial anisotropy, K , and volume, V , is KV , as the volume is reduced the magnetic energy becomes increasingly smaller. Eventually, if the volume becomes sufficiently small, at finite temperatures, the thermal energy, $k_B T$ (k_B is the Boltzmann's constant), may be sufficient to induce magnetic fluctuations and spontaneously reverse the magnetization of a particle from one easy direction to the other, $\theta = 0$ and $\theta = \pi$, even in the absence of an applied field.

In the superparamagnetic state, the temperature of the system is sufficient to overcome the magnetic energy barrier, thus the magnetization spontaneously reverses ($KV \rightarrow k_B T$), however, the temperature of the system is below to the Curie or Néel transition temperature to the paramagnetic state ($T \rightarrow$

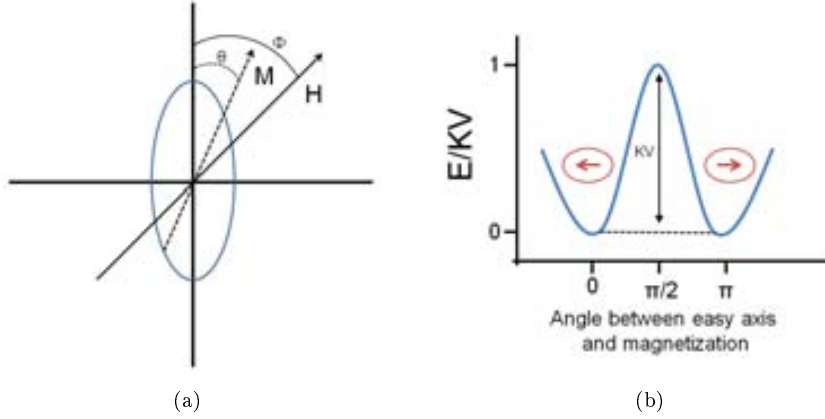


Figure 2.6: (a) Definition of the axis system for a fine particle and (b) the angular dependence of the energy barrier for zero external field.

T_C or T_N). Therefore the exchange energy which maintains all the atomic moments, in the particles, parallel or antiparallel aligned is still valid. Accordingly, the thermal fluctuations must spontaneously reverse all the magnetic moments of the particle at the same time, keeping them parallel (or antiparallel). The moment of each nanoparticle behaves like a large paramagnet with the notable exception that the independent moments are not those of single atoms, but rather sum of all the magnetic moments in the particle, which may contain more than 10^5 atoms. [13, 14, 98]

It is worth noting the importance of the relaxation time in superparamagnetic systems. The simplest model to account the characteristic time of the magnetization thermal fluctuation in nanoparticle with uniaxial anisotropy is given by Arrhenius law:

$$\lambda = \lambda_0 \exp(KV / k_B T) \quad (2.8)$$

where λ is the characteristic relaxation time and λ_0 is a time constant characteristic of the material (i.e., the reversal attempt time, usually in the 10^{-12} - 10^{-9} s range). Then, it can be defined a transition temperature known as blocking temperature, T_B , below T_C or T_N at which the thermal energy reach the magnetic energy of the particle and the system becomes SPM.

$$T_B = \frac{KV}{k_B \ln(\frac{\tau_m}{\tau_0})} \quad (2.9)$$

As can be seen in equation 2.9, where λ_m is the characteristic measuring time of the technique, T_B depends on the time scale of the measurements, for example for neutrons, X-Ray and Mossbauer measurements the time scale is in the range of 10^{-8} to 10^{-12} s and for standard laboratory magnetometers (SQUID) is 10^2 s. [119, 120]. Then for experimental techniques with λ_m bigger than the characteristic λ of the SMD structure the relaxation is faster than the magnetization orientation observed in this time window, allowing the system reach the thermodynamical equilibrium, so nanoparticles are in the SPM regime. On the other hand when λ_m is lower than the characteristic λ the system relaxation proceeds very slowly and quasi static properties (similar to bulk materials) are obtained, i.e., the particles are in the so-called blocked regime, a non SPM regime. Namely, the same nanoparticles can be in the SPM or blocked state depending on the measuring technique.

Then, for typical SQUID measurements, the value of the logarithm in the equation 2.9 is in the order of 25. [14]

$$T_B = \frac{KV}{25k_B} \quad (2.10)$$

Importantly, these approximations are thought for perfect, non-interacting, single SPM nanoparticle. However, in real systems the experimental conditions can be far away from these approximations. Firstly, T_B is proportional to the volume of the SPM nanoparticle, then in a system formed by n SPM nanoparticles the particle size distribution may play an important role. Thus, T_B can be understood as an average of the different nanoparticles volumes in the system. Other important factors that can affect T_B in SMD nanoparticles are the interparticle interactions and the surface effects. Both effects can increase the value of the T_B due to increased energy given by the dipolar and/or exchange interaction and extra anisotropy.

2.2.3 Surface effects

Surface and finite-size effects govern the magnetic properties of nanoparticles systems. It is clear that both SMD and SPM are a direct consequence of the size reduction from bulk to the nanoscale. In many cases both, finite-size and surface, effects occur simultaneously and it is often not easy to distinguish if some variation from the bulk properties comes from one or another effect. [99]

Finite size effects are originated by the small size of nanostructures, which can constrain some characteristic lengths of the material. In contrast surface effects arise due to atoms located at the nanoparticle surface getting a predominant role in the physics of the system. For example for a face-centered cubic (fcc) Co nanoparticles with 1.6 nm in diameter about of 60% of the total number of atoms are situated on the surface. Surface atoms suffer by lack of translation symmetry at the boundaries of the particle and can show changes in lattice constants, atom coordination and the electronic band structure. These effects can lead to broken magnetic exchange bonds, spin disorder and frustration. [14, 99] In this case, the nanoparticles can be modeled as a two phase system, core-surface structure, with highly crystalline core, governed by the magnetic bulk properties, and disordered surface layer. [14, 99–102].

Then, the ideal model where all the spins of the nanoparticles are pointing along the easy axis and that they reverse coherently is not longer valid. In fact, surface spins can suffer strong deviations from the bulk behavior. In particular, a new type of anisotropy, surface anisotropy, K_S , comes into play. Surface anisotropy has a crystal-field nature and it appears due the breaking of the atomic boundaries at the particle surface. Many theoretical and experimental works have demonstrated the increment of the magnetic anisotropy due to the contribution of the surface anisotropy of the reduction in size . [99, 100, 102] Notably, the shape of the particle, i.e. rods, disks, cubes, rhombohedral, tetrapods, or more complex shapes, also can affect or induce different degrees of surface anisotropy. [121–123]

As a result of the core-surface structure, an effective total anisotropy, K_{eff} , for a spherical nanoparticle with diameter D can be defined as:

$$K_{eff} = K + \frac{6}{D}K_S \quad (2.11)$$

Other effects associated to the atomic disorder at the surface are canted spins, frustration and spin-glass like behavior [14, 99, 100]. Canted spins commonly found in nanoparticles are associated to the surface anisotropy. The distortion in the lattice constant and changes in atom coordination can align surface spins in different preferred magnetic directions instead of the easy axis of the core spins. [124, 125] Frustration can be understood as an uncompensation of one of the magnetic sublattices, in AFM and FiM materials, at the surface. [126–128] Spin-glass behavior is somewhat more complex. Namely, spins at the surface can suffer different interactions at the same time, with the concomitant changes of spin direction and/or frustration between spins, which results in a lack of long-range magnetic order leading to a spin-glass behavior of the system. [129, 130]

Many studies have tried to reveal the role played by the surface effects in the final magnetic properties of the nanoparticles. Surface anisotropy which, increases the overall particle anisotropy, can lead to different reversal magnetization processes for the core and the surface giving rise to an enhancement of the coercivity field, H_C . Given the increasing role of the surface anisotropy as the size decreases (see equation 2.11), the increase in H_C is strongly related with the reduction of the particle size. [122] A reduction in the saturation magnetization when the particle size is decreased has been extensively

reported in metal oxide particles. The surface spin disorder or the canting can originate the reduction of the overall saturation magnetization [131,132] or in other cases their enhancement. [133,134] In contrast, in some cases, for metallic nanoparticles the reduction in size has been shown to result in an increment of the saturation magnetization. The magnetic moment per atom increases as the number of magnetic atoms in the near-neighbor shell (coordination number) decreases. This is caused by the decrease in the overlap of the nearby atomic orbitals as coordination numbers decrease. [135]

Further, in both metal oxide FiM and FM nanoparticles the hysteresis loops display large irreversibilities (i.e., the loops do not close up to high fields) at low temperatures and they do not reach saturation even for extremely large fields. These effects can be ascribed to the spin-glass like properties of the disordered spins at the surface. [124,125] In addition, this spin-glass state can create an exchange field interaction with the core which is responsible for the experimentally observed loop shifts in the field axis, H_E (exchange bias). [130]

Interestingly, antiferromagnetic nanoparticles have novel properties due to surface and finite-size effects which are drastically different from the bulk properties. For example, the magnetization of nanoparticles below T_N is often significantly larger than the bulk value due to uncompensated surface spins. Moreover, this surface magnetism can lead to ferromagnetic-like properties in AFM materials, with finite M_S and large H_C . Other effects such as changes in the Néel temperature can also take place. [136–138]

On the other hand, an exchange coupling between the spin-glass surface and the AFM core brings about an increase of H_C and the appearance of exchange bias, H_E . [132,133]

Diverse numerical calculations for different particle systems and experimental results have evidenced that the effective critical temperature, T_C or T_N , in nanoparticles is strongly size dependent and usually decreases as the particle volume is reduced. [99,121,138]

2.2.4 Inter-particle interaction effects

In nanostructured magnetic materials, interactions between, for example, nanoparticles or the different layers in multilayer structures often play an important role. Long-range magnetic dipole interactions can have a strong influence on the magnetic dynamics in samples containing ferromagnetic or ferrimagnetic nanoparticles. If nanoparticles or thin films are in close proximity, exchange interactions between surface atoms can also be significant. An important example of interaction effects is exchange bias, which manifests itself as a shift of the hysteresis loops obtained after field cooling of a ferromagnetic or ferrimagnetic material in contact with an antiferromagnetic material. In nanoparticle assemblies in a matrix, where both the matrix and particles are metallic, RKKY (Rudermann-Kittel-Kasuya- and Yosida) interactions can also occur.

The dipole-dipole interaction is a long-range anisotropic interaction. The strength of this interaction depends on the separation between the nanostructures and the degree of mutual alignment. Dipole-dipole interactions modify the energy barrier arising from the anisotropy contributions of each particle and, in the limit of strong interactions, its effects become dominant and individual energy barriers, KV, can no longer be considered and only the total energy of the assembly being the relevant magnitude. Extensive experimental and theoretical works agree that the interaction among magnetic particles play a fundamental role in the magnetic behavior of granular systems. [103,104,139–145] However, several inconsistencies have been discussed. Theoretical models [139,141,146] predict the increase of the blocking temperature with strength of the dipolar interactions, i.e. increasing particle concentration or decreasing particle distance. However, in the weak interaction limit theoretical models [141] propose the opposite dependence of the blocking temperature with the dipole interaction strength. Both different behaviors have been experimentally reported. For instance, in the limit of weak interactions, an increase of the blocking temperature with particle density has been observed in some experiments, [104,139,140] but other results show the opposite trend. [141] For high density particle systems, the picture is more complex since the blocking process of each nanoparticle is highly dependent on its neighborhood. The observation of properties resembling spin glasses has suggested the existence of a spin-glass like state or magnetic order (superferromagnetism) in such systems. [147,148]

Dipole-dipole interactions can also affect the shape of the hysteresis loop in magnetic nanoparticles. In fact, when the particles are randomly oriented the reduction of the inter-particle distance causes the reduction of the coercivity due to collective response of magnetic moments that leads to a reduction of the energy barrier for magnetization reversal. This behavior has been theoretically predicted [149, 150] and experimentally demonstrated. [151] In contrast, when the particles are not randomly oriented the coercivity can increase or decrease depending on the type of arrangement. [152, 153] Less attention has been paid in the role of interactions on the loop shift, in core|shell FM|AFM nanoparticles, due to the inter-particle dipolar effects. Monte Carlo simulations reveal a similar behavior of the loop shift as the one demonstrated for the coercivity. [150, 153]

Exchange interactions are a quantum mechanical effect, without classical analogue, which increases or decreases the expectation value of the energy between two or more identical particles when their wave functions overlap. In fact, exchange interaction is an interfacial effect which takes place by the direct touching between subsequent layers. From the magnetic point of view when two magnetic layers are in contact two main exchange effects can appear. For FM|AFM and FM|FM interface contacts the related exchange effects are exchange bias and spring-magnet effects, respectively. However, importantly, most of the magnetic nanoparticles synthesized via wet chemistry exchange inter-particle effects are avoided since organic molecules covering the particles, surfactant, prevent the inter-particle touching.

2.3 Exchange-spring magnets

Permanent (hard) magnets, are defined as a magnet that retains its magnetism after it is removed from a magnetic field. A permanent magnet is *always on*. This kind of magnetic materials presents a broad range of applications, and is particularly interesting since they are vital components of many electromechanical machines and electronic devices and has significant impact in the development of electric motor components, magnetic recording media, medication imaging systems, undulators at synchrotrons. Also permanent magnets pervade our transportation, homes, workplaces, and research laboratories. [154, 155]

The magnetic properties of permanent magnets are characterized by the parameters of their hysteretic magnetization, M , response in front an external field applied, H ; such as: coercivity, H_C , remanence, M_R , and saturation, M_S , magnetization. In principle, when greater are these parameter better is the permanent magnet. Mainly two different intrinsic parameters control the final magnetic response of the material. In the case of the coercivity, it is intimately linked to the magnetocrystalline anisotropy, K , of the system and the saturation magnetization depends in the value of the exchange energy of the system. In order to present one unique parameter to fit the goodness of a permanent magnet the $(BH)_{max}$ product has become the figure of merit of permanent magnets. $(BH)_{max}$ can be defined as the magnetic field strength at the point of maximum energy product of a magnetic material and is measured in Mega Gauss Oersteds, MGOe (see figure 2.7). [156]

In recent years the search for new permanent magnets has been focused mainly on the enhancement of the energy density product $(BH)_{max}$ by using magnets based on rare-earth elements. However, from the theoretical point of view, materials with larger H_C ($H_C > 2\pi M_S$) have a limit for the maximum value of the energy product (see equation 2.12).

$$(BH)_{max} \leq (2\pi M_S)^2 \quad (2.12)$$

To overcome this limitation, Kneller and Hawig [157] proposed a new concept to develop permanent magnets with higher $(BH)_{max}$ product: a bi-magnetic nanocomposite exchange-coupled hard/soft permanent magnet. In principle the hard-FM phase is dominated by the magnetocrystalline anisotropy (high H_C) and the soft phase is governed by the exchange energy (high M_S). This new type of magnets is known as exchange-spring permanent magnets. In order to gain the maximum value of $(BH)_{max}$ product Skomsky and Coey [158] theorized that the optimal exchange-spring system could yield a $(BH)_{max}$ of up to 120 MG Oe, i.e., more than three times the one of commercial permanent magnets. The behavior

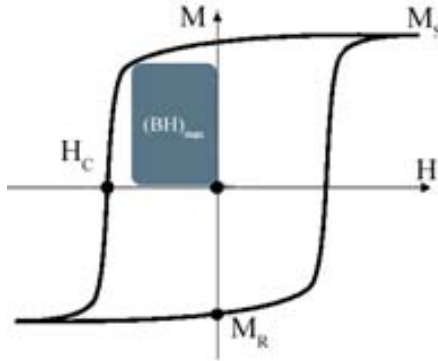


Figure 2.7: magnetic hysteresis loop of permanent magnets as a function of an external applied field, H . The main components of this hysteretic behavior are the saturation, M_S , and remanence magnetization, M_R , and coercivity, H_C . The $(BH)_{max}$ product is depicted as the area of the blue square.

in these systems can be primarily understood from the intrinsic parameters of the hard and soft phases, where the resultant hysteresis loop should maintain the high H_C of the hard phase and the large M_S of the soft phase. [159] Exchange-spring permanent magnets have been thoroughly studied in thin films (bilayers and multilayers) structures due to the high degree of control of the crystallinity and their crystal orientation. [159–163]

Interestingly, nanophase materials allow an easy control of the magnetic properties, which can lead to optimized properties for spring magnets. For example, the size dependence of the coercivity, H_C , [97] where H_C of powdered magnets increases with the reduction of particle size going through a maximum at the single domain size, can be used to enhance the coercivity. On the other hand, according to the Stoner-Wohlfarth prediction [118] the remanence M_R of polycrystalline material being a mixture of single domain, non-interacting magnetically particles is equal to the half of the saturation magnetization M_S ($M_R = M_S/2$). However, it has been extensively proven that the effect of the remanence enhancement (remanent magnetization, M_R) exceeds that of the estimated theoretical value of $M_S = 2M_R$ for the ensemble of the single-domain, randomly oriented nanoparticles. [156, 164, 165]

On the other hand, the exchange coupling between soft and hard magnets causes the magnetization vector of the soft phase to align with that of the hard phase. Consequently, the exchange coupling and the use of nanophase materials can lead us an overall increase leading to an increase of the predicted M_R above $M_S/2$ in a crystallographically isotropic structure along with a reasonable coercivity. Because of this, a higher $(BH)_{max}$ would be expected in exchange coupled magnets as compared to the conventional isotropic uncoupled magnets.

Hence, for these two reasons nanostructured exchange spring magnets are perfect candidates to enhance the final permanent magnetic properties and thus lead to the overall increase in their magnetic energy density, $(BH)_{max}$. [166]

Other interesting properties have been discovered in this kind of magnets, such as: large degree of reversibility and enhanced Curie temperature of the hard magnet. [166] The enhancement in Curie temperature is believed to be the result of the penetration of the exchange field of the higher Curie temperature phase (soft magnet) into the adjacent lower Curie (hard magnet) temperature phase, i.e., a **magnetic proximity effect**. This leads to an increase of the average effective molecular field of the latter phase resulting in a spontaneous magnetization at temperatures above its normal Curie temperature for the hard magnets. [166]

An important issue for assessing the applicability of exchange-spring magnets is the nature of the magnetic reversal processes. A large number of different theoretical [158, 167–169] and experimental studies [159–161, 163, 170] have been devoted to try to elucidate this behavior.

In general, these approaches find that the most important parameter in characterizing the switching behavior is the dimension of the soft phase (soft magnet), t_S . For a thin soft phase layer there is a

critical thickness below which the soft phase is rigidly coupled to the hard phase, and the two phases reverse at the same nucleation field, H_N , resulting in a rectangular hysteresis loop; then the system is considered as completely exchange coupled. In contrast, for thicker soft layers, the soft phase nucleates the reversal at significantly lower fields and the switching is characterized by an inhomogeneous reversal, and the system is not totally coupled and it is usually called exchange-spring magnet (see figure 2.8).

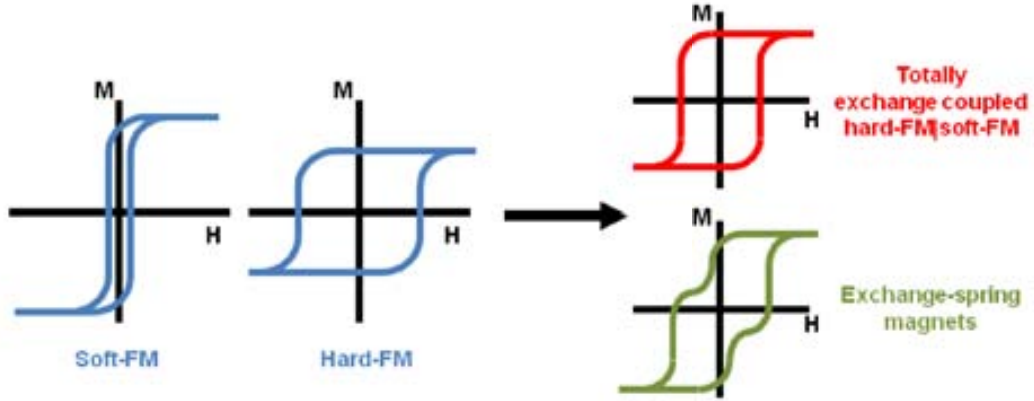


Figure 2.8: Hysteresis loops for soft and hard FM and their possible combinations, totally exchange-coupled and exchange-spring magnet.

Although the value of H_N depends on the material parameters of both the hard and soft layers, the critical soft-layer thickness is found to be roughly twice the width of a domain wall δ_H in the hard phase,

$$\delta_H = \pi\sqrt{A_H K_H} \quad (2.43)$$

where A_H and K_H are the exchange stiffness and anisotropy constants, respectively, of the hard phase. Thus, this length scale determines many of the physical properties of these systems independent of sample geometry.

In fact, assuming small values for the anisotropy of the soft-phase, $K_S \sim t$, when the thickness of the soft layer is less or equal of the critical value δ_H the two phases are rigidly coupled and the system is characterized by the average magnetic properties of the two layers. Then the expected value for the nucleation field, H_N can be expressed as:

$$H_N = \frac{2(t_H K_H + t_S K_S)}{t_H M_H + t_S M_S} \quad (2.44)$$

with anisotropy (K_S and K_H), magnetization (M_S and M_H) and thickness values (t_S and t_H) of the soft and hard phases, respectively. Then, assuming rectangular hysteretic behavior with $H_C = H_N$ and vanishing values of soft-phase anisotropy (i.e., $K_S \sim K_H$); the coercivity can be estimated as:

$$H_C = 2\pi \frac{2(t_H M_H + t_S M_S)}{t_H + t_S} \quad (2.45)$$

Therefore, for large K_H the energy product approaches the value of the theoretical limit of the soft phase ($2\pi M_S^2$) with a hard phase volume fraction of only $\sim \pi M_S^2 / K_H$. [45]

In contrast, for systems composed by thicker soft phase layer, i.e. $t_S > \delta_H$, the coercivity of the soft layers drops quickly, which degrades the hard magnet properties of composite systems. This arises

Because the soft layer nucleates reversal at fields well below that of the hard layer. Under the assumption that the hard layer is perfectly rigid and $K_S = 0$, solving for the magnetization of the soft layer with an applied field opposed to the hard layer it can be seen that the soft layer remains parallel to the hard layer for fields less than the nucleation field for the exchange field H_{ex} given by equation 2.40.

$$H_{ex} = \frac{\pi^2 A_S}{2M_S t_S^2} \quad (2.40)$$

Once the magnetic field exceeds H_{ex} magnetic reversal proceeds via a twist of the magnetization in the soft layer. This occurs because the soft layer is strongly pinned at the interface while away from the interface it is free to follow the external field. For $H > H_{ex}$, the spins in the soft layer exhibit continuous rotation, as in a magnetic domain wall, with the angle of rotation increasing with increasing distance from the hard layers. Such magnets exhibit reversible demagnetization curves since the soft layers rotate back into alignment with the hard phase if the reverse field is removed. This reversing process is often referred to as an exchange-spring process by analogy with the elastic motion of a mechanical spring (see figure 2.5).

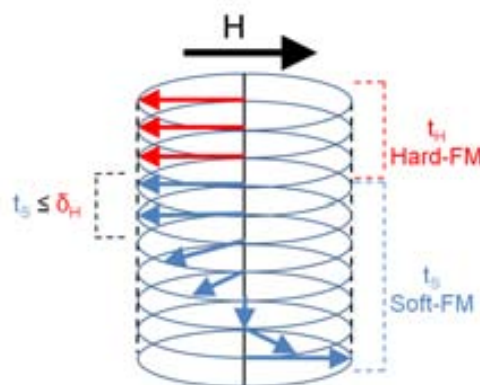


Figure 2.5: Schematic diagram of soft magnetic phase switching in an exchange-spring magnet.

2.4 Exchange bias

It has been amply demonstrated that nanostructured systems formed by a FM and a AFM phase in close contact, when they are cooled through the Neel temperature (T_N) of the AFM (with the Curie temperature, T_C , of the FM larger than T_N) an additional unidirectional anisotropy (exchange bias) is created in the FM phase. Exchange bias was discovered almost half a century ago, by Meiklejohn and Bean, [474] and its characteristic signature is the shift of the center of magnetic hysteresis loop from its normal position at $H = 0$ to $H_E \neq 0$ and the enhancement of the coercivity, [472]

In addition to AFM|FM interfaces, exchange bias and related effects have also been observed in other types of interfaces, e.g. involving ferrimagnets, FIM|AFM|ferrim, FIM|FM and FIM|FIM or spin-glass materials, where due to its random character spin-glasses can play the role of both the AFM and FM in exchange biased structures, [473]

Assuming a nanostructured system composed by an AFM|FM interphase where the Curie temperature, T_C of the FM phase is larger than the Neel temperature, T_N , of the AFM ($T_C > T_N$). Then, when a static external field is applied and the system is cooled down from a temperature above T_N but below T_C ($T_C > T > T_N$) to a temperature below T_N ($T < T_N$) the hysteresis loop suffered a shift along the field axis generally in the opposite direction to the cooling field, i.e. $H_E < 0$ when $H_{FC} > 0$.

This loop shift is generally known as exchange bias, H_E (see figure 2.10(a)). The hysteresis loops also have an increased of the coercivity, H_C , after the field cooling procedure (see figure 2.10(b)). Both of these effects disappear at, or close to, the AFM Néel temperature confirming that it is the presence of the AFM material which causes this induced anisotropy.

The new type of induced unidirectional anisotropy, K_{ua} which is the intrinsic parameter of the exchange bias coupling, presents a $K_{ua}\cos(\theta)$ angular dependence rather than $K_u\sin^2(\theta)$, as the common uniaxial anisotropy (see figure 2.10(c)). As can be seen in the figure 2.10(c) the energy of the uniaxial anisotropy presents two minima, 0 and 180°, however due to the AFM|FM coupling the unidirectional induced anisotropy, $K_{ua}\cos(\theta)$, create a net anisotropy with unique minimum in the energy at 0°. In other words, in contrast to uniaxial anisotropy, i.e. two equivalent easy configurations in opposite directions, the magnetization in AFM|FM systems has only one easy direction. Thus, the AFM|FM anisotropy is often referred to as unidirectional anisotropy.

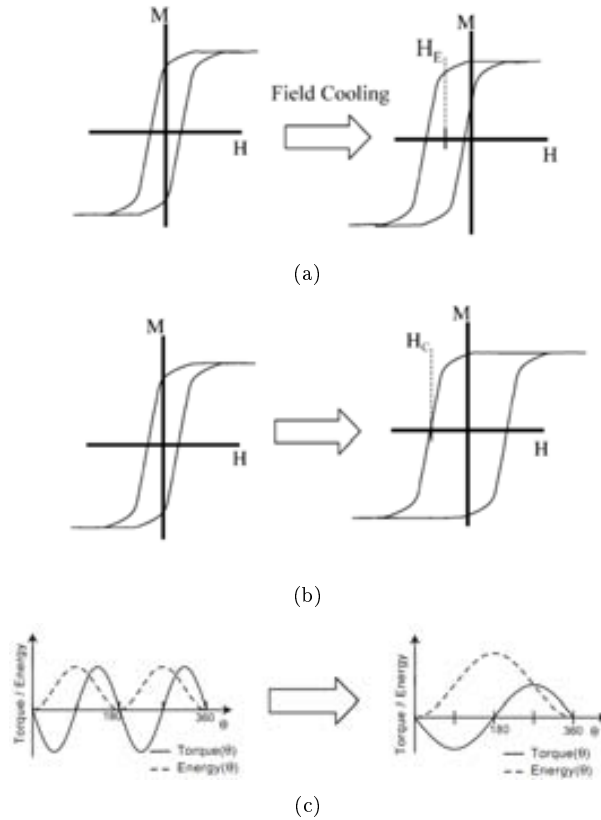


Figure 2.10: Schematic representation of the main effects induced by the FM|AFM exchange coupling, i.e., (a) loop shift, (b) coercivity enhancement and (b) change from uniaxial anisotropy to unidirectional anisotropy (represented as torque measurements, $\sin\theta$, and global magnetic energy, $\sin^2\theta$). [173]

Unidirectional anisotropy and exchange bias can be qualitatively understood by assuming an exchange interaction at the AFM|FM interface. [172,173] The physical origin of exchange bias is rather generally accepted to be the exchange coupling between the AFM and FM components at the interface. The microscopic cause of exchange bias is more controversial and many models have been proposed to explain it. [173–175] However, the intuitive view of exchange bias is simple and can be described in terms of an alignment of the AFM spins at the FM|AFM interface parallel to the FM spins occurring

during the field cooling procedure. This coupling leads to an extra energy barrier for the FM spins to rotate with the external field. Within this simple intuitive model, two different opposite limiting cases can be described, depending on the strength of the AFM magnetic anisotropy. If the AFM anisotropy is large, one should only observe a shift of the hysteresis loop, while for small AFM anisotropies, the only observed effect should be a coercivity enhancement (without any loop shift). Nevertheless, in general, both effects can be observed simultaneously, due to, for example, structural defects or grain size distribution, which bring about local variations of the AFM anisotropy.

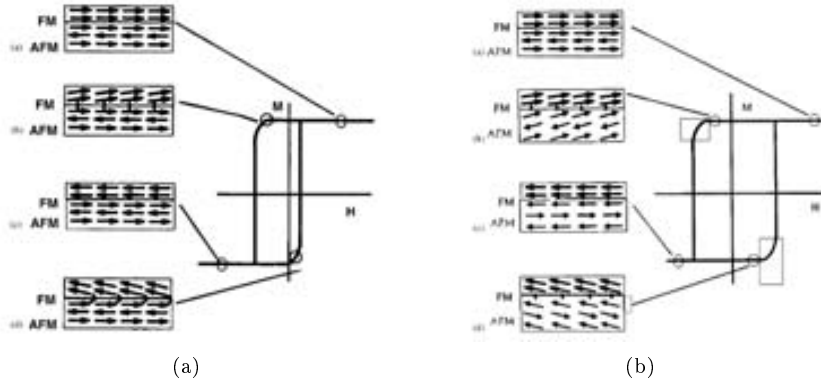


Figure 2.11: (a) Schematic diagram for a FM/AFM spins system in a hysteresis loop with large K_{AFM} , (b) Schematic diagram for a FM/AFM spins system in a hysteresis loop with small K_{AFM} . [173]

For systems which present $K_{AFM} - K_{FM}$ the AFM phase cannot switch at the same time of the FM one. Firstly, AFM and FM phases are parallel coupled and when the FM starts reversing its spins, the extra energy given by the AFM phase makes it difficult for them to switch, increasing the coercive field values in the negative field branch. After reaching negative saturation, when the FM phase starts rotating towards positive fields, the coupling energy given by AFM phase makes, now, the switching easier, to reach the parallel coupling (lower energy), obtaining, thus, lower values of coercive field. Consequently, the resulting hysteresis loop presents a shift in the field axis, H_E . On the other hand for systems with $K_{AFM} \rightarrow K_{FM}$ the AFM phase rotates together with the FM phase (see figure 2.11(b)). Then, the energy needed to switch the FM spins is increased (since the FM needs to drag the AFM spins) equally in both branches of the hysteresis loop, from positive to negative fields and viceversa. Therefore the effect associated to this process is the enhancement of both coercive fields, resulting in larger values of H_C .

Notably, there exist several different models to understand the exchange bias effect, [173–175] although there is some convergence towards the microscopic picture of the effect arising from a few spins of the AFM which lack their compensating spin, i.e., **uncompensated spins**. In fact, two different types of uncompensated spins have been postulated **pinned and unpinned** based on XMCD studies of exchange biased systems. [176–179] Namely, using element-specific XMCD it can be observed that if the magnetization of the AFM is irreversible under field reversal, the uncompensated spins are pinned and can be identified as a small vertical shift of the hysteresis loop of the AFM system. On the other hand if the magnetization of the AFM is reversible, the uncompensated spins display a FM-like hysteresis loop. The pinned uncompensated spins are strongly coupled to the AFM layer and do not reverse with the applied field and are the origin of H_E . On the other hand, the unpinned ones are only loosely coupled to the AFM layer and reverse together with the FM layer and are, thus, responsible for the H_C enhancement. However, despite some consensus on the role of the uncompensated spins their origin remains controversial (e.g., defects, domain walls, interface disorder and so on). Finally, it should be

emphasized that although the uncompensated spins are assumed to be at the interface, there is some evidence that bulk uncompensated spins may also be a factor in the exchange bias properties. [180]

Despite the microscopic origin of exchange bias, some simple macroscopic models can accurately account for many of the observed phenomena. The first theoretical approach developed to explain exchange bias was the model by Meiklejohn and Bean [181,182], which assumes that all the AFM spins at the interface are uncompensated. Two of the main assumptions of this model are that the magnetization rotates coherently and that the FM and AFM easy axes are parallel. Within this approach, the energy per unit surface in the FM|AFM couple can be expressed in equation 2.17.

$$E S = -HM_{FM}t_{FM}\cos(\theta - \beta) + K_{FM}t_{FM}\sin^2(\beta) + K_{AFM}t_{AFM}\sin^2(\alpha) - J_{INT}\cos(\beta - \alpha) \quad (2.17)$$

where H is the applied magnetic field, M_{FM} is the saturation magnetization in the FM, t_{FM} and t_{AFM} are the thicknesses of the FM and AFM layers, K_{FM} and K_{AFM} are the magnetic anisotropies in the FM and the AFM and J_{INT} is the exchange coupling constant at the interface. The angles α , β and θ are the angles between the spins in the AFM and the AFM easy axis, the direction of the spins in the FM and the FM easy axis and the direction of H and the FM easy axis, respectively. [172,173,175] As can be seen from the different energy terms, if no coupling exists between the FM and the AFM and the applied magnetic field becomes zero, the overall energy of the FM|AFM system reduces to the terms due to the FM and the AFM magnetic anisotropies (2nd and 3rd terms). When a magnetic field is applied, a certain work has to be carried out to rotate the spins in the FM (1st term-Zeeman term). Finally, the 4th term represents the FM|AFM coupling.

Assuming that the AFM has a very large anisotropy and that its spins do not rotate with the field ($\alpha = 0$), then it can be deduced that the horizontal shift for the hysteresis loop is $H_E = J_{INT}/M_{FM}t_{FM}$. In contrast, for low values of the antiferromagnetic anisotropy is more energetically favorable the joint rotation of the FM and AFM spins, thus, no horizontal shift is induced. However, since the overall anisotropy of the system has been modified, an increase of the coercivity is induced.

The Meiklejohn-Bean model represents the most intuitive approach to exchange bias by relating the loop shift only to the net magnetization originating from the antiferromagnet located right at the interface. However, many other studies attempt to account for different important parameters (e.g. domain walls), in exchange bias systems which are not considered in the basic formula. [172,173,175]

From the theoretical expression deduced in equation 2.17 for large anisotropy values of the AFM component the exchange bias dependence should be inversely proportional with the FM thickness, $H_E \propto 1/t_{FM}$. This can have a profound effect in nanostructured systems, since the FM thicknesses involved are rather small, hence large loops shifts would be expected. The dependence of H_C with the FM thickness is more complex, although a power-law behavior, $H_C \propto 1/(t_{FM})^n$, has been observed and predicted theoretically, there are some discrepancies on the exponent. Independently of the exponent, it is clear that coercivity should be larger for thinner (or smaller diameter) nanostructured systems. [173]

Similarly, the dependence of H_E and H_C on the AFM thickness, t_{AFM} , can also affect the properties of nanostructured systems. Actually, the H_E and H_C behavior on the AFM thickness can be rather complex. From equation 2.17 it can be deduced that if the $K_{AFM}t_{AFM} < J_{INT}$ the value of the exchange bias should be zero, $H_E = 0$. In contrast above this critical thickness, $t_{AFM} = J_{INT}/K_{AFM}$, H_E should reach a constant $H_E = J_{INT}/M_{FM}t_{FM}$ value. Concerning the dependence of the coercivity, it should increase with t_{AFM} until the critical thickness is reached. Then above this value the coercivity should drop to the H_C of the uncoupled FM. [173]

Another important property of exchange biased systems is the so called, training effects. This property was first discovered by Paccard et al. [183] and shows that H_E and H_C in exchange bias systems depends on the number of consecutive hysteresis loop measurements performed. In fact, there are two types of training effect, one between the first and second loop and another one involving subsequent higher number of loops. The first type of training effect has been proposed to arise from the AFM magnetic symmetry and the second one due to the reconfiguration of the AFM moments or domains during the magnetization cycling. [173]

Remarkably, the main theories of exchange bias systems are defined assuming that the T_C of the FM is higher than the T_N of the AFM. However, in recent years it has been extensively proved that exchange bias in inverted systems, i.e. $T_C < T_N$. [184–187] In some cases, it was observed that the exchange coupling induced in these systems can persist well into the paramagnetic (PM) state of the FM (i.e., $T > T_C$) and close to T_N . The behaviors of H_E and H_C can be quite different from those in traditional systems with $T_C > T_N$. However, usually, H_C vanishes close to T_C . The origin of the effect has been proposed to arise because the moments of the FM layer at the interface are polarized by the magnetic field when in the PM regime. Under certain conditions these polarized moments couple to the AFM above T_N leading to the exchange bias properties. [186, 187]

Chapter 3

Core|Shell (CS) magnetic nanoparticles

In recent years Core-Shell (CS) nanoparticles have become increasingly appealing to develop efficient ways to stabilize, functionalize and improve properties of single phase nanoparticles. Traditionally shells were developed as protecting layers for the nanoparticles, for example, to avoid oxidation of transition metal particles. In the case of transition metal magnetic nanoparticles (i.e., Fe, Co, Ni and their alloys), silica, carbon and even Au or Ag coatings were used to stabilize and protect metallic nanoparticles from oxidation. However, it was soon realized that, in fact, the shells could be used as an active part of the novel structure. Actually, even the oxidation protective layers were progressively found to have practical uses. For example, they can enhance biocompatibility, facilitate the functionalization, or induce plasmonic properties. This initiated a new, rapidly expanding, field in nanoparticle synthesis. Thus, novel families of CS nanoparticles are continuously emerging that exhibit the combination of diverse materials (oxides, metals, organic, semiconductors and so on) with dissimilar properties (e.g., magnetic, optical, catalytical, or biomedical). [188–191] Moreover, other more complex structures, such as heterodimers systems, i.e., crystalline materials anchored onto the nanoparticles but without covering the whole surface, are also being pursued to tune and/or modify their properties. [192, 193] The CS systems can combine in a synergetic way the diverse properties of the different constituents leading to multifunctional materials with novel and improved characteristics, paving the way for an even broader applicability of nanoparticles. In addition, these systems have an extra degree of freedom since the properties can often be tuned not only by the core and shell characteristics, but also through their interactions. Given the unprecedented ability to control growth parameters during the synthesis (i.e., core diameter, shell thickness, and material composition) the overall properties of the particles can be accurately tailored to match specific applications, which make CS nanoparticles particularly attractive.

Currently, there is a great number of applications arising from the multifunctionality of CS nanoparticles, which include (without trying to be exhaustive) biomedical uses, pharmaceutical purposes, magnetism, catalysis, electronics, or photoluminescence. An important example related to magnetic nanoparticles is the use of organic or inorganic coatings to allow the functionalization of the nanoparticle surface, stabilize the nanoparticles in a solution (colloidal suspensions) and make them biocompatible. This combination of properties has resulted in a wide range of new applications for magnetic nanoparticles in biomedicine, i.e., in fields such as hyperthermia, [109, 194] magnetic resonance imaging (MRI), [195] high sensitive sensing biosensing, [196, 197] magnetic separation [81] or drug delivery. [198] Moreover, if shells with optical properties (e.g., plasmonic -Au or Ag- or fluorescence -CdSe-) are grown on magnetic nanoparticles, these have the added advantage of bio-labeling which allows tracking the position of the nanoparticles in biological media. [199, 200] Another important field for CS nanoparticles is catalysis where often the CS nanoparticles are more efficient than nanoparticles of each individual constituent, as for example the CO oxidation by Ni/Pd CS nanoparticles. [201] In some cases, CS nanoparticles allow consecutive or more complex reactions than for single phase nanoparticles. [202] An additional burgeoning field in CS nanoparticles is the one of semiconductor nanoparticles. The combinations of materials with different band gaps allows, for example, to increase the photoluminescence

efficiency, band gap tuning, stability against photobleaching, or enhancement of the photoluminescence decay time. [203]

Importantly, there exist a great variety of fabrication methods to obtain CS nanoparticles such as precipitation, [204, 205] thermal decomposition, [192, 206–208] grafted polymerization, [209, 210] microemulsion, [211, 212] sol-gel condensation, [213, 214] layer-by-layer absorption, [215, 216] electrodeposition, [217, 218] and so on. In particular, the seed-growth approach, based on the thermal decomposition method (which is the one used in the thesis), is particularly appealing since it allows to synthesize heterogeneous structures (with core and shell composed of different materials) with an exquisite control of the sizes. However, interestingly, one of the simplest routes to form CS nanoparticles arises from the surface treatment of the nanoparticles (e.g., oxidation, reduction or nitration), which leads to the formation of a layer on their surface with a different phase (this approach has also been used in the thesis). In the case of transition metal nanoparticles, controlled oxidation leads to the formation of an oxide passivation layer which has physicochemical properties different from the ones of the metallic core. Similarly, for oxide nanoparticles oxygen passivation can lead to the formation of an oxide shell with a different oxidation state and hence new physicochemical properties. The main drawback of this approach is that the shell is always derived from the core, thus the possible choice of physicochemical properties of the shell are somewhat limited.

A special case of CS nanoparticles is bi-magnetic CS nanoparticles, where both core and shell are either ferromagnetic (FM), ferrimagnetic (FiM) or antiferromagnetic (AFM). Different combinations of magnetic structures in the core and the shell have been studied. Probably the most studied type of system is the FM|AFM CS structure based on the partial oxidation of magnetic transition metal oxides, where for example Co is FM and CoO is AFM [219–222]. More recently, the interest exchange coupled hard|soft FiM|FiM or FM|FiM CS morphologies is steadily increasing to search for novel types of rare-earth free permanent magnets. Nevertheless, the combination of magnetic properties in the core and the shell and, in particular, their interface exchange coupling, has led to novel effects which can be exploited in diverse applications, ranging from permanent magnets to biomedical applications [109, 110]. In fact, promising results showing enhanced blocking temperatures, [223–225] increased energy products, [226, 227] advanced magnetic separation, [81] superior microwave absorption, [228, 229] highly sensitive biosensing, [82, 83] improved magnetic resonance imaging, [84] novel magnetic resonance amplification [107] or optimized hyperthermia, [109, 230] have already been demonstrated.

This thesis is focused on the development of novel types of bi-magnetic CS structures. The aim of the work is to control and improve the magnetic properties of the core material by the presence of the shell. Two types of structures AFM|FiM and soft|hard FiM have been studied. Note that these structures are inverted with respect to the more common FM|AFM and hard|soft morphologies.

3.1 FM(FiM)|AFM exchange-coupled CS nanoparticles

Bi-magnetic exchange-coupled CS nanoparticles composed by AFM and FM(FiM) materials have been extensively studied and developed due to their novel properties and potential applications. Their research has been mainly focused on the synthesis of CS structures formed by transition metals as the basic component. Typical CS nanoparticles are composed by two different materials such as: metal|metal, metal|metal oxide and metal oxide|metal oxide (although other combinations are possible). In addition, these two phases should fulfill the magnetic condition that one layer must be AFM and the other FM or FiM. [173] The interest in these CS structures is not only due to the appearance of hysteresis loop shifts, H_E , due to the AFM-FM coupling, but also for other related phenomena which can be used to tune the initial magnetic properties of the FM (FiM) core, such as increase their blocking temperature [224] or coercivity. [231]

FM(FiM)|AFM exchange-coupled CS nanoparticles can be classified in function of their constituent materials. In fact, the first FM|AFM CS nanoparticles studied were based in metal|metal oxide structures, where the initial FM metal, Fe, Co, Ni, or their alloys are surface chemically modified by their exposure to air leading to the formation of a metal oxide passivation shell. The passivation process usually results in the formation the less oxidized state for the TM metals, i.e., the monooxide compound,

which presents always an AFM behavior. Notably, for sufficiently small nanoparticles or instable passivation layers, the oxidation can take place over the whole nanoparticle, losing, thus, the CS structure. Moreover, since TMs can have more than one oxidation state, the oxide layer can have different phases with diverse magnetic properties, e.g., FeO (AFM) or Fe₃O₄ (FiM). A part from oxidation, other different approaches have been used to try to stabilize the metal core, such as nitration or sulphuration of the metal surface. Interestingly, due to the similar physicochemical properties between nitrides, sulfurs and oxides many of these TM compounds present similar AFM or FiM magnetic properties.

Co|CoO, [219–222] Ni|NiO, [232, 233] Fe|Fe_xO_y, [234] Co₈₀Ni₂₀|CoO, [235] Fe|FeN₂ [236] and Fe|FeS [237] are examples of these FM metal core and surface chemically modify AFM shell nanoparticles.

Alternatively, surface chemically modified CS systems can be formed not only by the metal|metal oxide configuration but also by different metal oxides of the same TM with different oxidation states. In this case, the different oxidation states of the TM metal oxide can present different magnetic properties. On example of this behavior is the iron oxide compounds, whereas the initial metal state, Fe, is FM, the related possible magnetic oxides are FeO (Fe²⁺) AFM, Fe₃O₄ (Fe²⁺ + Fe³⁺) FiM, γ -Fe₂O₃ (Fe³⁺) FiM, α -Fe₂O₃ (Fe³⁺) weakly FiM and ϵ -Fe₂O₃ (Fe³⁺) hard FiM. [238].

Examples of this metal oxide|metal oxide FM (FiM)|AFM CS nanoparticles are CrO₂|Cr₂O₃, [239] FeO|Fe₃O₄ [240, 241] and Fe₃O₄| α -Fe₂O₃. [242]

All these examples can be classified as standard CS FM (FiM)|AFM nanoparticles. These standard CS systems present a structural arrangement where, the core is the FM or FiM magnetic material and the shell layer is AFM. In addition, from the magnetic point of view all of these nanoparticles show the typical relationship between their magnetic transition temperatures. Specifically, the FM T_C of the core is larger than the T_N of the AFM metal oxide (nitride or sulfur) layer (T_C > T_N), which is the magnetic structure usually studied in thin films. [172]

In contrast, surface chemically modify CS systems have also been studied with different architectures. Firstly, structurally inverted CS systems are defined as when the core present the AFM behavior and the FM or FiM material is in the shell layer. Secondly, from the magnetic point of view a magnetic inversion is achieved when the T_N of the AFM material is larger than the T_C of the FM or FiM material (T_N > T_C). Thirdly, double-inverted systems are defined as systems which present, at the same time, structural and magnetic inversions, i.e, the AFM core present larger values of T_N than the T_C of the FM (FiM) shell. For example, the FeO|Fe₃O₄ [240, 241] system is classified as structural inverted or single inverted system, since the FeO core is AFM and T_C(Fe₃O₄) > T_N(FeO). On the other hand the most common double inverted systems (AFM-core|FM-shell with T_N > T_C) for CS nanoparticles are based in the use of Mn oxides, i.e., Mn AFM or MnO AFM as cores and Mn₃O₄ FiM or γ -Mn₂O₃ FiM as shells. [243–246]

Finally, importantly, although modifying chemically the surface of magnetic nanoparticles is a simple and inexpensive approach to create CS structures, it presents some drawbacks. The main disadvantage of this approach is that the shell is always derived from the core, thus the possible choice of physicochemical properties of the shell are somewhat limited. Moreover, since the surface layers are passivation layers, they are very stable and usually have a well determined thickness for each material. Thus, controlling the shell thickness is often difficult in this type of systems. Another drawback is that, due to the shape of the nanoparticles and their reduced size, the AFM or FiM shells usually grow highly disordered and/or polycrystalline, making the control of the microstructures rather difficult. Furthermore, for small nanoparticles the core could be completely oxidized or be exceedingly small, becoming SPM, which could lead to a deterioration of the exchange bias properties. [173, 222, 225, 233, 247]

To overcome these drawbacks a broad range of different synthetic routes have been recently developed to try to controllably synthesize magnetic shells to create CS nanoparticles starting from pre-made FM, AFM or FiM cores. Contrarily to the surface treated CS nanoparticles, for these new CS synthetic routes the shell does not grow at the expense of the initial core. Thus, the final thickness (even shape in some cases) of the shell can be adjusted and, more interestingly, the core size and shell thickness can be controlled independently. Another significant benefit of these new approaches is the possibility to create highly crystalline shells. Finally, one the most important advantages is the possibility to create heterostructures, i.e., the shell deposited can be formed by distinct material form that the pre-made

core. However, bi-magnetic heterostructures have not been extensively studied due to the difficult to find specific magnetic materials which can be structurally core|shell anchored (i.e., lattice mismatch) to results in high quality structures.

Some examples of these heterostructured bi-magnetic CS systems are SrFe₁₂O₁₉|CoO [248], CoFe₂O₄|MnO, [249] FePt|MnO [250] and Cr₂O₃|Fe₃O₄. [251]

The magnetic properties of many conventional FM(FiM)|AFM exchange coupled CS nanoparticles have demonstrated an excellent exchange coupling between the FM(FiM) and AFM layers both in surface treated and heterostructured bi-magnetic CS nanoparticles. Similarly, single and double inverted systems also exhibit good exchange coupling between the FM(FiM) and AFM layers. For example, coercivity, H_C , enhancement after field cooling from above T_B , or T_C , of the FM(FiM) phase have been observed in conventional systems, [173, 219–222, 239, 248, 250] structurally inverted [240, 241, 251] and cooling from above T_N for magnetically inverted systems (i.e, double inverted manganese based CS structures). [231, 243–246] Correspondingly, large values of horizontal loop shift, H_E , i.e., the most revealing sign of the FM-AFM exchange coupled systems, have also been demonstrate in many systems. [173, 219–222, 231, 234, 243–246] However, low shell crystallinity [225, 233] or ion migration between core and shell phases (in heterostructured bi-magnetic structures) [249] can lead to a small or vanishing H_E values.

Interestingly, different studies have been developed to understand the role played by size of the constituents, i.e. core size and shell thickness, on the exchange bias properties (i.e., the loop shape, H_E and H_C). [173]

The role of the FM core diameter, d_{core} , in conventional FM(FiM)|AFM systems has been found to be similar to the FM thickness in bilayer systems for a certain thickness range. Specifically, H_E and H_C decrease with increasing core diameter, roughly inversely proportional to d_{core} . However, more complex behaviors have been reported in some cases, where a decrease of H_E is observed for sufficiently small diameters. Moreover, for very large d_{core} (i.e., larger than the critical single domain radius) the $1/d_{core}$ is no longer valid and the shift becomes roughly independent of d_{core} .

In the case of doubly inverse MnO|Mn₃O₄ system [243] the dependence H_E and H_C on the AFM diameter d_{core} has been studied. Interestingly, the FiM shell thickness, t_{shell} , was maintained roughly constant only varying the AFM d_{core} . Both H_E and H_C exhibit a non-monotonic dependence with d_{core} . H_C increases dramatically between the sample with no MnO core and the sample with a small MnO core size, $d_{core} = 2.2$ nm. H_C then decreases as the core size is further increased. Similarly, H_E , also exhibits a peak as a function of MnO core size. However, in this case, the maximum appears for a core size of $d_{core} = 18$ nm, with values as high as $H_E = 1.8$ kOe (see figure 3.1).

Less effort has been devoted to studying the effect of the shell thickness, t_{shell} , since given the passivation character of the shell in surface treated nanoparticles, they are difficult to control. Thus, the most systematically studied system involving an AFM is the heterostructured SrFe₁₂O₁₉|CoO system, in which the thickness of the shell can be controllably changed keeping the core diameter constant. [248] As expected, H_E increases steeply for small t_{shell} thickness and saturates at about 500 Oe, while H_C shows a broad maximum, tending to decrease and eventually saturate for larger t_{shell} (see figure 3.2(a) and 3.2(b)).

3.2 Hard-FM(FiM)|Soft-FM(FiM) exchange-coupled CS nanoparticles

In recent years, the interest in hard-FM(FiM)|soft-FM(FiM) exchange-coupled CS nanoparticles has been steadily increasing. In this case, the particles must be composed of two different FM(FiM) materials, where one should have hard magnetic properties (i.e., high anisotropy) and the other one should

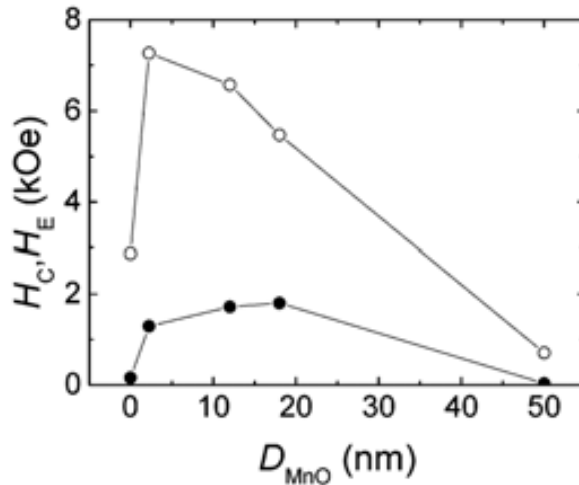


Figure 3.1: Dependence of the loop shift, H_E , (filled symbols) and coercivity, H_C , (empty symbols) on the AFM MnO core diameter for MnO|Mn₃O₄ CS nanoparticles. [243]

display soft magnetic properties (i.e., low anisotropy). From the material point of view the CS structure can be formed by metal|metal, metal|metal oxide or metal oxide|metal oxide, where the main component is usually a transition metal, TM, although there exist also a few examples involving rare-earth ions.

Notably, although CS systems are the main aim of this thesis, in this section some non-CS structures will also be discussed. Namely, heterodimer bi-magnetic structures with hard|soft architectures [192,193] are also generating some interest and they have been shown to be good candidates to display spring-magnet properties.

Part of the systems studied in nanoparticle stem from different approaches to synthesize hard-FM face-centered tetragonal (fct) L1₀-FePt phase. One of the synthetic approaches to create this structures usually starts with the synthesis of disordered face-centered cubic (fcc)-FePt nanoparticles onto which iron oxide, Fe₃O₄, is deposited or the inverse procedure using Fe₃O₄ as seeds and depositing (fcc)-FePt on top. [226,227,252–255] These materials are annealed to induce the transformation of the soft fcc-FePt phase into hard fct-FePt. The Fe₃O₄ acts as a barrier for nanoparticle coalescence during the annealing. [254,255] This process results in hard|soft FePt|Fe₃O₄ structures. Alternatively, the fcc-FePt|Fe₃O₄, is annealed in a reducing atmosphere leading the formation of fct-FePt|Fe₃Pt hard|soft nanocomposites, where fct-FePt and Fe₃Pt act as hard and soft FM phases, respectively. [226,253–255]. A similar approach is proposed by Chaubey et al. [227] where the nanocomposite are composed of FePt|CoFe₂O₄ and the posteriorly annealing treatment lead to the formation of a hard(FM)-FePt|soft(FM)-FeCo nanocomposite. A distinct procedure to obtain fct-FePt|Fe₃Pt hard|soft nanocomposites was proposed by Zeng et al. [252] where Fe₃O₄ and FePt nanoparticles are self-assembled on a substrate and posteriorly annealed.

Of particular interest are the studies, based on the FePt|Fe₃O₄ system, where the dependence of the magnetic properties on the core diameter and shell thickness have been investigated. [226,256]

Importantly, we define the CS nanoparticles with a hard-FM|soft-FiM core|shell structure as conventional systems. Other conventional hard|soft structures include, metal|metal CS nanoparticles such as Nd₂Fe₁₄B|CoFe, [257,258] metal|metal oxide like Sm(Co_{1-x}Fe_x)₅|Fe₃O₄ [259], Fe|Fe_xO_y, [84,260,261] Fe|MnFe₂O₄ [84] and metal oxide|metal oxide as CoFe₂O₄|MFe₂O₄ (M = Zn, Mn). [262,263]

Remarkably, far less attention have been paid for the inverse structures, i.e., soft|hard systems where the core is soft and the shell is hard. In fact, all of the studies carried on in soft-FM(FiM)|hard-FM(FiM) exchange coupled CS nanoparticles have performed combining two metal oxides, i.e., metal oxide|metal oxide structures. Particular attention has been devoted to iron ferrite spinel structures due to capability to easily control their magnetic hardness changing one of the iron ions for some other metals (MFe₂O₄, M = Mn, Co, Cu, Zn, and so on). [112]

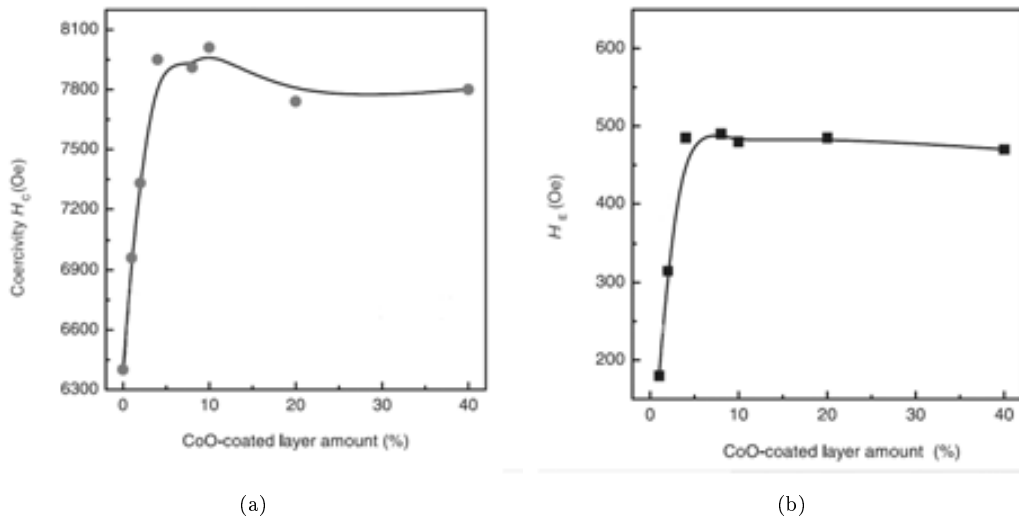


Figure 3.2: (a) Dependence of the coercivity, H_C , and (b) loop shift, H_E , on the AFM CoO shell thickness for $\text{SrFe}_{12}\text{O}_{19}|\text{CoO}$ CS nanoparticles. [248]

Some examples of this CS inverted soft|hard architecture are $\text{Fe}_3\text{O}_4|\text{CoFe}_2\text{O}_4$, [84, 223, 263] $\text{MFe}_2\text{O}_4|\text{CoFe}_2\text{O}_4$ ($M = \text{Zn}$ and Mn), [262, 263] and $\text{Fe}_3\text{O}_4|\text{Mn}_3\text{O}_4$. [208, 264]. Note that the $\text{Fe}_3\text{O}_4|\text{CoFe}_2\text{O}_4$ [223] CS system has been created using a similar procedure to the one reported by Zeng et al. [252] for $\text{FePt}|\text{Fe}_3\text{O}_4$. Namely, Fe_3O_4 and Co nanoparticles have been deposited together forming a perfect self-assembly. The posterior annealing leads to ion segregation between the particles and the creation of $\text{Fe}_3\text{O}_4|\text{CoFe}_2\text{O}_4$ CS nanoparticles.

The magnetic properties of conventional hard-FM(FiM)|soft-FM(FiM) and inverse soft-FM (FiM)|hard-FM(FiM) exchange coupled CS nanoparticles have demonstrated the exchange coupling between soft and hard FM(FiM) phases. As have been discussed in section 2.3, large $(\text{BH})_{max}$ energy product and single-phase like switching would probably be the most prominent characteristics for spring-magnet systems if they present a good exchange-coupling between the different FM layers. Interestingly, in most of the above systems single-phase switching is achieved only for a narrow range of core diameters and shell thicknesses used. Note that even for the $\text{FePt}|\text{Fe}_3\text{O}_4$ CS annealed systems (i.e., fct- $\text{FePt}|\text{Fe}_3\text{O}_4$ nanocomposites) only for small soft-FM shell thickness, i.e. iron oxide, the single-phase switching is maintained for the hybrid structure. [252] In some cases the dual-phase switching may be caused by the morphology created during the high temperature annealing, which induces some shell-shell coalescence. Thus, to some extent the systems do not behave as true CS structures but they behave more like hard-FM(FiM) nanoparticles embedded in a soft-FM(FiM) matrix. [110, 164, 227] In other systems, like the one formed by $\text{Fe}|\text{MnFe}_2\text{O}_4$ [84] the two-phase like switching can be understood due to, first, the large core used, 16 nm, and, second, the disordered FeO layer formed between the two FM(FiM) phases.

On the other hand, $(\text{BH})_{max}$ product enhancement, respect to the separated phases, arising from the good FM(FiM)-FM(FiM) exchange coupling, has been demonstrated in several systems. [226, 227, 252, 253] In contrast for $\text{Sm}(\text{Co}_{1-x}\text{Fe}_x)_5|\text{Fe}_3\text{O}_4$ system the $(\text{BH})_{max}$ product is reduced, in comparison from the expected values. In this case, this behavior can be understood due to the low crystallinity phase used as core. [259]

The work of Masala et al. [262] shows the excellent exchange coupling present in both conventional $\text{CoFe}_2\text{O}_4|\text{ZnFe}_2\text{O}_4$ soft-core|hard-shell and inverted $\text{CoFe}_2\text{O}_4|\text{ZnFe}_2\text{O}_4$ hard-core|soft-shell systems. The magnetization as a function of the temperature show a single magnetic transition for both, single phase and CS, systems confirming the good exchange coupling between magnetic layers. The values of the blocking temperature increase at the same time as the relative volume of the hard phase is larger. From

the hysteresis loops the CS system present some $(BH)_{max}$ enhancement compared to the pure CoFe_2O_4 nanoparticles. M_S and H_C is increased with regards to the relative values for the hard and soft phases, respectively. Importantly, these systems present an important influence of the interparticle dipole-dipole interaction, where measurements performed in pressed or dispersed ($\sim 2 - 10\%$ in volume) show clear differences. The strong dipole interaction creates kinks in the hysteresis loops and reductions of the coercivity.

Another important aspect ascribed to the good exchange-coupling between the two FM(FiM) phases is the appearance of loop shifts, H_E . [173] However, only some systems have been reported to exhibit H_E ; for example, fct-FePt|iron-rich phase|iron oxide onion-like nanoparticles [255], Fe| Fe_xO_y CS system. [260, 264]

Finally, it should be emphasized that the role played for d_{core} and t_{shell} in the different magnetic properties ascribed to the spring-magnet has been rarely been systematically addressed. For fct-FePt| Fe_3Pt nanocomposites some studies have focused on the dependence of H_C , H_E , M_S and $(BH)_{max}$ product as a function of the ratio between FePt and Fe_3O_4 (before the annealing). [227, 252, 253, 255, 265] These works reveal that for small initial Fe_3O_4 shells the H_C and the $(BH)_{max}$ can be enhanced due to the formation of small crystals of soft-FM Fe_3Pt . In contrast, for larger Fe_3O_4 shell thickness H_C and $(BH)_{max}$ decrease due to the major role played by the soft FM phase formed in the final nanocomposites. On the other hand Fe_3O_4 thickness dependence for FePt| Fe_3O_4 heterodimers [256] and not annealed CS [226] nanoparticles reveal similar properties. Particularly, in the work of Figuerola et al. [256] it is demonstrated that H_C values measured for the initial FePt seeds decreased monotonically with increasing d_{FePt} and were further reduced following the growth of the iron oxide domains. A more careful analysis suggested that the coercive fields were better correlated to the ratio between the sizes of the respective domains, $d_{\text{Fe}_3\text{O}_4}/d_{\text{FePt}}$, rather than to their absolute values. FePt| Fe_3O_4 heterodimers became magnetically harder when they adopted roughly symmetric configurations ($d_{\text{Fe}_3\text{O}_4}/d_{\text{FePt}} \approx 1-2$) (see figure 3.3(a) and 3.3(b)).

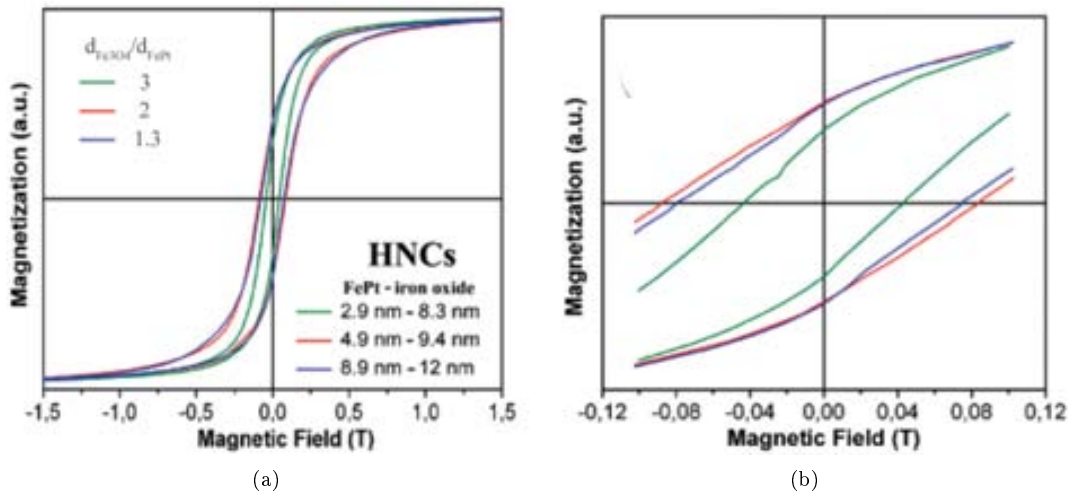


Figure 3.3: (a) Normalized hysteresis loops measured at 5 K for FePt| Fe_3O_4 heterodimers structures and (b) enlarged hysteresis loops in the low field region. [256]



Chapter 4

Experimental Techniques

In this chapter the main different experimental techniques used to characterize the CS nanoparticles will be discussed. Techniques such as transmission electron microscopy (TEM), electron energy loss spectra (EELS), X-ray powder diffraction (XRD) and X-rays absorption spectroscopy (XAS) have been used to identify different morphological and structural aspects like size and shape, ion distribution, crystallographic parameters and so on. On the other hand, the magnetic characterization has been carried on using diverse techniques such as magnetometry (superconducting quantum interference device -SQUID- and vibrating sample magnetometer), which in some cases has been analyzed using first-order reversal curve (FORC), electron spin resonance (ESR), neutron diffraction, X-ray magnetic circular dichroism (XMCD) and Monte Carlo simulations (MC).

4.1 Transmission electron microscopy, TEM

Transmission electron microscopy (TEM) is a microscopy technique in which a beam of electrons is transmitted through an ultra thin sample, interacting with the specimen as it passes through it. An image is formed using the transmitted electrons. The image is magnified and focused onto an imaging device, such as a fluorescent screen, a layer of photographic film, or a CCD camera.

The transmission electron microscope operates on the same basic principles as the light microscope but uses electrons instead of light. However, the resolution in light microscopes is limited by the wavelength of light. In contrast, TEM uses electrons as light source and their much shorter wavelength makes it possible to reach a resolution thousand times better than that of a light microscope. Moreover, remarkably, electrons can interact with matter thus rendering also chemical and structural information of the sample.

Based on the particle character of electrons, the electron scattering with the specimen can be divided in: unscattered and elastically and inelastically scattered. The transmission of unscattered electrons is inversely proportional to the specimen thickness. Thicker specimens will have fewer transmitted, unscattered, electrons hence they will appear darker, conversely the thinner specimens will have more transmitted electrons and thus they will appear lighter. Unscattered electrons create, then the contrast of the final image. Another part of the incident electrons, are scattered, i.e. deflected from their original path, by atoms in the specimen in an elastic fashion (no loss of energy). Elastically scattered electrons are the major source in TEM imaging (grey part of the final image) and also of electron diffraction patterns. Inelastically scattered electrons are the incident electrons that interact with specimen atoms in an inelastic fashion, i.e., losing energy during the interaction. Historically, in operating a TEM only elastic signals were taken into account; therefore, the information about the specimen resulting from inelastic scattering was wasted (although information was collected in related instruments such as SEM and Auger electron spectrometry). However, the signal from the inelastically scattered electrons can also be detected using TEM to obtain a more complete characterization of the specimen. Importantly, the energy lost when the electron beam crosses the specimen is the basis of electron energy loss spectroscopy

(EELS). The EELS signal, together with the X-ray signal, constitute analytical electron microscopy (AEM) (see figure 4.11a).

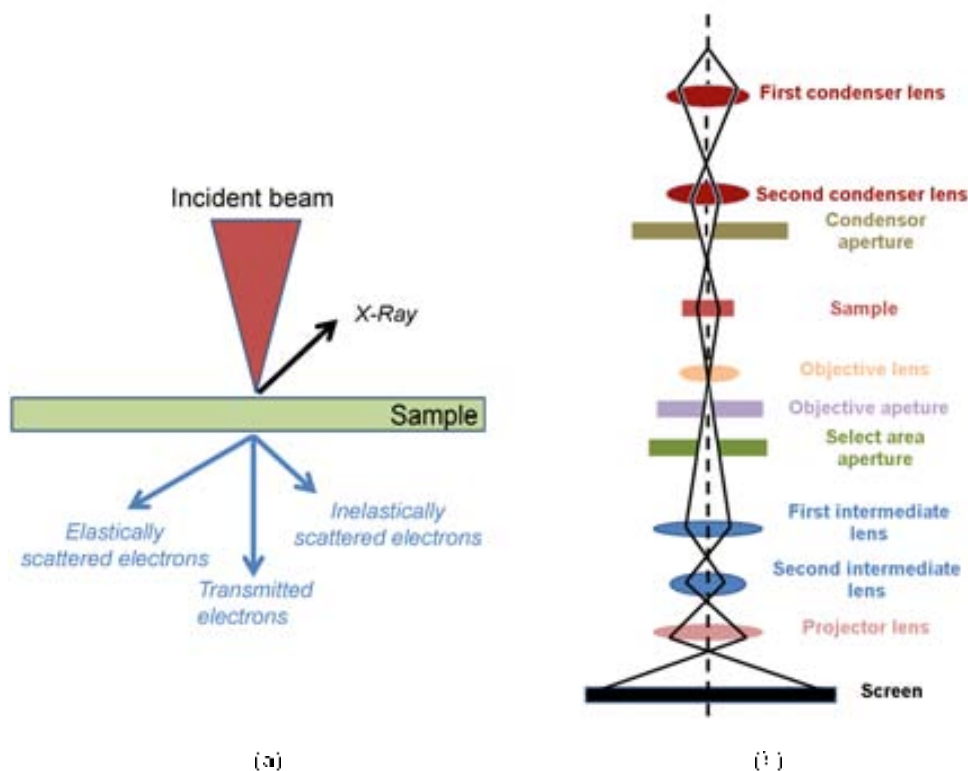


Figure 4.11: (a) Schematic diagram illustrating scattering process of the electrons in a TEM and (b) the main components of a TEM.

In electron microscopy techniques, electrons are emitted from the electron gun, the beam is driven by different magnetic lens crossing the sample and, finally, the image is viewed on a screen or CCD camera. The two most usual types of electron guns are the conventional electron guns, made of LaB_6 or tungsten, and the field emission guns (FEG). FEGs produce much brighter sources than in conventional guns (electron current > 4000 times) and better monoenergeticity, although it requires a very good vacuum ($\sim 10^{-11}$ Torr). Below the electron gun there are two or more condenser lenses. Together, they demagnify the beam emitted by the gun and control its diameter as it hits the specimen. An aperture is present between the condenser lenses (the condenser aperture) which can be used to control the convergence angle of the beam. In a simple view, the condenser controls can be thought of as brightness controls, although, in fact, they permit a wide range of control over the region of the specimen. Below the condenser lies the specimen chamber. The specimen must be held in precisely the correct position inside the objective lens. However, the system should be capable moving the specimen by several millimeters and allow tilting it by large angles. After the specimen chamber are placed the objective lenses. Their role is to form the first intermediate image and diffraction pattern, which are enlarged by subsequent projector lenses and displayed on the viewing screen. The first projector lens (often called intermediate or diffraction lens) can be switched between two settings: In the image mode, it is focused on the plane of the objective. Contrary, in the diffraction mode, the intermediate lens is focused on the back focal plane of the objective and the diffraction pattern is projected onto the viewing screen (see figure 4.10.10). Some specialized microscopes have an energy filter below the specimen which can be tuned to

allow the passage of only elastically scattered electrons. For example, this is of special interest in high resolution electron microscopy since inelastic scattering degrades image quality or in the quantitative interpretation of diffraction pattern intensities. Nowadays, typically, CCD cameras are used to record images and diffraction patterns in electron microscopies. Combining the output signal/image with a camera and a computer which has image processing software and control of the microscope lenses, it is now possible to perform some alignment procedures quickly and automatically. [266–268]

4.1.1 Image mode in TEM

To operate in imaging mode, suitably sized objective lens apertures are placed in the back focal plane of the objective lens. In this way, diffracted beams can be deliberately excluded and only the central beam is allowed to pass through. The image built up is called bright field image. Alternatively, a dark field image is formed by excluding all beams, except a particular diffracted beam of interest. This dark field image reveals the regions contributing to the diffracted beam intensity selected, which can be useful in the characterization of complex micro and nanostructures. At smaller magnifications TEM image contrast is due to absorption of electrons in the material, which is driven by their thickness and composition. At higher magnifications, complex wave interactions modulate the intensity of the image, requiring expert analysis of the observed images. Alternate modes of use allow for the TEM to observe modulations in chemical identity, crystal orientation, electronic structure and sample induced electron phase shift as well as the regular absorption based imaging.

The images obtained by transmission electron microscopy allow us to characterize, mainly, the shape and size of the nanoparticles (see figure 4.2(a)). For spherical particles the measurement of a large number particle diameters gives us information about the particle size distribution. In addition, other types of information can be extracted through the analysis of the TEM images. High resolution TEM images (HR-TEM) can allow us to distinguish the crystallographic planes of the specimen (see figure 4.2(b)). In fact, to make their analysis easier the fast-Fourier transform (FFT) of these images show the repetitive interatomic planes in clear differentiated spots (see figure 4.2(c)). Spots from the same crystallographic plane are disposed around the center of the image and the distance from the center of the image to the specific spot is given by the precise interplanar distance.

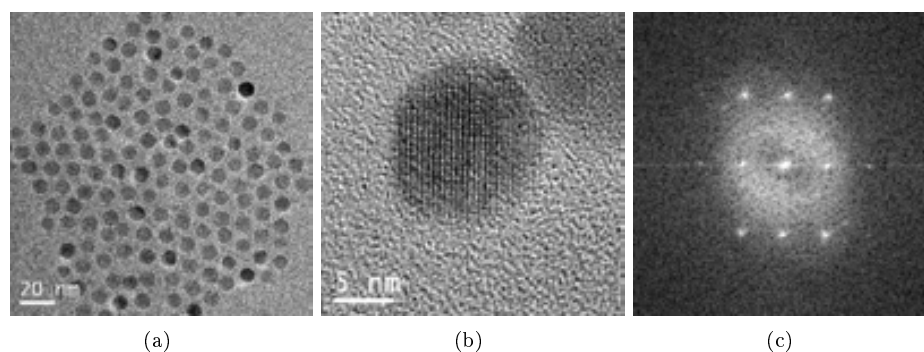


Figure 4.2: (a) TEM image in a magnification of 120 K, (b) HR-TEM image in a magnification of 1200 K and (c) FFT of the (b) image for a 6.5 nm Fe_3O_4 nanoparticle.

TEM images were obtained using a Jeol JEM-2010 [269] microscope with a LaB_6 filament operated at 200 kV. The nanoparticles were dispersed in hexane, or any other apolar solvent, and placed dropwise onto a holy carbon supported copper grid. The particle size and its standard deviation of the different samples were obtained by manually measuring the equivalent diameters of >200 particles from TEM

micrographs and fitting the data to a distribution function (gaussian or log-norm) from which the average and the standard deviation are obtained.

The TEM, HR-TEM images and their respective FFT analysis were carried out by me using the Jeol JEM-2010 TEM of Centre de Microscòpia of the Universitat Autònoma de Barcelona.

4.1.2 Electron energy loss spectroscopy, EELS

As has been discussed above in the TEM some of the electrons will undergo inelastic scattering, which means that they lose energy and have their paths slightly and randomly deflected. The amount of energy loss can be measured via an electron spectrometer. The inelastic interactions, i.e., the energy loss, can have several origins which include phonon excitations, inter and intra band transitions, plasmon excitations and inner shell ionizations. Electron energy loss spectroscopy (EELS) is the study of the vibrational motion of atoms and molecules on and near the surface by the analysis of the energy spectrum of low-energy electrons backscattered from it. An electron passing through a material can interact with the electron clouds of the atoms present and transfer some of its kinetic energy to them. EELS detects electrons, in a range of 0.1 to 10 keV, which have passed through the material. At high energies, the transmitted beam contains inelastically scattered electrons whose energy has been decreased by amounts corresponding to characteristic absorption frequencies in the sample.

An EEL spectrum is conventionally considered to consist of three regions. The majority electrons have suffered negligible inelastic scattering and form the *zero loss peak*. The *low loss region* contain electrons which have lost about 50 eV, arising mainly from plasmon scattering. In contrast, for analytical purposes it is more useful to study the characteristic element edges at higher energy. Importantly, although the number of electrons which suffer high energy losses is small, the energies which correspond to inner shell excitations (see section 4.5) are just as characteristic of the element as are X-ray absorption peaks. Hence, these energies (usually denoted as edges) are commonly used for EELS analysis. Quantitative analysis is carried out by determining the energies of the edges which are observed in the 100 to 2000 eV range. Moreover, in principle, the size of each edge is proportional to the number of atoms of that element in the analyzed region of the specimen. Consequently, identifying the edge from each element in the specimen, measuring their relative sizes and taking into account, first, the different cross-sections for each elements and, second, the plasmon excitations; the composition of the sample can be determined. [266]

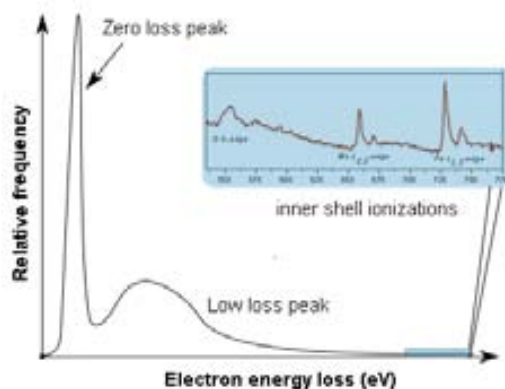


Figure 4.3: Spectrum range for the whole electron energy loss signal.

In a TEM, it is possible to cross the particle with the electron beam acquiring EEL spectra at point by point with an energy resolution of 0.8 eV (steps of ~ 0.5 nm, thus element quantification can be

determined locally with sub nanometer precision (see figure 4.4(a)). Interestingly, for samples composed by phases with the same main element in different oxidation state, e.g., core-MnO(Mn²⁺)|shell-Mn₃O₄(Mn²⁺ + Mn³⁺), the composition can also be determined in a similar procedure to the one described above, where the specific oxidation state can be quantified along the particle diameter using the intensity ratio of L₃ and L₂ the peaks of the corresponding EELS edge (see figure 4.4(b)).

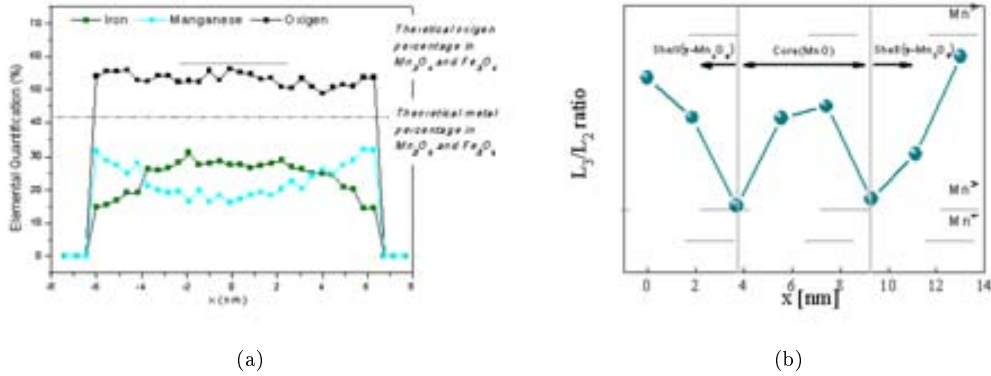


Figure 4.4: (a) EELS elemental quantification for core-Mn_xFe_(3-x)O₄|shell-Fe_xMn_(3-x)O₄ and (b) oxidation state quantification for core-MnO|shell-Mn₃O₄ CS spherical nanoparticles.

EEL spectra were measured using a Jeol-JEM-2010F microscope with a field-emission gun operated at 200 kV. EEL spectra were acquired every 0.5 nm along the diameter of the nanoparticles with an energy resolution of 0.8 eV. For MnO|Mn₃O₄ (γ -Mn₂O₃) and Mn_xFe_(3-x)O₄|Fe_xMn_(3-x)O₄ nanoparticles the O K, Mn L_{2,3} and O K, Mn L_{2,3} and Fe L_{2,3} energy edges were, respectively, acquired. The elemental quantification was carried out using Gatan Digital Micrograph commercial software. [270] Specifically the Mn oxidation state was obtained from the Mn-L₃ peak onset and L₃/L₂ intensity ratios [271, 272] using the homemade software package MANGANITAS. [273–275]

EELS measurements were carried out and analyzed by Sonia Estradé (LENS-MIND-IN2UB, Departament d'Electrònica, Universitat de Barcelona, Spain) using the commercial software Gatan Digital Micrograph and the homemade software MANGANITAS.

4.2 Diffraction analysis techniques

In classical physics, the diffraction phenomenon is described as the apparent bending of waves around small obstacles and the spreading out of waves past small openings. Diffraction occurs with all waves, including sound waves, water waves, and electromagnetic waves such as visible light, X-rays and radio waves. As physical objects have wave-like properties (at the atomic level), diffraction also occurs with matter and can be studied according to the principles of quantum mechanics. While diffraction occurs when propagating waves find small objects, its effects are generally most pronounced for waves where the wavelength is roughly similar to the dimensions of the diffracting objects. If the obstructing object provides multiple, closely spaced openings, a complex pattern of varying intensity can result. This is due to the superposition, or interference, of different parts of a wave that traveled to the observer by different paths.

X-ray (XRD) and neutron diffraction are versatile, non-destructive techniques that reveal detailed information about the chemical composition, physical properties and crystallographic structure of matter. X-ray and neutron diffraction are based on observing the scattered intensity of an X-ray or neutron

beam, respectively, hitting a sample as a function of incident and scattered angle, polarization, and wavelength or energy.

4.2.1 Bragg's law

Bragg's law gives the angles for coherent and incoherent scattering from a crystal lattice and/or unpaired spins for X-ray and neutron beams.

If one assumes that an incident wave beam is perfectly collimated and monochromatic (with a single wavelength λ) and makes an incident angle θ with respect to the reticular planes of the crystal, it can be demonstrated that the following condition is fulfilled:

$$n\lambda = 2d_{(hkl)}\sin(\theta) \quad (4.1)$$

Where n is the reflection order and $d_{(hkl)}$, or d-spacings, is the interplanar distance of one family of (hkl) crystallographic planes, and the beam will be completely in phase and give constructive interferences. This condition, known as the Bragg's law, is schematically represented in figure 4.5 and it can be used to determine the angular positions of the diffraction peaks diffracted by each family of planes. Also, $d_{(hkl)}$ can be understood as a geometric function of the size and shape of the unit cell of the diffracted crystallographic structure. As can be seen in equation 4.2 for a simple cubic crystallographic structure $d_{(hkl)}$ for an specific (hkl) planes can be related to the cell parameter, a . [276, 277]

$$d_{(hkl)} = \frac{a}{h^2 + k^2 + l^2} \quad (4.2)$$

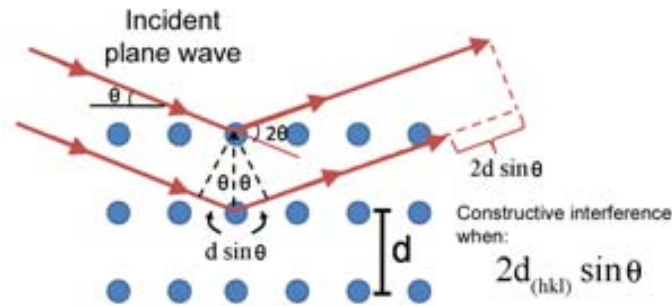


Figure 4.5: Schematic representation of the conditions for constructive interference resulting in Bragg's law.

4.2.2 Intensity of diffraction peaks

The measured diffraction pattern includes information about peak positions and intensity. The position of diffraction peaks, and the corresponding $d_{(hkl)}$, provide information about the location of lattice planes, the crystal structure and symmetry of the contributing phase. Each peak measures a d-spacing that represents a family of lattice planes, $d_{(hkl)}$. Moreover, each peak also has a fixed intensity which differs from other peaks in the pattern and reflects the relative strength of the diffraction. In a diffraction pattern, the strongest peak is, by convention, assigned an intensity value of 100, and other peaks are scaled relative to that value. Although peak height may be used as a qualitative measure of relative intensity, the most accurate measure of intensity relationships in a pattern is obtained by measuring the area (minus background) under the peaks. The intensity of a (hkl) diffraction peak from a flat rectangular sample of phase α in a diffractometer with a fixed receiving slit (neglecting air absorption), may be described by equation 4.3.

$$I_{(hkl)\alpha} = \frac{K_e K_{(hkl)\alpha} V_\alpha}{\mu_s} \quad (4.3)$$

Here, K_e is a constant for a particular experimental system, $K_{(hkl)\alpha}$ is a constant for each diffraction reflection (hkl) from the crystal structure of phase α , μ_s is the linear attenuation coefficient of the specimen and V_α is the volume fraction of phase α in specimen. Interestingly, the $K_{(hkl)\alpha}$ factor is directly proportional to the structure factor, $F_{(hkl)\alpha}$, for any (hkl) reflection.

The structure factor quantifies the amplitude of light scattered by a crystal. Then, the patterns of atoms in the unit cell scatters strongly in some directions and weakly in others owing to interference of the waves scattered by the atoms. $F_{(hkl)\alpha}$ sums the result of scattering from all of the atoms in the unit cell to form a diffraction peak from the (hkl) planes of atoms. The diffraction peak intensity is calculated using $F_{(hkl)\alpha}$ and additional terms should be taken into account to know how these waves, coming from successive crystal planes, combine together to form the resulting diffracted wave. Any change in $F_{(hkl)\alpha}$ will produce an observable change in the diffraction peak intensity. Then, $F_{(hkl)\alpha}$ can be defined as the overall atomic factor, atomic form factor, for all the atoms present in each crystallographic (hkl) diffracted plane. Notably, other factors can affect the relative intensity of the diffraction peaks, such as Lorentz factor, monochromator polarization or multiplicity factors.

Importantly, in certain lattice types, the arrangement and spacing of lattice planes produces diffractions from certain classes of planes in the structure that are always exactly 180° out of phase producing a phenomenon called extinction. In these cases, certain classes of reflections from valid lattice planes will not produce visible diffractions. [276, 278]

The $F_{(hkl)\alpha}$ and the corresponding peak intensities have been calculated theoretically for most crystal structures and comparing the experimental peak intensity to the theoretical one allows determining the phase of the diffracting material.

4.2.3 Peak shape function

Bragg's law assumes that the crystal is ideal (without structural defects) and the incident beam is perfectly monochromatic and collimated. Experimentally these conditions are never fulfilled completely. Moreover, usually, the particles are found to be composed of several grains, with different orientation and with certain amount of defects. Each of these grains is called a crystallite. The size of these crystallites and the microstrains present in them can also be obtained from the diffraction pattern, since both effects contribute to the width of the diffraction peaks. [276]

The peak shape function, $H(\Delta 2\theta)$, of conventional materials can usually be fit by a simple Gaussian function, Gf. However, when crystallite size drops below certain values, less than 100 nm or large strains are present, a deviation of the shape occurs from pure Gaussian to a mixture of a Gaussian and a Lorentzian, Lf, function, also referred to as a pseudo-Voigt function, Vf, in equation 4.4.

$$H(\Delta 2\theta) = Vf = \eta Lf(\Delta 2\theta \ X \ Y) + (1 - \eta) Gf(\Delta 2\theta \ U \ V \ W \ P) \quad (0 \leq \eta \leq 1) \quad (4.4)$$

Where η is the variable proportion between Gf and Lf functions, X and Y are the variables of the Lf function and U, V, W and P are the variables of the Gf function.

Pseudo-Voigt functions allow the separation of the Gf and Lf contributions to the peak shape function. The full width at half maximum, FWHM, contributions for the Gaussian and Lorentzian functions are instrumental and specimen broadening, respectively. The dependence of the specimen broadening on θ usually exhibits a $X^*(1/\cos\theta) + Y^*(\tan\theta)$ dependence, where the coefficients X and Y can be directly associated with the crystallite size and microstrain, respectively. If the broadening is anisotropic more complex dependencies can be introduced using two additional parameters. [278]

Then using this formalism, the crystallite size, d, can be easily estimated from the Lorentzian contribution to the FWHM of each diffraction peak, as given by the Scherrer formula (equation 4.5):

$$d = \frac{K_\alpha \lambda}{(FWHM)_i \cos\theta_i} \quad (4.5)$$

Where K is a constant dependent on the crystallite shape and λ is the incident wavelength. [276]

Note that the instrumental broadening, Gf function, can be calculated measuring standard samples, e.g., LaB₆, which present sufficiently large crystallite sizes and negligible stress values to avoid the presence of the Lf function in peak shape refinement.

4.2.4 Rietveld refinement

The Rietveld method is used to fit the experimental diffraction patterns by assuming a certain crystal structure and adjusting different structural parameters, such as atomic displacements, anisotropy, microstrain and so on. The chosen parameters are adjusted in an iterative process until convergence is reached between the values of the experimental intensities and the theoretical model. Different programs which use Rietveld method, such as Fullprof [279,280] and MAUD [281], are available in free form.

The function minimized in the refinement of the diffracted pattern by the Rietveld method is the residue, S_I , which is defined in equation 4.6.

$$S_I = \sum_i w_i (I_i - I_{calc})^2 \quad (4.6)$$

Here $w_i = 1/I_i$, I_i is the experimental intensity for the i step and I_{calc} is the calculated intensity for the same i step.

The intensities of I_{calc} (see equation 4.7) are determined from the structure factor, $F_{(hkl)\alpha}$, the scale factor, s (which depends on the amount of irradiated sample and the efficiency of the detector), the Lorentz factor, $L_{f(hkl)}$ (monochromator polarization and multiplicity factors), the peak shape function, $H(\Delta 2\theta)$, the preferred orientation factor, $O_{(hkl)}$, absorption factor, A , and the background intensity, I_{bkg} .

$$I_{calc} = s \sum_{(hkl)} L_{f(hkl)} F_{(hkl)}^2 H(\Delta 2\theta) O_{(hkl)} A + I_{bkg} \quad (4.7)$$

From a purely mathematical point of view, R_{WPF} (equation 4.8) is the function that best reflects the evolution of refinement.

$$R_{WPF} = \frac{\sum_i w_i (I_i - I_{calc})^2}{\sum_i w_i I_i}^{1/2} \quad (4.8)$$

However, this parameter is strongly influenced by the function chosen to fit the peak shape. Another parameter to consider is the *goodness* of the fit is X_R (equation 4.9), where N is the data number and P is the number of parameters varied in equation 4.9.

$$X_R = [S_I (N - P)]^{1/2} = R_{WPF} R_e \quad (4.9)$$

where

$$R_e = [(N - P) \sum_i w_i I_i^2]^{1/2} \quad (4.10)$$

When a value of $X_R \leq 1.3$ is reached, it is usually considered as satisfactory for a properly fitted diffractogram. [278,282]

4.2.5 Powder X-ray diffraction, XRD

X-rays is a form of electromagnetic radiation which have a wavelength in the range of 0.01-10 nm, corresponding to frequencies and energies in the range of $3 \cdot 10^{16}$ - $3 \cdot 10^{19}$ Hz and 0.12-120 keV. Given that the wavelength of X-rays is in the order of the interatomic distances, it makes interference effects possible. X-ray diffraction is based on observing the scattered intensity of an X-ray beam hitting a sample as a function of incident and scattered angle, polarization, and wavelength or energy.

When an X-ray beam encounters an atom, each electron in it scatters part of the radiation as can be seen in Thomson equation (equation 4.11).

$$I = I_0 \frac{e^2}{r^2 m_e^2 c^4} \sin^2 \theta \quad (4.11)$$

Here, I_0 is intensity of the incident beam, e and m are the single electron charge and mass, respectively, r is the distance between the incident beam and the electron, c the speed of light and θ the angle between the scattering direction and the direction of acceleration of the electron.

However, the nucleus has an extremely large mass compared with that of the electron, thus, the interaction with the nucleus is weak. The net effect is that coherent scattering by an atom is due only to the electrons contained in that atom.

Therefore, the wave scattered by an atom is simply the sum of the waves scattered by its electrons in the forward direction ($2\theta = 0$). This is not true for other directions of scattering. Since the electrons of an atom are situated at different points in space, differences in phase between the waves scattered by different electrons are generated.

A quantity f , the atomic form, or scattering, factor, is used to describe the *efficiency* of scattering of a given atom in a given direction. It is defined as a ratio of amplitudes:

$$f = \frac{\text{amplitude of the wave scattered by an atom}}{\text{amplitude of the wave scattered by one electron}} \quad (4.12)$$

Finally, it is clear that $f = Z$ for any scattering atom in the forward direction. However, as θ increases, the waves scattered by individual electrons become increasingly more out of phase and f decreases (see figure 4.6(a)). Moreover, the atomic form factor also depends on the wavelength of the incident beam.

The resultant wave scattered by all the atoms of the unit cell is called the structure factor, F . It is obtained by simply adding together all the waves scattered by the individual atoms (see equation 4.13).

$$F_{(hkl)} = \sum_1^N f_N \exp[2\pi(hkl)] \quad (4.13)$$

The analysis of the XRD patterns allows us to obtain different types of structural information for our studies. For example, the analysis of the peak position and their intensity provides us with the types of phases present in the samples and their relative amounts. As can be seen in figure 4.7, two types of phases have been identified (Fe_3O_4 and Mn_3O_4) and 60% in volume of the sample corresponds to Fe_3O_4 phase. Another important piece of information, obtained from the analysis of the peak width (and shape) is the crystallite size and the microstrains. In certain cases, the relative intensity of different peaks of the same phase also supplies further information about the atomic relative percentage, i.e. vacancies.

The X-ray diffractograms were obtained on loosely-packed powdered samples using a Philips 3050 and Panalytical X'Pert Pro diffractometers with $\text{Cu K}\alpha$ radiation using the Bragg-Brentano geometry. The measurements were carried out in the 2θ range 25-100 2θ with a step size of 0.04 θ and collection time of 10 s and 10-100 2θ with a step size of 0.012 θ and collection time of 300 s for Articles #3 and #4, respectively. All diffraction patterns were analyzed using the FULLPROF program [279,280]. The instrumental broadening have been calculated measuring a NIST powder LaB_6 standrad [283]

The powder XRD experiments were carried mostly by me using the diffractometer of Centre d'Investigació en Nanociència i Nanotecnologia. I also carried out some of the preliminary analysis using the Rietveld program MAUD. A more detailed analysis of the patterns was performed by Igor V. Golososky (St. Petersburg Nuclear Physics Institute, Russia) using the FullProf code.

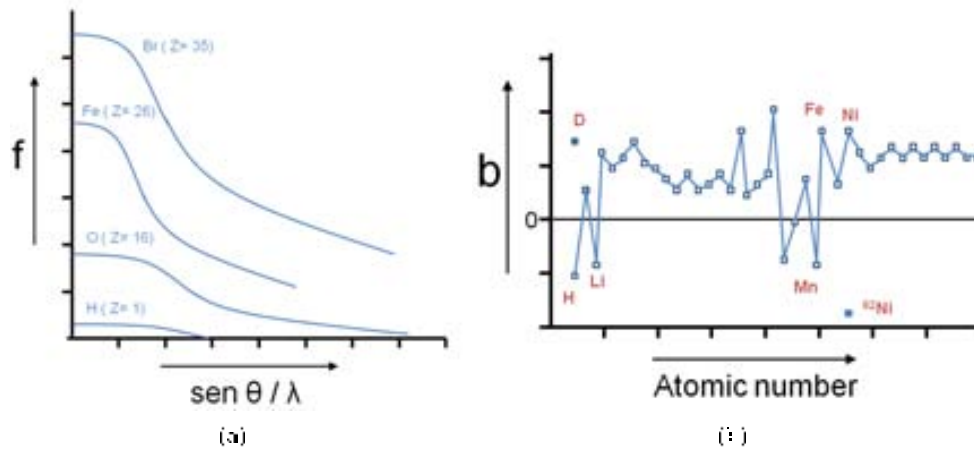


Figure 4C: (a) Atomic scattering factor, f , dependence in function of the 2θ angle and (b) neutron-nuclear scattering length of the different elements

4.2.6 Neutron diffraction

The scattering of slow neutrons is a very powerful technique to investigate the structure and dynamics of condensed matter. In contrast to photons, neutrons can be considered as particles and have a mass value of $1.6749286 \times 10^{-24}$ g. They are usually classified as function of their energy, wavelength, λ , and temperature:

| | Energy (meV) | Temperature (K) | Wavelength (Å) |
|------------------|--------------|-----------------|----------------|
| Cold neutrons | 0.4-10 | 4-120 | 30-5 |
| Thermal neutrons | 5-100 | 00-1000 | 4-1 |
| Hot neutrons | 100-500 | 1000-5000 | 1-0.1 |

Similarly to X-rays, the wavelength of thermal neutrons, of about 4.5 Å, is in the order of the interatomic distances in materials, thus making interference effects possible. The neutrons have zero net charge and consequently they interact very weakly with electrons, i.e., there is no Coulomb interaction with the electronic charge cloud and, hence, neutrons interact directly with the nuclei of atoms. The neutrons present a spin value of $\vec{s} = 1/2$ and has a magnetic moment of $-1.913042705 \mu_N$, nuclear magneton. Therefore it can interact with unpaired electrons of magnetic atoms. Thus, neutron scattering can yield valuable information about the magnetic structure and spin dynamics of magnetic materials. [284,285]

There exist two different scattering interactions between neutrons and atoms, termed nuclear and magnetic scattering. Therefore, two different form factors are present, i.e., neutron-nuclear and neutron-magnetic scattering form factors.

From the point of view the nuclear scattering the wave function of the scattered wave, of the free neutron by the nucleus, is directly proportional to term named scattering length, l . [284] This term, l , can be defined as the nuclear-neutron form, or scattering, factor. As l is a constant is independent of the angles 2θ and its quantity has a dimension of length.

There exists no sufficiently accurate theory of nuclear forces so far to allow scattering lengths to be calculated. Fortunately scattering lengths of most nuclei have been determined experimentally and have been tabulated in the literature. [285] The neutron scattering length depends on the details of the interaction between the neutron and the components of the nucleus and therefore the sign and the magnitude of l change irregularly with the atomic number (see figure 4C(b)).

Then the main differences between X-ray scattering and neutron-nuclear scattering are the following:

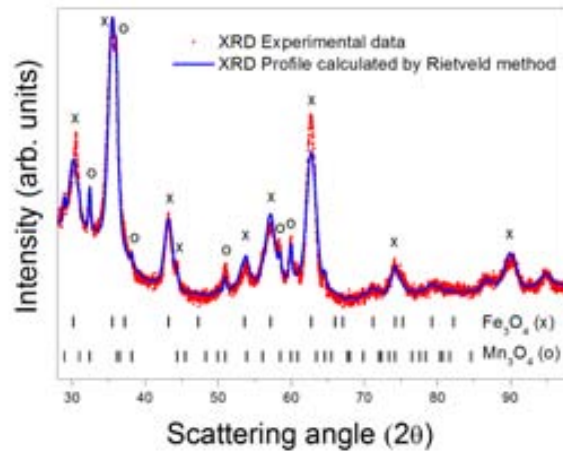


Figure 4.7: X-ray powder diffraction of a core- Fe_3O_4 |shell- Mn_3O_4 nanoparticles. The red dots are the experimental data obtained from a powder X-ray diffractometer and the blue line is the profile calculated using the Rietveld method approach.

1. Unlike the case of X-ray scattering, the neutron scattering lengths of light atoms, like hydrogen and oxygen, are quite large and therefore their positions can be easily determined in presence of heavier atoms.
2. Neutrons can distinguish between atoms of comparable atomic number.
3. Neutrons can usually distinguish isotopes of the same element due to their different scattering lengths.

These properties sometimes lead to the choice of the neutrons rather than X-rays as the favorable probe for structural investigations.

In neutron scattering of materials, magnetic scattering refers to the interaction of the nuclear moment with the magnetic moments arising from unpaired electrons in the outer orbital, of certain atoms. Due to the strength of the magnetic scattering signal is often very similar to that of the nuclear scattering in many materials, it allows the simultaneous exploration of both nuclear and magnetic structure.

Since these orbitals are typically of a comparable length scales to the wavelength of the free neutrons, the resulting atomic, and the global structure, form factors, for neutron-magnetic scattering, resembles that of the X-ray form factor. However, for neutron-magnetic scattering the coherent magnetic scattering arises only from the electrons that contribute to the net moment on the atom, and these tend to be in the outer shells, resulting in a faster decrease of the form factor with the angle 2θ .

The analysis of both the structural and magnetic contribution to the neutron diffraction patterns can be analyzed using Rietveld refinement. The nuclear-neutron diffraction contribution gives structural information. In a similar procedure described for X-ray diffraction, the analysis of the peak position and their intensity provides us with the types of phases present in the samples, their relative amounts and the crystallographic information of each one. On the other hand magnetic-neutron diffraction is only specific for FM, AFM and FiM materials and can reveal magnetic information such as the magnetic order. Shown in figure 4.8 is the neutron diffraction pattern for a sample composed of MnO nanoparticles measured at two different temperatures. At temperatures below the transition temperature of the AFM MnO, T_N , the patterns show both the magnetic and nuclear diffraction peaks. However the pattern measured above T_N , where the magnetic order is lost, only the nuclear peaks are still present. From

the magnetic-neutron pattern the atomic moment, magnetic order or magnetic domain size and their temperature dependence can be analyzed.

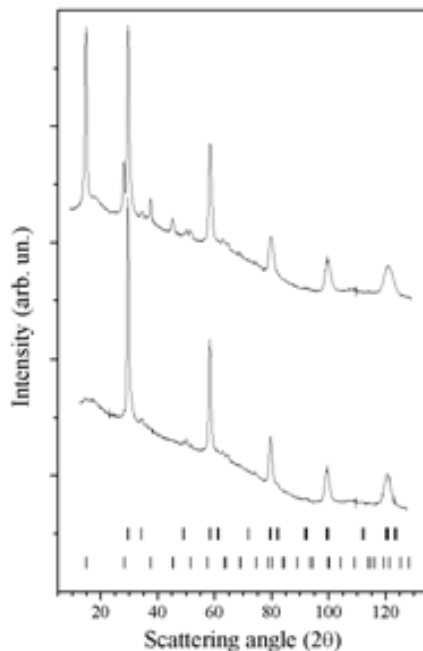


Figure 4.8: Neutron diffraction patterns measured at $T < T_N$ (upper) and $T > T_N$ (lower) for MnO nanoparticles. The stripes mark the positions of the Bragg reflections from MnO, upper and lower rows correspond to the magnetic and nuclear reflections, respectively.

Neutron diffraction measurements were carried out at the D20 diffractometer [287] of the Institute Laue-Langevin (ILL) [288]. The powdered sample where introduced in vanadium sample holder. The wavelength used was 1.305 Å and the measurements were performed in a temperature range of 10 to 300 K. All diffraction patterns were analyzed using the Fullprof program [279, 280]. The instrumental broadening was assessed by measuring a NIST powder LaB₆ standards. [283]

Neutron diffraction measurements were carried by me at the D20 diffractometer of ILL. The analysis was performed by Igor V. Golososky (St. Petersburg Nuclear Physics Institute, Russia) using the FullProf code.

4.3 Magnetometric measurements

The principle aim of magnetometry is to measure the magnetization (either intrinsic or induced by an applied field) of a material. This can be achieved in a number of ways using various magnetic phenomena. Magnetometers can be classified as AC types that measure using fields that vary relatively rapidly in time, and DC types that measure in quasi-static fields.

In this thesis, the magnetometric measurements have been carried on using a magnetic property measurement system (MPMS) (for DC measurements) and a physical property measurement system (PPMS) (for AC measurements) of Quantum Design Inc. [289]

The MPMS instrument is equipped with a superconducting quantum interference device (SQUID) detector which is able to measure extremely small magnetic fields. This instrument allows measuring the magnetization and/or the DC-susceptibility of the sample. The SQUID detector uses a superconducting coil which presents one or two Josephson junctions, [290] that allows to measure small variations of the magnetic flux inside the coil. A DC current is applied in the SQUID coil. Then, the sample, placed in the middle of the detectors, is moved perpendicularly to generate a magnetic flux which can create voltage changes in the junction, which allow obtaining the magnetization of the sample. The SQUID detectors can measure small variations of the voltage (i.e, single magnetic flux quantum, π_0 , variations into the Josephson junctions). As can be seen in equation 4.14 the theoretical limit of the magnetic flux that can be measured is in the order of 10^{-19} Oe.

$$\pi_0 = \frac{2\pi\hbar}{2e} \cong 2.06783\Delta 10^{-19} \text{Oe} \quad (4.14)$$

The PPMS with AC Susceptibility & DC Magnetization Option (ACMS) contains an AC-drive coil set that provides an alternating excitation field and a detection coil set that inductively responds to the combined sample moment and excitation field.

The SQUID and detection coils for MPMS and PPMS present a concentric superconducting DC magnet to apply the external magnetic to the specimen studied.

Specifically, MPMS-XL instrument is equipped with a reciprocating sample option (RSO) transport and temperature and magnetic field range of 1.9-400 K and ± 70 kOe respectively. The RSO servomotor permits the detection of small magnetic signals reducing signal-to-noise ratio due to the rapid and sinusoidally movement of the sample through the SQUID coils. On the other hand the PPMS instrument is equipped with a AC Susceptibility & DC Magnetization Option (ACMS) and temperature, DC-magnetic field and AC excitation range of 1.9-400 K, ± 90 kOe and 0.1-15 Oe (frequency range 10Hz to 10kHz), respectively.

The experiments have been carried out by measuring the magnetic moment of the sample (i.e, emu in cgs units) and scaled to the mass of the sample to obtain the magnetization (i.e, emu/g). The powdered sample, in a weight range of 1-5 mg, was tightly packed in a teflon film, to avoid its movement due to high magnetic fields, and subsequently mounted in gelatin capsules.

Magnetometric measurements allow us to determine the main magnetic properties for magnetic materials. Concerning the DC-measurements, two main types of studies have been performed: the temperature dependence of the magnetization, $M(T)$, and the field dependence of the magnetization, i.e., hysteresis loop measurements, $M(H)$. $M(T)$ measurements have been performed using two different approaches: (i) Zero-field cooling (ZFC), where the samples have been cooled without any field applied, at low temperature a small magnetic field is applied and, then, the temperature is increased step by step and the magnetization measured at each step; (ii) Field cooling (FC), where the sample is cooled in the presence of a magnetic field and the magnetization is measured during stepwise warming in the same applied field. Usually, both measurements are plotted together (see figure 4.9(a)) as a function of the temperature. From this representation we can extract the magnetic transition temperatures such as T_C , T_N or T_B . From the shape of the curves, indirect qualitative information of, for example, interparticle dipolar interactions or particle size distribution can be obtained. In fact, fitting the ZFC/FC can give quantitative information on the above parameters. [291]

In contrast, for hysteresis loop measurement the sample is cooled to the desirable temperature in a FC or ZFC procedure. Then the sample is magnetically saturated with the maximum positive high field (+ 70 kOe). Then, the magnetization is measured while decreasing stepwise the field until the opposite, negative, saturation (- 70 kOe) is reached. Finally, the magnetization is measured while the field is increased back to positive saturation (see figure 4.9(b)). Subsequently, the temperature is increased and the same process is repeated. As can be seen in figure 4.9(b) the shape and size of the hysteresis loop permit us to determine some magnetic characteristics of the samples (see section 2.1), such as coercivity, H_C , exchange bias field, H_E , and saturation magnetization, M_S .

As for the AC-measurements, only the temperature dependence of the in-phase and out-of-phase susceptibility, δ' (T) and δ'' (T), respectively, for a ZFC procedure have been performed. However,

these measurements have been carried out using an AC-field of constant magnitude but at different frequencies (see figure 4.9(c)). From the shape of the $\delta(T)$ and $\delta'(T)$ curves information about the magnetic transitions is obtained. Nevertheless, the study at different frequencies allow us to distinguish between thermodynamic transitions, e.g., T_C , T_N , and blocking or spin-glass transitions.

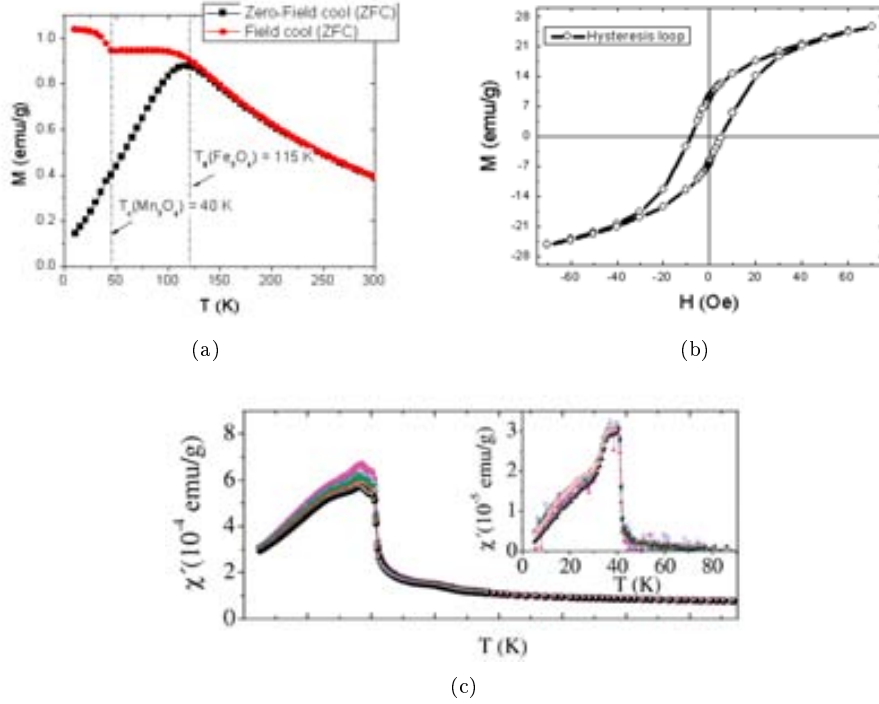


Figure 4.9: Magnetometry measurements of (a) $M(T)$ for $\text{Fe}_3\text{O}_4|\text{Mn}_3\text{O}_4$, (b) hysteresis loop for $\text{MnO}|\text{Mn}_3\text{O}_4$ core-shell nanoparticles and (c) $\delta(T)$ and $\delta'(T)$ curves.

The $M(T)$ and $M(H)$ (hysteresis loop) measurements were carried out in a MPMS instrument. The $M(T)$ measurements were done by cooling the sample from room temperature (RT) to 10K, in FC (20 Oe) or ZFC modes, and measuring during warming in a field of 20 Oe. Hysteresis loop measurements are carried out after cooling from RT to 10 K either in FC (usually in 20 kOe field) or ZFC modes. The loops were measured at different temperatures upon warming. AC-susceptibility measurements were performed in a PPMS machine by applying an AC-field of 10 Oe and a frequency range from 10 Hz to 10 kHz, from 10 K to 300 K after ZFC.

The DC-magnetic measurements and their analysis were carried out by me using the MPMS magnetometer of Centre d'Investigació en Nanociència i Nanotecnologia and the PPMS of the Institut de Ciència de Materials de Barcelona, respectively. AC-magnetic measurements were performed and analyzed by Dina Tobia, Elin Winkler and Roberto D. Zysler (Centro Atómico Bariloche, S.C. de Bariloche, Argentina).

4.3.1 First-order reversal curve, FORC

Hysteresis loops can yield a tremendous amount of information yet much of this is lost by simply estimating the set of parameters δ , M_S , M_R , H_C and H_E from a standard major hysteresis loop.

Maenoskyz in IOSC [202] developed a method using what are known as first-order reversal curves or FCRCs to represent hysteresis data. The first-order reversal curve (FCRC) method is an experimental tool to characterize hysteretic processes in samples containing mixtures of magnetic phases or grain sizes. Until the 60's major hysteresis loops, which present bulk averages, were most widely used for magnetic characterization. By contrast, the FCRC method is based on a set of minor partial hysteresis loops below and up to saturation. From this data the distribution of switching fields and local interaction fields between particles or grains can be determined, which allows modeling of more complex magnetic interactions in nanomaterials. [203]

FCRC measurements were conducted using the following procedure. After positive saturation the applied field is reduced to a given reversal field, H_R . From this reversal field the magnetization is then measured back towards positive saturation thereby tracing out a single FCRC. This process is repeated for a series of decreasing reversal fields thus filling the interior of the major hysteresis loop, which can be seen as the outer boundary of the family of FCRCs. The FCRC distribution is then defined in equation 4.42 as a mixed second order derivative of the normalized magnetization:

$$\rho(H, H_R) \equiv -\frac{1}{2} \frac{\partial M(H, H_R)/M_S}{\partial H \partial H_R} \quad (4.42)$$

Which is then plotted against (H, H_R) coordinates on a contour map. For a given reversal field, H_R , the magnetization is measured for increasing applied fields, H , and therefore $H \geq H_R$ by design. Following the measurement procedure the FCRC distribution is read in a "top-down" fashion and from left to right for a particular reversal field. The FCRC distribution provides a useful fingerprint of the reversal mechanism by mapping out, in (H, H_R) coordinates, only the irreversible switching processes. It is often useful to have a one-dimensional visualization of the irreversibility by projecting the FCRC distribution onto the H_R -axis. This is equivalent to an integration over the applied field H :

$$\int \frac{\partial^2 M(H, H_R)}{\partial H \partial H_R} dH = \frac{\partial M(H_R)}{\partial H_R} \quad (4.43)$$

and is termed a FCRC-switching field distribution (FCRC-SFD).

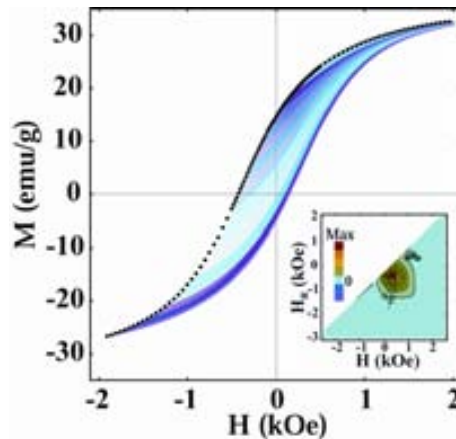


Figure 4.40: FCRC hysteresis loop and FCRC-switching field distribution (inset).

FCRC measurements were carried by me using the MPMS magnetometer of Centre d'Investigació en Nanociència i Nanotecnologia. The analysis was performed by Randy Barnes (Department of Physics, University of Gothenburg, Sweden).

4.4 Electron spin resonance, ESR

Electron spin resonance (ESR) or electron paramagnetic resonance (EPR) spectroscopy is a technique for studying chemical species that have one or more unpaired electrons. The basic physical concepts of ESR are analogous of nuclear magnetic resonance (NMR), but it is electron spins that are excited instead of spins of atomic nuclei.

The electron spin, $\bar{s} = 1/2$, can be degenerate into two different quantum levels ($m_S = \pm 1/2$) when an magnetic field, H_0 is apply to the electron (i.e, of the material to be studied). Then, the difference energy, ΔE , needed to excite an electron from the down ($m_S = - 1/2$) level to the upper ($m_S = + 1/2$) level is defined as the difference of the energy of these two quantum states (see equation 4.17).

$$\Delta E = E_{m_S=+1/2} - E_{m_S=-1/2} = g_e \mu_B H_0 \quad (4.17)$$

where g_e is the electron g-factor or gyromagnetic constant and μ_B is the Bohr magneton. With analogous interpretation, the energy gap can be defined as the related absorbed/emitted electron magnetic radiation energy for resonance condition, $\Delta E = \hbar \nu$ where $\hbar \nu$ are the Plank's constant and the electromagnetic frequency. Then,

$$\hbar \nu = g_e \mu_B H_0 \quad (4.18)$$

Experimentally, equation 4.18 permits a large combination of frequency and magnetic field values, but the great majority of ESR measurements are carried out using microwaves in the 9 to 10 GHz region, in the fields kOe range.

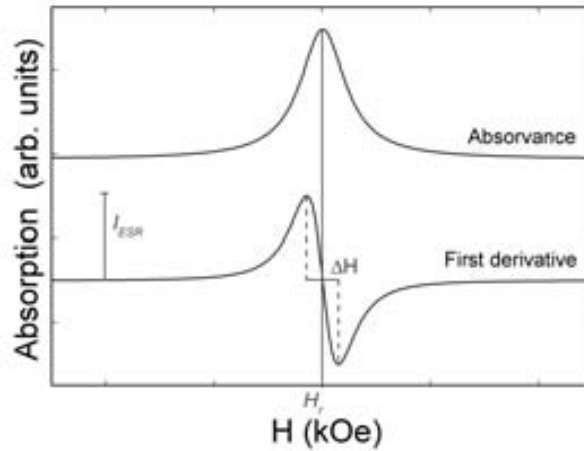


Figure 4.11: ESR spectrum for absorbance and its first derivative.

The most common way to depict ESR spectra is the first derivative of the absorbance spectra. The parameters that characterize the resonance signal are the resonance field H_r , the line width, ΔH , and the spectrum intensity, I_{ESR} (see figure 4.11).

The I_{ESR} value is proportional to the amount the specific ion in the sample resonating at a given frequency/field.

H_r is defined as the resonance field for a specific specimen absorption. In short, this value should vary only with the magnetic field applied. But for exchange-coupled systems (i.e., exchange bias or spring-magnets systems) the extra anisotropy created due to the interphase coupling generates an additional field that can increase or reduce the H_r value. Also, solving the equation 4.18 using the specific H_r

value the gyromagnetic factor can be obtained. The gyromagnetic factor for a non-isolated electron (i.e., electron confined in atom or molecule) differs from the well known value of 2.0023193043617(15). Then, the magnitude of the change with respect to the standard value of g gives information about the nature of the atomic or molecular orbital containing the unpaired electron.

The shape or profile of the resonance lines are determined by the type of interactions between the spin system and its environment, while the line width, ΔH , depends on the intensity of interaction and the relaxation time. ΔH is measured as the distance between the two main peaks present into the first derivative absorbance. The line width is related to the *width* of upper energy level ($m_S = +1/2$) and is strongly related with the energy indeterminacy of the upper level, or half live time of the electrons in this quantum state.

The ESR analysis allows us to study the magnetic materials in their paramagnetic state (see figure 4.12(a)). Some different information can be extracted from this technique. In principle, through fitting the derivative of the total spectra one can extract the gyromagnetic factor of the resonant atom. The gyromagnetic factor is strongly related to the crystallographic structure of the atom under study, thus rendering information on the phase containing the resonant atom. On the other hand, we have investigated the resonant field, H_r , line width, ΔH , and the spectrum intensity, I_{ESR} , as a function of the temperature. Their dependence with the temperature allows to study the transitions of the material (see figure 4.12(b)) and to extract the ΔH factor which is strongly related to magnetic environment of the material, thus with information on the anisotropy and the exchange energy.

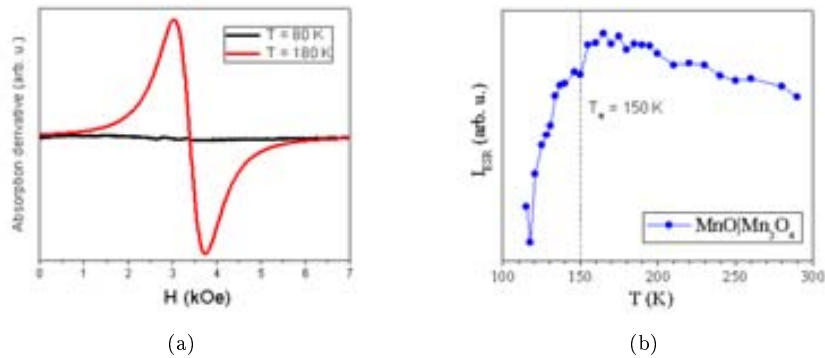


Figure 4.12: (a) EPS first derivative of a core|shell MnO|Mn₃O₄ nanoparticles at 80 K (below T_N (MnO)) and 180 K (above T_N (MnO)) and (b) I_{ESR} as a function of the temperature.

ESR spectra have been recorded at different temperatures using a Bruker ESP300 spectrometer [294] at 9.5 GHz. From which the resonance field H_r , the line width ΔH , and the spectrum intensity, I_{ESR} have been obtained.

ESR measurements were carried out and analyzed by Dina Tobia, Elin Winkler and Roberto D. Zysler (Centro Atómico Bariloche, S.C. de Bariloche, Argentina).

4.5 X-ray Absorbtion spectroscopy, XAS

X-ray absorption spectroscopy (XAS) [295] is a technique which uses the photons in the X-ray region. These photons are characterized by an energy range from $5 \cdot 10^2$ to $5 \cdot 10^6$ eV, or wavelengths from 25 to 0.25 Å. In this regime the light absorbed by matter is driven by the photo-electric effect and the photons strictly interact with the electrons located in the core level (such as the 1s and 2p orbital levels, i.e., K

and L band levels). For a particular electronic core level to participate in the absorption, the energy of this core level must be less than the energy of the incident X-ray. If the incident energy is greater than the energy of the X-ray, the core level electrons will not be perturbed from the well-defined quantum state and will not absorb the X-rays. In contrast, if the binding energy of the electron is less than of the X-ray, the electron may be removed from its quantum level. In this case, the X-ray is destroyed (i.e., absorbed) and any energy in excess of the electronic energy is given to a photo-electron that is ejected from the atom (see figure 4.13).

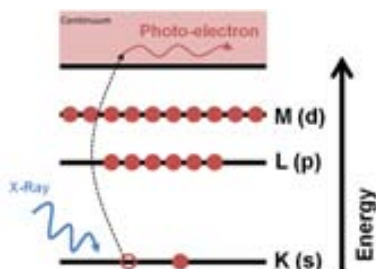


Figure 4.13: Photoelectric effect, in which an X-ray is absorbed and a core level electron is promoted out of the atom.

The XAS can be divided into two spectral regions, firstly, the so called X-ray Absorption Near Edge Structure (XANES) which reflects excitations of the photoelectron into the unoccupied states (valence holes), and secondly, the extended X-ray absorption fine structure (EXAFS), where the photoelectron is excited into the continuum. In short, EXAFS defines the spectral region beyond the edge. Then the modulations in the absorption coefficient above the edge provides local structural information of the atomic environment of the perturbed element. The information content consists of numbers of ligands (coordination number), the identity of the ligand atoms, and precise radial distances. On the other hand, XANES is essentially a spectroscopy. The position of the peaks in the spectrum gives information about oxidation state, covalency, molecular symmetry of the site, and coordination number.

In this thesis we have only used XANES, or commonly named XAS, spectra and special attention has been given to the of 2p → 3d transitions for TM elements in an oxide environment. As can be seen in figure 4.14, the XAS spectrum for Fe L-edge (2p → 3d) in Fe₃O₄ nanoparticles, is dominated by the appearance of two main peaks, separated by about 15 eV, due to the spin-orbit coupling ($j = l \pm s$) of the 2p core levels. These two peaks are related to the 2p_{3/2} and 2p_{1/2} levels, i.e., L₃ and L₂ edges (in the standard X-ray notation), respectively.

Importantly, some differences can be found between pure TM and TM oxide in the XAS spectra. The empty oxide states are more localized than metal states and their energies are determined by crystal field and multiplet effects. Multiplet effects arise from the spin and orbital momentum coupling of different 3d valence holes (or electrons) in the electronic ground state, and from coupled states formed after X-ray absorption between the 3d valence holes and the 2p core holes. On the other hand crystal field effects appear due to the different symmetry environment at which the TM elements can be located in a TM oxide material, i.e. octahedral, tetrahedral, and so on.

The XAS spectra can be measured in three different ways: i) the transmission mode, which is mostly used in hard-XAS experiments. In contrast, for soft-XAS experiments, (ii) the total electron yield mode (TEY) and (iii) fluorescence yield mode (TFY), are mostly used. Namely, the spectrum is obtained by measuring the outgoing particles, i.e, photons for TFY and electrons for TEY, that result from the decay of the core hole produced by the incident photon. [296]

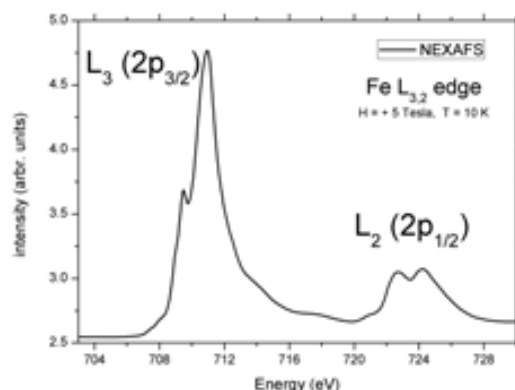


Figure 4.14: XAS spectrum of the Fe $L_{2,3}$ -edge for Fe_3O_4 nanoparticles.

XAS allows characterizing structurally the sample through the absorption edges of the elements that compose the specimen. Ideally, XAS permits distinguishing between different materials containing the same element, since for a giving element XAS can distinguish between different oxidation states, atomic symmetry, crystal field energy and so on (see figure 4.15).

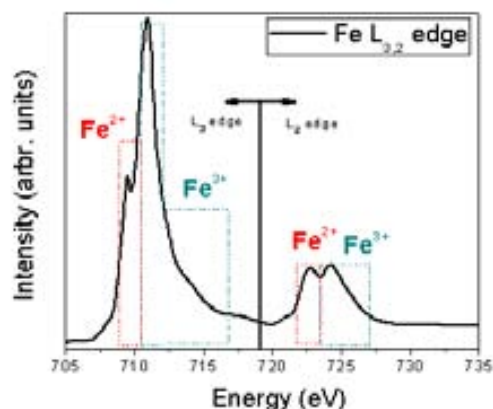


Figure 4.15: XAS spectrum for Fe_3O_4 nanoparticles in the $L_{2,3}$ edge. Note that Fe_3O_4 is structurally composed of both Fe^{2+} and Fe^{3+} ions.

XAS and XMCD measurements were performed on dried CS nanoparticles spread onto carbon tape at ID08 Dragon beamline of the European Synchrotron Radiation Facility, ESRF, (Grenoble, France), [297] 4-ID-C beamline of the Advance Photon Source, APS, of the Argonne National Laboratory (Chicago, U.S.A.) [298] and X11MA beamline of the Swiss Light source, SLS, of the Paul Scherrer Institut, PSI, (Villigen, Switzerland). [299] XAS spectra were recorded at the Fe and Mn $L_{2,3}$ edges (700-750 eV and 630-680 eV, respectively) using total electron yield (TEY) mode at 10 K in a magnetic field of 50 kOe after field cooling (FC) from 300 K under an applied field of 50 kOe.

XAS measurements and analysis were carried by me in APS, ESRF and SLS facilities. I also analyzed the XAS results.

4.5.1 X-ray Magnetic circular dichroism, XMCD

In optics, the term *dichroism* refers to changes in the absorption of polarized light on passing through a material in two different directions. Since materials typically absorb one color of white light preferentially, the material appears with two different colors for the two light directions - i.e., it is di-(two-)chroic(colored). Today, the term dichroism is used in a more general way to reflect the dependence of photon absorption of a material on polarization. The origin of the dichroism effect can be for example due to the anisotropy in the charge or the spin of the material. In the latter case we speak of magnetic dichroism.

XMCD is a variant of XAS, in which circularly a polarized light is used. XMCD is obtained by measuring two different absorption spectra, one with right circularly polarized light (RCP) and another with left circularly polarized light (LCP). Then, XMCD spectrum is defined as the RCP and LCP spectra subtraction (see figure 4.16(a)).

The concepts of XMCD spectroscopy, pioneered by G. Schütz et al. in 1987, [300] are illustrated in figure 4.16(b). As is well known for TM the 3d orbital, valence shell, can hold up to 10 electrons which are filled into band states up to the Fermi level and the number of filled states is, therefore, (10-N). For a magnetic material the d shell present a spin moment due to the imbalance in the number of spin-up and spin-down electrons, or holes. In order to measure the difference in the number of d holes with up and down spin, the x-ray absorption process needs to be spin dependent. This is done by using right or left circularly polarized photons which transfer their angular momentum to the excited photoelectron.

The photoelectron carries the transferred angular momentum as a spin or an angular momentum, or both. [301, 302] If the photoelectron originates from a spin-orbit split level, e.g. the $p_{3/2}$ level (L_3 -edge), the angular momentum of the photon can be transferred in part to the spin through the spin-orbit coupling ($j = l \pm s$). Right circular photons transfer the opposite momentum to the electron as left circular photons photons, and photoelectrons with opposite spins are created in the each of two cases. Since the $p_{3/2}$, L_3 , ($j = l + s$) and $p_{1/2}$, L_2 , ($j = l - s$) levels have opposite spin-orbit coupling, the spin polarization will be opposite at the two edges (see figure 4.16(a)). In the absorption process, spin-up and spin-down are defined relative to the photon helicity or photon spin.

Since spin flips are forbidden in electric dipole transitions, spin-up (spin-down) photoelectrons from the 2p core shell can only be excited into spin-up (spin-down) 3d hole states. Hence the spin-split valence shell acts as a *detector* for the spin of the excited photoelectron and the transition intensity is simply proportional to the number of empty 3d states of a given spin. The quantization axis of the valence shell *detector* is given by the magnetization direction. The size of the dichroism effect scales like $\cos(\theta)$, where θ is the angle between the photon spin and the magnetization direction. Hence the maximum dichroism effect (typically 20%) is observed if the photon spin direction and the magnetization directions are parallel and anti-parallel. When the photon spin and the magnetization directions are perpendicular the resonance intensities at the L_3 and L_2 edges lie between those obtained for parallel and anti-parallel alignments.

The L_3 and L_2 resonance intensities and their differences for parallel and anti-parallel orientation of photon spin and magnetization directions are quantitatively related by sum rules to the number of 3d holes and the size of the spin and orbital magnetic moments. Angle dependent measurements in external magnetic fields give the anisotropies of the spin density and orbital moment.

XMCD spectroscopy allows us to characterize structurally and magnetically the specimen to study. Specifically, XMCD is an equivalent magnetic XAS spectrum where only the atoms which present magnetic moment, i.e. unpaired electrons, participate (see figure 4.17(a)). XMCD spectra can give us information about the magnetic moment and the direction of the magnetic atoms. Moreover, the intensity of the absorption peaks can be measured as a function of different parameters such as the temperature or the magnetic applied field. Thus, for example, element specific hysteresis loop can be carried out in samples composed by two or more different magnetic atoms (see figure 4.17(b)) by tuning to the corresponding absorption edges.

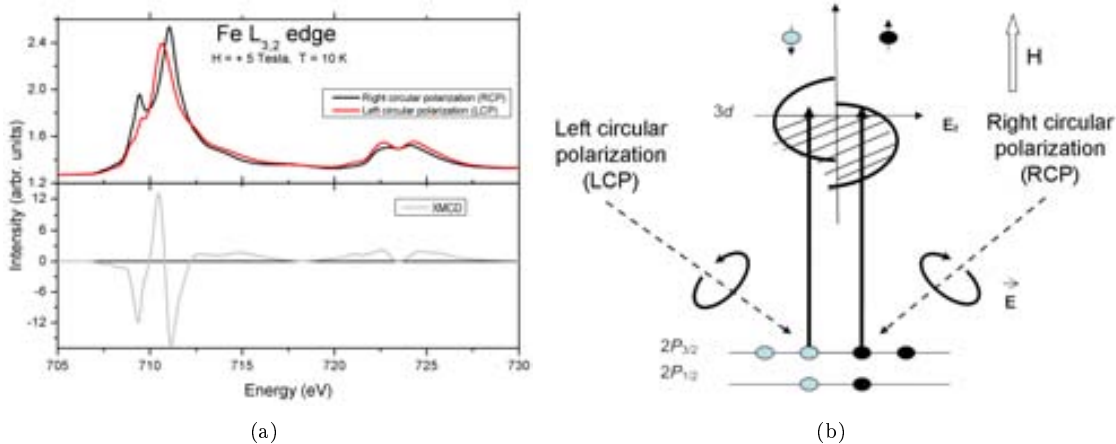


Figure 4.16: (a) RCP, LCP and XMCD spectra for Fe L_{2,3}-edge for Fe₃O₄ nanoparticles and (b) illustration of XMCD in the 2p → 3d excitation.

XMCD spectra were recorded at the Fe and Mn L_{2,3} edges using total electron yield (TEY) mode at 10 K in a magnetic field of 50 kOe after field cooling (FC) from 300 K under an applied field of 50 kOe. The element resolved XMCD hysteresis loops, for the Fe and Mn L₃ edges, were acquired by recording the field dependence of the XMCD signal at the energies corresponding to three main peaks of the Fe-edge (i.e., 707.6, 708.7, 709.3 eV) and for the main energy of the Mn edge (640.1 eV). The XMCD signal was normalized by the area of the XAS spectra after correcting for the background.

XMCD measurements were carried by me at APS, ESRF and SLS facilities. I also analyzed of the XMCD results.

4.6 Monte Carlo, MC, simulations

A Monte Carlo (MC) method is a technique that involves random numbers and probabilities to solve problems. Monte Carlo methods are often used in computer simulations of physical and mathematical systems. These methods are most suited for calculation by a computer and tend to be used when it is impossible to compute an exact result with a deterministic algorithm. This method is also used to complement theoretical results.

Monte Carlo iteratively evaluates a deterministic model using sets of random numbers as inputs. This method is often used when the model is complex, nonlinear, or involves more than just a couple uncertain parameters. A simulation can typically involve over 10000 evaluations of the model, a task which in the past was only practical using super computers. [303]

The Monte Carlo (MC) simulation technique with the implementation of the Metropolis Algorithm [304] has been proved to be a very powerful tool for the systematic study of the magnetic behavior of nanoparticles and nanoparticle assemblies. The two major advantages of this technique are i) the possibility for atomic scale treatment of the nanoparticles, so that the details of their microstructure can be studied and ii) the implementation of finite temperature through the Metropolis algorithm.

Then the magnetization of the simulated particle can be driven to depend on external (temperature, applied field), intrinsic (size, size of shell and core, size and type of anisotropy, magnetic structure) and extrinsic particle parameters (interparticle interactions). [303]

The starting point of the simulations is the appropriate choice of a model Hamiltonian and then the use of random numbers to simulate statistical fluctuations in order to generate the correct ther-

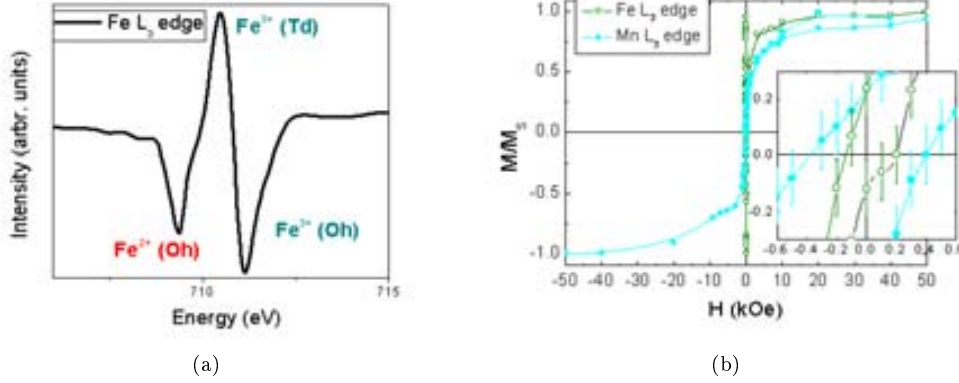


Figure 4.17: (a) XMCD spectra of Fe_3O_4 nanoparticles at the Fe L_3 -edge. Note that Fe_3O_4 is composed by Fe^{2+} in octahedral and Fe^{3+} in octahedral and tetrahedral positions and (b) element selective hysteresis loops for Fe and Mn in core- Fe_3O_4 /shell- Mn_3O_4 nanoparticles.

modynamical probability distribution according to a canonical ensemble. To simulate the magnetic nanoparticles and the nanoparticle assemblies and to derive thermodynamic averages, the spin, s , is the elementary physical quantity that is used. In the case of single nanoparticles, it is considered a classical spin at each atomic site and it is simulated using the MC technique the stochastic movement of the system in the phase space. In the case of assemblies, often effective spins to represent the magnetic state of each nanoparticle are considered.

The MC simulation consists of many elementary steps. In every elementary step a spin $s_{i,old}$ is randomly chosen from a system of N spins and an attempted new orientation $s_{i,new}$ of the spin is generated with a small random deviation. The attempted direction is chosen in a spherical segment around the present orientation $s_{i,old}$. Then the energy difference ΔE between the attempted and the present orientation is calculated. In the Metropolis Monte Carlo algorithm, if i) $\Delta E \leq 0$ the new orientation is accepted, but if ii) $\Delta E > 0$ the new orientation is accepted with a random number u , $0 < u < 1$, in order to achieve the thermal fluctuation of the spins. If u is bigger than the probability $\exp(-\Delta E/k_B T)$ the system remains to its present state, $s_{i,old}$.

Monte Carlo simulations for core- $\text{Mn}_x\text{Fe}_{3-x}\text{O}_4$ /shell- $\text{Fe}_x\text{Mn}_{3-x}\text{O}_4$ were carried out considering a single spherical nanoparticle of radius R , expressed in lattice spacings, on a simple cubic lattice, with FiM order. Then, atomic-scale modeling is used. In this model the spins in the particle interact with nearest neighbors Heisenberg exchange interaction, and at each crystal site they experience a uniaxial anisotropy. We consider the size of the atomic spins in the two sublattices of the FiM particle equal to 1 and $3/2$, respectively. The energy of the system includes the exchange interaction between the spins in the nanoparticle and the single-site anisotropy energy terms. In the presence of an external magnetic field, the total energy of the system is:

$$\begin{aligned}
 H = & -J_{core} \sum_{i,j \in core} s_i s_j - J_{IF} \sum_{i \in core, j \in shell} s_i s_j \\
 & -J_{shell} \sum_{i,j \in shell} s_i s_j - K_{core} \sum_{i,j \in core} (s_i \hat{e}_i)^2 \\
 & -K_{IF} \sum_{i,j \in IF} (s_i \hat{e}_i)^2 - K_{shell} \sum_{i,j \in shell} (s_i \hat{e}_i)^2 \\
 & -K_{surface} \sum_{i,j \in surface} (s_i \hat{e}_i)^2 - H \sum_i s_i
 \end{aligned} \tag{4.19}$$

Here s_i and \hat{e}_i are the the atomic spin and the unit vector in the direction of the easy axis at site i . The first three terms give the Heisenberg nearest neighbor exchange interaction between the spins in

the core, in the shell and at the interface, IF. The following four terms are the anisotropy energies of the core, the interface, the shell and the surface, respectively. The anisotropy is assumed uniaxial and directed along the z-axis in the core, the shell and at the interface and random at the surface. The last term is the Zeeman energy.

To take into consideration the random distribution of easy axis directions with respect to the applied fields present experimentally, we have calculated hysteresis loops for different angles between the easy axis and the applied field direction. The results for the magnetization are averaged as:

$$\langle M \rangle = \frac{1}{4} \int_0^{2\pi} d\theta \int_0^{2\pi} d\theta M(\theta) \cos\theta = \frac{1}{2} \int_0^{2\pi} d\theta M(\theta) \quad (4.20)$$

The Monte Carlo simulations are performed using the Metropolis algorithm where the microstructure and the temperature are explicitly included.

Monte Carlo simulations have been performed by Marianna Vasilakaki and Kalliopi N. Trohidou (Institute of Materials Science, NCSR Demokritos, Attiki, Greece)



Chapter 5

Synthetic aspects and parameters

5.1 Nucleation and growth theory

The process to form monodisperse nanoparticles is based on two main mechanisms: nucleation and growth. [23, 25, 305] Although nucleation and growth mechanisms are strongly correlated, they can be well described from a theoretical point of view separately, which allows to better understand the forces driving each of them. [23, 25, 305–307]

It has been established that to synthesize monodisperse nanoparticles (defined as nanoparticles with a size distribution, ρ^2 , lower than 10%) nucleation and growth steps should take place separately. Moreover, the nucleation must be instantaneous, i.e., to generate all the nuclei simultaneously. This will ensure that the growth process will be similar for all the nuclei. In fact, any variation in nanoparticle size, size distribution and shape can be achieved by varying these two steps. In general, the final size depends mainly on the nucleation process, while the size distribution and shape depend on the growth stage. Importantly, the nucleation and growth processes depend on a number of parameters such as interface energy of the nanoparticles, chemical potential of the monomers, the different atomic species in the monomers and particle, and so on. Moreover, stabilizing agents (e.g., surfactants) can also modify these parameters and/or the whole process. Finally, it should be emphasized that the mechanisms for nanometer-sized particles (as compared to micrometer-sized ones) can be more complex because of their high surface-to-volume ratios.

5.1.1 Nucleation

The nucleation process describes the spontaneous formation the smallest stable crystallites. Concerning the synthesis of monodisperse nanocrystals the nucleation process was first described in the works of LaMer in the 40's [306]. In this process, many nuclei are generated at the same time, and then these nuclei start to grow without additional nucleation. The nucleation process involves basically an initial homogeneous solution which is transformed into a heterogeneous solution due to the formation of the nuclei. In this homogeneous nucleation process, there exists a high energy barrier for nucleation, since the solution has to spontaneously change from a homogeneous to a heterogeneous system. Therefore, for the homogeneous nucleation to occur favorable kinetic and thermodynamic conditions are required. In contrast, heterogeneous nucleation is governed by pre-existing nuclei in the solution, i.e., heterogenous initial solution, where the nanocrystals tend to grow on the pre-existing nuclei, consequently avoiding the need to overcome the high energy barrier for nuclei formation. [23, 25, 305–307]

On the other hand, the homogeneous nucleation takes place when the concentration of precursors, C , of the reagents overcome their saturation concentration, C_S , inside the solution (see figure 5.1). From the thermodynamic point of view, when the concentration increases the system chemically evolves to form the new phase, i.e., the nuclei, and as a result the precursor concentration tends to decrease, thus avoiding the formation new nuclei. [306]

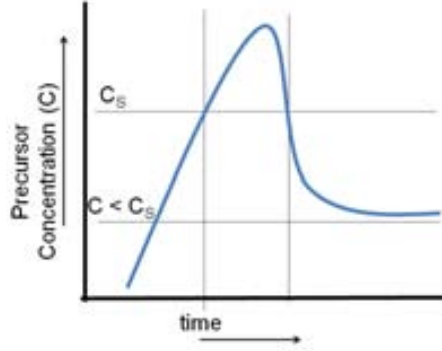


Figure 5.1: LaMer plot: Change of degree of precursor concentration as a function of time. [306]

The energy barrier which must be overcome to reach the nucleation step can be thermodynamically understood as the sum of the Gibbs free energy needed to create a nucleus, ΔG_V , (see equation 5.1) and the surface energy of the formed nucleus (see equation 5.2).

$$\Delta G_V = -\frac{RT}{V_M} \ln S \quad \text{for} \quad S = \frac{C - C_S}{C_S} \quad (5.1)$$

$$\Delta G_{surf} = 4\pi r^2 \gamma \quad (5.2)$$

where R is the gas constant, T the temperature, V_M is the molar volume of the precursor, S is the supersaturation parameter, γ is the surface free energy per unit area and r is the radius of the formed nuclei.

In equation 5.1 when the concentration overcomes the supersaturation regime, S reaches positive values leading to negative ΔG_V . Contrarily, equation 5.2 presents always positive values. Then combining both equations assuming spherical shape the total Gibbs free energy becomes:

$$\Delta G = \frac{4}{3}\pi r^3 \Delta G_V + 4\pi r^2 \gamma \quad (5.3)$$

As a consequence of the opposite signs of equations 5.1 and 5.2, a plot of ΔG versus r has a maximum. The value of r at which ΔG is maximum is called the critical radius, r_c , and can be defined as the minimum radius of a nucleus that can nucleate spontaneously in the supersaturated solution regime (see equation 5.4).

$$r_c = \frac{-2\gamma}{\Delta G} = \frac{2\gamma V_M}{RT \ln S} \quad (5.4)$$

Therefore, to ensure nucleation it is not enough that precursor concentration must be larger than the saturation concentration, but the smallest nuclei formed must be sufficiently large, at least $r \geq r_c$, to overcome the energy barrier of the nucleation process. Substituting equation 5.4 into equation 5.3 gives the critical Gibbs free energy, ΔG_{r_c} , (see equation 5.5) to form a stable nucleus.

$$\Delta G_{r_c} = \frac{16\pi\gamma^3}{3(\Delta G_V)^2} = \frac{16\pi\gamma^3 V_M^2}{3(RT \ln S)^2} \quad (5.5)$$

Equation 5.5 can be written in the Arrhenius form to obtain the nucleation rate, dN/dt , where N is the number of nuclei.

$$\frac{dN}{dt} = A \exp\left[-\frac{\Delta G_{r_c}}{k_B T}\right] = A \exp\left[\frac{16\pi\gamma^3}{3(\Delta G_V)^2} 3(k_B T)^3 N_A^2 (\ln S)^2\right] \quad (5.6)$$

Then solving S from equation 5.6, the critical supersaturation level at which nucleation begins can be obtained.

$$\ln S = \left[\frac{16\pi\gamma^3}{3(\Delta G_V)^2} 3(k_B T)^3 (\ln A N) \right] \quad N = dN/dt \quad (5.7)$$

Interestingly, this equation shows another necessary condition pertaining to the degree of supersaturation. Namely, to start the precipitation of the nuclei, the nucleation rate should be high enough as to overcome the re-dissolution rate of the particles. It should be taken into account that although nucleation takes place ($dN/dt > 0$) the re-dissolution of the formed nuclei can occur ($dN/dt < 0$). Finally S_c can be defined as the point at which the nucleation rate is sufficiently high ($dN/dt - 0$) that the number of nuclei increases even the smaller nuclei may dissolve away.

5.1.2 Growth

The growth process can be divided in two different stages. The first one is the diffusion step, which includes i) creation of monomer precursor (a molecule of low molecular weight capable of reacting with identical or different molecules of low molecular weight to form a polymer, i.e. nanoparticles) for particle growth, ii) diffusion of the monomers from the solvent to the particle surface and iii) surface adsorption of monomers by the nuclei. The second step of the growth process is mediated by physical growth of the particle. Then, as a typical kinetic problem, the growth rate can be easily treated by choosing one of the step slower than the others, i.e., a limiting step. Taking into account that the nucleation mechanism is an instantaneous process, the diffusion step of the growing mechanism can be defined as the limiting step of nanoparticle formation process. [23, 305–308]

In the Reiss model [23, 309], or *growth by diffusion* model, the growth rate of spherical particles depends solely on the flux of the monomers supplied to the particles, π_{mon} . In this case, the relationship between the monomer flux and the growth rate, dr/dt , is given by equation 5.8.

$$\pi_{mon} = \frac{4\pi r^2}{V_M} \frac{dr}{dt} \quad (5.8)$$

Fick's law for π_{mon} in equation 5.9 gives the flux of monomers diffusing through the surface of a sphere enclosing the particle. D is the diffusion coefficient, C is the monomer concentration, $x(\geq r)$ is the monomer distance inside the solution from the center of the particle and r is particle radius.

$$\pi_{mon} = 4\pi x^2 D \frac{dC}{dx} \quad (5.9)$$

Assuming π_{mon} constant for any x, π_{mon} can be C(x) integrated and, then, combined with equation 5.8 leading the growth rate in function of the bulk concentration, C, and surface concentration, C_{Surf} (see equation 5.10).

$$\frac{dr}{dt} = \frac{V_M D}{r} (C - C_{Surf}) \quad (5.10)$$

Comparing the dependence equations 5.8 and 5.10 on the nanoparticle radius, r, it can be assumed that growth rate is inversely proportional of the particle radius. However, the number of monomers diffused onto the surface of a particle increases in proportion to the square of its radius. Therefore, it can be shown, that for an ensemble of spherical particles, the radius distribution ρ^2 decrease during the growth step. This implies that the size distribution of the particles is always smaller than the distribution of the nuclei, assuming that all the particles are growing at the same time and no new nuclei appear. This is a self-regulating mechanism of the size distribution during the growth process and is often referred to as the *focusing* effect. [23, 310]

As can be seen, the Reiss model can properly describe the growing mechanism driven by the diffusion process. However, some aspects such as the particle re-dispersion, and its dependence on the particle size, are not considered. Assuming that mass-transport process (monomers diffusion into the solution) is

equal to the kinetic process (re-dispersion), i.e., that the growth rate is zero, and the rates of precipitation (growing) and dissolution are balanced, the nanoparticle radius, r , can be expressed as: [23, 243, 307]

$$r - r_c = \frac{64\gamma DV_M C}{9RT} t \quad (5.11)$$

where t is the digestion time, i.e., the time at which the reaction is maintained at the selected decomposition temperature T (i.e., the temperature at which the reaction is carried out).

From equation 5.11 it is clear that the size of nanoparticles in the growth step is directly proportional to initial precursor concentration, C , the surface free energy of the particle, γ and the reaction time, t , and is inversely proportional to the decomposition temperature T .

5.1.3 Separating the Nucleation and Growth processes

As has been described above, the main feature to synthesize monodisperse nanoparticles (i.e., size distribution, ρ^2 , less than 10%) is to separate the nucleation and growth processes and to control the growth via diffusion of monomers as the limiting step.

Heterogeneous nucleation is, probably, the most apparent case for the separation of nucleation and growth. In this case the separation is achieved by the physical separation of both process, i.e., avoiding the nucleation step by using pre-synthesized nanoparticles as seed-nuclei and controlling the precursor concentration far below of the supersaturation regime. The seed-growth mediated synthetic route, carried out by heterogeneous nucleation, allows the possibility to create a broad range of different nanocrystalline structures. For example, in the case of nanoparticles the seed-growth method has been extensively used in the synthesis of large particles of a single material, [206, 207] CS heterogeneous nanoparticles [192, 208, 264] and heterodimers. [192, 193]

Nevertheless, in wet-chemistry there exist two main different approaches to separate the nucleation and growth processes starting from a homogeneous nucleation and finally establishing the diffusion process as the limiting step: *hot-injection* and *warming-up* methods. Hot-injection is based on injecting the precursor into the hot solvent to force the nucleation by reaching the supersaturation regime just after the addition of the precursor. [40, 41] The warming-up approach consists in mixing the precursors with the solvent at room temperature and subsequently warming the mixture to the decomposition temperature of the precursor and thus reaching the nucleation and, at the same time, decreasing faster the supersaturation regime. [48, 206, 207]

5.2 Synthesis of manganese and iron oxide nanoparticles

In this thesis, different types of nanoparticle systems are presented. However, the synthesis of the diverse structures is based on iron oxide and manganese oxide materials, which have been synthesized via thermal decomposition of the related metalorganic salts.

The first system presented is based on the one-step synthesis of CS nanoparticles of two different manganese oxides. Core-MnO|shell-Mn₃O₄ (γ -Mn₂O₃) nanoparticles have been synthesized with different core sizes and same shell thickness. The shell formation have been driven by the passivation of the initial MnO core, Mn²⁺, to a total γ -Mn₂O₃ (Mn³⁺) shell oxidation or partial Mn₃O₄ (Mn²⁺ + Mn³⁺) shell oxidation.

The second system is the seed-growth synthesis of CS and onion-like nanoparticles (i.e., CS nanoparticles formed by more than one different shell). In this case, first single and CS iron oxide nanoparticles have been synthesized to be used as seeds for the posterior growth of manganese oxide in a similar procedure described in the MnO|Mn₃O₄ synthesis. The core-FeO|shell-Fe₃O₄ and single Fe₃O₄ nanoparticles seeds have been prepared by synthesizing pure FeO nanoparticles and controlling the surface passivation of the initial FeO (Fe²⁺) to create FeO|Fe₃O₄ (Fe²⁺ + Fe³⁺) or allowing the complete oxidation of the FeO particles to form, Fe₃O₄. Subsequently the manganese oxide is surface deposited via seed-growth method. The possibility to control the passivation degree of the manganese oxide surface can lead the formation of CS structures with different materials and onion-like nanoparticles. Following this procedure

diverse types of heterogeneous nanoparticle systems have been obtained: two-components $\text{Fe}_3\text{O}_4|\text{Mn}_3\text{O}_4$ (CS); three-components $\text{FeO}|\text{Fe}_3\text{O}_4|\text{Mn}_3\text{O}_4$ (onion-like); and four-components $\text{FeO}|\text{Fe}_3\text{O}_4|\text{MnO}|\text{Mn}_3\text{O}_4$ (onion-like).

In this chapter the different synthetic parameters chosen to adjust the size, size distribution and shape control will be discussed. Importantly, different experimental techniques allow us to determine these parameters. However, although diffraction techniques give information on the particle size, only TEM images can provide a direct observable image of the particle size and shape. Hence, in this chapter only TEM images have been taken into account to discuss the above mentioned parameters.

I carried out most of the different syntheses described in the thesis under the supervision of Dr. G. Salazar-Alvarez and Dr. M. Estrader.

5.2.1 Products used in the synthesis

The starting chemicals used in the synthesis were purchased from different companies: manganese(II) acetylacetonate ($\text{Mn}(\text{acac})_2$, Aldrich), sodium oleate (NaOl, Riedel-de Haën), iron(III) chloride ($\text{FeCl}_3 < 97\%$, Sigma-Aldrich), 1,2-hexadecanediol (HDD, Aldrich), oleic acid (OlOH, Fluka), oleylamine (OA 70%, Aldrich) dibenzyl ether (DBE, Aldrich), 1-octadecene (ODE 90%, Aldrich), hexane (Fluka) and ethanol (EtOH 99.5%, Panreac). The products were used without any further purification.

All the synthesis have been carried out in either a 100 mL or a 250 mL three necks round-bottomed flasks (Afora) equipped with a coiled condenser (Afora) and magnetically stirred with a magnetic bar. The reaction was heated using a heating mantle (Sigma-aldrich) controlled with an external temperature regulator (Winkler) connected to the reaction via a NiCr-Ni thermocouple (Winkler). Also a Shlenk line (Afora) has been used to allow the control of the atmosphere inside the reaction vessel. The inert atmosphere has been reached by pumping the reaction at 100 °C using a rotary pump during 30 to 60 min ($p \sim 10^{-3}$ Torr) and, then, refilling the system with Argon gas as the inert gas.

As a final step the particles were washed from the reaction media by several cycles of coagulation with ethanol, centrifugation at 2000 xg (5000 rpm), disposal of supernatant solution and re-dispersion in hexane.

5.2.2 Synthesis of the core- MnO |shell- Mn_3O_4 ($\gamma\text{-Mn}_2\text{O}_3$) system

The manganese oxide system has been synthesized following the procedure published by Salazar-Alvarez et al. [243]. This method allows the possibility to tune the particle size by controlling the synthetic parameters (e.g., surfactant(OA)-to metal precursor($\text{Mn}(\text{acac})_2$) molar ratio, decomposition temperature and reaction time) and, in addition, it allows the control of the passivation layer thickness, Mn_3O_4 ($\gamma\text{-Mn}_2\text{O}_3$), by adjusting the temperature at which the reaction is opened to air (i.e., removing the condenser coil and maintaining the magnetic stirring).

In a typical synthesis 7.5 mmol of $\text{Mn}(\text{acac})_2$ (1.9 g) and 7.5 mmol of HDD (1.9 g) are mixed in a 250 mL round bottomed flask and 150 mmol of OA (50 mL) and 150 mL of DBE are later added. The reaction vessel is degassed and refilled with Argon. The mixture is warmed to reach the temperature of 240 °C and then the temperature is maintained during 30 min. Lastly, the reaction is removed from the heating mantle and cooled down in argon until 80 °C. At this point, the coil condenser is removed and the reaction is cooled down in air atmosphere to obtain the passivation layer.

Following the above procedure the nanoparticles synthesized present an average diameter of 5 nm and due to their small size the whole particle passivates to form the oxidized Mn_3O_4 phase.

Remarkably, 1,2-hexadecanediol (HDD) is a reducing agent which is usually used in thermal decomposition methods to obtain FeO (Fe^{2+}) and Fe_3O_4 ($\text{Fe}^{2+} + \text{Fe}^{3+}$) nanoparticles starting from iron (III) acetylacetonate precursor. [23, 206] The function of the HDD is the total or partial reduction of the initial Fe^{3+} to Fe^{2+} . In contrast, in our case the use of this reducing agent has been carried out to assure the non oxidation of the initial Mn^{2+} ions to Mn^{3+} and, hence, guaranteeing the formation of pure MnO nanoparticles.

As have been proved by the synthetic experiments presented in Article #2 and in the work of Salazar-alvarez et al. [243] different synthetic parameters can control the particle growth. The surfactant to

metal precursor molar ratio, (in our case OA and $\text{Mn}(\text{acac})_2$, respectively) plays an important role controlling the particle size. On the other hand digestion time, decomposition temperature and the concentration of metal precursor have also played a significant contribution.

As discussed in section 5.1.2, if the growth is driven by the diffusion process as the limiting step, the nanoparticle size can be described by equation 5.11. As can be seen, the decomposition temperature, the digestion time and the precursor concentration, all play a role in the size control. Another key parameter is the surface free energy, γ , which can be controlled via using surfactants. Namely, a surfactant which acts as stabilizer for polar nanoparticles (e.g., oxides) in an apolar solvent (e.g., DBE) can also control the surface free energy of the nanoparticles. Accordingly, increasing the surfactant concentration the surface free energy tends to decrease leading smaller particle sizes. [19,20] Furthermore, interestingly, different types of surfactants used in the synthesis can control the final shape of the particles. [311]

During the preparation of the particles for Article #2 different synthetic parameters were varied to understand their importance in the control of the particle size to be able to obtain the most suitable sizes to study the size effect on the magnetic and structural properties.

During the different syntheses, diverse parameters were studied separately and maintaining the other variables constant: surfactant-to-metal precursor ratio ($[\text{S}]:[\text{M}]$), digestion time (t), decomposition temperature (T) and precursor concentration ($[\text{Mn}(\text{acac})_2]$). Note that in all the cases the molar ratio between the precursor, $[\text{Mn}(\text{acac})_2]$, and the reducing agent, HDD, have been maintained constant at 1.

The results of the variation of the diverse synthetic parameters are summarized in the following table.

| Sample | $[\text{S}]:[\text{M}]$ | T ($^{\circ}\text{C}$) | t (min) | $[\text{Mn}(\text{acac})_2]$ | diameter (nm) |
|--------|-------------------------|--------------------------|---------|------------------------------|---------------|
| S1 | 20 | 150 | 10 | 0.05 | 4.8 |
| S2 | 20 | 200 | 30 | 0.05 | 14 |
| S3 | 20 | 290 | 60 | 0.05 | 23.4 |
| S4 | 1 | 240 | 30 | 0.05 | 25 |
| S5 | 4 | 220 | 30 | 0.05 | 13 |
| S6 | 40 | 205 | 60 | 0.05 | 15 |
| S7 | 2 | 290 | 60 | 0.03 | 24.4 |
| S8 | 2 | 290 | 60 | 0.05 | 50.4 |

For samples from S1-S3 the $[\text{S}]:[\text{M}]$ ratio have been maintained constant while the temperature and digestion time have been increased from S1 to S3. The particle size increase from 4.8 nm to 14 and 23.4 nm from S1 to S3, respectively (see figure 5.2(a), 5.2(b) and 5.2(c)). Consequently, when the decomposition temperature and the digestion time of the reaction increase the particles become larger. The digestion time dependence is easily understood from the theoretical equation 5.11, where the particle size is directly proportional to this factor. On the other hand according to equation 5.11 the particle size should be inversely proportional to the temperature. However, the opposite behavior observed in our experiments can be understood as a yielding effect. Due to the fact that at higher temperatures the metal precursor decomposition is favored, the concentration of monomers increases, allowing larger monomer diffusion onto the initial nuclei surface allowing the particles to grow.

On the other hand the $[\text{S}]:[\text{M}]$ ratio were studied in samples S2, S4, S5 and S6. It is clear for samples S4 and S5 that when the concentration of the surfactant is increased from 1 to 4, there is a particle size reduction, from 25 nm to 13 (see figure 5.2(d) and 5.2(d)). In contrast, it is demonstrated that for ratios larger than 4 (i.e, 20 and 40 for S2 and S6, respectively) there is no further particle size reduction (see figure 5.2(b) and 5.2(f)). Therefore, the particle size control via surfactant concentration presents a limiting threshold at roughly $[\text{S}]:[\text{M}]$ of 4. In fact, from equation 5.11 can be understood that the increase of the surfactant concentration leads us to a reduction of the final surface free energy of the nanoparticles and posterior reduction of the final particle size. In contrast, for large values of surfactant

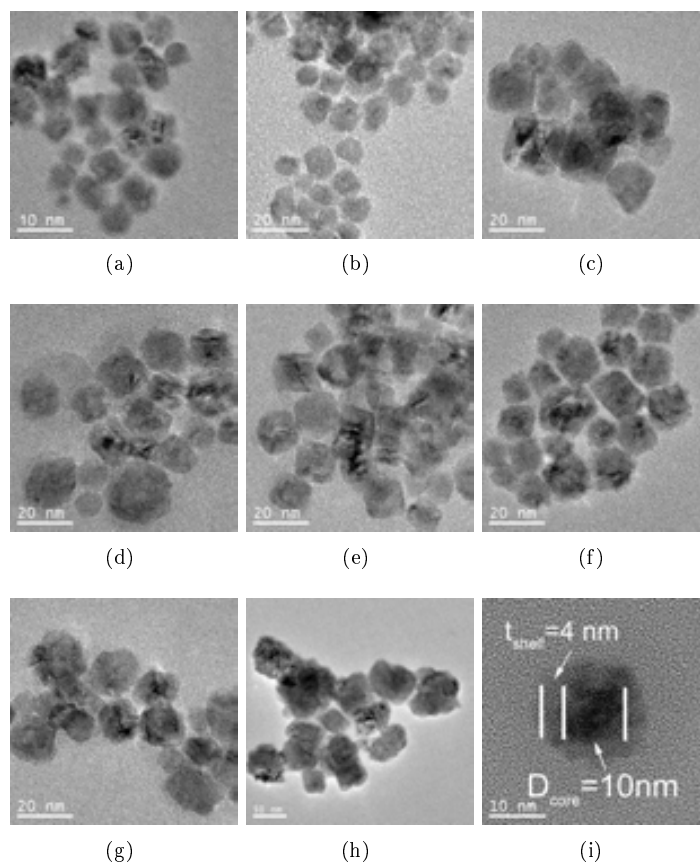


Figure 5.2: TEM images for samples (a) S1, (b) S2, (c) S3, (d) S4, (e) S5, (f) S6, (g) S7, (h) S8 and (i) distinguishable CS structure for sample S1.

concentration this process is blocked since the surface of the nanoparticles is fully covered by surfactant molecules, and an increase in concentration can not longer reduce the surface free energy.

Finally, the precursor concentration dependence was studied for samples S7 and S8, which have been synthesized in equal values of $[S]:[M]$, digestion time and decomposition temperature but with different initial precursor concentration, 0.03 M and 0.05 M for S7 and S8, respectively. The results show that for larger values of precursor concentration larger particle sizes are obtained, where the particle size increases, from 24.4 nm to 50.4 nm, as the concentration is increased from 0.03 M to 0.05 M (see figure 5.2(g) and 5.2(h)). These results highlight the important role of the precursor concentration in the final particle size. The results are in agreement with, equation 5.11 which shows that increasing the precursor concentration allows us obtaining larger particle sizes.

After synthesizing MnO nanoparticles of different sizes, the aim of the experiments was obtaining a controllable passivation layer. Two different approaches were attempted to reach this CS structure. Firstly, the as-made nanoparticles were exposed to the air at different temperatures as the reaction was cooled down. Secondly, the obtained particles were precipitated and subsequently re-dispersed in highly boiling point solvents and heated to different temperatures. After several experiments, the first procedure was chosen due to the better control and reproducibility to obtain the passivation layer. Importantly, as-made MnO nanoparticles presented a thin passivation layer (Mn_3O_4 or γ - Mn_2O_3 oxides), even when the exposition to the air was carried on at room temperature. This effect can be understood in terms of the nanoparticle surface tending to stabilize the surface stress (defects, unbalance coordination and so on) by forming the passivation layer. To form a thicker and homogeneous passivation layer,

the particles (of different sizes) were exposed to air at different temperatures (50, 80 and 120 °C). For lowest temperature, 50 °C, the passivation layer obtained did not differ substantially with the obtained for room temperature exposure. In contrast, for the experiment at 120 °C it was found that the passivation layer increased to passivate completely small (5nm) and medium (15 nm) nanoparticles. Then for the experiment performed at 80 °C the small nanoparticles were fully passivated, however, the medium and larger ones presented a rather homogeneous passivation layer of roughly 3 to 5 nm (see figure 5.2(i)). Consequently, 80 °C was established temperature to expose the MnO nanoparticles to reach a reproducible passivation layer of 3-5 nm. Following this procedure we could obtain nanoparticles with diameters in the range of 5 to 50 nm, composed of different core sizes and equal shell thickness.

5.2.3 Synthesis of core-FeO|shell-Fe₃O₄ and Fe₃O₄ systems

Iron oxides nanoparticles (i.e., core-FeO|shell-Fe₃O₄ and Fe₃O₄) have been synthesized by thermal decomposition using a procedure similar described in the previous section for MnO. The work by Park et al. [48] demonstrates the possibility to synthesize highly monodisperse Fe₃O₄ nanoparticles starting from a new metalorganic precursor, iron oleate (FeOl), and following the synthetic procedure used in the case of the acetylacetonate precursors. However, the main drawbacks of this procedure are the need to prepare the metalorganic precursor, since it does not exist commercially, and the reproducibility of the FeOl product. [312] Nevertheless, despite the drawbacks, we decided to use FeOl to synthesize the iron oxide nanoparticles. The synthetic procedure to obtain FeOl was to mix 21.6 mmol of FeCl₃ (3.5 g) and 65.7 mmol of NaOl (20 g) with 75 mL of hexane, 45 mL of EtOH and 30 mL of deionized H₂O in a 250 mL round-bottomed flask. The mixture was magnetically stirred and heated to the boiling point (T ~ 60 °C) during 4 hours. After cooling, the reaction consisted of two phases, which were separated using a separatory funnel, discarding the bottom part (i.e., the water phase). The organic part was washed with water several times, discarding each time the water part. To finish the preparation of the FeOl, the organic phase was vacuumed and heated at 100 °C until all the organic solvents and traces of water had evaporated. The precursor, which presents a dark-brown viscous liquid texture, was stored in a flask for the posterior synthesis of the nanoparticles.

Note that the formation of the FeOl precursor is an ionic exchange reaction, where the initial NaOl changes its Na⁺ ion for the Fe³⁺ ions of the FeCl₃. The selected solvents with high different degree of polarity were chosen to solve the two different powder reactives, i.e. NaOl and FeCl₃. NaOl which presents an apolar behavior was solved with hexane and the FeCl₃, which is an ionic salt, was solved in the mixture of H₂O-EtOH solvents. Although, hexane and H₂O-EtOH solvents are immiscible, the stirring and the boiling process favors the mixture and the ion exchange to reach the FeOl formation in the polar part, hexane. On the other hand, the discarded water solution contains the other products of the reaction, i.e., the Na⁺ and Cl⁻ ions.

After obtaining the iron precursor, FeOl, it was thermally decomposed to synthesize the iron oxide nanoparticles. Namely, 1.8 mmol (1.6 g) of FeOl were mixed with 0.31 mmol (100 μL) of OlOH and 30 mL of ODE in a round-bottomed flask. The reaction was degassed in vacuum at 110 °C during 30 min and refilled with argon gas using the Shlenk line. Then the mixture was heated to the boiling point of the solvent, ODE, i.e., 320 °C, with a controlled heating rate of 3 °/min and maintained for a digestion time of 30 min. The reaction was subsequently cooled down by removing the flask from the heating mantle.

Importantly, if the cooling down procedure is carried out in inert atmosphere, argon, until room temperature, the resulting nanoparticles obtained present a CS structure (i.e., FeO|Fe₃O₄). However, if the reaction flask is opened at air at high enough temperatures, roughly 200 °C, the complete oxidation of the particles is achieved and the nanoparticles present de single phase structure, i.e., Fe₃O₄. Remarkably, even the synthesis is carried out in an air atmosphere, i.e., without degassing the reaction and without opening the reaction flask to air, the resulting nanoparticles have always a CS structure, rather than the expected single phase system. This behavior can be explained by the high boiling point used in the decomposition of the precursor. Note that the oleate complex presents a higher decomposition temperature than the more commonly used metal-organic precursors (i.e, acetylacetonates, acetates, cuprates,

and so on). At higher temperatures, when nanoparticles are being synthesized, the iron-monomer is formed and the long carbon chains of the precursor (oleate $\text{CH}_3(\text{CH}_2)_7\text{CH}=\text{CH}(\text{CH}_2)_7\text{COO}^-$) are broken, leading the formation satellite products as CO and H_2 . Due to their reducing character these products are responsible for the reduction of Fe^{3+} ions into Fe^{2+} and consequently the formation of FeO nanoparticles as a final product. [313]

Interestingly, using FeOl as precursor, only small amounts of surfactant need to be added to the synthesis, in this case OI(OH), since to some extent the precursor itself can act as surfactant. Although, the need to use small amounts of surfactant is an advantage, the presence of the long carbon chains, which probably are not completely broken and decomposed after the nanoparticle synthesis, becomes the main drawback of this procedure. The final product presents a black viscous liquid appearance, similar to the precursor, which is virtually impossible to turn into powder. Thermogravimetric analysis of the final product has shown that the major part of this viscous liquid (roughly 60%) are organic materials and only 40% comes from the inorganic part, i.e., the nanoparticles. Nevertheless, in return, the colloidal suspension is exceptionally stable, making these nanoparticles great candidates to use as seeds for the seed-growth deposition method.

A systematic study, as in the case of the MnO synthesis, has been carried out to investigate the role of the different synthetic parameters on the particle size. Note that in this case a new parameter, heating rate (HR, which is defined as the heating velocity to reach the desirable decomposition temperature) has also been studied. In the following table the main experiments are summarized.

| Sample | [S]:[M] | T (°C) | t (min) | HR (°/min) | [FeOl] | diameter (nm) |
|--------|---------|--------|---------|------------|--------|---------------|
| F1 | 2 | 320 | 10 | 3 | 0.15 | 11 |
| F2 | 2 | 320 | 30 | 3 | 0.15 | 13.6 |
| F3 | 2 | 320 | 60 | 12 | 0.26 | 11 |
| F4 | 2 | 320 | 30 | 25 | 0.15 | 9 |
| F5 | 2 | 275 | 30 | 3 | 0.15 | 9 |
| F6 | 0.8 | 320 | 30 | 3 | 0.15 | 6 |
| F7 | 0.8 | 320 | 30 | 3 | 0.08 | 6.5 |
| F8 | 2 | 320 | 30 | 3 | 0.14 | 11 |

Digestion time dependence can be summarized in samples F1 and F2, where they were synthesized in identical conditions, only differing in the digestion time. Although the particle size of F1 and F2 is slightly different, i.e., 11 vs. 13.5 nm, respectively (see figure 5.3(a) and 5.3(b)), further studies have revealed that this parameter does not play any important role in the final particle size control. However, particles synthesized in digestion times lower than 10 min present large particle dispersion, ρ^2 . Thus, it can be assumed that the growth process happens faster than for others metal precursors (at least, not longer than the first 10 minutes). As has been described in the synthesis of MnO nanoparticles, from equation 5.11, longer digestion times lead larger particle sizes due to the longer exposure time of the monomers to diffuse from the solution to the nuclei. However, this longer digestion times present a main drawback. The increase of the final particle size distribution should be assumed to be due to i) increase of particle size and, therefore, the particle size distribution and ii) a possible redissolution process which favors the growth of some nanoparticles at the expenses of the redissolution of others, i.e., this process is known as Ostwald ripening. [314]

In F6 and F7 FeOl concentration was varied maintaining the other parameters equal. Although, the FeOl concentration has been doubled for going from F7 to F6 there was no apparent size difference. Samples F6 and F7 present a sizes of 6 and 6.5 nm respectively (see figure 5.3(f) and 5.3(g)). This result is in contrast to the model presented in equation 5.11 in which an increase of the particle size for larger

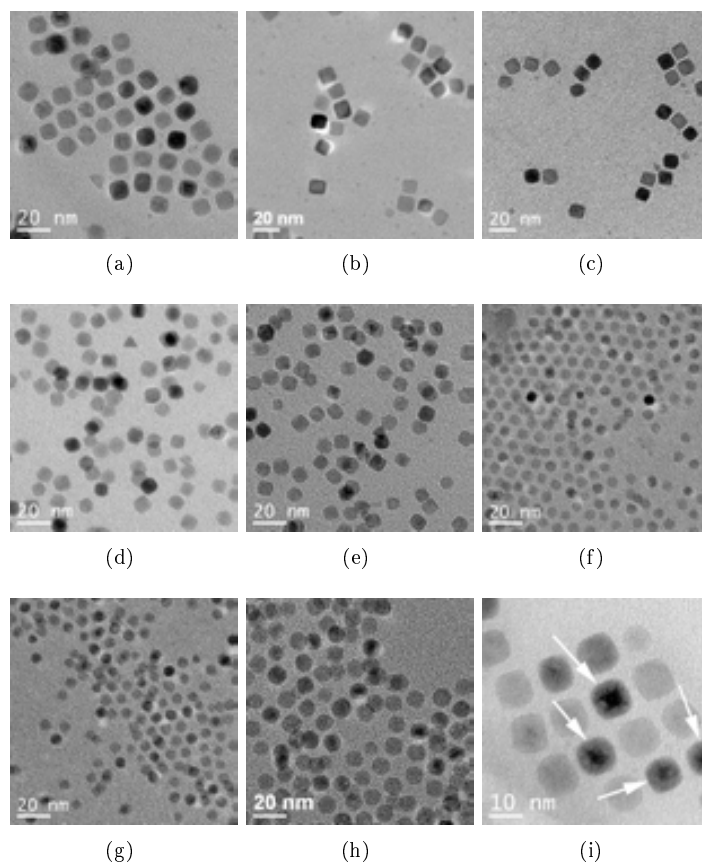


Figure 5.3: TEM images for samples (a) F1, (b) F2, (c) F3, (d) F4, (e) F5, (f) F6, (g) F7, (h) F8 and (i) , marked with arrows, distinguishable CS structure for sample F1.

precursor concentrations. Thus, it can be concluded that the concentration does not play an important role in our work range, i.e. $[\text{FeOl}] \geq 0.8$, and, probably, for lower concentrations values it can affect as is predicted by the theory.

In the work by Park et al. [48] much importance was given to maintain the HR at constant values of $3^\circ/\text{min}$. Thus, we also decided to study this parameter to better understand the synthesis process. Different HR values, 3, 12 and $25^\circ/\text{min}$, were used for samples F2, F3 and F4, respectively. Decreasing particle sizes have been obtained by increasing the HR values, 13.6, 11 and 9 nm respectively (see figure 5.3(b), 5.3(c) and 5.3(d)). However, the particle size distribution also increases concurrently with the particle size. In contrast with other synthetic parameters, heating rate is not predicted as a variable that should affect the reaction process. From a fundamental point of view, an increase in the HR works against the stable control of the growth process driven by the diffusion step and leads to an increase of the final particle size distribution through raising the redissolution process.

The surfactant-to-metal ratio, $[\text{S}]:[\text{M}]$, was also investigated. Although, here only two experiments are shown, F6 and F8, the results clearly demonstrate the importance of the $[\text{S}]:[\text{M}]$ in controlling the particle size. As the $[\text{S}]:[\text{M}]$ ratio is raised from 0.8 (F6) to 2 (F8) the particle size increases from 6 nm to 11 nm (see figure 5.3(f) and 5.3(h)). As has been described for the synthesis of MnO nanoparticles, an increase of the surfactant concentration brings about a reduction of the surface free energy of the nanoparticles which results in a particle size reduction, as can be seen in equation 5.11.

Finally, the role of the decomposition temperature was studied by using similar solvents with different boiling point: 1-octadecene, ODE, 1-hexadecene, HDE, and 1-tetradecene, TDE, with boiling points of 320, 275 and 250°C , respectively. All the samples were synthesized using ODE except for

F5 where HDE was used. When comparing samples F2 and F5 (where only the solvent, and thus the decomposition temperature, has been changed) a size reduction for the lower decomposition temperature can be observed. From equation 5.11 it can be seen that the particle size present an inversely proportional dependence with the decomposition temperature, therefore, for lower temperatures larger particles sizes should be obtained. However, in our case the lower decomposition temperature leads to an enhancement of particle size distribution and the particle shape is no longer homogeneous. Hence, it can be assumed that the proper decomposition is not reached at the boiling point of HDE, 275 °C. In fact, thermogravimetric measurements have shown that the FeOl decomposition starts, roughly, at 270 °C. Thus, at lower temperatures, probably, the growth process and the diffusion limiting step are not favored.

In view of the results of the different experiments, we can conclude that the main parameter to control the size of the iron oxide nanoparticles is the surfactant-to-metal ratio. However, other groups have recently shown that increasing the decomposition temperature even further, using mixed solvents such as: 1-Octadecene or diphenyl ether with tetracosane (391 °C) the decomposition temperature can be increased, > 320 °C, resulting in larger nanoparticles. [315]

Finally, as can be seen in the different panels of figure 5.3(a), 5.3(b), 5.3(c), 5.3(d), 5.3(e), 5.3(f), 5.3(g) and 5.3(h) the different conditions do not only affect the size but also the shape of the nanoparticles. Samples from F1 to F3 present a clear cubic shape. On the other hand, samples F6 to F8 show perfect spherical shapes. In contrast, F4 and F5 have grown with an intermediate shape, i.e., a high degree of sphericity but with facets. However, from our experiments no clear conclusion can be reached concerning the effect of the different synthetic parameters on the nanoparticle shape. Even so, the difference in nanoparticle shape could be driven by slight differences between of FeOl precursors used. In fact, using FeOl as precursor allows us to prepare not more than four or five synthesis for each FeOl batch. Then, we can classify the nanoparticles synthesized as a function of the batch of the FeOl used, where three nominally equal FeOl precursors have been used: FeOl₁ for F1, F2 and F3, FeOl₂ for F4 and F5 and FeOl₃ for F6, F7 and F8. Notably, it has been reported that the shape control of the nanoparticles could be due to different amounts of NaOl or KOl products in the FeOl precursor. [315]

The control of the final nanoparticle structure, i.e single Fe₃O₄ and core|shell core-FeO|shell-Fe₃O₄, have been achieved controlling the temperature at which the reaction flask is opened to air and, therefore, the inert atmosphere is lost. The entry of oxygen inside the reaction vessel tends to passivate the initial FeO nanoparticles to the next oxidation state, Fe₃O₄. Although the reaction is spontaneous due to the instability under air conditions of the FeO phase, the temperature can play an important role in the degree of the shell passivation, i.e., from thin shells to the complete particle oxidation. Different temperatures have been studied to try to understand this process. High temperatures, > 250 °C, lead the complete particle passivation to form the pure Fe₃O₄ single nanoparticles. In contrast, temperatures in the range of 80 °C to 250 °C allow obtaining shell thickness from 2 to 4 nm (see figure 5.3(i)). Interestingly, in contrast to the MnO nanoparticles, the FeO phase is not stable and the nanoparticles tend to suffer the complete oxidation with time to form the Fe₃O₄ phase. Our experiments have shown that this process reach the complete oxidation for times around two or three weeks, depending on the different parameters like particle size or initial passivation layer thickness. .

5.2.4 Seed-growth synthesis of core-iron oxides|shell-manganese oxides systems

This section describes the synthesis of core|shell and onion-like nanoparticles synthesized via the seed-growth approach. Three different systems: Fe₃O₄|Mn₃O₄ (CS), FeO|Fe₃O₄|Mn₃O₄ (three-components onion-like), FeO|Fe₃O₄|MnO|Mn₃O₄ (four-components onion-like) will be discussed. In fact, all of them are based on the same or very similar synthetic procedure, where the formation of different morphologies is driven, only, by choosing reaction atmosphere and the shell thickness. Thus, depending on the desired structure of the nanoparticles the process encompasses either two or four steps. In the first step the iron oxide nanoparticles are synthesized and their oxidation process is controlled to obtain one of the two possible iron oxide systems, FeO|Fe₃O₄ or Fe₃O₄. The second part is governed by the manganese

oxide deposition. Again, by adjusting oxidation process, two different morphologies can be obtained: bilayer shells $\text{MnO}|\text{Mn}_3\text{O}_4$ ($\gamma\text{-Mn}_2\text{O}_3$) or fully oxidized shells Mn_3O_4 ($\gamma\text{-Mn}_2\text{O}_3$).

Commonly, seed-growth methods have been used to create nanoparticles with sizes unattainable by on-step synthesis. Pre-synthesized nanoparticles are used as seeds and the same material is deposited onto their surface. [206,207] However, as has been described in the nucleation section, the heterogeneous nucleation is thermodynamically favored instead the homogeneous one, provided that the supersaturation regime is not reached. Thus, the seed-growth approach has been extended to other, more complex, core/shell systems by using small amounts of precursor to growth shells of a different material. [191,192]

In our case, to synthesize the heterogeneous CS nanoparticles, pre-made Fe_3O_4 nanoparticles, were used. Notably, care must be taken to evaluate the adequate amount of seeds to avoid reaching the supersaturation regime. Hence, ten drops of the solution (hexane+nanoparticles) were placed on a precision balance, waiting for the complete evaporation of the hexane. The weight obtained is related to the total non-hexane part, although taking into account the previous thermogravimetric analysis (which show that only the 40 % in weight is inorganic) only about half of the weight corresponds to the nanoparticles. Taking into account these factors, our starting nanoparticles/hexane solution can be assessed to be about 0.1 g/L.

To proceed with the CS synthesis, in a round bottomed flask 2 mL (200 mg of nanoparticles) of the iron oxide/hexane suspension have been mixed with 7.5 mmol of $\text{Mn}(\text{acac})_2$ (1.9 g), 7.5 mmol of HDD (1.9 g), 150 mmol of OA (50 mL) and 15 mmol of OIOH (5 mL) in 150 mL of DBE. The mixture, magnetically stirred, was degassed in vacuum at 100 °C during 15-30 min and re-gassed with argon. The reaction was heated at the maximum heating rate (~ 10 °/min) to reach the decomposition temperature of 200°C, where the digestion time was adjusted to 60 min. Afterwards, the reaction vessel was cooled down to room temperature removing it from the heating mantle. Importantly, depending on the desired shell structure (i.e., the passivation degree) the reaction vessel was opened to air at the appropriate temperature.

One of the drawbacks of this synthesis procedure is the control of the thickness of the Mn-oxide shell. Several experiments have been devised trying to control the shell thickness. However, different tests, varying the synthetic parameters, demonstrate that essentially only two different manganese shell thickness can be stabilized, i.e., 1 nm and 22 nm. The manganese shell thickness of 1nm (see figure 5.4(a)) spontaneously passivated to form Mn_3O_4 or $\gamma\text{-Mn}_2\text{O}_3$ oxides. This behavior allows to synthesize two different CS structures depending on the seeds used: $\text{Fe}_3\text{O}_4|\text{Mn}_3\text{O}_4$, $\text{FeO}|\text{Fe}_3\text{O}_4|\text{Mn}_3\text{O}_4$, where the latter structure is formed by two different shells, i.e., onion-like nanoparticles. On the other hand the formation of thicker manganese shell thickness (see figure 5.4(b)) has allowed to synthesize three and four components CS/onion-like structures, $\text{Fe}_3\text{O}_4|\text{MnO}|\text{Mn}_3\text{O}_4$ and $\text{FeO}|\text{Fe}_3\text{O}_4|\text{MnO}|\text{Mn}_3\text{O}_4$, respectively. In this case the degree of manganese passivation can be controlled due to the thicker shell. For all the experiments the seed concentration has been maintained in a range from 0.5 to 1 g/L and in a seed/precursor ratio of 0.1 in weight. For smaller ratios, i.e., larger amount of precursor, the supersaturation limit is reached and homogeneous nucleation takes place and pure MnO nanoparticles are obtained. In contrast, for smaller seed/precursor ratios no deposition is observable.

Remarkably, for the formation of manganese oxide shell two different surfactant have been used to improve the growth, contrarily to the procedure used in the synthesis of single Mn-oxide nanoparticles. Initially, only OA was used, however, the size distribution obtained was exceedingly broad. In contrast when OIOH is used, mixed with OA, the particle size distribution decreased and the particle shape became more homogeneous. Experiments performed using only OIOH did not lead to any manganese deposition. This behavior can be understood as the OA playing the main role in the formation of manganese monomers, although, after deposition, OIOH can better control the size distribution and the particle shape. Thus, diverse OA/OIOH and $[\text{S}(\text{OA}+\text{OIOH})]/[\text{M}]$ ratios have been studied in order to control the manganese shell thickness. However, despite the broad range of ratios used (e.g., [S/M] ratios 1, 2, 20 or 40) no noticeable changes in the shell thickness was observed.

Finally, the decomposition temperature was studied. For lower decomposition temperatures, i.e. ~ 200 °C, thinner shells in the range of 0.5 to 1 nm were obtained. Interestingly, for thinner shell depositions, the initial perfectly spherical iron oxide shapes evolves into faceted shapes. This behavior

can be understood due to the fast manganese oxidation from MnO to Mn₃O₄ and the tendency of Mn₃O₄ to crystallize forming octahedrons. This change in shape of the nanoparticles allows easily distinguishing the manganese oxide deposition.

On the other hand, when the decomposition temperature is increased, i.e. ~ 250 °C, the manganese deposition is particularly favored, resulting in the deposition of thicker manganese shells, on the order of 20 nm. However, intermediate decomposition temperatures do not allow controlling the manganese shell thickness. Experiments carried out at different intermediate temperatures, i.e. 210 and 230 °C, result in 1 nm and 20 nm shell thickness, respectively. Surprisingly, these nanoparticles present a slightly concave geometry, similar to a tetracube. The formation of this type of concave geometry can be understood due to the presence of water during the reaction, which induces some etching of defective areas on specific crystallographic faces. Water then helps solubilize some metal (oxy)- hydroxide, which recrystallizes on the edges and along the corners, forming the concave geometry.

Other experiments were pursued to obtain intermediate shell thicknesses, such as the hot-injection method of the manganese precursor. When the injection was controlled using an injection pump, adjusting the injection velocity, concentration and decomposition temperature no changes in the shell thickness could be achieved in the final nanoparticles for slow or moderate injection speeds. In contrast, when the addition of the precursor was carried out at ultra-fast injection velocities the shell could be grown to an average thickness of 3 to 5 nm. However, although an intermediate shell thickness is reached, the shell growth is rather inhomogeneous. Namely, the manganese oxide deposited, which is completely formed by Mn₃O₄, creates a homogeneous thin shell of 0.5 nm (similar to the standard thin shell) and then the manganese oxide grows preferentially at specific surface regions leading to a non homogeneous shell thickness (see Fig. 5.4(c)).

As a final step of this synthetic procedure, the exposition temperature to air of the CS Fe₃O₄|Mn₃O₄ system, has been studied. If the reaction vessel is allowed to cool down to room temperature in an argon atmosphere the final system obtained exhibits a sharp interface with the designed Fe₃O₄|Mn₃O₄ system. In contrast, if the reaction vessel is opened at air at 180 °C interdiffusion between Mn and Fe ions is favored and the interface evolves from a sharp interface to a graded interface. Moreover, the final CS nanoparticles lose their nominal Fe₃O₄|Mn₃O₄ structure. Specifically, the particles present an iron rich core and a manganese rich shell with the interface showing graded increasing/decreasing, manganese and iron ions concentration (from the core to the shell), respectively. Consequently, the structure CS system can be described as Mn_xFe_(3-x)O₄|Fe_xMn_(3-x)O₄ although maintaining the cubic/tetragonal structure. In fact, from EELS data the composition was calculated as Mn_{0.75}Fe_{2.25}O₄(8 nm)|Fe_{1.75}Mn_{1.25}O₄ (0.6 nm) shell 1|Fe_{1.5}Mn_{1.5}O₄ (0.6 nm) shell 2|Fe_{0.75}Mn_{2.25}O₄ (0.6 nm) shell 3.

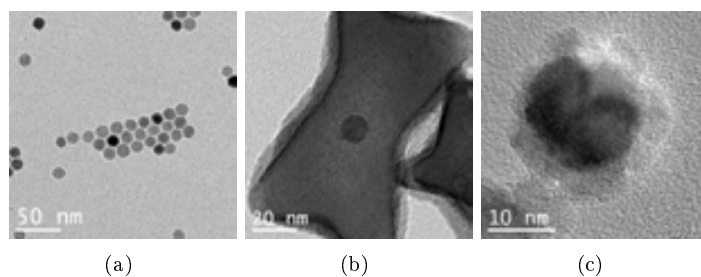


Figure 5.4: TEM images for samples (a) thicker, (b) thinner and (c) intermediate manganese oxide shell thickness.



Chapter 6

Articles

6.1 AFM|FiM MnO-core|Mn₃O₄ (γ -Mn₂O₃)-shell nanoparticles

In this section two articles dealing with CS nanoparticles formed by a core of MnO and a shell of Mn₃O₄ or γ -Mn₂O₃ are presented. From the magnetic point of view, this system is composed by an AFM core (MnO) and FiM shell (Mn₃O₄ or γ -Mn₂O₃). Interestingly, these CS nanoparticles present a double inverted CS structure where the AFM is placed in the core and the FiM in the shell and the Curie temperature (T_C) of the shell is lower than the Néel temperature (T_N) of the core, which is in contrast with conventional FM|AFM core|shell systems with $T_C > T_N$. Based on the previous experience of the group, [243] the synthesis of these CS nanoparticles is based on the synthesis of monodispersed AFM MnO nanoparticles and their posterior passivation to form a FiM Mn₃O₄ or γ -Mn₂O₃ shell and, thus, an AFM|FiM core|shell structure. This procedure allows a fine control of the sizes (core diameter and shell thickness) of the system with an epitaxial growth of Mn₃O₄ or γ -Mn₂O₃ shell onto the MnO core. [244,245] Interestingly, the phase of the shell passivation, Mn₃O₄ or γ -Mn₂O₃, depends on the size of the initial MnO nanoparticles.

From the magnetic point of view, these systems present large values of coercivity (H_C) and exchange bias (H_E) due to the strong magnetic anisotropy of the Mn₃O₄ or γ -Mn₂O₃ shell and the good exchange coupling between both the AFM and FiM counterparts. In addition, the coercivity and exchange bias values present a non monotonic dependence with the core diameter when the shell thickness is maintained constant. Further, the magnetic investigations revealed that the magnetization of the FiM shell is maintained above its T_C , which is ascribed to a proximity effect of AFM at the AFM|FiM interphase.

Article #1

Title: Magnetic Proximity Effect Features in Antiferromagnetic/Ferri-magnetic Core-Shell Nanoparticles

Authors: I.V. Golosovsky, G. Salazar-Alvarez, A. López-Ortega, M. A. González, J. Sort, M. Estrader, S. Suriñach, M. D. Baró, and J. Nogués

Journal: Physical Review Letters

Article #2

Title: Size-Dependent Passivation Shell and Magnetic Properties in Anti-ferromagnetic/Ferrimagnetic Core/Shell MnO Nanoparticles

Authors: A. López-Ortega, D. Tobia, E. Winkler, I. V. Golosovsky, G. Salazar-Alvarez, S. Estrade, M. Estrader, J. Sort, M. A. González, S. Surin.ach, J. Arbiol, F. Peiró , R. D. Zysler, M. D. Baró, and J. Nogués

Journal: Journal of the American Chemical Society

6.1.1 Article #1: Magnetic proximity effect features in antiferromagnetic/ferrimagnetic core-shell nanoparticles

In order to understand the magnetic behavior in MnO-core/ γ -Mn₂O₃-shell nanoparticles in this article we present a systematic neutron diffraction study. Neutron diffraction patterns at different temperatures were performed at the D20 instrument [287] of the ILL institute [288] in Grenoble. The analysis was carried out by means of Rietveld refinement [282] using the Fullprof code. [279,280] Two CS nanoparticles were studied in this article, i.e. small, S , and large, L . Both samples were formed by the manganese oxide CS structure although with different core sizes (~ 5 - S and ~ 17 nm - L), while maintaining the shell thickness roughly constant (~ 5 nm). The structural results obtained from the nuclear neutron diffraction analysis have shown that the core is formed by a MnO phase with the well-known NaCl (rock salt) structure with some defects at the Mn sites for the small (S) nanoparticle and, in contrast, a high crystallinity for the larger, L , sample. On the other hand the shell for the small sample, S , is composed by a tetragonal manganese oxide spinel formed only by Mn³⁺ ion, i.e. γ -Mn₂O₃. The core size and shell thickness calculated through the neutron diffraction peak broadening agree well with the previous results obtained from the TEM analysis.

The analysis of the pure magnetic neutron diffraction peaks have confirmed that the MnO core phase and the γ -Mn₂O₃ shell present the expected AFM and FiM magnetic structure, respectively. However, the values of saturated magnetic moments of both manganese oxides are lower than the theoretical ones. These effects can be explained due to the lower occupancy of the Mn²⁺ ions of the MnO AFM core and the spin canting and weak coupling of the manganese Mn³⁺ ions of the γ -Mn₂O₃ FiM shell.

In fact, the most novel result presented in this article is observation, for the first time, of a magnetic proximity effect in CS nanoparticles. This effect, which has been extensively proven in magnetic thin films and superconductors, is the driving force which maintains the stability of magnetization of the FiM layer well above its T_C . This effect has been studied by analyzing independently magnetic diffraction peaks of the AFM core and the FiM shell as a function of the temperature. The experimental result confirms the presence of magnetic diffraction peaks for the FiM shell far above its T_C and, in fact, even above the T_N of the AFM core. The origin of this second effect, i.e., the stability of the FiM magnetization above the T_N of the AFM core is not clear at present although it could originate from the oxygen vacancies of the γ -Mn₂O₃ phase.



Magnetic Proximity Effect Features in Antiferromagnetic/Ferrimagnetic Core-Shell Nanoparticles

I. V. Golosovsky,¹ G. Salazar-Alvarez,^{2,3} A. López-Ortega,^{2,4} M. A. González,⁵ J. Sort,⁶ M. Estrader,² S. Suriñach,⁴ M. D. Baró,⁴ and J. Nogués⁷

¹*St. Petersburg Nuclear Physics Institute, 188300, Gatchina, St. Petersburg, Russia*

²*Centre d'Investigació en Nanociència i Nanotecnologia (ICN-CSIC), Campus Universitat Autònoma de Barcelona, E-08193 Bellaterra, Spain*

³*Materials Chemistry Group, Department of Physical, Inorganic, and Structural Chemistry, Arrhenius Laboratory, Stockholm University, S-106 91 Stockholm, Sweden*

⁴*Departament de Física, Universitat Autònoma de Barcelona, E-08193 Bellaterra, Spain*

⁵*Institut Laue Langevin, 6 rue Jules Horowitz, BP 156, F-38042 Grenoble, France*

⁶*Institució Catalana de Recerca i Estudis Avançats (ICREA) and Departament de Física, Universitat Autònoma de Barcelona, E-08193 Bellaterra, Spain*

⁷*Institució Catalana de Recerca i Estudis Avançats (ICREA) and Centre d'Investigació en Nanociència i Nanotecnologia (ICN-CSIC), Campus Universitat Autònoma de Barcelona, E-08193 Bellaterra, Spain*

(Received 8 December 2008; published 16 June 2009)

A study of “inverted” core-shell, MnO/ γ -Mn₂O₃, nanoparticles is presented. Crystal and magnetic structures and characteristic sizes have been determined by neutron diffraction for the antiferromagnetic core (MnO) and the ferrimagnetic shell (γ -Mn₂O₃). Remarkably, while the MnO core is found to have a T_N not far from its bulk value, the magnetic order of the γ -Mn₂O₃ shell is stable far above T_C , exhibiting two characteristic temperatures, at $T \sim 40$ K [$T_C(\gamma\text{-Mn}_2\text{O}_3)$] and at $T \sim 120$ K [$\sim T_N(\text{MnO})$]. Magnetization measurements are consistent with these results. The stabilization of the shell moment up to T_N of the core can be tentatively attributed to core-shell exchange interactions, hinting at a possible magnetic proximity effect.

DOI: 10.1103/PhysRevLett.102.247201

PACS numbers: 75.50.Tt, 61.05.F–, 75.30.Kz, 75.75.+a

Magnetic nanoparticles are currently being extensively studied [1]. Among them, bimagnetic core-shell systems, where both the core and the shell are magnetic, are gaining increased interest due to appealing novel properties and promising applications, such as enhanced superparamagnetic blocking temperatures or tunable coercivities [2–10]. Most of the conventional bimagnetic core-shell nanoparticles have been obtained from the oxidation of transition metal nanoparticles, leading to a ferromagnetic (FM) core and the corresponding antiferromagnetic (AFM) or ferrimagnetic (FIM) shell [2,3]. In this case, the exchange coupling between the core and the shell gives rise to diverse effects such as loop shifts (“exchange bias”) and coercivity enhancement [2,3].

Recently so-called “inverted” core-shell systems with an AFM core and a FIM shell, e.g., MnO/Mn₃O₄, have come into focus [11–14]. In this particular system the Curie temperature (T_C) is below the Néel temperature (T_N), in contrast to most of the exchange biased thin film and core-shell systems [2]. This doubly inverted (i.e., AFM core, not FM, and $T_N > T_C$) structure gives rise to a number of interesting effects, such as a nonmonotonic dependence of the loop shift on the core diameter and the existence of loop shifts above T_C [11–13]. Importantly, the latter effect is different from the known enhancement of the blocking temperature in usual core-shell systems, which arises from the increase of the effective anisotropy of the FM core induced by the coupling to the AFM shell [15].

In thin film systems consisting of two different magnetic materials the enhancement of T_N or T_C of one of the layers due to exchange interactions (i.e., a magnetic proximity effect) has been reported [16–22]. However, this effect has never been reported in nanoparticles.

In this Letter we present the study of inverted core-shell nanoparticles consisting of a ~ 5 nm (sample *S*) or ~ 17 nm (sample *L*) antiferromagnetic MnO core and a ~ 5 nm-thick ferrimagnetic γ -Mn₂O₃ shell [23]. It is found that the ordered magnetic moment of the γ -Mn₂O₃ shell remains finite *far above* T_C of the γ -Mn₂O₃ shell and T_N of the MnO core.

Neutron diffraction measurements were carried out at the diffractometer D20 of the Institut Laue-Langevin with a neutron wavelength of 1.305 Å [24]. All diffraction patterns were analyzed using the FULLPROF program [25] based on the known crystal structures of the core and the shell. This method, in contrast to the so-called “matching mode,” provides more stable refinement in the present case due to the strong overlapping of the principal peaks and the presence of small parasitic reflections. Magnetization measurements were carried out using a SQUID magnetometer.

The MnO core exhibits the expected NaCl structure. However, refinement of the occupancy factors shows that sample *S* has defects in the Mn sites, with an occupancy factor of only 0.74(2). Sample *L* exhibits the stoichiometric structure. Since the detected defects are only observed in the samples with smaller cores (i.e., with a large surface to

volume ratio) it can be inferred that they should be at the MnO surface. Interestingly, the detection of defects is consistent with the model of Mn_3O_4 growing on MnO proposed by Berkowitz *et al.* [12]. These defects could lead to so-called uncompensated spins [26], which, in turn, could explain the large loop shifts observed in this type of nanoparticles [11–13].

The shell of the smaller particles has a spinel-type tetragonal structure with two types of voids: tetrahedral (eightfold *A* position) and octahedral (16-fold *B* position). From the profile analysis it follows that the shell has the structure formulas $(\text{Mn}_{2/3}^{3+}\square_{1/3})[\text{Mn}^{3+}]_2\text{O}_4$, which, in fact, corresponds to the defect structure, known as $\gamma\text{-Mn}_2\text{O}_3$ [27,28], not the expected hausmannite $(\text{Mn}^{2+})[\text{Mn}^{3+}]_2\text{O}_4$ (or Mn_3O_4). Here, the parentheses and square brackets refer to the tetrahedral and octahedral voids, respectively, and the symbol \square corresponds to vacancies. Note that for the larger particles the structure of the shell cannot be univocally established due to the relatively small diffraction signal.

The temperature dependence of the lattice parameter of the MnO cores is consistent with a well structured core [23,29–33]. Similarly, the lattice parameters of $\gamma\text{-Mn}_2\text{O}_3$ are also close to bulk values [23,27,28].

The diffraction lines are broadened with respect to the instrumental resolution, indicating that the correlation length is finite. However, from the neutron diffraction patterns the expected stresses appeared to be negligible within the experimental error. Thus, from the peak broadening the characteristic sizes of the nanoparticles were evaluated. The volume average diameter of the core and the characteristic size of the ferrimagnetic shell are 4.9(3)/4.7(3) and 17.0(5)/5(1) nm, at 170 K, for samples *S* and *L*, respectively. Note that the values in the brackets correspond to the error defined as the estimated standard deviation.

Using the known AFM order in bulk MnO and taking into account the trigonal distortion due to magnetostriction [34], the ordered magnetic moments in the MnO core were refined. The values of the saturated magnetic moment of MnO are smaller than the expected $5\mu_B$ for the free Mn^{2+} ion [Fig. 1(a)], which can be explained partly due to the lower occupancy of the Mn^{2+} sites, that increases the effective valence state and consequently decreases the averaged magnetic moment, and partly by surface spin disordering [30]. The temperature dependence of the magnetic moment shows a continuous transition, in contrast with the first order transition in bulk, due to size effects [30]. Interestingly, $T_N \sim 130(9)$ K (for sample *S*) and 120.9(2) (for sample *L*) are enhanced with respect to the bulk value of 117 K [29], similar to what was observed in MnO nanoparticles with different shapes and sizes confined within diverse porous media [30,32].

$\gamma\text{-Mn}_2\text{O}_3$ nanoparticles are known to be ferrimagnetic with a T_C of about 40 K with large coercivities at low

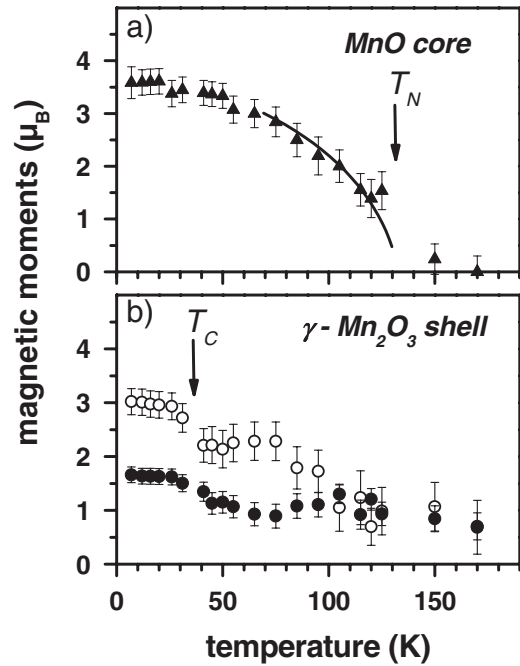


FIG. 1. Temperature dependence of the magnetic moment of (a) Mn^{2+} in MnO (the solid lines correspond to a power law fit) and (b) at the tetrahedral sites (\circ) and at the octahedral sites (\bullet) of the $\gamma\text{-Mn}_2\text{O}_3$ for sample *S*. Arrows mark the magnetic transition temperatures.

temperatures [35]. However, the magnetic structure of $\gamma\text{-Mn}_2\text{O}_3$ is unknown. For the related hausmannite Mn_3O_4 structure, a complex magnetic order with a doubled nuclear cell has been reported [36]. However, we did not observe any superstructure magnetic reflections at low temperatures, implying that the magnetic cell coincides with the chemical one. Therefore we worked in the frame of the two-sublattice collinear ferrimagnetic model of Néel [37], similar to $\gamma\text{-Fe}_2\text{O}_3$. Any small distortions of such structure were beyond our statistic accuracy. The temperature dependence of the magnetic moment in the tetrahedral (*A*) and the octahedral [*B*] sites for sample *S* (Fig. 1) exhibits two remarkable features. First, there is a large difference between the magnetic moments in *A* and *B* sites, and second, the moments are noticeably reduced with respect to the $4\mu_B$ expected for the free Mn^{3+} ion. Although the orbital moment of the Mn^{3+} ion and the crystalline field (which is different for the *A* and *B* voids) could affect the value of the magnetic moment, similar effects have been observed in $\gamma\text{-Fe}_2\text{O}_3$, where Fe^{3+} does not possess orbital moment. In Néel-type order the effective exchange magnetic field in position *B* from the surrounding magnetic moments is about twice weaker than those in position *A*. The spins which are more weakly coupled should be more disordered due to the breaking of local symmetry, and, consequently, their mean value should be smaller [38]. Hence, we attribute the observed

difference of magnetic moments in the γ - Mn_2O_3 shell to this mechanism. Moreover, spin canting in the γ - Mn_2O_3 structure (similar to what is observed in γ - Fe_2O_3 shells [39]) could also contribute to the reduced moment, although due to high anisotropy of γ - Mn_2O_3 the canting is expected to be smaller than in γ - Fe_2O_3 and probably confined in the interface layers. Taking into account the number of tetrahedral and octahedral sites the net moment at $T = 10$ K per formula unit is about $\mu \sim 1.0(2)\mu_B$. Note that due to peak overlapping meaningful magnetic information for the shell can only be obtained for sample *S*.

The temperature dependence of the magnetic moment of both sublattices of the γ - Mn_2O_3 shell shows a kink around the known T_C of this material (40 K) [arrow in Fig. 1(b)] and exhibits a finite moment even above T_C (see also [23]). Since the error bars obtained from the refined profile are somewhat large, in Fig. 2 the intensity of the isolated magnetic peak for sample *S*, which is proportional to the square of magnetic moment, with the dominant contribution of the γ - Mn_2O_3 moments and a smaller contribution of the magnetic moments of the MnO core are shown. The last contribution, calculated from the profile analysis, is displayed in Fig. 2 separately. Indeed, the magnetic reflections from the shell have a sizable intensity even above 40 K in concordance with the magnetic moments obtained from the profile analysis. Note that the presence of magnetic signal above T_C is consistent with recent magnetic results of Berkowitz *et al.* [13] and the presence of two maxima (around T_C and T_N) in the Mn_3O_4 electron spin resonance linewidth observed in MnO- Mn_3O_4 systems

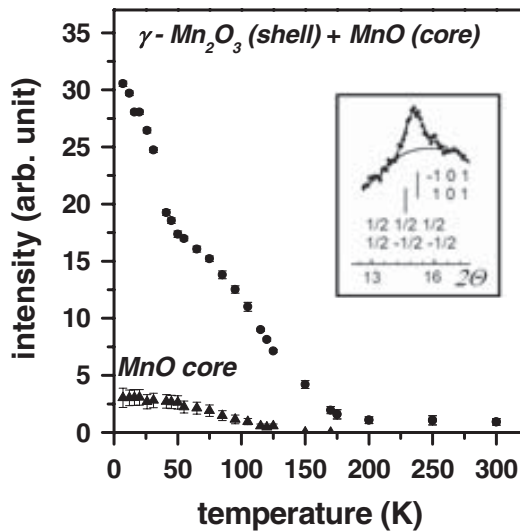


FIG. 2. Temperature dependence of the intensity of the magnetic peak at 15.4° (\bullet) for sample *S*. There are contributions from the MnO core: reflections $(1/2, 1/2, 1/2)$, $(1/2, -1/2, -1/2)$, and from the γ - Mn_2O_3 shell: reflections $(1, 0, 1)$ and $(-1, 0, 1)$. The contribution from the MnO calculated from the profile analysis is shown by \blacktriangle . Shown in the inset is the observed magnetic peak at $T = 250$ K.

[14,40]. Remarkably, a second kink in the temperature dependence of the magnetic moment is observed around T_N of MnO (~ 130 K) as highlighted by an arrow in Fig. 1(a). Surprisingly, the induced moment does not vanish at $T_N(\text{MnO})$ and persists far above. Certainly, a weak peak at the position of the γ - Mn_2O_3 $(1, 0, 1)$ reflection is clearly seen up to 300 K (inset in Fig. 2). A comprehensive x-ray inspection at these angles does not show any coherent reflections. The peak broadening corresponds to the size of the nanoparticles composing the shell. Hence, we attribute this peak to the coherent magnetic scattering from the shell. The profile analysis renders a magnetic moment of about $1.3(3)\mu_B$. Within the experimental accuracy, neither intensity nor line shape appear to vary with temperature. Nevertheless, a structural contribution to the peak at ca. 15° , due to a possible ordering of vacancies, cannot be completely ruled out, although x-ray diffraction does not show any clear coherent reflections.

To search for further evidence of the presence of potential proximity effects magnetization measurements were also carried out. However, due to the small core size of sample *S* and the long characteristic measuring time of SQUID ($\tau_m \sim 100$ s) no proximity effects are observable using magnetometry (see Fig. 3 and [23]). Interestingly, for sample *L*, both the temperature dependence of $M_{\text{FC}}(T) - M_{\text{ZFC}}(T)$ (field cooled–zero field cooled) magnetization curves at 5 T (Fig. 3) and the saturation magnetization $M_S(T)$ [23] exhibit a considerable signal well above T_C and up to about T_N (in agreement with Berkowitz *et al.* [12]), which is consistent with a proximity effect. It should be taken into account that magnetization measurements are not equally as distinctive as neutron diffraction measurements (where the signal comes solely from the γ - Mn_2O_3 shell), since in this case uncompensated spins in the MnO could also contribute to the magnetic signal.

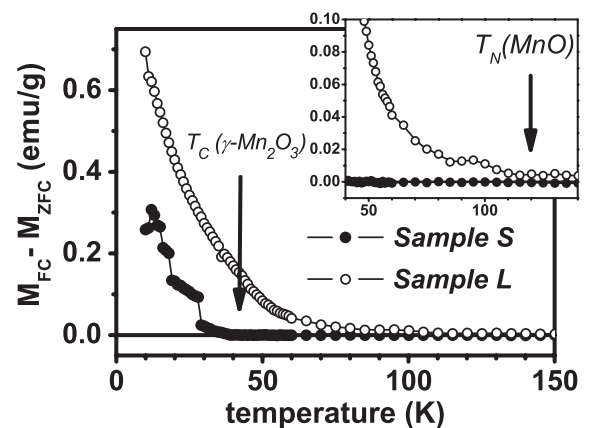


FIG. 3. Temperature dependence of the difference between the FC and ZFC magnetizations, $M_{\text{FC}} - M_{\text{ZFC}}$, for samples *S* (\bullet) and *L* (\circ). Shown in the inset is an enlargement of the high temperature region. The error bars are smaller than the size of the symbol, and the solid lines are guides for the eye.

Interestingly, in contrast to thin film AFM/FM systems, where magnetic proximity effects are observed in the AFM (since $T_C > T_N$), in the MnO/ γ -Mn₂O₃ system induced moments are observed in the FM shell. We attribute the observed stable magnetic moment in the γ -Mn₂O₃ shell well above T_C to the interface exchange coupling between the MnO core and the shell, as has been experimentally and theoretically observed in film systems [16–22,41,42], that can tentatively be considered as a magnetic proximity effect. Namely, although uncompensated spins may play a role in the proximity effect [12], the exchange field of each sublattice of the AFM core, which penetrates a few atomic layers, stabilizes the magnetic structure of the sublattices of the FIM shell [41,42]. These results are in agreement with the theoretical results in bilayer thin films from Jensen *et al.* who predicted an increase of the temperature range of stable moments to above T_C in AFM/FM systems with $T_N > T_C$ [41]. Probably both the moderately strong core-shell interface exchange coupling (evidenced by the large exchange bias observed in these systems [11–13]) and the small shell thickness contribute to make the effect more evident. The possible persistence of a magnetic moment in γ -Mn₂O₃ above $T_{C,shell}$ and $T_{N,core}$ is not clear at present, although it could be related to oxygen vacancies in γ -Mn₂O₃, as has been proposed [43] for other transition metal oxides exhibiting persisting magnetic signal well above their corresponding transition temperatures [43–45].

In conclusion, the magnetic order and temperature dependence of the magnetic moments in the doubly inverted “core-shell” MnO/ γ -Mn₂O₃ system were determined. It is found that an induced moment in the γ -Mn₂O₃ shell persists above its T_C due to the exchange coupling with the MnO core (i.e., a likely magnetic proximity effect).

The work was supported by the Russian Foundation for Basic Researches (Grant No. N07-02-00608), the Spanish MICINN (Grants No. MAT2007-66302-C02 and No. CSD2006-00012 Consolider-Ingenio 2010), and the Institut Català de Nanotecnologia. J.N. thanks M. Kiwi and J. Borchers for fruitful discussions. We acknowledge the ILL for the provision of neutron beam time.

-
- [1] A. H. Lu, E. L. Salabas, and F. Schuth, *Angew. Chem., Int. Ed.* **46**, 1222 (2007).
 [2] J. Nogués *et al.*, *Phys. Rep.* **422**, 65 (2005).
 [3] O. Iglesias, A. Labarta, and X. Batlle, *J. Nanosci. Nanotechnol.* **8**, 2761 (2008).
 [4] M. Casavola *et al.*, *Eur. J. Inorg. Chem.* **6** (2008) 837.
 [5] W. Liu, W. Zhong, and Y. W. Du, *J. Nanosci. Nanotechnol.* **8**, 2781 (2008).
 [6] E. Eftaxias, M. Vasilakaki, and K. N. Trohidou, *Mod. Phys. Lett. B* **21**, 1169 (2007).
 [7] G. Salazar-Alvarez *et al.*, *J. Mater. Chem.* **17**, 322 (2007).
 [8] J. Nogués *et al.*, *Phys. Rev. Lett.* **97**, 157203 (2006).
 [9] X. S. Liu *et al.*, *Appl. Phys. A* **77**, 673 (2003).
 [10] H. Zeng *et al.*, *Appl. Phys. Lett.* **85**, 792 (2004).
 [11] G. Salazar-Alvarez *et al.*, *J. Am. Chem. Soc.* **129**, 9102 (2007).
 [12] A. E. Berkowitz *et al.*, *Phys. Rev. B* **77**, 024403 (2008).
 [13] A. E. Berkowitz *et al.*, *J. Phys. D* **41**, 134007 (2008).
 [14] I. Djerdj *et al.*, *J. Phys. Chem. C* **111**, 3614 (2007).
 [15] D. Givord, V. Skumryev, and J. Nogués, *J. Magn. Magn. Mater.* **294**, 111 (2005).
 [16] C. A. Ramos *et al.*, *Phys. Rev. Lett.* **65**, 2913 (1990).
 [17] P. J. van der Zaag *et al.*, *Phys. Rev. Lett.* **84**, 6102 (2000).
 [18] K. Lenz, S. Zander, and W. Kuch, *Phys. Rev. Lett.* **98**, 237201 (2007).
 [19] V. V. Volobuev, A. N. Stetsenko, and J. van Lierop, *J. Appl. Phys.* **103**, 07C905 (2008).
 [20] E. N. Abarra *et al.*, *Phys. Rev. Lett.* **77**, 3451 (1996).
 [21] J. A. Borchers *et al.*, *Phys. Rev. Lett.* **70**, 1878 (1993).
 [22] J. van Lierop *et al.*, *Phys. Rev. B* **75**, 134409 (2007).
 [23] See EPAPS Document No. E-PRLTAO-103-004927 for the details of the synthesis of the nanoparticles, supplementary figures that show the temperature dependence of the MnO and γ -Mn₂O₃ lattice parameters, the total moment of γ -Mn₂O₃ for sample S, the magnetic measurements and the temperature dependence of M_S for samples L and S. For more information on EPAPS, see <http://www.aip.org/pubservs/epaps.html>.
 [24] T. C. Hansen *et al.*, *Meas. Sci. Technol.* **19**, 034001 (2008).
 [25] J. Rodriguez-Carvajal, *Physica (Amsterdam)* **192B**, 55 (1993); <http://www.ill.eu/sites/fullprof>.
 [26] K. Takano *et al.*, *Phys. Rev. Lett.* **79**, 1130 (1997).
 [27] J. B. Goodenough and A. L. Loeb, *Phys. Rev.* **98**, 391 (1955).
 [28] D. Bonnenberg and H. P. J. Wijn, in *Magnetic and Other Properties of Oxides and Related Compounds*, edited by K.-H. Hellwege and A. M. Hellwege, Landolt-Bornstein, Group III, Vol. 4b, Pt. B (Springer-Verlag, Berlin, 1970).
 [29] B. Morosin, *Phys. Rev. B* **1**, 236 (1970).
 [30] I. V. Golosovsky *et al.*, *Phys. Rev. Lett.* **86**, 5783 (2001).
 [31] I. V. Golosovsky *et al.*, *Phys. Rev. B* **74**, 054433 (2006).
 [32] I. V. Golosovsky *et al.*, *Phys. Rev. B* **72**, 144409 (2005).
 [33] I. V. Golosovsky *et al.*, *Phys. Rev. B* **74**, 155440 (2006).
 [34] W. L. Roth, *Phys. Rev.* **110**, 1333 (1958).
 [35] S. H. Kim *et al.*, *J. Korean Phys. Soc.* **46**, 941 (2005).
 [36] G. B. Jensen and O. V. Nielsen, *J. Phys. C* **7**, 409 (1974).
 [37] L. Néel, *Ann. Phys. (Paris)* **3**, 137 (1948).
 [38] I. V. Golosovsky *et al.*, *JETP Lett.* **83**, 298 (2006).
 [39] L. Theil Kuhn *et al.*, *J. Phys. Condens. Matter* **14**, 13 551 (2002).
 [40] M. S. Seehra and G. Srinivasan, *J. Appl. Phys.* **53**, 8345 (1982).
 [41] P. J. Jensen, H. Dreyseé, and M. Kiwi, *Eur. Phys. J. B* **46**, 541 (2005).
 [42] A. S. Carriço and R. E. Camley, *Phys. Rev. B* **45**, 13 117 (1992).
 [43] D. P. Dutta *et al.*, *Nanotechnology* **19**, 245609 (2008).
 [44] C. Nethravathi *et al.*, *J. Phys. Chem. B* **109**, 11 468 (2005).
 [45] A. Sundaresan and C. N. R. Rao, *Nano Today* **4**, 96 (2009).

SUPPLEMENTARY INFORMATION

Magnetic proximity effect features in antiferromagnetic/ferrimagnetic core/shell nanoparticles.

I. V. Golosovsky, G. Salazar-Alvarez, A. López-Ortega, M. A. González, J. Sort, M. Estrader, S. Suriñach, M. D. Baró, and J. Nogués

SYNTHESIS

The nanoparticle synthesis has been described elsewhere [1]. In brief, MnO nanoparticles were obtained by dissolving 7.5 mmol of manganese (II) acetylacetonate with 5 mmol of 1,2-hexadecanediol and a given amount of oleylamine (50 mL: small particles - sample S and 12.5 mL: large particles - sample L) in 150 mL of benzylether followed by heating to 200 °C or 290 °C for 30 min for sample S or sample L, respectively. After exposure to air, the passivation of the MnO takes place leading to a defect Mn₃O₄ shell.

LATTICE PARAMETERS

The temperature dependence of the unit cell parameter for MnO displays a distinct feature around 120 K (Fig. 1a), i.e., close to T_N (MnO), similar to what is observed in bulk [2],

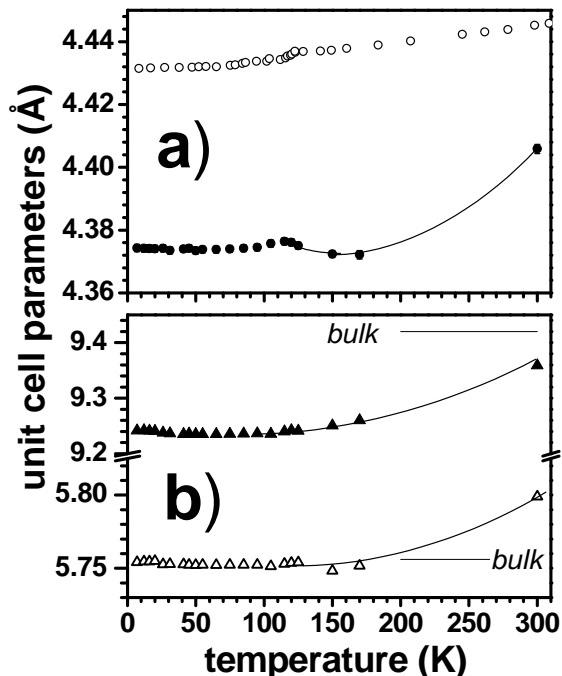


FIG. 1: Temperature dependence of the unit cell parameters for (a) MnO core (●) and bulk MnO [2] (○) and (b) γ -Mn₂O₃ (shell), parameters a (Δ) and c (\blacktriangle). The bulk values for a and c are also indicated. Solid lines are guides for the eye.

implying a well structured MnO core. Such feature has been already observed for isotropic nanoparticles of MnO embedded within porous glass [3], but not in highly anisotropic "ribbon" shaped nanoparticles [4–6]. The smaller lattice parameter of MnO with respect to the bulk could be explained by the presence of the large number of defects and/or the effect of inner pressure due to the covering shell. However, the defects should strongly reduce the effect of the interface stresses. The lattice parameters for γ -Mn₂O₃ exhibit a more monotonic temperature dependence and while the c is smaller than the corresponding bulk value [7, 8], a is larger (Fig. 1b). This is probably induced by the growth of a thin layer of the tetragonal γ -Mn₂O₃ on the cubic MnO.

MAGNETIC MOMENT

In order to make more evident the anomaly at T_N , the total moment of γ -Mn₂O₃ is shown in Fig. 2, rather than the moment of each sub-lattice.

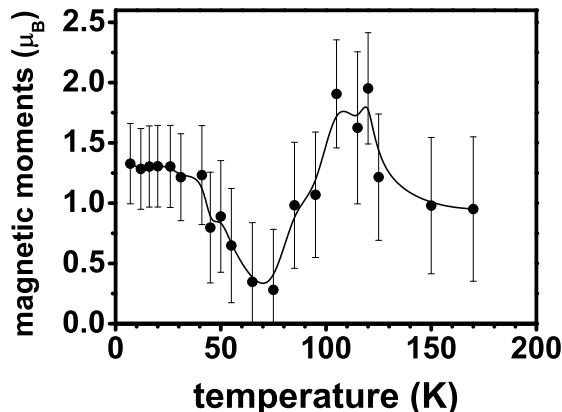


FIG. 2: Temperature dependence of the total magnetic moment of the γ -Mn₂O₃ shell for sample S. Solid lines are guides for the eye.

MAGNETIC MEASUREMENTS

Given the very small size of the core for sample S and the weak anisotropy of MnO, the blocking temperature, T_B , of the core is below the T_C of the shell when measured using magnetometry. Namely, T_B depends of the "characteristic measuring time", τ_m , of the technique used to determine it

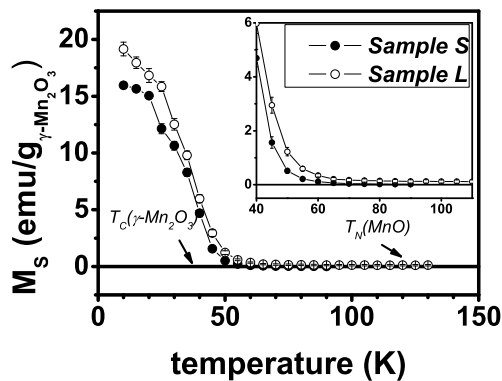


FIG. 3: Temperature dependence of the saturation magnetization, M_S , for samples S (●) and L (○). Solid lines are guides for the eye.

[9].

$$T_B = KV/k_B[\ln(\tau_m/\tau_0)],$$

where K is the anisotropy, V the volume, k_B is the Boltzmann constant and τ_0 is a time constant characteristic of the material (i.e., the reversal attempt time, usually in the $10^{-9} - 10^{-12}$ s range). For SQUID measurements τ_m is usually taken of the order of $\tau_m(\text{SQUID}) \sim 100$ s, while neutron diffraction is $\tau_m(\text{Neutron}) \sim 10^{-11} - 10^{-12}$ s [10]. Using the core size of sample S ($d = 4.7$ nm), the measured effective anisotropy of MnO nanoparticles, $K(\text{MnO}) = 3.5 \times 10^4$ J/m³ [11] and $\tau_0 = 10^{-9}$ s we obtain $T_B = 5$ K!. Thus, since $T_B(\text{MnO}) \ll T_C(\gamma\text{-Mn}_2\text{O}_3)$ no proximity effect should be observable using SQUID. Contrarily, since $\tau_m(\text{Neutron})$ is of the order of the attempt time, τ_0 , this implies that the material will be stable up to its bulk T_N when measured using neutron diffraction. This fact allows us to observe the proximity effects using neutron diffraction but not using magnetometry.

In the case of sample L ($d = 17$ nm) the estimated SQUID

T_B (~ 200 K) is larger than $T_N = 117$ K, thus for this size the core should be stable up to T_N , therefore, proximity effects should be observable using magnetometry.

To further confirm the existence of magnetic moment in the $\gamma\text{-Mn}_2\text{O}_3$ the temperature dependence of the saturation magnetization, $M_S(T)$, of the samples was also measured. It can be clearly seen in Fig. 3 that for the sample with the small core (Sample S) M_S virtually vanishes at about 60 K, while for the large core (Sample L) it remains finite up to over 100 K, as expected from a proximity effect.

-
- [1] G. Salazar-Alvarez, J. Sort, S. Suriñach, M.D. Baró, and J. Nogués, *J. Am. Chem. Soc.* **129**, 9102 (2007).
 - [2] B. Morosin, *Phys. Rev. B* **1**, 236 (1970).
 - [3] I. V. Golosovsky, I. Mirebeau, G. André, D. A. Kurdyukov, Yu. A. Kumzerov, and S. B. Vakhrushev, *Phys. Rev. Lett.* **86**, 5783 (2001).
 - [4] I. V. Golosovsky, I. Mirebeau, F. Fauth, D. A. Kurdyukov, and Yu. A. Kumzerov, *Phys. Rev. B* **74**, 054433 (2006).
 - [5] I. V. Golosovsky, I. Mirebeau, V. P. Sakhnenko, D. A. Kurdyukov, and Yu. A. Kumzerov, *Phys. Rev. B* **72**, 144409 (2005).
 - [6] I. V. Golosovsky, I. Mirebeau, F. Fauth, M. Mazaj, D. A. Kurdyukov, and Yu. A. Kumzerov, *Phys. Rev. B* **74**, 155440 (2006).
 - [7] J. B. Goodenough and A. L. Loeb, *Phys. Rev.* **98**, 391 (1955).
 - [8] Book Series Landolt-Börnstein - Group III Condensed Matter, Volume 4b, Part B, (Springer-Verlag, Berlin, 1970).
 - [9] M. Popovici, M. Gich, A. Roig, L. Casas, E. Molins, C. Savii, D. Becherescu, J. Sort, S. Suriñach, J.S. Muñoz, M.D. Baró, and J. Nogués, *Langmuir* **20**, 1425 (2004).
 - [10] D.F. Farrell, Y. Ijiri, C.V. Kelly, J.A. Borchers, J.J. Rhyne, Y. Ding and S.A. Majetich, *J. Mag. Magn. Mater.* **303**, 318 (2006).
 - [11] M.A. Morales, R. Skomski, S. Fritz, G. Shelburne, J.E. Shield, M. Yin, S. O'Brien, and D.L. Leslie-Pelecky, *Phys. Rev. B* **75**, 134423 (2007).

6.1.2 Article #2: Size-dependent passivation shell and magnetic properties in antiferromagnetic/ferrimagnetic core/shell MnO nanoparticles

In this article we studied the structural and magnetic properties of four different MnO|Mn₃O₄ (γ -Mn₂O₃) CS nanoparticles with similar shell thickness but different core size. The aim of this work was to elucidate the structural composition of the shell as a function of the different core sizes. It was demonstrated that the crystallographic phase created by the passivation of the MnO core depends on the initial size of the MnO nanoparticles. Interestingly, the two possible crystallographic phases found on the shell are based in a tetragonal manganese oxide spinel. The Mn₃O₄ phase is a divalent cation structure formed by Mn²⁺ and Mn³⁺ ions. In contrast the other possible phase is solely formed by Mn³⁺ ions and is labeled as γ -Mn₂O₃. Both structures present a FiM behavior with rather similar magnetic properties. To allow discerning between the two phases, we performed a large number of structural and magnetic characterizing techniques such as neutron diffraction, TEM, EELS, magnetometric measurements (DC and AC) and ESR. The overall particle size, i.e. core size + shell thickness, was obtained from TEM images. This study reveals that the core size/shell thickness are 21/4-5, 15/2-3, 13/3-4 and 5/2-3 nm for *M1*, *M2*, *M3* and *M4*, respectively. We can assume a shell thickness constant roughly 2-5 nm. In addition, the profile refinement of the nuclear neutron diffraction pattern reveals the expected NaCl (rock salt) composition of the MnO core, with Mn²⁺ defects for the small particles. In contrast, the structural characterization of the shell was more difficult due to the overlap with the signal of the core and the strongly anisotropic shape of the shell. In fact, only in the smaller CS nanoparticle, *M4*, it was possible to unambiguously distinguish the shell and it was ascribed as γ -Mn₂O₃. On the other hand the differences obtained in the core size and shell thickness from TEM and neutron diffraction can be understood by the different averaging methods used, i.e. number average vs. volume average for TEM and diffraction, respectively. To further evaluate the structure of the particles EELS analysis was performed analyzing the Mn/O ratio in many points along the diameter of particle and simulating the manganese oxidation state at each point. This analysis confirmed the presence of a MnO core for all the particles and γ -Mn₂O₃ shell for sample *M4* and Mn₃O₄ for larger particles, i.e., *M1-M3*.

Magnetic neutron diffraction confirmed the AFM behavior of the MnO core and the FiM behavior of the γ -Mn₂O₃ shell for sample *M4*. Note that it is not possible to distinguish the shells for samples *M1-M3*. The magnetic domains of the MnO core, for larger particles, have been found smaller than the crystallographic size and their reduction close to T_N was also confirmed. Finally, neutron diffraction have revealed a size dependent T_N enhancement compared to the bulk value, i.e., smaller core sizes present larger T_N . This feature can be ascribed to the finite-size and surface effects such as broken symmetry and surface disorder. Magnetometric measurements were used to try to elucidate the structural composition of the FiM shell of the different samples. Hysteresis loops show larger M_S values (corrected by the weight of the AFM core) for larger particles than for *M4*, which given the larger M_S for Mn₃O₄ in comparison with γ -Mn₂O₃, hint towards the presence of Mn₃O₄ in the larger particles. The coercivity increases at the same time that the core size is reduced, while the exchange bias presents a non-monotonic behavior. These results arise from the exchange coupling between the core and the shell and thus do not allow us to differentiate between the possible shell phases. The temperature dependence of the magnetization and the susceptibility were used to distinguish the small differences in T_C for Mn₃O₄ and γ -Mn₂O₃ (42 and 39 K, respectively) and the spin reorientation transitions present at 20, 36 and 41 K for Mn₃O₄ phase. Interestingly, corroborating the previous results, the smallest sample, *M4*, presents only the transition at 39 K of the γ -Mn₂O₃ phase. In contrast, larger particles, *M1-M3*, show various transition which can be ascribed to the spin reorientation and T_C of the Mn₃O₄ phase. Finally, the ESR analysis demonstrated the presence of two different phases showing two resonance lines at $T > T_N$ (core and shell paramagnetic) and only one at $T < T_N$ (shell paramagnetic). The intensity of the resonance line, I_{ESR} , confirms the T_N enhancement observed in the neutron diffraction analysis. Moreover, I_{ESR} was used to quantify the presence of Mn²⁺ ions in the core and the shell (note that Mn³⁺ ions usually do not show ESR signals). The results indicate that the small particles only present a small amount of these ions in the shell, hence confirming the presence of a pure Mn³⁺ phase, γ -Mn₂O₃. In contrast, larger samples display increasing amounts of Mn²⁺ ions in the shell hinting the presence of the Mn₃O₄

phase.

In conclusion, magnetic and structural characterization of the different particles confirm that the larger nanoparticles present mainly Mn_3O_4 as shell, although as the core size diminishes, the density of defects increases and as a consequence $\gamma\text{-Mn}_2\text{O}_3$ is the more stable shell phase.

Size-Dependent Passivation Shell and Magnetic Properties in Antiferromagnetic/Ferrimagnetic Core/Shell MnO Nanoparticles

Alberto López-Ortega,[†] Dina Tobia,[‡] Elin Winkler,[‡] Igor V. Golosovsky,[§]
 German Salazar-Alvarez,^{†,||} Sònia Estradé,[‡] Marta Estrader,^{*,†} Jordi Sort,^{||,¶}
 Miguel Angel González,[@] Santiago Suriñach,[#] Jordi Arbiol,^{||,Δ} Francesca Peiró,[‡]
 Roberto D. Zysler,[‡] Maria Dolors Baró,[#] and Josep Nogués^{||,†}

Centre d'Investigació en Nanociència i Nanotecnologia (ICN-CSIC), Campus Universitat Autònoma de Barcelona, E-08193 Bellaterra, Spain, Centro Atómico Bariloche, CNEA-CONICET, 8400 S.C. de Bariloche, Río Negro, Argentina, St. Petersburg Nuclear Physics Institute, 188300 Gatchina, St. Petersburg, Russia, Department of Materials and Environmental Chemistry, Stockholm University, S-10691 Stockholm, Sweden, MIND-IN2UB, Departament d'Electrònica, Universitat de Barcelona, Martí i Franquès 1, E-08028 Barcelona, Spain, Institució Catalana de Recerca i Estudis Avançats (ICREA), Barcelona, Spain, Departament de Física, Universitat Autònoma de Barcelona, E-08193 Bellaterra, Spain, Institut Laue Langevin, 6 rue Jules Horowitz, BP 156, F-38042 Grenoble, France, and Institut de Ciència de Materials de Barcelona (CSIC), Campus Universitat Autònoma de Barcelona, E-08193 Bellaterra, Spain

Received March 15, 2010; E-mail: marta.estrader.icn@uab.cat

Abstract: The magnetic properties of bimagnetic core/shell nanoparticles consisting of an antiferromagnetic MnO core and a ferrimagnetic passivation shell have been investigated. It is found that the phase of the passivation shell (γ -Mn₂O₃ or Mn₃O₄) depends on the size of the nanoparticles. Structural and magnetic characterizations concur that while the smallest nanoparticles have a predominantly γ -Mn₂O₃ shell, larger ones have increasing amounts of Mn₃O₄. A considerable enhancement of the Néel temperature, T_N , and the magnetic anisotropy of the MnO core for decreasing core sizes has been observed. The size reduction also leads to other phenomena such as persistent magnetic moment in MnO up to high temperatures and an unusual temperature behavior of the magnetic domains.

Introduction

Magnetic nanoparticles are attracting a great deal of interest from both fundamental and applied points of view.^{1–4} Magnetic recording media, catalysis, ferrofluids, pigments, hyperthermia, medical diagnostics, and drug delivery are among the increasing number of applications of magnetic nanoparticles. Due to their small size and, particularly, their large surface-to-volume ratio magnetic nanoparticles exhibit properties different from those of their bulk counterparts, which can be exploited to obtain new functionalities. Although ferromagnetic (FM) and ferrimagnetic (FiM) nanoparticles have been extensively studied, antiferromagnetic (AFM) nanoparticles have been far less investigated

and are thus less understood.⁵ Nevertheless, antiferromagnetic nanoparticles and nanostructures play an important role in spintronic devices⁶ and have been proposed as means to overcome the superparamagnetic limit in recording media or to enhance the coercivity of ferromagnets.^{7,8} Although finite size effects in antiferromagnetic nanoparticles are similar to those of FM or FiM materials (e.g., superparamagnetism or reduced blocking temperatures), some effects are specific to AFMs (e.g., the appearance of finite magnetization due to sublattice uncompensation).^{1–5}

Special types of magnetic nanoparticles are core/shell nanoparticles. Although in most cases the shell serves just for protection purposes, the study of bimagnetic nanoparticles, where both the shell and the core are magnetic, is steadily increasing.^{6,9–30} In fact, the shell properties and exchange coupling between the core and the shell open new degrees of freedom to tailor the overall properties of the nanoparticles,

[†] ICN-CSIC, Campus Universitat Autònoma de Barcelona.

[‡] CNEA-CONICET.

[§] St. Petersburg Nuclear Physics Institute.

^{||} Stockholm University.

[‡] Universitat de Barcelona.

[¶] ICREA, Universitat Autònoma de Barcelona.

[#] Departament de Física, Universitat Autònoma de Barcelona.

[@] Institut Laue Langevin.

^Δ Institut de Ciència de Materials de Barcelona (CSIC), Campus Universitat Autònoma de Barcelona.

(1) Lu, A. H.; Salabas, E. L.; Schuth, F. *Angew. Chem., Int. Ed.* **2007**, *46*, 1222–1244.

(2) Tartaj, P.; Morales, M. P.; Veintemillas-Verdaguer, S.; González-Carreño, T.; Serna, C. J. *J. Phys. D* **2003**, *36*, R182–R197.

(3) Batlle, X.; Labarta, A. *J. Phys. D* **2002**, *35*, R15–R42.

(4) Willard, M. A.; Kurihara, L. K.; Carpenter, E. E.; Calvin, S.; Harris, V. G. *Int. Mater. Rev.* **2004**, *49*, 125–170.

(5) Mørup, S.; Madsen, D. E.; Frandsen, C.; Bahl, C. R. H.; Hansen, M. F. *J. Phys.: Condens. Matter* **2007**, *19*, 213202.

(6) Nogués, J.; Sort, J.; Langlais, V.; Skumryev, V.; Suriñach, S.; Muñoz, J. S.; Baró, M. D. *Phys. Rep.* **2005**, *422*, 65–117.

(7) Skumryev, V.; Stoyanov, S.; Zhang, Y.; Hadjipanayis, G.; Givord, D.; Nogués, J. *Nature (London)* **2003**, *423*, 850–853.

(8) (a) Sort, J.; Suriñach, S.; Muñoz, J. S.; Baró, M. D.; Nogués, J.; Chouteau, G.; Skumryev, V.; Hadjipanayis, G. C. *Phys. Rev. B* **2002**, *65*, 174420. (b) Sort, J.; Nogués, J.; Suriñach, S.; Muñoz, J. S.; Baró, M. D.; Chappel, E.; Dupont, F.; Chouteau, G. *Appl. Phys. Lett.* **2001**, *79*, 1142–1144.

Table 1. Summary of the Synthesis Conditions and the Structural Parameters Obtained from Neutron Diffraction and TEM Analyses

| sample | synthesis params | | | | neutron analysis | | | | TEM | | |
|--------|-------------------|------------------------------|--------|---------|-----------------------|----------------------|-------------------------|-------------------------|-----------------------|-----------------------|-------------------------|
| | [S]:[M] (mol/mol) | [Mn ²⁺] (mol/mL) | T (°C) | t (min) | D _{MnO} (nm) | a _{MnO} (Å) | D _{shell} (nm) | t _{shell} (nm) | D _{tot} (nm) | D _{MnO} (nm) | t _{shell} (nm) |
| M1 | 1.03 | 0.05 | 240 | 30 | 19(2) | 4.4200(8) | 2.8(3) | 1.5 | 25(6) | 21 | 4–5 |
| M2 | 41.3 | 0.03 | 205 | 60 | 17.0(5) | 4.4424(2) | 5.0(2) | 0.15 | 15(5) | 14 | 2–3 |
| M3 | 4.1 | 0.05 | 220 | 30 | 15.7(5) | 4.4431(6) | 5.0(2) | 0.5 | 13(5) | 10 | 3–4 |
| M4 | 20 | 0.04 | 190 | 30 | 4.7(3) | 4.374(2) | 4.9(3) | 2 | 5(1) | 3 | 2–3 |

leading to novel applications (such as enhanced coercivity and energy products, tunable blocking temperatures, improved electromagnetic radiation absorption, and hyperthermia treatment).^{7,13,31–33} Core/shell nanoparticles with a FM (or FiM) core and a AFM (or FiM) shell have been widely investigated.^{6,9–11} Recently, “inverse” core/shell nanoparticles, with AFM cores and FiM or spin-glass shells, have been synthesized, leading to a number of novel magnetic properties.^{34–46} In particular, the

magnetic properties of inverse core/shell nanoparticles based on the passivation of AFM MnO nanoparticles have been investigated.^{34–38,40} These materials exhibit novel properties at low temperatures^{34–37,40} such as very large exchange bias and coercivity with a nonmonotonic dependence on the core diameter³⁴ and spontaneous magnetization and ferrimagnetic order above the Curie temperature of the shell.^{35–37} However, in these nanoparticles, although the shell material is usually identified as Mn₃O₄,^{34,36–38,40} it has been recently shown that γ -Mn₂O₃ can also be formed as a result of MnO passivation.³⁵

In this article we present the study of MnO (AFM)– γ -Mn₂O₃ or Mn₃O₄ (FiM) core/shell nanoparticles by diverse techniques (i.e., neutron diffraction, TEM, EELS, ac susceptibility, magnetometry, and electron spin resonance). The magnetic and structural results indicate that the structure of the passivation shell of the MnO nanoparticles depends on the core size, being primarily γ -Mn₂O₃ for small cores and progressively transforming to Mn₃O₄ for larger cores. Moreover, the core/shell nanoparticles exhibit a range of interesting properties such as large coercivities, exchange bias or enhanced anisotropy, and Néel temperatures of the core.

Experimental Section

Nanoparticles with different sizes were obtained by adding 7.5 mmol of manganese(II) acetylacetonate (Mn(acac)₂ purum, Aldrich) and 7.5 mmol of 1,2-hexadecanediol (HDD 90%, Aldrich) to 150 mL of dibenzyl ether (DBE analytical, Aldrich) in a 250 mL round-bottomed flask under an inert argon atmosphere followed by the addition of a surfactant, oleylamine (OA 70%, Aldrich), in a surfactant-to-metal ratio, [S]:[M] (mol/mol), from 1 to 40. The solution was mechanically stirred and heated, at a heating rate of 8–10 °C/min, to a given temperature, in the range of 190–240 °C with reflux and a residence time of 30–60 min. The flask was removed from the heating source, cooled in argon to 80 °C, and subsequently exposed to air and cooled to room temperature to obtain the passivated shell. The particles were washed from the reaction media by subsequent steps of precipitation under ethanol, centrifugation, and redispersion in hexane. The synthesis parameters are summarized in Table 1.

- (9) Iglesias, O.; Labarta, A.; Batlle, X. *J. Nanosci. Nanotechnol.* **2008**, *8*, 2761–2780.
- (10) Liu, W.; Zhong, W.; Du, Y. W. *J. Nanosci. Nanotechnol.* **2008**, *8*, 2781–2792.
- (11) Casavola, M.; Buonsanti, R.; Caputo, G.; Cozzoli, P. D. *Eur. J. Inorg. Chem.* **2008**, 837–854.
- (12) Eftaxias, E.; Trohidou, K. N. *Phys. Rev. B* **2005**, *71*, 134406.
- (13) Salazar-Alvarez, G.; Sort, J.; Uheida, A.; Muhammed, M.; Suriñach, S.; Baró, M. D.; Nogués, J. *J. Mater. Chem.* **2007**, *17*, 322–328.
- (14) Liu, X. S.; Gu, B. X.; Zhong, W.; Jiang, H. Y.; Du, Y. W. *Appl. Phys. A: Mater. Sci. Process.* **2003**, *77*, 673–676.
- (15) Zeng, H.; Sun, S.; Li, J.; Wang, Z. L.; Liu, J. P. *Appl. Phys. Lett.* **2004**, *85*, 792–794.
- (16) Figuerola, A.; Fiore, A.; Di Corato, R.; Falqui, A.; Giannini, C.; Micotti, E.; Lasciari, A.; Corti, M.; Cingolani, R.; Pellegrino, T.; Cozzoli, P. D.; Manna, L. *J. Am. Chem. Soc.* **2008**, *130*, 1477–1487.
- (17) Nogués, J.; Skumryev, V.; Sort, J.; Stoyanov, S.; Givord, D. *Phys. Rev. Lett.* **2006**, *97*, 157203.
- (18) Masala, O.; Seshadri, R. *J. Am. Chem. Soc.* **2005**, *127*, 9354–9355.
- (19) Seo, W. S.; Jo, H. H.; Lee, K.; Kim, B.; Oh, S. J.; Park, J. T. *Angew. Chem., Int. Ed.* **2004**, *43*, 1115–1117.
- (20) Riveiro, J. M.; De Toro, J. A.; Andrés, J. P.; González, J. A.; Muñoz, T.; Goff, J. P. *Appl. Phys. Lett.* **2005**, *86*, 172503.
- (21) Morel, R.; Brenac, A.; Portemont, C. *J. Appl. Phys.* **2004**, *95*, 3757–3760.
- (22) Dobrynin, A. N.; Ievlev, D. N.; Temst, K.; Lievens, P.; Margueritat, J.; Gonzalo, J.; Afonso, C. N.; Zhou, C. Q.; Vantomme, A.; Piscopiello, E.; Van Tendeloo, G. *Appl. Phys. Lett.* **2005**, *87*, 012501.
- (23) Del Bianco, L.; Fiorani, D.; Testa, A. M.; Bonetti, E.; Savini, L.; Signoretti, L. *Phys. Rev. B* **2002**, *66*, 174418.
- (24) Si, P. Z.; Li, D.; Choi, C. J.; Li, Y. B.; Geng, D. Y.; Zhang, Z. D. *Solid State Commun.* **2007**, *142*, 723–726.
- (25) Johnston-Peck, A. C.; Wang, J. W.; Tracy, J. B. *ACS Nano* **2009**, *3*, 1077–1084.
- (26) Zhou, S. M.; Imhoff, D.; Yu-Zhang, K.; Leprince-Wang, Y. *Appl. Phys. A: Mater. Sci. Process.* **2005**, *85*, 115–118.
- (27) Tracy, J. B.; Weiss, D. N.; Dinega, D. P.; Bawendi, M. G. *Phys. Rev. B* **2005**, *72*, 064404.
- (28) Luna, C.; Morales, M. D.; Serna, C. J.; Vazquez, M. *Nanotechnology* **2004**, *15*, S293–S297.
- (29) Inderhees, S. E.; Borchers, J. A.; Green, K. S.; Kim, M. S.; Sun, S.; Strycker, G. L.; Aronson, M. S. *Phys. Rev. Lett.* **2008**, *101*, 117202.
- (30) Gangopadhyay, S.; Hadjipanayis, G. C.; Sorensen, C. M.; Klabunde, K. J. *IEEE Trans. Magn.* **1993**, *29*, 2602–2607.
- (31) Zeng, H.; Li, J.; Wang, Z. L.; Liu, J. P.; Sun, S. H. *Nano Lett.* **2004**, *4*, 187–190.
- (32) Lu, B.; Huang, H.; Dong, X. L.; Zhang, X. F.; Lei, J. O.; Sun, J. P.; Dong, C. *J. Appl. Phys.* **2008**, *104*, 114313.
- (33) Habib, A. B.; Ondeck, C. L.; Chaudhary, P.; Bockstaller, M. R.; McHenry, M. E. *J. Appl. Phys.* **2008**, *103*, 07A307.
- (34) Salazar-Alvarez, G.; Sort, J.; Suriñach, S.; Baró, M. D.; Nogués, J. *J. Am. Chem. Soc.* **2007**, *129*, 9102–9108.
- (35) Golosovsky, I. V.; Salazar-Alvarez, G.; López-Ortega, A.; González, M. A.; Sort, J.; Estrader, M.; Suriñach, S.; Baró, M. D.; Nogués, J. *Phys. Rev. Lett.* **2009**, *102*, 247201.
- (36) Berkowitz, A. E.; Rodriguez, G. F.; Hong, J. I.; An, K.; Hyeon, T.; Agarwal, N.; Smith, D. J.; Fullerton, E. E. *Phys. Rev. B* **2008**, *77*, 024403.

- (37) Berkowitz, A. E.; Rodriguez, G. F.; Hong, J. I.; An, K.; Hyeon, T.; Agarwal, N.; Smith, D. J.; Fullerton, E. E. *J. Phys. D* **2008**, *41*, 134007.
- (38) Djerdj, I.; Aëcon, D.; Jagličić, Z.; Niederberger, M. *J. Phys. Chem. C* **2007**, *111*, 3614–3623.
- (39) Wang, Z. H.; Geng, D. Y.; Hu, W. J.; Ren, W. J.; Zhang, Z. D. *J. Appl. Phys.* **2009**, *105*, 07A315.
- (40) Si, P. Z.; Li, D.; Lee, J. W.; Choi, C. J.; Zhang, Z. D.; Geng, D. Y. *U. Appl. Phys. Lett.* **2005**, *87*, 133122.
- (41) Zhou, S. M.; Shi, L.; Yang, H. P.; Wang, Y.; He, L. F.; Zhao, J. Y. *Appl. Phys. Lett.* **2008**, *93*, 182509.
- (42) Markovich, V.; Fita, I.; Wisniewski, A.; Puzniak, R.; Mogilyansky, D.; Titelman, L.; Vradman, L.; Herskowitz, M.; Gorodetsky, G. *Phys. Rev. B* **2008**, *77*, 054410.
- (43) Kavich, D. W.; Dickerson, J. H.; Mahajan, S. V.; Hasan, S. A.; Park, J. H. *Phys. Rev. B* **2008**, *78*, 174414.
- (44) Shin, J. M.; Anisur, R. M.; Ko, M. K.; Im, G. H.; Lee, J. H.; Lee, I. S. *Angew. Chem., Int. Ed.* **2009**, *48*, 321–324.
- (45) An, K.; Kwon, S. G.; Park, M.; Na, H. B.; Baik, S. I.; Yu, J. H.; Kim, D.; Son, J. S.; Kim, Y. W.; Song, I. C.; Moon, W. K.; Park, H. M.; Hyeon, T. *Nano Lett.* **2008**, *8*, 4252–4258.
- (46) Yun, B. K.; Koo, Y. S.; Jung, J. H. *J. Magn. Mater.* **2009**, *14*, 147–149.

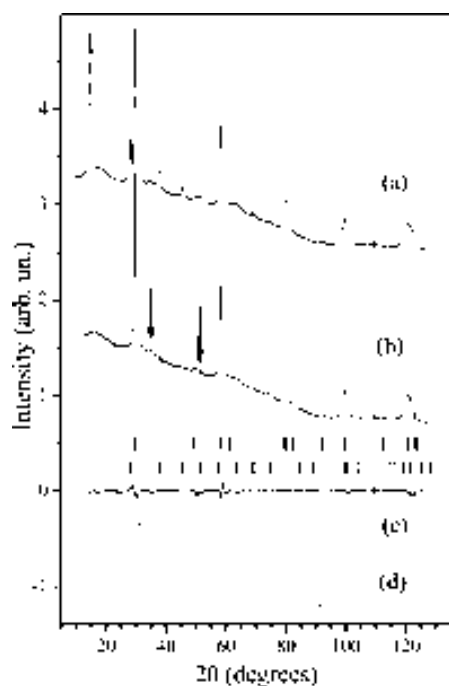


Figure 1. Neutron diffraction patterns measured at (a) 20 K and (b) 250 K for sample M2. The small reflections shown by the arrows are due to the cryostat and the sample holder. (c) Difference pattern (calculated – observed) at 250 K. (d) Calculated pattern from the shell $\gamma\text{-Mn}_2\text{O}_3\text{-Mn}_3\text{O}_4$, showing its contribution to the total patterns (a) and (b). The stripes mark the positions of the Bragg reflections from the MnO core: upper and lower rows correspond to the magnetic and nuclear reflections, respectively.

Neutron diffraction measurements were carried out at different temperatures, in the range 10–250 K, at the D20 diffractometer of the Institute Laue-Langevin with a neutron wavelength of 1.305 Å.⁴⁷ Typical neutron diffraction patterns are shown in Figure 1 and Figure S1 (Supporting Information). All diffraction patterns were analyzed using the FullProf code⁴⁸ based on the known crystal structures of MnO and $\gamma\text{-Mn}_2\text{O}_3$ (or Mn_3O_4). This method, in contrast with the so-called “matching mode”, provides more stable refinement (see curve c in Figure 1 and Figure S1) in the present case due to the strong overlapping of the principal peaks and the presence of small parasitic reflections (see arrows in Figure 1). Note that the rather large diffuse background is due to the remains of surfactants used in the synthesis.

Transmission electron microscopy (TEM) images were obtained using a JEM-2010 instrument with a LaB₆ filament and a JEM-2010F instrument with a field-emission gun operating at 200 kV, the latter equipped with a postcolumn Gatan Image Filter (GIF) energy spectrometer. The particle size, D_{MnO} , and its standard deviation were obtained by calculating the number average by manually measuring the equivalent diameters of >200 particles from TEM micrographs (Figure 2).

Electron energy loss spectra (EELS) were acquired at about every 0.5 nm along the diameter of the nanoparticles (as schematically shown in Figure 3a) at an energy range containing the Mn-L_{2,3} and the O-K edges, with an energy resolution of 0.8 eV (see Figure 3b). Mn/O quantification was carried out using Gatan Digital Micrograph commercial software. The Mn oxidation state was obtained from the Mn-L₃ peak onset and L₃/L₂ intensity ratios^{49,50}

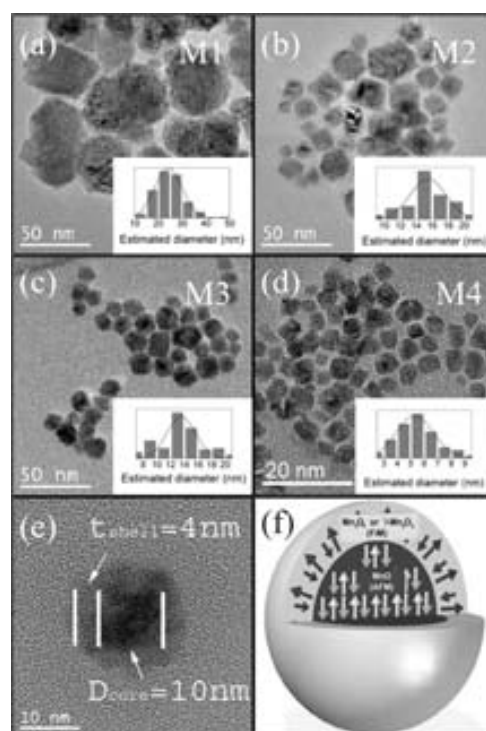


Figure 2. Transmission electron micrographs of samples (a) M1, (b) M2, (c) M3 and (d) M4 (note the different magnification). Shown in the respective insets are the corresponding particle size distributions with a fit to a log-norm function. (e) High-resolution image of an M2 nanoparticle. (f) Schematic representation of the morphological and magnetic structures of the nanoparticles.

using the homemade software package MANGANITAS.^{51–53} The L₃/L₂ intensity ratio for all samples is subject to a relative error of about 5% except for sample M1, where the nanoparticles are exceedingly large, leading to a weaker EELS signal and consequently to larger errors. Note that several particles were measured for each sample.

dc magnetic measurements were carried out on loosely packed powdered samples using a superconducting quantum interference device (SQUID, Quantum Design) magnetometer with 70 kOe maximum field. The magnetization measurements were carried out at 50 Oe. The hysteresis loops were measured at $T = 10$ K after field cooling in $H_{\text{FC}} = 20$ kOe from $T = 200$ K.

The ac susceptibility measurements were performed at different frequencies, between 10 Hz and 10 kHz, applying an ac field of 10 Oe using physical properties measurement system (PPMS, Quantum Design) equipment.

The temperature dependence of the electron spin resonance (ESR) spectra were recorded by a Bruker ESP300 spectrometer at 9.5 GHz. The parameters that characterize the resonance signal are the resonance field H_r , the line width ΔH , and the spectrum intensity, I_{ESR} . From the H_r value, at room temperature, we derived the gyromagnetic factor g through the resonance condition $h\nu = g\mu_B H_r$, where h and μ_B are Planck’s constant and Bohr magneton, respectively. The line width is a measurement of the spin-relaxation mechanism, and it is measured as the distance between the peaks in the derivative of the absorption spectrum. The spectrum intensity

(47) Hansen, T. C.; Henry, P. F.; Fischer, H. E.; Torregrossa, J.; Convert, P. *Meas. Sci. Technol.* **2008**, *19*, 034001.

(48) Rodríguez-Carvajal, J. *Phys. B* **1993**, *192*, 55–69. (<http://www.ill.eu/sites/fullprof>).

(49) Kurata, H.; Colliex, C. *Phys. Rev. B* **1993**, *48*, 2102–2108.

(50) Egerton, R. F. *Electron Energy-Loss Spectroscopy in the Electron Microscope*, 2nd ed.; Kluwer: Dordrecht, The Netherlands, 1996.

(51) Estradé, S.; Arbiol, J.; Peiró, F.; Abad, L.I.; Laukhin, V.; Balcells, L.I.; Martínez, B. *Appl. Phys. Lett.* **2007**, *91*, 252503.

(52) Estradé, S.; Arbiol, J.; Peiró, F.; Infante, I. C.; Sánchez, F.; Fontcuberta, J.; de la Peña, F.; Walls, M.; Colliex, C. *Appl. Phys. Lett.* **2008**, *93*, 112505.

(53) Estradé, S.; Rebled, J. M.; Arbiol, J.; Peiró, F.; Infante, I. C.; Herranz, G.; Sánchez, F.; Fontcuberta, J.; Córdoba, R.; Mendis, B. G.; Bleloch, A. L. *Appl. Phys. Lett.* **2009**, *95*, 072507.

(54) Schmid, H. K.; Mader, W. *Micron* **2006**, *37*, 426–432.

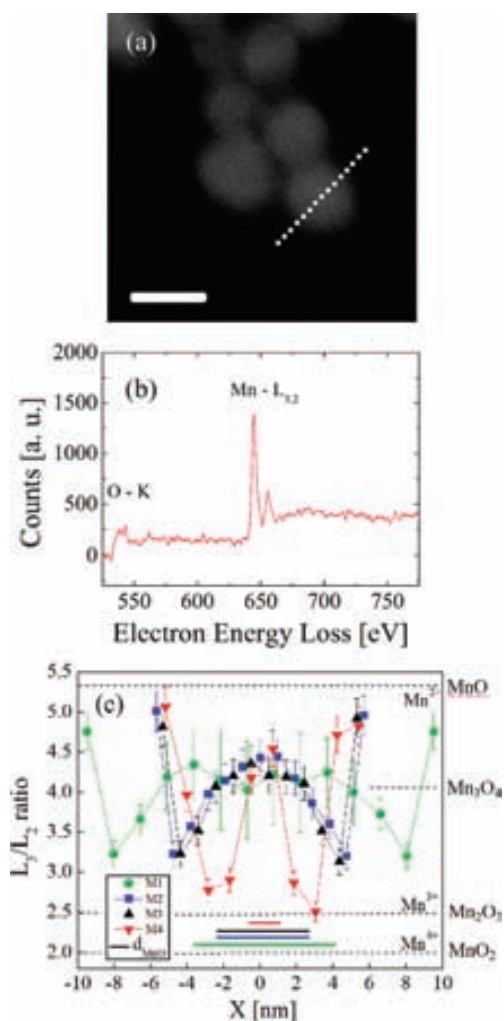


Figure 3. (a) High-angle annular dark field (HAADF) image of M4 nanoparticles, where the approximate positions at which spectra were taken are indicated by dots. (b) Typical background-subtracted EEL spectrum of the shell part for M4. (c) Mn- L_3/L_2 intensity ratio along the diameter of the M1–M4 nanoparticles. The lines joining the data points are guides to the eye. The dotted lines in the figure are the expected L_3/L_2 ratios for Mn^{2+} , Mn^{3+} , and Mn^{4+} ions, respectively.^{49,54} The thick solid lines in (c) indicate the diameter of the core as estimated from the position dependence of the Mn- L_3/L_2 intensity ratio.

is the area under the absorption curve and is proportional to the concentration of resonant magnetic ions.

Results and Discussion

Structural and Morphological Characterization. As can be seen from the high-temperature neutron diffraction (shown in curve b in Figure 1 and Figure S1 for samples M2 and M4, respectively), the MnO core exhibits the expected rock salt crystal structure. However, although samples M1–M3 show a stoichiometric structure, sample M4 has defects on the Mn sites with a 0.74(2) occupancy ratio.³⁵ Concerning the shell structure sample, M4 does not exhibit the expected hausmannite, Mn_3O_4 , structure^{34,36,37} but a spinel type tetragonal γ - Mn_2O_3 structure.^{35,55} For samples M1–M3 the neutron diffraction signal is overwhelmed by the MnO spectrum (see curve d in Figure 1); thus, it is impossible to distinguish between the γ - Mn_2O_3 and the Mn_3O_4 structures for the shell.

All the studied samples show a similar temperature dependence of the lattice parameter for MnO, which displays a distinct feature around 125 K, i.e., at the MnO Néel temperature.³⁵ This is similar to the behavior observed in the bulk,⁵⁶ implying a rather well structured MnO core. Interestingly, the lattice parameter of MnO is contracted with respect to the bulk and becomes smaller as the core size decreases (see Table 1), in contrast with most oxide nanoparticle systems which show a lattice expansion for reduced particle sizes.⁵⁷ The smaller lattice parameter is likely caused by the presence of a large number of defects, since no stresses due to the outer passivation layer were detected. In most of the samples the contribution from the MnO core dominates in the diffraction patterns; therefore, the lattice parameters of the shell were determined with lower accuracy. We did not observe any essential difference in the temperature dependence of the lattice parameters of the different samples, which were evaluated as $a = 5.844(5)$ Å and $c = 9.13(1)$ Å.

From the fitting of the different patterns at diverse temperatures the structural and magnetic characteristic sizes and structures can be readily obtained. The diffraction peak broadening comprises two contributions, which have different q dependencies: internal stresses (i.e., microstrains) and crystallite size effect. The profile analysis of the diffraction patterns shows that the stresses are negligible within experimental error. Therefore, from the peak broadening one can easily obtain the volume-averaged crystallite size and the magnetic domain size.

The volume-averaged diameter of the MnO core, D_{MnO} , and the characteristic sizes of ferrimagnetic nanoparticles forming the shell, D_{shell} , are shown in Table 1. Interestingly, while D_{MnO} ranges from 5 to 19 nm on adjusting the synthesis conditions, D_{shell} remains rather constant at around 3–5 nm. Note that due to the limited statistics it is not possible to directly evaluate any anisotropy in the particle shape, from the peak profile analysis. However, from the core/shell volume ratios obtained from the fit, indirect information can be inferred. Taking into account the volume ratios and the measured diameters of the cores and assuming a uniform core/shell structure, the corresponding averaged effective thickness of the shell, t_{shell} , can be estimated (see Table 1). Hence, on comparison of the effective shell thickness and the shell crystallite sizes obtained from the profile refinement it can be concluded that the nanoparticles forming the ferrimagnetic shell layer are strongly anisotropic (e.g., pancake-like).

In order to confirm this feature, TEM images of the samples were obtained, and the results are summarized in Table 1. All the samples exhibit a clear core/shell structure with average overall particle sizes, D_{tot} , of 25(6) nm for M1, 15(5) nm for M2, 13(5) nm for M3, and 5(1) nm for M4 (where the value in parentheses is the log-norm standard deviation; see insets in Figure 2). The shell thicknesses, t_{shell} , remain rather homogeneous, in the range of ~ 2 –5 nm (see Table 1). Note that the shells are more difficult to image, since each individual particle needs a specific imaging tilt to allow the shell to be clearly observed (see Figure 2e). Thus, the statistics are not sufficient to evaluate standard deviations and only estimates are given. The values of the core diameter obtained from TEM and neutron diffraction follow a similar trend, where the small discrepancies probably arise from the different averaging methods (number

(55) Goodenough, J. B.; Loeb, A. L. *Phys. Rev.* **1955**, *98*, 391–408.

(56) Morosin, B. *Phys. Rev. B* **1970**, *1*, 236–243.

(57) Zheng, X. G.; Kubozono, H.; Yamada, H.; Kato, K.; Ishiwata, Y.; Xu, C. N. *Nat. Nanotechnol.* **2008**, *3*, 724–726.

(58) Allen, T. *Particle Size Measurements*, 5th ed.; Chapman & Hall: London, 1997.

average vs volume average).^{58,59} As for the shell thicknesses, the TEM values follow a trend similar to the effective thickness.

To further evaluate the structure of the particles, a detailed EELS study was carried out by indirectly evaluating the Mn oxidation state from the Mn/O ratio, the Mn-L₃ onset, and the Mn-L₃/L₂ intensity ratios. Importantly, data obtained for different particles belonging to the same sample showed no relevant differences. The dependence of the Mn-L₃/L₂ ratio on the position for the four samples, M1–M4, is given in Figure 3c. For all the analyzed nanoparticles a MnO core is observed and its radius increases from M4 to M1 (see the solid lines at the bottom of Figure 3c), in agreement with TEM and neutron diffraction analyses shown in Table 1. Note that when an EELS signal is obtained from the center of a nanoparticle, the signal arises from both the core and the enveloping shell, making it thereby impossible to obtain the Mn-L₃/L₂ values reported in the literature for MnO.^{49,54} However, a quantitative simulation taking into account the core–shell structure confirms the MnO character of the core. Concerning the shell part, the L₃/L₂ values for M4 almost reach those corresponding to a Mn³⁺ oxidation state indicating a Mn₂O₃ structure, in agreement with the neutron diffraction results. A noticeable increase of the L₃/L₂ values toward the value for a Mn²⁺ oxidation state can be observed for the rest of the samples, thus indicating the presence of Mn₃O₄ in the shell for the larger particles (M1–M3). Additionally, a very thin (less than 1 nm) MnO superficial layer was observed in all the studied particles. The origin of this effect is unclear. It could be attributed to either an artifact resulting from the reduction of some outer Mn³⁺ ions to Mn²⁺ by the electron beam,⁶⁰ although it is not possible to rule out an increase of the reducing power of the surfactant due to some external parameters (e.g., electron or neutron beams).

Magnetic Properties. From the low-temperature neutron diffraction pattern (curve a in Figure 1 and Figure S1 for M2 and M4, respectively) it is found that for all samples the MnO cores exhibit the expected AFM structure observed in the bulk.⁶¹ However, for sample M4, the γ -Mn₂O₃ shell has a simple Néel type FiM structure³⁵ rather than the more complex structure observed in Mn₃O₄ (see Figure S2b in the Supporting Information).⁶² For samples M1–M3, due to the large MnO scattering caused by the large core/shell volume ratio, no magnetic signal from the shell can be detected within the limits of our accuracy (about 0.5 μ_B) (see Figure S2a).

Remarkably, T_N of the nanoparticles appears to be higher than that in the bulk and increases for smaller MnO cores. To further confirm this T_N enhancement, the temperature dependence of the neutron diffraction pattern was analyzed in detail. In Figure 4a the magnetic moment derived from the temperature dependence of the integral intensity of the ($1/2, 1/2, 1/2$) magnetic reflection of MnO is shown for sample M2. The value of the magnetic moment in saturation was defined from the profile analysis of the pattern measured at 10 K. In this calculation we used the known magnetic order for MnO, observed in the bulk as well as in “restricted geometry”,^{63,64} taking into account the

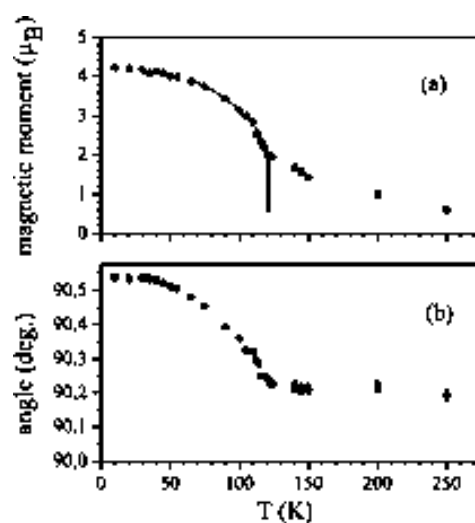


Figure 4. (a) Temperature dependence of the magnetic moment/ion in the MnO core for sample M2. The solid lines correspond to a fit with a power law. (b) Temperature dependence of the angle of trigonal distortion.

Table 2. Summary of the Effective Néel Temperature and Sublattice Magnetization for the MnO Core, M_{MnO}

| sample | T_N (K) | M_{MnO} (μ_B) |
|--------|-----------|-----------------------|
| M1 | 123(1) | 4.25(7) |
| M2 | 120.9(2) | 4.21(2) |
| M3 | 126.0(2) | 3.83(8) |
| M4 | 139(10) | 4.3(5) |

trigonal distortion due to magnetostriction⁶⁵ shown in Figure 4b. As expected, the value of the saturated magnetic moment appears smaller than the 5 μ_B for the free Mn²⁺ ion (see Table 2). This is a known effect and is readily explained by the spin disordering at the core surface (i.e., at the interface in our case),⁶³ although some spin canting in the core⁶⁶ or partial oxidation of the Mn ions cannot be ruled out. Assuming the temperature dependence of the magnetic moment follows a power law in the temperature range of the main drop of magnetic moment (note the “tail” in m for higher temperatures), the effective Néel temperature of the MnO cores was evaluated as 120.9(2) K for M2 (Figure 4a). Similar analyses for the other samples lead to $T_N = 120.9(2)$ –139(10) for M1–M4 (see Figure 5 and Table 2). Note that a T_N enhancement has been also observed in MnO confined in different porous templates^{63,64} (see Figure 5) and in other manganese oxides,^{67,68} although it is not present in MnF₂ films.⁶⁹ The origin of this effect has been proposed to arise from size and surface effects, where the broken symmetry at the surface and the concomitant local disorder may lead to (i) enhancement of the exchange interaction between surface atoms with respect to bulk exchange interactions⁷⁰ and (ii) variations in the crystal field resulting in high-spin–low-spin

(59) Chen, D. X.; Sanchez, A.; Taboada, E.; Roig, A.; Sun, N.; Gu, H. C. *J. Appl. Phys.* **2009**, *105*, 083924.

(60) Pan, Y.; Sader, K.; Powell, J. J.; Bleloch, A.; Gass, M.; Trinick, J.; Warley, A.; Brydson, A. L.; Brown, A. *J. Struct. Biol.* **2009**, *166*, 22–31.

(61) Roth, W. L. *Phys. Rev.* **1958**, *110*, 1333–1341.

(62) Jensen, G. B.; Nielsen, O. V. *J. Phys. C* **1974**, *7*, 409–424.

(63) Golosovsky, I. V.; Mirebeau, I.; André, G.; Kurdyukov, D. A.; Kumzerov, Y. A.; Vakhrushev, S. B. *Phys. Rev. Lett.* **2001**, *86*, 5783–1786.

(64) Golosovsky, I. V.; Mirebeau, I.; Sakhnenko, V. P.; Kurdyukov, D. A.; Kumzerov, Y. A. *Phys. Rev. B* **2005**, *72*, 144409.

(65) Lines, M. E.; Jones, E. D. *Phys. Rev.* **1965**, *113*, A1313.

(66) Theil Kuhn, L.; Bojesen, A.; Timmermann, L.; Meedom Nielsen, M.; Mørup, S. *J. Phys.: Condens. Matter* **2002**, *14*, 13551–13567.

(67) Tang, Z. X.; Sorensen, C. M.; Klabunde, K. J.; Hadjipanayis, G. C. *Phys. Rev. Lett.* **1991**, *67*, 3602–3605.

(68) Yang, A.; Chinnasamy, C. N.; Greneche, J. M.; Chen, Y. J.; Yoon, S. D.; Chen, Z. H.; Hsu, K. L.; Cai, Z. H.; Ziemer, K.; Vittoria, C.; Harris, V. G. *Nanotechnology* **2009**, *20*, 185704.

(69) Golosovsky, I. V.; Sokolov, N. S.; Gukasov, A.; Bataille, A.; Boehm, M.; Nogués, J. *J. Magn. Magn. Mater.* **2010**, *322*, 664–667.

(70) Wesselinowa, J. M. *J. Magn. Magn. Mater.* **2010**, *322*, 234–237.

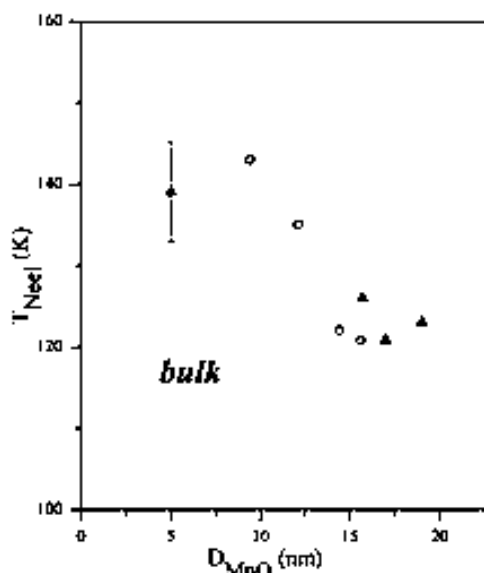


Figure 5. Dependence of the Néel temperature, effective T_N , for the MnO cores in the core/shell nanoparticles (triangles) and MnO nanoparticles embedded within porous glass (circles)⁷³ on the core size D_{MnO} .

transitions⁷¹ and/or the appearance of new degrees of freedom which interact with the AFM order parameter.⁶⁴ Moreover, other effects such as the observed size dependence of the lattice parameter may also play a role.⁷²

Remarkably, as can be seen in Figure 4a for sample M2, with a thin passivation shell, the observed antiferromagnetic order in MnO does not vanish at the Néel temperature and persists up to room temperature, where the sublattice magnetization of MnO exhibits a “tail” up to high temperatures rather than vanishing above T_N .

Interestingly, the averaged diameter of the magnetic domains in the MnO core calculated from the broadening of the antiferromagnetic peak appears to be significantly smaller than the core diameter: 6.7(5) vs 17.0(5) nm (M2) and 9(1) vs 19(2) nm (M1). Note that due to peak overlapping the magnetic size could only be determined for samples M1 and M2. Similar domain size effects were observed in MnO nanoparticles embedded within different porous media.^{63,64} In Figure 6 the temperature dependence of the full width at half-maximum (fwhm) of the MnO ($1/2, 1/2, 1/2$) magnetic reflection and volume average domain diameter are shown for M2. It is seen that the diameter drastically changes with temperature, reaching a minimum at temperatures well above $T_N = 120.9$ K. The results resemble a fragmentation of the magnetic domains observed in first-order transitions. However, due to size effects there should be a continuous magnetic transition,^{74,75} in contrast to the bulk first-order transition.⁶¹ In fact, the magnetic domain fragmentation may explain the large “tail” in the temperature dependence of the magnetic moment (Figure 4a), since smaller MnO entities have larger T_N values. Although some of these effects could be

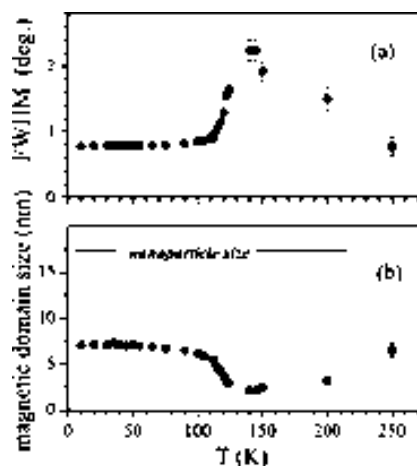


Figure 6. (a) Temperature dependence of the fwhm of the MnO ($1/2, 1/2, 1/2$) magnetic reflection for sample M2. (b) Size (averaged diameter) of the magnetic domain deduced from the peak broadening.

partially explained by the concomitant particle size distribution, they are exceedingly large to arise solely from this effect.

Shown in Figure 7 are the hysteresis loops of the samples at 10 K after field cooling in 20 kOe from 200 K. The saturation magnetization, M_S (obtained by using the total mass), is different for each sample. Using the TEM values for the particle size and the shell thickness and assuming that the MnO core does not contribute to M_S , we can estimate the saturation magnetization of the shell. Despite the crude approximations the M_S values are rather consistent with $M_S \approx 32.0$ – 37.7 emu/g for M1–M3 and are slightly smaller for M4, $M_S \approx 27$ emu/g. These results are consistent with saturation magnetization for bulk Mn_3O_4 ($M_S \approx 38$ emu/g)⁷⁶ and γ - Mn_2O_3 nanoparticles ($M_S \approx 28$ emu/g).⁷⁷

All the loops exhibit a large coercivity, H_C (see Figure 7), which is consistent with the rather large anisotropy of the γ - Mn_2O_3 or Mn_3O_4 phases.^{77–80} Moreover, the coercivity is influenced by the coupling to the AFM core,⁶ where the smallest core gives rise to the largest coercivity, in agreement with previous reports.³⁴ Moreover, as expected,^{34,36,37} all the samples exhibit a loop shift along the field axis (exchange bias, H_E), evidencing the exchange coupling between the AFM core and the FiM shell.⁶ The nonmonotonic dependence of H_E with the MnO core size (see Figure 7) is consistent with earlier results in the same system,³⁴ characterized by its inverse, $T_N > T_C$, magnetic structure.^{81,82}

The temperature dependence of the FC and ZFC magnetization measured with $H = 50$ Oe (Figure 8) reveals that all the samples exhibit their main magnetic features below $T \approx 50$ K, consistent with the known Curie temperature, $T_C = 39$ and 42 K, of the γ - Mn_2O_3 and Mn_3O_4 phases, respectively.^{77,80,83} Thus, the magnetization is largely dominated by the ferrimagnetic counterpart. Interestingly, it can be seen that the ZFC branch of samples M1–M3 exhibits fine structure below $T_C \approx 42$ K

(71) Morales, M. A.; Skomski, R.; Fritz, S.; Shelburne, G.; Shiled, J. E.; Yin, M.; O'Brien, S.; Leslie-Pelecky, D. L. *Phys. Rev. B* **2007**, *75*, 134423.
 (72) Kantor, I.; Dubrovinsky, L.; McCammon, C.; Dubrovinskaja, L.; Goncharenko, I.; Kantor, A.; Kuznetsov, A.; Crichton, W. *Phase Trans.* **2007**, *80*, 1151–1167.
 (73) Golosovsky, I. V. Private communication.
 (74) Imry, Y. *Phys. Rev. B* **1980**, *21*, 2042–2043.
 (75) Challa, M. S. S.; Landau, D. P.; Binder, K. *Phys. Rev. B* **1986**, *34*, 1841–1852.

(76) Jacobs, I. S. *J. Phys. Chem. Solids* **1959**, *11*, 1–11.
 (77) Kim, S. H.; Choi, B. J.; Lee, G. H.; Oh, S. J.; Kim, B.; Choi, H. C.; Park, J.; Chang, Y. *J. Korean Phys. Soc.* **2005**, *46*, 941–944.
 (78) Dwight, K.; Menyuk, N. *Phys. Rev.* **1960**, *119*, 1470–1479.
 (79) Du, C. S.; Yun, J. D.; Dumas, R. K.; Yuan, X. Y.; Liu, K.; Browning, N. D.; Pan, N. *Acta Mater.* **2008**, *56*, 3516–3522.
 (80) Tackett, R.; Lawes, G.; Melot, B. C.; Grossman, M.; Toberer, E. S.; Seshadri, R. *Phys. Rev. B* **2007**, *76*, 024409.
 (81) Cai, J. W.; Liu, K.; Chien, C. L. *Phys. Rev. B* **1999**, *60*, 72–75.
 (82) Nogués, J.; Schuller, I. K. *J. Magn. Magn. Mater.* **1999**, *192*, 203–232.
 (83) Srinivasan, G.; Seehra, M. S. *Phys. Rev. B* **1983**, *28*, 1–7.

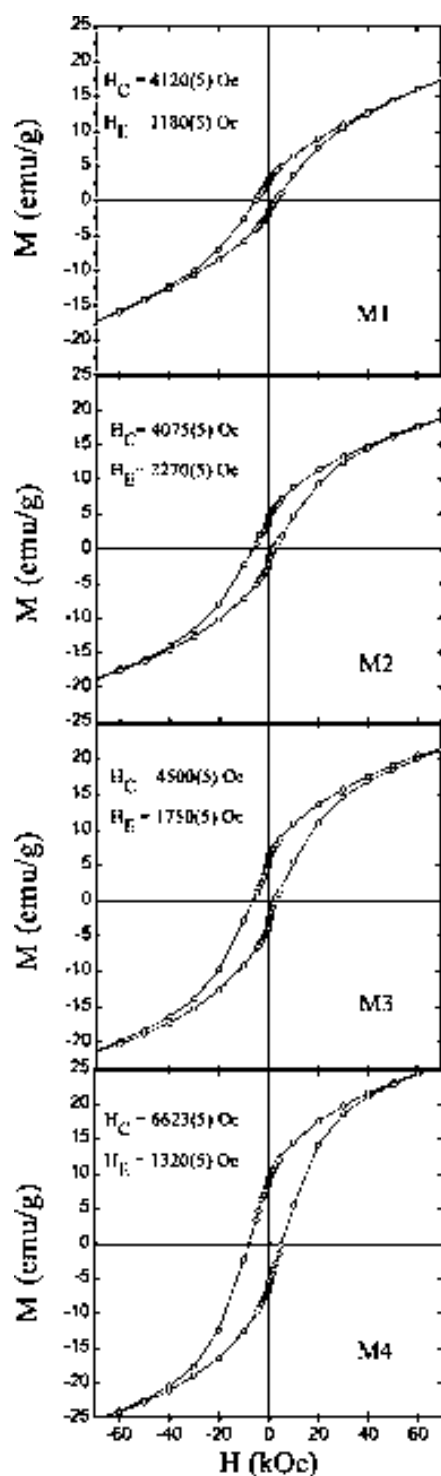


Figure 7. Hysteresis loops for samples M1–M4 at $T = 10$ K after field cooling from $T = 200$ K in $H_{FC} = 20$ kOe. The values of H_E and H_C are indicated in the respective panels.

and there is a hump at $T \approx 33$ K and a second anomaly at $T \approx 20$ K. In contrast, for sample M4 both the FC and ZFC curves are featureless.

To gain further insight into the nature of the low-temperature anomalies, ac susceptibility measurements were carried out. Figure 9 shows the real (χ') and imaginary (χ'') components of the ac susceptibility measured at different frequencies from 10 Hz to 10 kHz on applying an ac field of 10 Oe. The larger nanoparticles present anomalies in χ' and χ'' at 41, 36, and 20 K. These anomalies are frequency independent, implying that

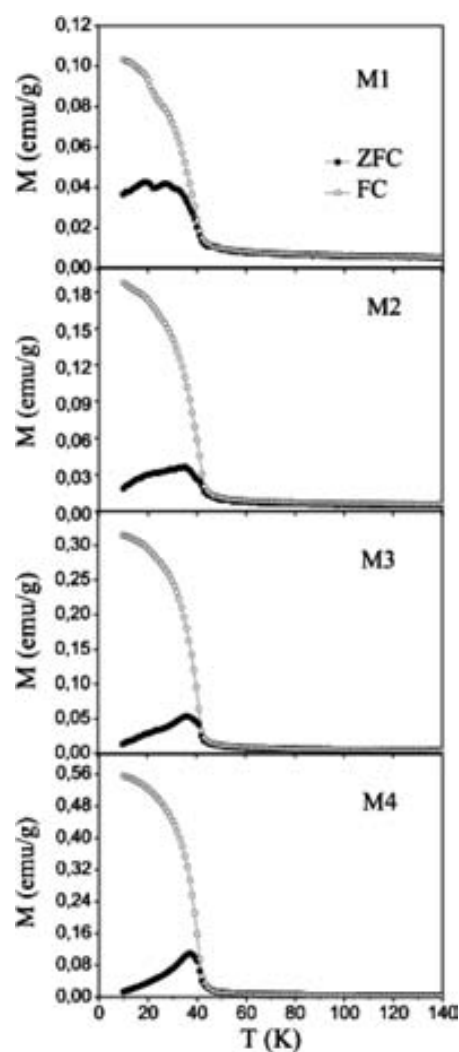


Figure 8. Temperature dependence of the field cooled (FC) and zero field cooled (ZFC) magnetizations for samples M1–M4 measured in $H = 50$ Oe.

they are thermodynamic transitions rather than blocking temperatures. The transition temperatures are consistent with the reported $T_C = 42$ K and the reorientation transitions of Mn_3O_4 ($T_{RO} = 39$ K and $T_{RO}^* = 33$ K).⁶² For M4, instead, the ac susceptibility exhibits a single transition, as was also observed in the $M(T)$ dc magnetization curve. This result is not consistent with the magnetic behavior of the Mn_3O_4 phase, in agreement with neutron diffraction and EELS results which indicate that the M4 shell is solely formed by $\gamma\text{-Mn}_2\text{O}_3$. The experimental results suggest the following picture for the systems: the nanoparticles present a core/shell structure with AFM MnO core and a FiM shell that changes its composition ($\gamma\text{-Mn}_2\text{O}_3$ and/or Mn_3O_4) depending on the nanoparticle size, as shown schematically in Figure 2f.

Electron Spin Resonance. In order to quantify the core/shell composition, we also performed an ESR spectroscopy study. Figure 10 shows representative ESR spectra for temperatures above and below T_N for M1–M4. Above T_N the spectra exhibit two resonance lines, one narrow and one broad, both centered at around $H_r = 3370$ Oe. This corresponds to a gyromagnetic factor of $g \approx 2.00$, which is consistent with the values reported in the literature ($g = 2.02\text{--}2.00$ for Mn_3O_4 ^{84,85} and $g = 1.997\text{--}2.001$ for MnO ^{86–88}). When the temperature decreases, ΔH increases for the broad signal, and at $T \approx 120$ K it is no

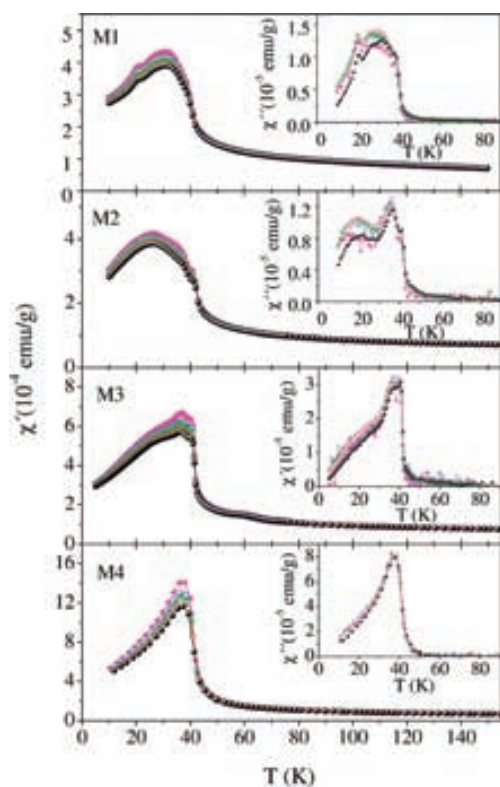


Figure 9. Temperature dependence of in-phase (χ') and out-of-phase (χ'') ac susceptibilities for samples M1–M4 measured at different frequencies: (▲) 80 Hz; (□) 600 Hz; (★) 1250 Hz; (○) 5000 Hz; (●) 10 000 Hz.

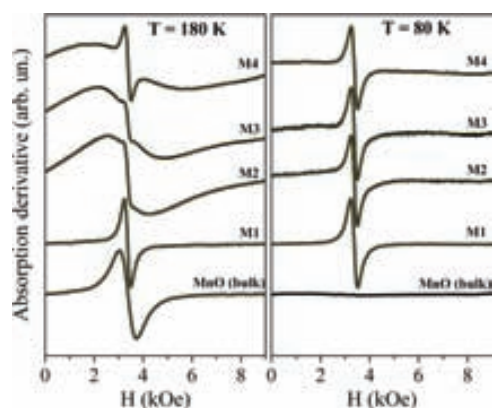


Figure 10. ESR spectra for the four samples M1–M4 and bulk MnO above and below T_N . The dotted line corresponds to the fitting curve (color on line). Note that for sample M1 the main ESR line corresponds to the shell resonance which remains below T_N .

longer detected. The narrow signal, instead, is observed in the entire measured temperature range and presents a nonmonotonic temperature evolution.

It is known that below the AFM transition temperature, because of the large anisotropy and exchange fields present, the spin equilibrium state changes and the AFM resonance modes cannot be excited. Therefore, T_N is usually determined

- (84) Seehra, M. S.; Srinivasan, G. *J. Appl. Phys.* **1982**, *52*, 8345–8347.
 (85) Winkler, E.; Zysler, R. D.; Fiorani, D. *Phys. Rev. B* **2004**, *70*, 174406.
 (86) Dormann, E.; Jaccarino, V. *Phys. Lett.* **1974**, *48A*, 81–82.
 (87) Ferrante, R. F.; Wilkerson, J. L.; Graham, W. R. M.; Weltne, W., Jr. *J. Chem. Phys.* **1977**, *67*, 5904–5913.
 (88) Golosovsky, I. V.; Arcon, D.; Jaglicic, Z.; Cevc, P.; Sakhnenko, V. P.; Kurdyukov, D. A.; Kumzerov, Y. A. *Phys. Rev. B* **2005**, *72*, 144410.

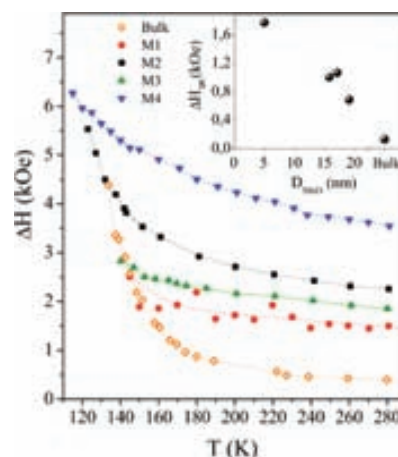


Figure 11. Temperature dependence of the ESR line width, ΔH , corresponding to the MnO core phase for samples M1–M4. For comparison, the parameters corresponding to the MnO bulk phase are also included. The inset shows the evolution of ΔH_∞ with the MnO core size.

by the disappearance of the ESR spectrum.⁸⁹ This behavior is reproduced by the AFM MnO pure phase, as was reported by several authors.^{86–88} This fact allowed us to identify the broad ESR resonance as coming from the AFM MnO (core) phase, while the narrow line is assigned to the shell phase, as will be explained later.

In order to quantify and extract reliable ESR parameters, we fitted the total spectral signal with two Lorentzian lines centered at $g \approx 2$. Figure 10 shows the ESR spectra with the corresponding fitting curve. For comparison the resonance signal of the MnO bulk sample is also included. Observe that all the samples present the same qualitative behavior: two resonance lines for $T > T_N$, where the relative intensities are different for each M1–M4 system, and a narrow resonance for $T < T_N$. Apart from the main narrow resonance, below $T \approx 40$ K a second broad low-field resonance was also observed in a small temperature range. This line shifts toward zero field, and at $T \approx 27$ K it is no longer detected. A low-field resonance with identical temperature and field behavior is present in the Mn_3O_4 pure oxide.^{84,85} This resonance is attributed to the FiM resonance of ordered magnetic domains at different orientation respect to the magnetic field.⁸⁴

The temperature dependence of ΔH obtained from the fitting curves for the core and the shell components are shown in Figures 11 and 12a. The ESR parameters for bulk MnO (Figure 11) and Mn_3O_4 (inset Figure 12a) are also included as reference. From Figure 11 it is manifested that the line width of the MnO core decreases when the size of the particle increases. At room temperature $\Delta H \approx 3500$ Oe for M4 and approaches the bulk value $\Delta H \approx 400$ Oe for larger sizes. The line width depends on the magnetization relaxation mechanism. In the paramagnetic range the following dependence was established: $\Delta H = C/(T\chi(T))\Delta H_\infty$,^{86,90,91} where C is the Curie constant and ΔH_∞ is the value reached by ΔH at high temperature. Assuming that the susceptibility follows a Curie–Weiss dependence with a Curie–Weiss temperature $\Theta \approx -600$ K, we have estimated ΔH_∞ as a function of the core particle size. From the inset of Figure 11 it is evident that ΔH_∞ increases, from the bulk value,

- (89) Huber, D. L.; Alejandro, G.; Caneiro, A.; Causa, M. T.; Prado, F.; Tovar, M.; Oseroff, S. B. *Phys. Rev. B* **1999**, *60*, 12155–12161.
 (90) Causa, M. T.; et al. *Phys. Rev. B* **1998**, *58*, 3233–3239.
 (91) Huber, D. L. *J. Phys. Chem. Solids* **1971**, *32*, 2145–2149.

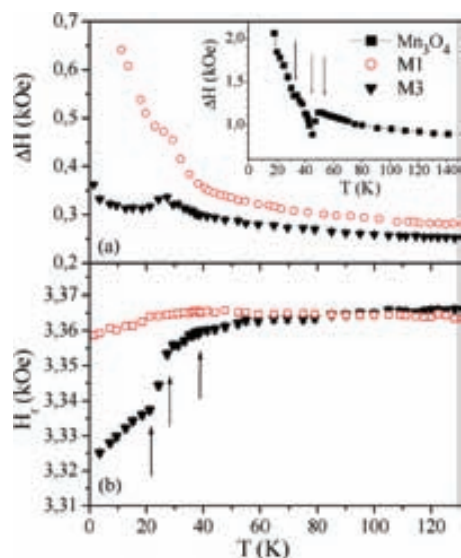


Figure 12. (a) Temperature dependence of the ESR line width, ΔH , corresponding to the Mn_3O_4 phase of the samples M1 and M3. For comparison, the measured parameters of the isolated Mn_3O_4 phase are also included in the inset. (b) Temperature dependence of the resonance field, H_r , for samples M1 and M3. The magnetic transitions are indicated by arrows.

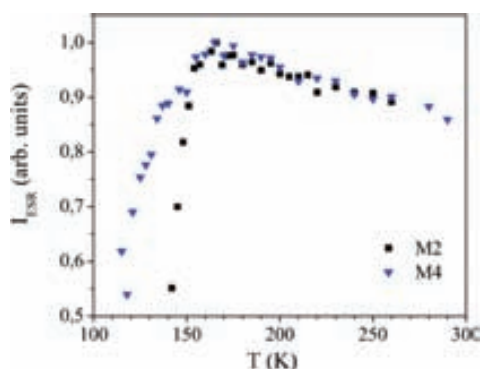


Figure 13. Temperature dependence of the ESR intensity of MnO, I_{ESR} , for samples M2 and M4.

by an order of magnitude when the size is reduced. The parameter ΔH_∞ is proportional to E_a^2/E_{ex} , where E_a and E_{ex} are the anisotropy and exchange interaction energies, respectively. When the particle size is reduced, E_{ex} should not be affected, in a first approximation, since it mainly originates from nearest neighbor interactions.⁹² Therefore, the increase of ΔH_∞ implies a core magnetic anisotropy enhancement (by a factor of ~ 3) when the size diminishes, as is observed for pure MnO nanoparticles,^{71,88} probably related to surface or interface effects.^{5,6,71} Note that the magnetization loops and the ESR experiment provide complementary information about the magnetic anisotropy; while in the first experiment the shell anisotropy is more significant, the ESR line width can sense the core anisotropy as a function of the size.

Figure 13 shows the temperature dependence of I_{ESR} for the MnO phase obtained from the fitting. As expected for an AFM compound, the ESR intensity decreases to zero at the ordering temperature. As can be observed, the AFM core transition is broad and the onset is located at $T \approx 150$ K. This result points

Table 3. Relative Concentration of Mn^{2+} in MnO and Mn_3O_4 Phase Obtained from the ESR Spectra^a

| sample | Mn^{2+} core | Mn^{2+} shell | $V_{\text{Mn}_3\text{O}_4}/V_{\text{shell}}$ |
|--------|-----------------------|------------------------|--|
| M1 | 0.82(2) | 0.18(2) | 1 |
| M2 | 0.985(3) | 0.011(3) | 0.1 |
| M3 | 0.960(4) | 0.032(3) | 0.1 |
| M4 | 0.995(1) | 0.005(1) | 0.005 |

^a From D_{tot} and D_{MnO} obtained by TEM, the shell ratio $V_{\text{Mn}_3\text{O}_4}/V_{\text{shell}}$ is estimated and included in the last column.

out the presence of AFM short-range interaction well above the bulk T_N , in agreement with neutron diffraction results. Moreover, the broad I_{ESR} curve correlates with the tails in the MnO sublattice magnetization (and the domain fragmentation) observed by neutron diffraction.

In order to analyze the behavior of the narrow ESR line due to the shell, we show the ΔH temperature dependence of the Mn_3O_4 pure phase in the inset of Figure 12a, where several anomalies as a function of the temperature can be observed. These anomalies correspond to the FiM transition at $T_C = 42$ K and the spin reorientation transitions at 39 and 33 K.⁸⁴ These particular ΔH features are also reproduced by the narrow resonance signal observed in samples M1–M4, which enables us to identify this line as coming from the Mn_3O_4 phase. The temperature dependence of H_r also presents anomalies at similar temperatures. As can be observed in Figure 12b, H_r shifts toward lower values near T_C and shows anomalies at $T \approx 30$ and 20 K. These features are consistent with the results reported on Mn_3O_4 ,⁸⁴ hence corroborating that the low-temperature features found in the ac and dc susceptibility originate at the shell. The temperature dependence of the resonance field is explained by the presence of an effective anisotropy field (H_a) below T_C , which modifies the resonance condition $h\nu = g\mu_B(H_r + H_a)$.⁹³

It is important to remark that the ground energy state of the Mn^{2+} ion corresponds to an orbital singlet $L = 0$; then the coupling with the lattice is very weak, and as a consequence the ESR line width is narrow and easily observed. On the other hand, the orbital degeneracy of the Mn^{3+} ion ground state ($3d^4$, $L = 2$) is not completely removed and presents important spin–orbit interaction; as a consequence Mn^{3+} usually does not show an ESR signal.⁹⁴ Therefore, it can be concluded that the narrow ESR line corresponds to the resonance of Mn^{2+} of the spinel Mn_3O_4 , while the resonance of Mn^{3+} could not be detected. This conclusion is supported by several reported results on manganese oxides.^{95,96} In these references, by thermal or chemical treatment, the valence of the manganese ions changes from Mn^{3+} to Mn^{2+} ; as a consequence the ESR signal increases proportionally to the fraction of ions that are reduced from Mn^{3+} to Mn^{2+} . Moreover, this is also the reason why the γ - Mn_2O_3 phase, where all the manganese ions are Mn^{3+} , does not present a detectable ESR signal.

From the I_{ESR} values obtained from the fit for the narrow and broad signals (for $T \gg T_C$, T_N), the relative concentrations of Mn^{2+} ions of the MnO and Mn_3O_4 phases for each sample are calculated. The results are presented in Table 3. From this quantification it became evident that the overall concentration

(92) Tobia, D.; Winkler, E.; Zysler, R. D.; Granada, M.; Troiani, H. E. *Phys. Rev. B* **2008**, *78*, 104412.

(93) Morrish, A. H., *The Physical Principles of Magnetism*; Wiley-IEEE Press: New York, 2001.

(94) Abragam, A.; Bleaney, B. *Electron Paramagnetic Resonance of Transition Ions*; Dover Publications: New York, 1986.

(95) Zhang, W.; Yang, Z.; Liu, Y.; Tang, S.; Han, X.; Chen, M. *J. Cryst. Growth* **2004**, *263*, 394–399.

(96) Kijlstra, W. S.; Poels, E. K.; Blik, B. M.; Weckhuysen, B. M.; Schoonheydt, R. A. *J. Phys. Chem. B* **1997**, *101*, 309–316.

of the Mn_3O_4 diminishes when the nanoparticle size decreases. From the D_{tot} and D_{MnO} values obtained by TEM (Table 1) for M1–M4, we can estimate the Mn_3O_4 relative volume with respect to the total volume of the shell. These data are included in the last column of Table 3. These results indicate that the surface passivation of the MnO nanoparticles depends on the size of the particles. Larger particles tend to form Mn_3O_4 shells, while the smaller particles have $\gamma\text{-Mn}_2\text{O}_3$ shells consistent with neutron diffraction, EELS, and magnetic results. This fact can be understood from the Catlow and Fender model.^{36,37,97} This model takes into account that the usual defects present in MnO are Mn vacancies, which are compensated by the oxidation of the manganese ion to Mn^{3+} . Therefore, the larger nanoparticles tend to form Mn_3O_4 at the surface. When the nanoparticle size is reduced, the density of defects increases, as was observed by neutron diffraction; consequently, $\gamma\text{-Mn}_2\text{O}_3$, where all the manganese ions are Mn^{3+} , will be the more stable shell phase.

Conclusions

In conclusion, we have studied the structural and magnetic properties of bimagnetic core/shell nanoparticles. We found that the nanoparticles present an AFM MnO core and an FiM surface shell. The shell composition depends on the nanoparticle size, the larger nanoparticles presenting mainly Mn_3O_4 ; however, when the size diminishes, the density of defects increases and as a consequence $\gamma\text{-Mn}_2\text{O}_3$ (where all the manganese ions are Mn^{3+}) is the more stable shell phase. The systems exhibit exchange coupling between the core and the shell manifested

by the exchange bias field and the large coercivity. Although the exchange field is strongly dependent on the magnetic anisotropy of the AFM core, we have observed (from the size dependence of the ESR line width) that while the magnetic anisotropy of the MnO core shows a smooth increase when the size is reduced, H_{ex} shows a nonmonotonic behavior. From neutron diffraction we have observed that the Néel temperature of the MnO core is substantially enhanced and that MnO presents an enhanced stability above T_{N} . The continuous magnetic phase transition in the AFM core is accompanied by the fragmentation–separation of the magnetic domains in smaller parts.

Acknowledgment. The work was supported by Spanish MICINN grants (Nos. MAT2007-66309-C02 and CSD2006-00012 Consolider-Ingenio 2010), the Catalan DGR (No. 2009-SGR-1292), the Institut Catala de Nanotecnologia, the European Union through the ONDA project (No. FP7-PEOPLE-2009-IRSES-247518), the Russian Foundation for Basic Researches (Grants N07-02-00608, N10-02-00576), CONICET Argentina PIP 5250/03, and UNC No. 882/07. We thank the ILL for the provision of neutron beam time. M.D.B. was partially supported by an ICREA ACADEMIA award. A.L.-O. acknowledges his FPI fellowship from the Spanish MICINN.

Supporting Information Available: Text giving the complete ref 88 and supplementary figures. This material is available free of charge via the Internet at <http://pubs.acs.org>.

(97) Catlow, C. R. A.; Fender, B. E. F. *J. Phys. C* **1975**, *8*, 3267–3279.

SUPPORTING INFORMATION

Size dependent passivation shell and magnetic properties in antiferromagnetic/ferrimagnetic, core/shell, MnO nanoparticles

Alberto López-Ortega,[†] Dina Tobia,[‡] Elin Winkler,[‡] Igor V. Golosovsky,[¶] German Salazar-Alvarez,^{†,§} Sònia Estradé,^{||} Marta Estrader,^{*,†} Jordi Sort,^{⊥,#} Miguel Angel González,[@] Santiago Suriñach,[#] Jordi Arbiol,^{⊥,△} Francesca Peiró,^{||} Roberto D. Zysler,[‡] Maria Dolors Baró,[#] and Josep Nogués^{⊥,†}

Centre d'Investigació en Nanociència i Nanotecnologia (ICN-CSIC), Campus Universitat Autònoma de Barcelona, E-08193 Bellaterra, Spain, Centro Atómico Bariloche, CNEA-CONICET, 8400 S.C. de Bariloche, Río Negro, Argentina, St. Petersburg Nuclear Physics Institute, 188300, Gatchina, St. Petersburg, Russia., Department of Materials and Environmental Chemistry, Stockholm University, S-10691 Stockholm, Sweden, MIND-IN2UB, Departament d'Electrònica, Universitat de Barcelona, Martí i Franquès 1, E-08028 Barcelona, Spain, Institució Catalana de Recerca i Estudis Avançats (ICREA), Barcelona, Spain, Departament de Física, Universitat Autònoma de Barcelona, E-08193 Bellaterra, Spain, Institut Laue Langevin, 6 rue Jules Horowitz, BP 156, F-38042 Grenoble, France, and Institut de Ciència de Materials de Barcelona (CSIC), Campus Universitat Autònoma de Barcelona, E-08193 Bellaterra, Spain

E-mail: marta.estrader.icn@uab.cat

Results and discussion.

Structural and morphological characterization

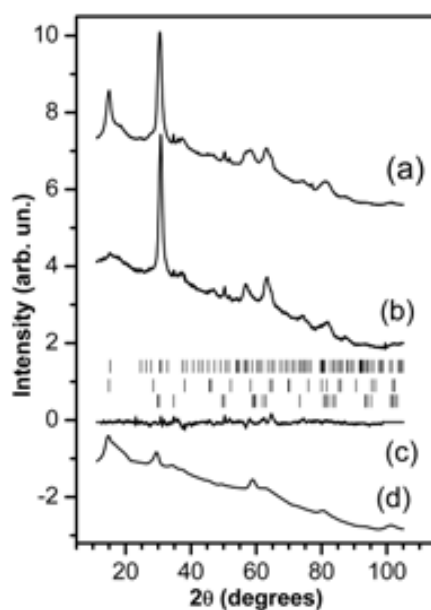


Figure S1: (a) and (b) Neutron diffraction patterns measured at 20 K and 250 K, respectively, for sample M4. The diffuse peak at low angles is caused by residues from synthesis. (c) Difference between the calculated profile and the measured pattern at 250 K. (d) Calculated pattern from the core MnO at low temperatures, showing its contribution to the total patterns (a) and (b). The stripes mark the positions of the Bragg reflections from bottom to top: MnO-core nuclear, γ -Mn₂O₃-shell (magnetic and nuclear reflections are partially overlapping) and MnO-core magnetic reflections, respectively.

*To whom correspondence should be addressed

†ICN-CSIC

‡CA Bariloche

¶PNPI

§Stockholm Univ.

||MIND-IN2UB

⊥ICREA

#UAB

@ILL

△ICMAB

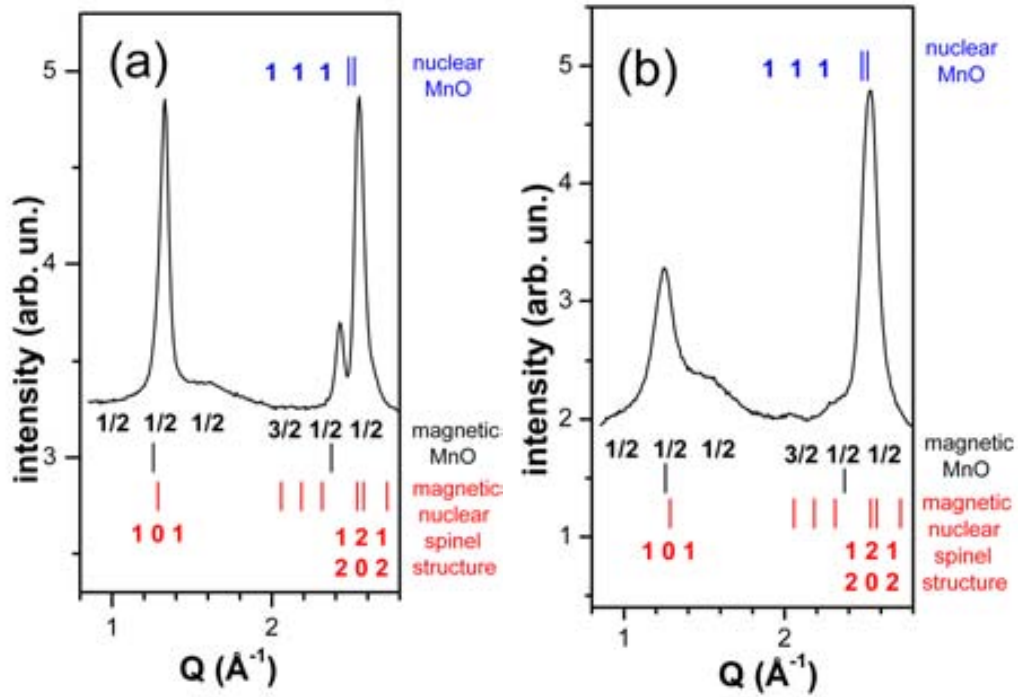


Figure S2: (a) and (b) Enlarged low temperature neutron diffraction pattern, at low q , for samples M2 and M4, respectively. The position of the magnetic (black) and nuclear (blue) peaks for MnO and the magnetic and nuclear reflections (partially overlapping) for the spinel structure of the shell (red) are also shown.

Complete Ref. 88

Causa, M.T.; Tovar, M.; Caneiro, A.; Prado, F.; Ibañez, G.; Ramos, A.; Butera, A.; Alascio, B.; Obradors, X.; Piñol, S.; Rivadulla, F.; Vázquez-Vázquez, C.; López-Quintela, M.A.; Rivas, J.; Tokura, Y.; Oseroff, S.B. *Phys. Rev B* **1998**, *58*, 3233-3239.



6.2 Soft-FiM|hard-FiM Fe₃O₄-core|Mn₃O₄-shell nanoparticles

In this section are presented the synthesis of different poly-magnetic heterostructures based manganese and iron oxides in CS and onion-like architectures.

Article #3 tackles the synthesis of two- (CS), three- and four-components onion-like nanoparticles based in the use of pre-made two-components, i.e. CS, iron oxide nanoparticles of an AFM FeO core and FiM Fe₃O₄ shell, for the subsequent deposition of a manganese oxide shell to yield the formation of a thin layer of FiM Mn₃O₄, i.e. three-component FeO|Fe₃O₄|Mn₃O₄, or thicker AFM MnO shell and its controlled passivation to form a thin Mn₃O₄ outer shell, i.e., four-components FeO|Fe₃O₄|MnO|Mn₃O₄. Their structural and magnetic characterization have been carried out in order to understand the growth mechanism of the manganese oxide layers and the magnetic properties.

In addition, in Article #4 the study of the structural and magnetic properties of a related bi-magnetic CS structure based on soft-FiM|hard-FiM core-Mn_xFe_{3-x}O₄|shell-Fe_xMn_{3-x}O₄ nanoparticles have been performed. Interestingly, this system is based on two dissimilar FiM materials, with a soft-FiM core and a hard-FiM shell. In addition, the samples present a rather novel architecture with an inverted core(soft-FiM)|shell(hard-FiM), in contrast to the conventional hard|soft structures. This system presents a strong exchange coupling between both FiM layers leading to a simultaneous reversal of the core and the shell, i.e., single-phase-like switching, with increased saturation magnetization and decreased coercivity with respect to a pure Mn₃O₄ case. This effect can be understood due to the small size of the constituents, being smaller than the domain wall width.

Article #3

Title: Two-, Three-, and Four-Component Magnetic Multilayer Onion Nanoparticles Based on Iron Oxides and Manganese Oxides

Authors: G. Salazar-Alvarez, H. Lidbaum, A. López-Ortega, M. Estrader, K. Leifer, J. Sort, S. Suriñach, M. D. Baró and J. Nogués

Journal: Journal of the American Chemical Society

Article #4

Title: Strongly exchange coupled inverse ferrimagnetic soft|hard, $\text{Mn}_x\text{Fe}_{3-x}\text{O}_4|\text{Fe}_x\text{Mn}_{3-x}\text{O}_4$, core|shell heterostructured nanoparticles

Authors: A. López-Ortega, M. Estrader, G. Salazar-Alvarez, S. Estradé, I. V. Golosovský, R. K. Dumas, D. J. Keavney, M. Vasilakaki, K. N. Trohidou, J. Sort, F. Peiró, S. Suriñach, M. D. Baró and J. Nogués

Journal: Nanoscale

6.2.1 Article #3: Two-, three-, and four-component magnetic multilayer onion nanoparticles based on iron oxides and manganese oxides

The synthesis design and growth mechanism of the two-, three- and four-component onion-like nanoparticles based on magnetic manganese and iron oxides were developed in this article. Firstly, the synthesis of the two-components, CS nanoparticles, of core-FeO|shell-Fe₃O₄ system is described. The formation of this CS structure is based on the synthesis of FeO nanoparticles and the posterior controlled shell passivation to form Fe₃O₄. Magnetically this system is composed by an AFM FeO core and FiM Fe₃O₄ shell. The analysis of the relative intensity between L₃/L₂ edges in the EELS spectrum allows us to demonstrate the presence of both phases. In addition, the XRD patterns show the typical diffraction peaks of the cubic FeO (NaCl, rock salt) and cubic spinel Fe₃O₄ structures. Subsequently, manganese oxide is deposited onto the surface of the CS iron oxide nanoparticles, through the seed-growth synthetic approach, leading to the formation of the poly-magnetic three- and four-components onion-like nanoparticles. The system composed of three-components is based on the deposition of a thin manganese oxide shell to form the highly oxidized Mn₃O₄ phase on the surface of the pre-made FeO|Fe₃O₄ CS nanoparticles to create the onion-like three-components FeO|Fe₃O₄|Mn₃O₄ system. On the other hand, the deposition of thicker manganese oxide shells has been carried out FeO|Fe₃O₄ seeds at higher decomposition temperature in comparison with the three-components system. The thicker manganese shell is, then, surface passivated to Mn₃O₄ leading the FeO|Fe₃O₄|MnO|Mn₃O₄ four-component system. The characterization of these three- and four-components onion-like nanoparticles confirms the formation of the manganese layers. In fact, EELS and XRD analysis can, only, demonstrate the formation of the three-components, since for the four-component samples the signal of the inner iron oxide phases are overwhelmed by the MnO signal. In contrast, EFTEM and magnetometric analysis indeed reveal the formation of the three- and four- components nanoparticles. The temperature dependence of the magnetization shows the evolution of the magnetic transitions from the two-component (CS) to the three- and four-component nanoparticles. Besides, the hysteresis loop of the three-component system shows exchange bias due to the coupling between AFM|FiM layers. For the two- and three-components nanoparticles the bias disappears at their transition temperatures, i.e. T_B and T_C, respectively. Interestingly, the four-components sample exhibit finite values of the bias well above their T_C and tend to decrease at the T_N of the AFM MnO, which is consistent with magnetic proximity effects. Concerning the growth mechanisms, the manganese deposition mechanism, the (111) planes of the manganese oxide grow epitaxially on to the (111) truncated faces of the initial cubic FeO|Fe₃O₄ seeds.



Two-, Three-, and Four-Component Magnetic Multilayer Onion Nanoparticles Based on Iron Oxides and Manganese Oxides

German Salazar-Alvarez,^{*,†} Hans Lidbaum,[‡] Alberto López-Ortega,[§] Marta Estrader,[§] Klaus Leifer,[‡] Jordi Sort,^{||,⊥} Santiago Suriñach,[⊥] Maria Dolors Baró,[⊥] and Josep Nogués^{§,||}

[†] Department of Materials and Environmental Chemistry, Stockholm University, SE-106 91 Stockholm, Sweden

[‡] Department of Engineering Sciences, Uppsala University, S-75121 Uppsala, Sweden

[§] CIN2 (ICN-CSIC) and Universitat Autònoma de Barcelona, Catalan Institute of Nanotechnology (ICN), Campus de la UAB, 08193 Bellaterra (Barcelona), Spain

^{||} Institució Catalana de Recerca i Estudis Avançats (ICREA), Barcelona, Spain

[⊥] Departament de Física, Universitat Autònoma de Barcelona, E-08193 Bellaterra, Spain

S Supporting Information

ABSTRACT: Magnetic multilayered, onion-like, heterostructured nanoparticles are interesting model systems for studying magnetic exchange coupling phenomena. In this work, we synthesized heterostructured magnetic nanoparticles composed of two, three, or four components using iron oxide seeds for the subsequent deposition of manganese oxide. The MnO layer was allowed either to passivate fully in air to form an outer layer of Mn₃O₄ or to oxidize partially to form MnO|Mn₃O₄ double layers. Through control of the degree of passivation of the seeds, particles with up to four different magnetic layers can be obtained (i.e., FeO|Fe₃O₄|MnO|Mn₃O₄). Magnetic characterization of the samples confirmed the presence of the different magnetic layers.

Magnetic nanoparticles are very attractive for their novel fundamental properties and numerous current and potential applications.^{1–3} The advances in chemical methods of synthesis have allowed the production of relatively large amounts of narrowly size-distributed nanoparticles with a broad range of compositions and morphologies.^{4–7} Recently, besides single-component nanoparticles, the interest in two-component nanoparticles has steadily increased because of the appealing novel properties and promising applications arising from the simple combination of properties of their constituents or the interaction between them (e.g., see refs 8 and 9 and references therein). Since the report on the use of exchange bias to overcome the superparamagnetic limit,¹⁰ the number of reports on bimagnetic core–shell (CS) configurations has increased considerably.¹¹ At present there are still just a few examples of heterostructured CS systems with distinct chemical compositions, such as M1Fe₂O₄|M2Fe₂O₄ (M1, M2 = Mn, Fe, Co, Zn),^{3,12} FeO|CoFe₂O₄,¹³ FePt|MnO,¹⁴ CoFe₂O₄|MnO,¹⁵ and FePt|M_xFe_{3–x}O₄ (M = Fe, Co).^{16,17} Nevertheless, reports on more complex multicomponent onion-like magnetic nanoparticles are very scarce.¹⁸

In this communication, we report the synthesis and microscopic and magnetic characterization of onion-like magnetic nanoparticles with two, three, or four components based on the antiferromagnets (AFMs) FeO and MnO and ferrimagnets

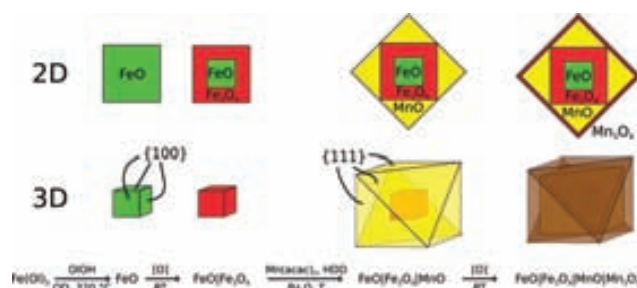


Figure 1. Schematic 2D projections (top) and 3D representations (middle) and the corresponding chemical path of the formation of multicomponent onion nanoparticles (bottom).

(FiMs) Fe₃O₄ and Mn₃O₄. The multicomponent nanoparticles were fabricated by the heterogeneous growth of manganese oxide shells on iron oxide cores using the latter as seeds, as depicted schematically in Figure 1.

The shape, size, and composition of the initial CS iron oxide nanoparticle seeds were controlled by adjusting the surfactant to precursor ratio, heating rate, and stirring during the reaction.^{7,19–24} The particles were truncated nanocubes with an edge length (*l*) of 11 ± 1 nm consisting of a more electron dense inner core with a size of ~ 5 nm and a less electron dense edge of ~ 3 nm.²⁴ Phase analysis of the X-ray diffraction (XRD) measurements suggested two components that could be associated with either Fe₃O₄ or γ -Fe₂O₃ and FeO.²⁴ Quantitative analysis of the Fe L₃/L₂ integrated intensity ratio obtained by electron energy loss spectroscopy (EELS) resulted in a ratio of 4.9, indicating that the CS particles had an average composition between FeO and Fe₃O₄.^{24,25} The passivation of the surface layer indicates that the original particles were composed of FeO, which upon exposure to air oxidized to Fe₃O₄, in agreement with previous reports (although the presence of γ -Fe₂O₃ as a result of lattice strains cannot be completely ruled out).^{26–28}

The iron oxide CS nanoparticles were used as seeds for the heterogeneous growth of manganese oxide.²⁴ Figure 2a shows

Received: June 30, 2011

Published: October 05, 2011

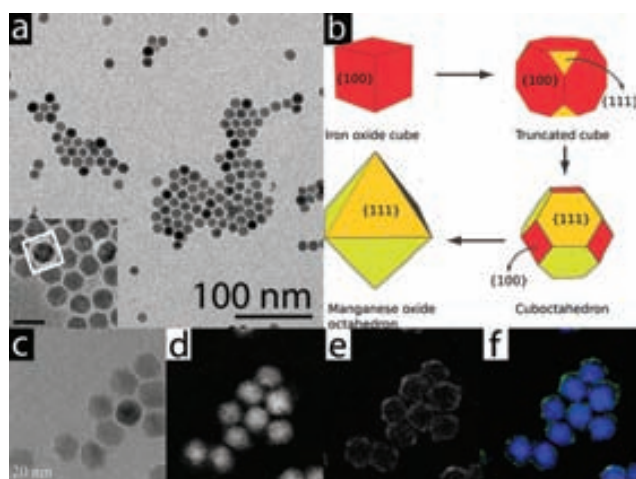


Figure 2. TEM images of the three-component $\text{FeO}|\text{Fe}_3\text{O}_4|\text{Mn}_3\text{O}_4$ onion nanoparticles. (a) Bright-field TEM image of the particles forming hexagonal arrays. In the inset, the marked particle is an octahedral particle with a cubic core, and the scale bar represents 20 nm. (b) Schematic representation of the composition of the particle highlighted in the inset of (a) and a cartoon showing how the CS seed becomes progressively coated with a manganese oxide layer to form an octahedral particle. (c) Bright-field TEM image of the three-component nanoparticles. (d–e) Corresponding EFTEM micrographs acquired at the (d) iron and (e) manganese L_3 edges. (f) Overlay map showing the distribution of iron and manganese in the particles.

bright-field transmission electron microscopy (TEM) micrographs for three-component onion nanoparticles. Remarkably, unlike the seeds with cubic morphology, these particles are larger and seem to have lost the corners to form, probably, cuboctahedrons or truncated octahedrons. Moreover, the self-assembly of the onion nanoparticles leads to the formation of hexagonal arrays, in contrast to the square arrays formed by the seeds.^{6,24} The inset of Figure 2a shows a cuboctahedron with an edge length l_{oh} of ~ 14 nm, indicating that it practically embeds a cubic particle with an edge length of ~ 11 nm. The formation of the cuboctahedrons (or truncated octahedrons) instead of cubes must arise from an increasing surface chemical potential of the $\{111\}$ faces relative to the $\{100\}$ faces.²⁹ Indeed, it has been shown that MnO nanoparticles tend to crystallize in the form of octahedrons with $\{111\}$ faces.^{5,30–33} It is expected that upon exposure to air, the manganese monoxide should oxidize to a higher oxide, i.e., Mn_3O_4 (or $\gamma\text{-Mn}_2\text{O}_3$ ³⁴), in a similar fashion to the $\text{MnO}|\text{Mn}_3\text{O}_4$ system.^{34–36} On the basis of the Mn L_3/L_2 ratio and the characteristic shape of the O K absorption edge³⁷ from the corresponding EEL spectra,²⁴ the composition of the manganese oxide layer was estimated to be Mn_3O_4 . The 2–3 nm thick manganese outer shell was confirmed by electron-filtered TEM (EFTEM) images taken at the Fe and Mn L_3 edges (Figure 2d–f). The growth of manganese oxide on the surface of the two-component seeds renders three-component onion nanoparticles with composition $\text{FeO}|\text{Fe}_3\text{O}_4|\text{MnO}$, which passivate toward $\text{FeO}|\text{Fe}_3\text{O}_4|\text{Mn}_3\text{O}_4$. XRD results are consistent with this structure.²⁴ The synthesis relies in air oxidation of some of the components. Previous reports have shown that the composition thus attained can be stable for months and even be size-dependent.^{34,38,39}

Thicker manganese oxide layers (>20 nm) can be grown on the CS seeds using higher decomposition temperatures than in

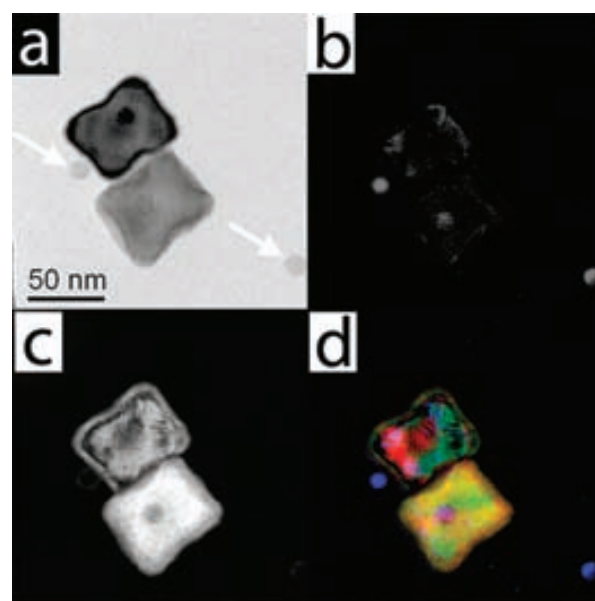


Figure 3. (a) Bright-field TEM image of the four-component $\text{FeO}|\text{Fe}_3\text{O}_4|\text{MnO}|\text{Mn}_3\text{O}_4$ onion nanoparticles. (b–d) EFTEM micrographs corresponding to (b) iron and (c) manganese and (d) an overlay map showing the distribution of cations in the particles. The arrows in (a) indicate the position of excess two-component CS seeds. The dark inner corona in (c) and (d) is due to diffraction contrast.

the three-component case (see Figure 3).³⁵ The manganese-containing layer was confirmed by EFTEM images taken at the Fe and Mn L_3 edges (Figure 3b–d). On the basis of the characteristics of the $\text{MnO}|\text{Mn}_3\text{O}_4$ system,³⁵ these particles are expected to be formed from four components, i.e., $\text{FeO}|\text{Fe}_3\text{O}_4|\text{MnO}|\text{Mn}_3\text{O}_4$. The presence of both MnO and Mn_3O_4 was determined from magnetization data, as discussed below. A proper differentiation between the different manganese oxides using the XRD and EEL spectra was not possible, as MnO dominates the signal because of its large volume fraction.²⁴ These nanoparticles present a slightly concave geometry, reminiscent of a tetracube. Hofmann et al.⁴⁰ argued that the formation of this type of concave geometry is due to the presence of water during the reaction, which induces some etching of defective areas on the $\{100\}$ faces. Water then helps solubilize some metal (oxy)-hydroxide, which recrystallizes on the edges and along the corners according to the Berg effect.⁴¹

The final size and shape of the three-component nanoparticles, $\text{FeO}|\text{Fe}_3\text{O}_4|\text{Mn}_3\text{O}_4$, is likely to depend on three interrelated mechanisms: (i) seeded growth, which can be discussed in the framework of the Gibbs–Thomson effect and is influenced mainly by the size and curvature of the seeds ($\text{FeO}|\text{Fe}_3\text{O}_4$) and the monomer concentration;⁴² (ii) the formation of a heterogeneous layer (MnO) on the initial seeds as manganese oxide is deposited on iron oxide, thereby creating an interface, which can be understood as the spherical case of the Frank–van der Merwe (FM) or Volmer–Weber (VW) regimes⁴³ and is affected mostly by the difference in surface energy, lattice mismatch, and degree of supersaturation of the monomer;⁴⁴ and finally (iii) the growth rates of the different crystal faces of the manganese oxide layer, which are likely to be dependent on the type and concentration of surfactant and the initial shape of the seeding particle according to the Wulff–Gibbs criteria of equilibrium.²⁹ The use of faceted seeds

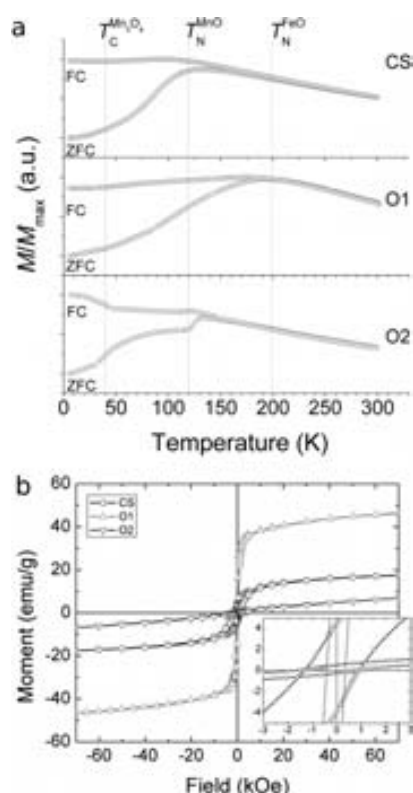


Figure 4. (a) Temperature dependence of the magnetization for the two- (CS), three- (O1), and four-component (O2) onion nanoparticle systems. The measurements were carried out using an applied field $H_{\text{app}} = 50$ Oe. The vertical lines indicate the transition temperatures for some of the components. (b) Hysteresis loops at $T = 10$ K for samples CS (○), O1 (△), and O2 (▽) cooled from 300 K under a static field $H_{\text{FC}} = 50$ kOe. The inset shows a magnified view of the central portion of the loops.

serves a twofold purpose: First, it delays the deposition of manganese oxide monomer, which preserves the very narrow size distribution of the seeds.^{8,29} This becomes more apparent upon comparison of the particles shown in Figure 2a with those prepared without the seeds (see ref 35). Second, the morphology of the particles (i.e., truncated cubes) provides well-defined high-energy {111} corners where the manganese oxide can be deposited (see Figure 2b). Hence, as the manganese oxide monomer is deposited on the truncated high-energy {111} corners of the iron oxide, these grow and the {100} planes dissolve to produce a cuboctahedron or truncated octahedron, as illustrated by the cartoon in Figure 2b. For the growth of a continuous coating on the seeds, both the outermost layer (mainly Fe₃O₄) and the developing shell (most probably MnO) must accommodate a relatively large lattice mismatch of ~5%. The simplest way to do this is by creating a graded defective interface that is rich in iron and poor in manganese (i.e., Mn_xFe_{3-x}O₄) and enriched toward MnO at the outermost layer with a low manganese occupancy (i.e., Mn_{1-x}O). The formation of such a defective structure then facilitates its oxidation toward a distorted Mn₃O₄ to release further the internal stresses, similar to the MnO|Mn₃O₄ system.^{34–36} The formation of the larger four-component nanoparticles proceeds likewise using higher decomposition temperatures.²⁴

Figure 4a shows the field-cooled (FC) and zero-field-cooled (ZFC) magnetization measurements carried out on

the two-component CS FeO|Fe₃O₄ seeds, the three-component FeO|Fe₃O₄|Mn₃O₄ onion nanoparticles, and the four-component FeO|Fe₃O₄|MnO|Mn₃O₄ onion particles. As can be seen in the figure, the initial seeds present a blocking temperature (T_B) of ~120 K, well below the transition temperature of bulk FeO ($T_N = 198$ K). Notably, although exchange coupling between the AFM core and the FiM shell should bring the blocking temperature of the nanoparticle toward the Néel temperature (T_N) of the AFM,¹⁰ this effect depends strongly on the size and anisotropy of the AFM counterpart.⁴⁵ Surprisingly, adding a 2–3 nm thick layer of Mn₃O₄ (with $T_C \approx 43$ K⁴⁶) to these cubes results in an increase in T_B toward ~200 K. This effect could have various origins: (a) There is some limited intermixing at the interface of the components (the first nanometer layer), as shown by the EFTEM images, which results in a larger effective volume of the FiM component. This is in agreement with our work on smaller particles.⁴⁷ (b) The growth of the manganese layer on the surface of the cubic seeds proceeds preferentially by growth of the {111} faces. This directional growth creates more facets than for a cubic morphology, which can be seen as an effective rounding of the particles, leading to an increase in the effective surface anisotropy and hence T_B .⁷ The absence of a clear transition for the Mn₃O₄ (except a small shoulder in the ZFC branch of the magnetization) implies strong exchange coupling between the Fe₃O₄ and Mn₃O₄ components. Lastly, the four-component FeO|Fe₃O₄|MnO|Mn₃O₄ onion nanoparticles display several transitions, with those related to the Néel and Curie transitions of MnO and Mn₃O₄ components, respectively, dominating the signal. A shoulder corresponding to the T_B of the FeO|Fe₃O₄ cores can also be observed at ~70 K in the ZFC branch of the magnetization. Moreover, the presence of loop shifts in the hysteresis (Figure 4b), i.e., exchange bias,¹¹ suggests the presence of AFM layers coupled to FiM layers in the particles, as designed. Figure 4b shows the hysteresis loops of the samples measured at $T = 10$ K after cooling under a field $H_{\text{FC}} = 50$ kOe. All of the samples show a loop shift (H_E), with the largest being that for the four-component nanoparticle system (sample O2). The temperature dependences of the coercivity and loop shift of the three different samples are shown in Figure S4 in the Supporting Information. As expected from its components, the coercivity and loop shift of the CS sample decay slowly toward the blocking temperature of the system. In the case of the Mn₃O₄-containing samples, the coercivity and loop shift decay rapidly near the Curie temperature ($T_C^{\text{Mn}_3\text{O}_4} \approx 40$ K). The effect is more pronounced in the four-component nanoparticle system, where most of the magnetic volume corresponds to the AFM MnO. Thus, the coercivity decays nearly 90%, although there is a remanent component that disappears near the Néel temperature ($T_N^{\text{MnO}} \approx 120$ K).

Taking advantage of the surface oxidation of FeO and MnO allows nanoparticles with various compositions and number of components to be produced: (i) two-component FeO|Fe₃O₄ nanoparticles can be synthesized directly, and (ii) three-component FeO|Fe₃O₄|Mn₃O₄ nanoparticles or (iii) four-component FeO|Fe₃O₄|MnO|Mn₃O₄ nanoparticles can be obtained from CS FeO|Fe₃O₄ seeds by growing a single Mn₃O₄ layer or a MnO|Mn₃O₄ double layer, respectively. Magnetic measurements suggest that the interfacial effects dominate in the three-component particles, whereas MnO dominates in the four-component particles.

■ ASSOCIATED CONTENT

S Supporting Information. Experimental details and additional results. This material is available free of charge via the Internet at <http://pubs.acs.org>.

■ AUTHOR INFORMATION

Corresponding Author

german@mmk.su.se

■ ACKNOWLEDGMENT

This work was supported by the Spanish MICINN (MAT2008-01939-E, MAT2010-20616-C02, CSD2006-00012 Consolider Ingenio 2010) and the Catalan DGR (2009-SGR-1292). The authors thank the Serveis Científics-tècnics de la UAB. G.S.-A. thanks the Wallenberg Wood Science Center for partial financial support. M.D. B. was partially supported by an ICREA ACADEMIA Award.

■ REFERENCES

- Laurent, S.; Forge, D.; Port, M.; Roch, A.; Robic, C.; Elst, L. V.; Muller, R. N. *Chem. Rev.* **2008**, *108*, 2064.
- Härmä, H.; Laakso, S.; Pihlasalo, S.; Hänninen, P.; Faure, B.; Rana, S.; Bergström, L. *Nanoscale* **2010**, *2*, 69.
- Lee, J.-H.; Jang, J.-T.; Choi, J.-S.; Moon, S.-H.; Noh, S.-H.; Kim, J.-W.; Kim, J.-G.; Kim, I.-S.; Park, K.-I.; Cheon, J. *Nat. Nanotechnol.* **2011**, *6*, 418.
- Cheon, J.; Kang, N.; Lee, S.; Lee, J.; Yoon, J.; Oh, S. *J. Am. Chem. Soc.* **2004**, *126*, 1950.
- Park, J.; An, K.; Hwang, Y.; Park, J.-G.; Noh, H.-J.; Kim, J.-Y.; Park, J.-H.; Hwang, N.-M.; Hyeon, T. *Nat. Mater.* **2004**, *3*, 891.
- Disch, S.; Wetterskog, E.; Hermann, R.; Salazar-Alvarez, G.; Busch, P.; Bergström, L.; Brückel, T.; Kamali, S. *Nano Lett.* **2011**, *11*, 1651.
- Salazar-Alvarez, G.; Qin, J.; Šepelák, V.; Bergman, I.; Vasilakakis, I.; Trohidou, K.; Ardisson, J.; Macedo, W.; Mikhaylova, M.; Muhammed, M.; Baró, M.; Nogués, J. *J. Am. Chem. Soc.* **2008**, *130*, 13234.
- Costi, R.; Saunders, A.; Banin, U. *Angew. Chem., Int. Ed.* **2010**, *49*, 4878.
- Carbone, L.; Cozzoli, P. D. *Nano Today* **2010**, *5*, 449.
- Skumryev, V.; Stoyanov, S.; Zhang, Y.; Hadjipanayis, G.; Givord, D.; Nogués, J. *Nature* **2003**, *423*, 850.
- Nogués, J.; Sort, J.; Langlais, V.; Skumryev, V.; Suriñach, S.; Muñoz, J. S.; Baró, M. D. *Phys. Rep.* **2005**, *422*, 65.
- Masala, O.; Hoffman, D.; Sundaram, N.; Page, K.; Proffen, T.; Lawes, G.; Seshadri, R. *Solid State Sci.* **2006**, *8*, 1015.
- Bodnarchuk, M. I.; Kovalenko, M. V.; Groiss, H.; Resel, R.; Reissner, M.; Hesser, G.; Lechner, R. T.; Steiner, W.; Schäffler, F.; Heiss, W. *Small* **2009**, *5*, 2247.
- Kang, S.; Miao, G. X.; Shi, S.; Jia, Z.; Nikles, D. E.; Harrell, J. W. *J. Am. Chem. Soc.* **2006**, *128*, 1042.
- Masala, O.; Seshadri, R. *J. Am. Chem. Soc.* **2005**, *127*, 9354.
- Zeng, H.; Li, J.; Wang, Z. L.; Liu, J. P.; Sun, S. *Nano Lett.* **2004**, *4*, 187.
- Zeng, H.; Sun, S.; Li, J.; Wang, Z. L.; Liu, J. P. *Appl. Phys. Lett.* **2004**, *85*, 792.
- Catala, L.; Brinzei, D.; Prado, Y.; Gloter, A.; Stéphan, O.; Rogez, G.; Mallah, T. *Angew. Chem., Int. Ed.* **2009**, *48*, 183.
- Park, J.; Lee, E.; Hwang, N.; Kang, M.; Kim, S.; Hwang, Y.; Park, J.; Noh, H.; Kim, J.; Park, J.; Hyeon, T. *Angew. Chem., Int. Ed.* **2005**, *44*, 2872.
- Kovalenko, M. V.; Bodnarchuk, M. I.; Lechner, R. T.; Hesser, G.; Schäffler, F.; Heiss, W. *J. Am. Chem. Soc.* **2007**, *129*, 6352.
- Ahniyaz, A.; Sakamoto, Y.; Bergström, L. *Proc. Natl. Acad. Sci. U.S.A.* **2007**, *104*, 17570.
- Shavel, A.; Rodríguez-González, B.; Spasova, M.; Farle, M.; Liz-Marzán, L. M. *Adv. Funct. Mater.* **2007**, *17*, 3870.
- Gao, G.; Liu, X.; Shi, R.; Zhou, K.; Shi, Y.; Ma, R.; Takayama-Muromachi, E.; Qiu, G. *Cryst. Growth Des.* **2010**, *10*, 2888.
- see the Supporting Information for more details.
- Colliex, C.; Manoubi, T.; Ortiz, C. *Phys. Rev. B* **1991**, *44*, 11402.
- Redl, F.; Black, C.; Papaefthymiou, G.; Sandstrom, R.; Yin, M.; Zeng, H.; Murray, C.; O'Brien, S. *J. Am. Chem. Soc.* **2004**, *126*, 14583.
- Chen, C.; Chiang, R.; Lai, H.; Lin, C. *J. Phys. Chem. C* **2010**, *114*, 4258.
- Hai, H. T.; Yang, H. T.; Kura, H.; Hasegawa, D.; Ogata, Y.; Takahashi, M.; Ogawa, T. *J. Colloid Interface Sci.* **2010**, *346*, 37.
- Sugimoto, T. *Adv. Colloid Interface Sci.* **1987**, *28*, 65.
- Djerdj, I.; Arçon, D.; Jagličić, Z.; Niederberger, M. *J. Phys. Chem. C* **2007**, *111*, 3614.
- Park, J.; Kang, E.; Bae, C. J.; Park, J.-G.; Noh, H.-J.; Kim, J.-Y.; Park, J.-H.; Park, H. M.; Hyeon, T. *J. Phys. Chem. B* **2004**, *108*, 13594.
- Seo, W.; Jo, H.; Lee, K.; Kim, B.; Oh, S.; Park, J. *Angew. Chem., Int. Ed.* **2004**, *43*, 1115.
- Li, Q.; Wang, J.; He, Y.; Liu, W.; Qiu, X. *Cryst. Growth Des.* **2009**, *9*, 3100.
- López-Ortega, A.; Tobia, D.; Winkler, E.; Golosovsky, I. V.; Salazar-Alvarez, G.; Estradé, S.; Estrader, M.; Sort, J.; González, M. A.; Suriñach, S.; Arbiol, J.; Peiró, F.; Zysler, R. D.; Baró, M. D.; Nogués, J. *J. Am. Chem. Soc.* **2010**, *132*, 9398.
- Salazar-Alvarez, G.; Sort, J.; Suriñach, S.; Baró, M. D.; Nogués, J. *J. Am. Chem. Soc.* **2007**, *129*, 9102.
- Golosovsky, I.; Salazar-Alvarez, G.; Lopez-Ortega, A.; González, M.; Sort, J.; Estrader, M.; Suriñach, S.; Baró, M.; Nogués, J. *Phys. Rev. Lett.* **2009**, *102*, No. 247201.
- Paterson, J. H.; Krivanek, O. L. *Ultramicroscopy* **1990**, *32*, 319.
- Santoyo Salazar, J.; Perez, L.; de Abril, O.; Truong Phuoc, L.; Ihiawakrim, D.; Vazquez, M.; Greneche, J.-M.; Begin-Colin, S.; Pourroy, G. *Chem. Mater.* **2011**, *23*, 1379.
- Spasova, M.; Wiedwald, U.; Farle, M.; Radetic, T.; Dahmen, U.; Hilgendorff, M.; Giersig, M. *J. Magn. Magn. Mater.* **2004**, *272–276*, 1508.
- Hofmann, C.; Rusakova, I.; Ould-Ely, T.; Prieto-Centurió, D.; Hartman, K. B.; Kelly, A. T.; Lüttge, A.; Whitmire, K. H. *Adv. Funct. Mater.* **2008**, *18*, 1661.
- Sunagawa, I. *Crystals: Growth, Morphology, and Perfection*; Cambridge University Press: Cambridge, U.K., 2005.
- In the case of diffusion-controlled growth, the growth rate is $dr/dt = (K/r)(1/r^* - 1/r)$, i.e., a function of the monomer diffusion constant K , the radius of critical solubility r^* , and the particle radius r (see ref 29).
- Bauer, E.; van der Merwe, J. H. *Phys. Rev. B* **1986**, *33*, 3657.
- The change in the surface energy is given by $\Delta\gamma = \gamma_s - \gamma_c + \gamma_{CS}$, where γ_c is the surface energy of the core, γ_s is the surface energy of the component to be deposited (the shell), and γ_{CS} the interfacial energy ($\gamma_{CS} < 0$ for small lattice mismatch and strong CS adhesion). When $\Delta\gamma < 0$, the deposition occurs homogeneously over the seed (FM regime), whereas in the opposite case with $\Delta\gamma > 0$, the deposition is not homogeneous, and the component instead grows as islands (VW regime).⁴³
- Nogués, J.; Skumryev, V.; Sort, J.; Stoyanov, S.; Givord, D. *Phys. Rev. Lett.* **2006**, *97*, No. 157203.
- Guillou, F.; Thota, S.; Prellier, W.; Kumar, J.; Hardy, V. *Phys. Rev. B* **2011**, *83*, No. 094423.
- Estradé, S.; Yedra, L.; López-Ortega, A.; Estrader, M.; Salazar-Alvarez, G.; Baró, M.; Nogués, J.; Peiró, F. *Micron* [Online early access]. DOI: 10.1016/j.micron.2011.04.002. Published Online: April 16, 2011.

SUPPORTING INFORMATION

Two-, three-, and four-component magnetic multilayer onion nanoparticles based on iron oxides and manganese oxides

German Salazar-Alvarez*, Hans Lidbaum, Alberto López-Ortega
Marta Estrader, Klaus Leifer, Jordi Sort, Santiago Surinach
Maria Dolors Baró, Josep Nogués
german@mmk.su.se

Contents

| | | |
|----------|---|----------|
| 1 | Experimental section | 2 |
| 1.1 | Synthesis details | 2 |
| 1.2 | TEM characterization | 2 |
| 1.3 | EELS and EFTEM characterization | 3 |
| 1.4 | Magnetic characterization | 3 |
| 1.5 | X-ray powder diffraction | 3 |
| 2 | Additional results | 3 |
| 2.1 | EEL Spectrum analysis | 3 |
| 2.2 | Additional figures | 5 |
| | Additional references | 9 |

1 Experimental section

1.1 Synthesis details

The synthesis of the iron oxide cores was carried out following a similar procedure reported earlier.[1, 2] Cubic core-shell nanoparticles with an edge $l = 11 \pm 1$ nm (Sample CS) were prepared by dissolving 7 mmol of the iron (III) oleate precursor and 3.4 mmol of oleic acid (Fluka) in 43 cm³ of 1-octadecene (90 %, Aldrich) at 70 °C. The mixture was heated to 320 °C (at 3.3 °C/min) and kept for 30 min. The reaction vessel was allowed to cool down to room temperature before exposure to air and addition of ethanol to coagulate the solids. The mixture was heated to 320 °C (at 5 °C/min) under mechanical stirring at 130 rpm and kept for 30 min. The particles were retrieved by several cycles of centrifugation at 2000×g, disposal of supernatant, re-dispersion in hexane and coagulation with ethanol.[3] The manganese oxide layers were laid on the iron oxide-based nanocubes by modifying an earlier reported procedure used for the synthesis of MnO|Mn_{3-x}O₄ nanoparticles.[4] The procedure is as follows: to a given amount of iron oxide seeds (see Table S1) an equimolar amount of 1,2-hexadecanediol (HDD, Aldrich) and manganese (II) acetylacetonate (Mn(acac)₂, Aldrich) were added to a solution of oleic acid (OIOH, Aldrich) and oleylamine (OINH₂, Fluka) in benzylether (Bz₂O, Fluka). The slurry was de-aerated with Ar for 15 min while heating at 100 °C. The temperature was then ramped at ~ 7 °C/min to a final temperature, T , kept under reflux during a 45 min, and then removed from the heating source and allowed to cool down to room temperature. The particles were washed from the reaction media by subsequent steps of precipitation under ethanol, centrifugation, and re-dispersion in hexane.[3]

Table SI: Table describing the conditions used for the synthesis of the samples.

| Sample | Seeds (mg) | Mn(acac) ₂ (mmol) | HDD (mmol) | OIOH (mmol) | OINH ₂ (mmol) | Bz ₂ O (cm ³) | T (°) |
|--------|---------------|---------------------------------|---------------|----------------|-----------------------------|---|------------|
| O1 | 20 | 1 | 1 | 10 | 10 | 20 | 200 |
| O2 | 50 | 1.5 | 1.5 | 15 | 15 | 30 | 250 |

1.2 TEM characterization

Samples for transmission electron microscopy (TEM) were prepared by drop-casting few microlitres of a diluted hexane suspension of nanoparticles onto a carbon-coated copper grid and letting the solvent evaporate. High-resolution transmission electron microscopy images (HRTEM) were obtained in a JEOL-2011 electron microscope operated at 200 kV. Particle size histograms were obtained

by manually measuring the edge length, l_i , or diameter, D_i , of at least 200-300 particles, respectively, on TEM micrographs. The mean size and its standard deviation, σ , were determined by fitting the corresponding histogram with a Gaussian distribution function.

1.3 EELS and EFTEM characterization

Electron energy loss spectra (EELS) and energy-filtered transmission electron microscopy micrographs (EFTEM) were acquired using a F-30ST (Tecnai) operated at 300 kV equipped with a GIF2002 (Gatan) spectrometer on areas containing >50 particles. EEL spectra of the Mn and Fe L edges were acquired using a dispersion of 0.2 eV/channel. In a typical run an energy resolution of 1.5 eV was determined from the full width at half maximum of the zero loss peak.

1.4 Magnetic characterization

Magnetic measurements were carried out on loosely packed powdered samples using a superconducting quantum interference device (SQUID) magnetometer Quantum Design MPMS-7XL. The field cooled (FC) and zero field cooled (ZFC) magnetization measurements were carried out in $H_{appl} = 50$ Oe. The hysteresis loops were measured using maximum fields of up to 70 kOe at 10 K after field cooling from room temperature in $H_{FC} = 50$ kOe.

1.5 X-ray powder diffraction

The X-ray diffractograms shown in Figure S3 were obtained on loosely-packed powdered samples using a Philips 3050 diffractometer with Cu K_α radiation using the Bragg-Brentano geometry. The measurements were carried out in the 2θ range $25 - 100^\circ$ with a step size of 0.04° and collection time of 40 s.

2 Additional results

2.1 EEL Spectrum analysis

The recorded spectra for the different samples showing the O- K , Mn- L and Fe- L regions are shown in Figure S2. Phase determination was carried out by comparing the L_3/L_2 ratio following the second derivative procedure described in [7]. Using the program Digital Micrograph (Gatan), the second derivative of the spectra was obtained using a numerical filter that averages over an interval w^+ units wide and subtracts half the averages in two adjacent windows of width w^- . Then,

Table SII: Correlation of composition to L_3/L_2 ratio for various iron and manganese oxides. Rightmost column indicates the suggested composition of the particles in this study.

| Sample | Fe- L_3/L_2 ratio | Mn- L_3/L_2 ratio | Composition |
|-------------|---------------------|---------------------|---|
| Ref. [5] | 4.6 | ∅ | FeO |
| Ref. [5] | 5.2 | ∅ | Fe ₃ O ₄ |
| Ref. [5] | 5.8 | ∅ | γ -Fe ₂ O ₃ |
| Ref. [6] | ∅ | 3.9 | MnO |
| Ref. [7, 6] | ∅ | 2.6, 2.8 | Mn ₃ O ₄ |
| Ref. [7, 6] | ∅ | 2.3, 2.4 | Mn ₂ O ₃ |
| CS | 4.9±0.1 | ∅ | FeO-Fe ₃ O ₄ |
| O1 | 4.9±0.1 | 2.7±0.1 | FeO-Fe ₃ O ₄ , Mn ₃ O ₄ |
| O2 | N/A ^[I] | 3.8±0.1 | FeO-Fe ₃ O ₄ ^[III] , MnO |

^[I] The element $\tilde{\Theta}$ signal is too low to be quantified.

^[III] Composition of the seeds is assumed to be the same as samples CS, and O1.

the spectrum is divided by the squared sum of w^+ and w^- to yield an approximation of the second derivative with respect to energy. The L_3/L_2 ratio is then calculated from the ratio of the maximum intensity of the peaks at the white line position. In this work we used window widths, $w^+ = 4$ eV and $w^- = 2$ eV. There are several reports that attempt to establish a correlation between spectral parameters (such as the intensity ratio of the white lines, position, and separation between white lines, and so on) and the stoichiometry of manganese or iron containing samples using different methods.[5, 6, 7, 8, 9, 10, 11, 12, 13, 14] However, although it is possible to see the general trend for the same report, there is a large scattering of data between the different reports.[12] The values thus obtained for the measured samples in this work as well as the probable stoichiometry given in Table SII should be taken with caution and used with a secondary parameter. Figure S2a shows the O- K spectra for the different samples. The O- K spectra corresponding to samples CS and O1 can be identified readily with that of a spinel oxide, i.e., Fe₃O₄ or γ -Fe₂O₃, [5] and Mn₃O₄. [14]

2.2 Additional figures

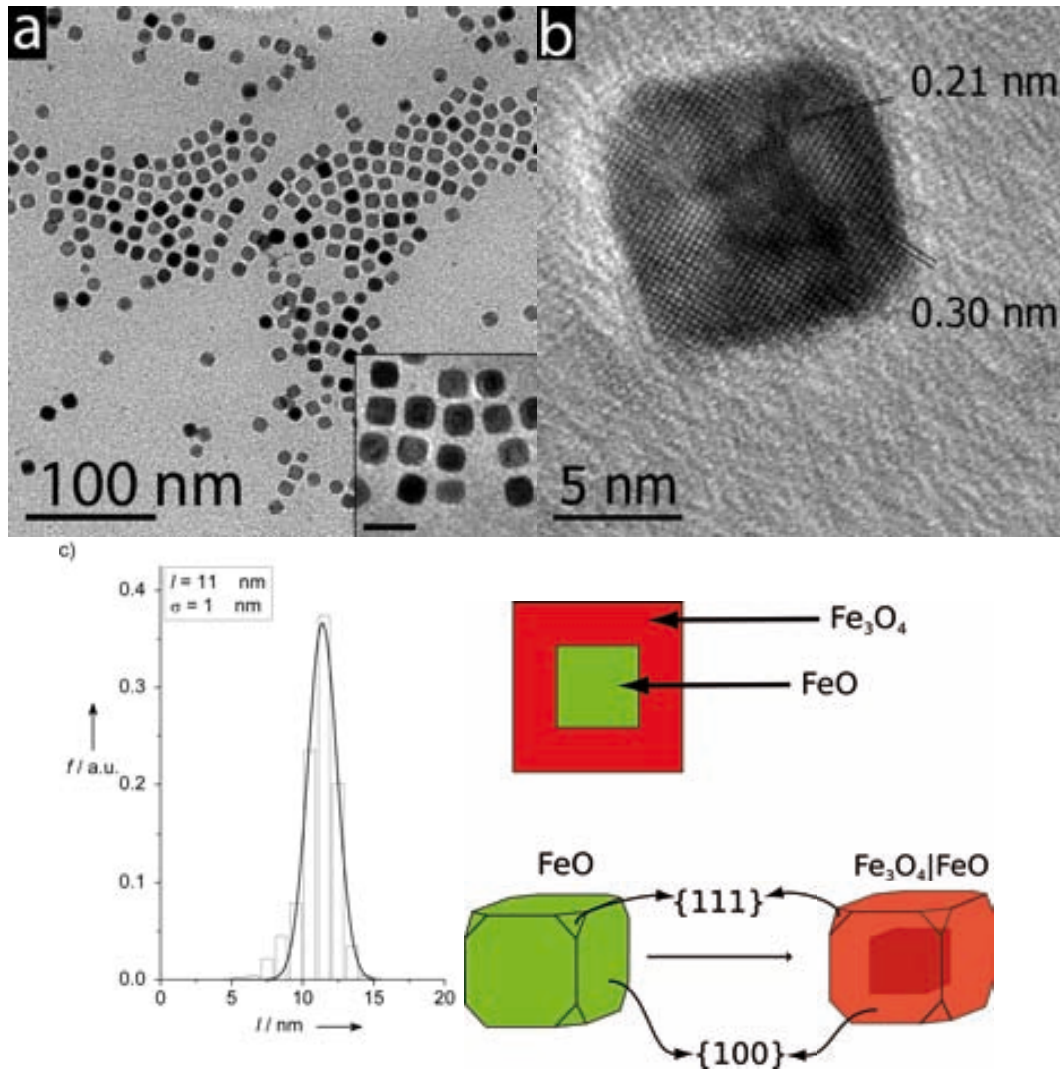


Figure S1: (a) Bright field TEM micrograph of several FeO|Fe₃O₄ cubic nanoparticles. Inset: magnified view of several particles with a core|shell structure exhibiting square arrays, the scale bar represents 20 nm. FFT filtering was applied for clarity. (b) High resolution TEM image of a single nanocube showing the interplanar distances corresponding to the (220)_{spinel} ($d=0.30 \text{ nm}$) and (400)_{spinel} or (200)_{FeO} ($d=0.21 \text{ nm}$). (c) Particle size distribution of the particles in (a). (d) Cartoon illustrating the structure of the particle shown in (b) from a top and perspective views.

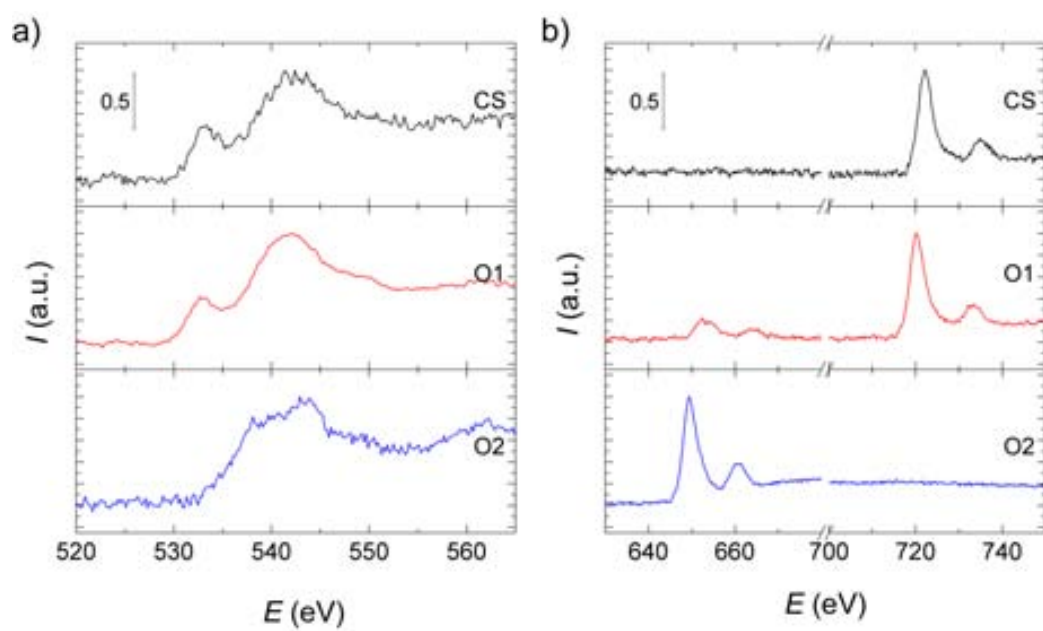


Figure S2: EEL spectra after background removal for the synthesized samples. Comparison of a) oxygen *K* spectra and b) manganese and iron *L*-lines.

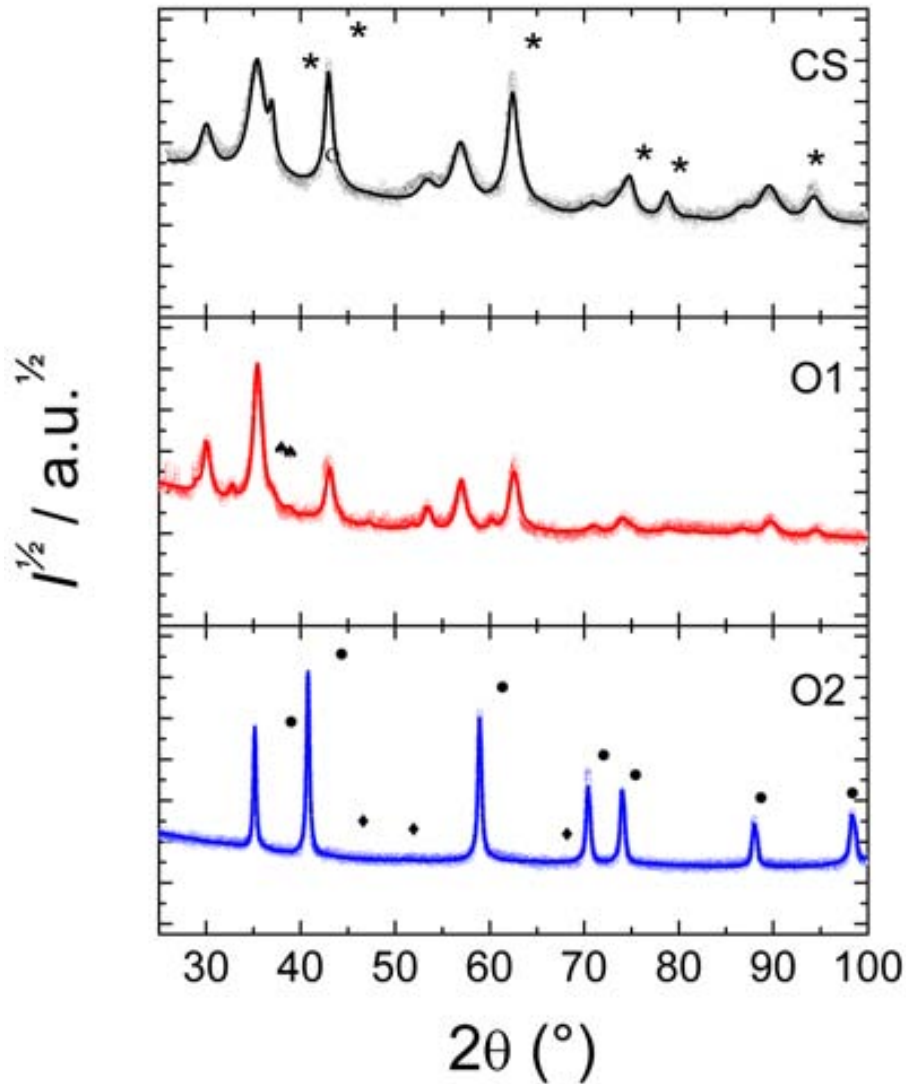


Figure S3: X-ray powder diffraction patterns corresponding to the samples shown in Table SI. The open symbols correspond to the experimental data and the line a fit to the data. Sample CS: The stars (\star) show the position of the reflections corresponding to FeO, all other reflections are assigned to Fe_3O_4 . Sample O1: The clovers (\clubsuit) show the position of the unassigned reflections, all other reflections correspond to Fe_3O_4 and Mn_3O_4 . Sample O2: The filled circles (\bullet) show the position of the reflections corresponding to MnO whereas the diamonds (\blacklozenge) indicate traces of the peaks corresponding to Mn_3O_4 .

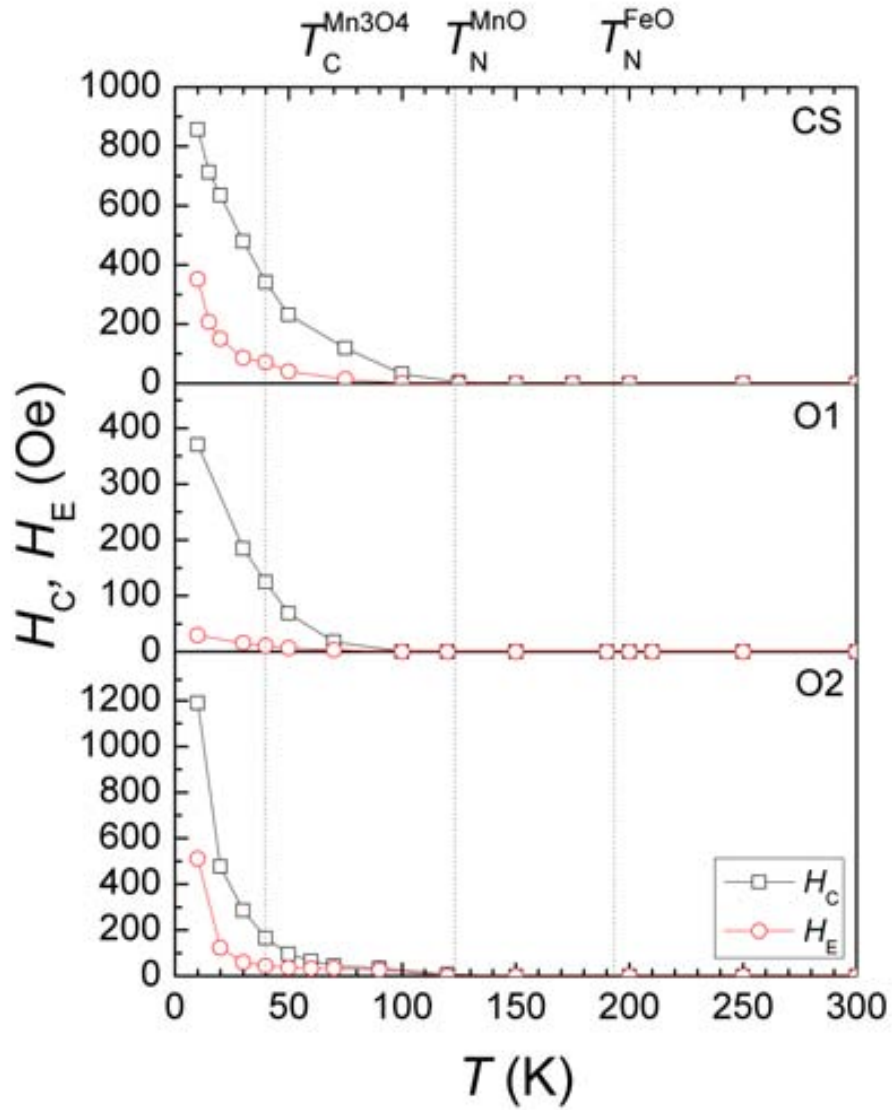


Figure S4: Temperature dependence of the coercivity (circles) and loop shift (squares) for samples CS1, O1, and O2 cooled under a static field, $H_{FC} = 50$ kOe, from 300 K.

References

- [1] J. Park, K. An, Y. Hwang, J.-G. Park, H.-J. Noh, J.-Y. Kim, J.-H. Park, N.-M. Hwang, T. Hyeon, *Nat. Mater.* **2004**, *3*, 891E895.
- [2] A. Ahniyaz, Y. Sakamoto, L. Bergström, *Proc. Natl. Acad. Sci. U. S. A.* **2007**, *104*, 17570E17574.
- [3] J. Park, E. Lee, N. Hwang, M. Kang, S. Kim, Y. Hwang, J. Park, H. Noh, J. Kim, J. Park, T. Hyeon, *Angew. Chem. Int. Ed.* **2005**, *44*, 2872E2877; *Angew. Chem.* **2005**, *117*, 2932E2937.
- [4] G. Salazar-Alvarez, J. Sort, S. Surinach, M. D. Baró, J. Nogues, *J. Am. Chem. Soc.* **2007**, *129*, 9102E9108.
- [5] C. Colliex, T. Manoubi, C. Ortiz, *Phys. Rev. B* **1991**, *44*, 11402E11411.
- [6] H. Schmid, W. Mader, *Micron* **2006**, *37*, 426 E432.
- [7] G. Botton, C. Appel, A. Horsewell, W. Stobbs, *J. Microsc.* **1995**, *180*, 211E216.
- [8] H. Kurata, C. Colliex, *Phys. Rev. B* **1993**, *48*, 2102E2108.
- [9] L. Garvie, A. Craven, *Ultramicroscopy* **1994**, *54*, 83E92.
- [10] P. L. Potapov, K. Jorissen, D. Schryvers, D. Lamoen, *Phys. Rev. B* **2004**, *70*, 045106.
- [11] Z. Chen, J. K. L. Lai, C.-H. Shek, *J. Chem. Phys.* **2006**, *124*, 184707.
- [12] T. Riedl, T. Gemming, K. Wetzig, *Ultramicroscopy* **2006**, *106*, 284E291.
- [13] L. Laffont, P. Gibot, *Mater. Charact.* **2010**, *61*, 1268E1273.
- [14] J. H. Paterson, O. L. Krivanek, *Ultramicroscopy* **1990**, *32*, 319E325.



6.2.2 Article #4: Strongly exchange coupled inverse ferrimagnetic soft|hard, $\text{Mn}_x\text{Fe}_{3-x}\text{O}_4|\text{Fe}_x\text{Mn}_{3-x}\text{O}_4$, core|shell heterostructured nanoparticles

This article presents the structural and magnetic characterization of bi-magnetic CS nanoparticles based on soft-FiM|hard-FiM core- $\text{Mn}_x\text{Fe}_{3-x}\text{O}_4$ |shell- $\text{Fe}_x\text{Mn}_{3-x}\text{O}_4$ nanoparticles. Firstly, two Fe_3O_4 nanoparticles with different sizes, i.e. 7.5 and 11.5 nm were prepared. These nanoparticles were formed by the complete oxidation of FeO nanoparticles. The posterior deposition of a thin manganese shell, using the seed-growth synthetic approach, leads to the formation of $\text{Fe}_3\text{O}_4|\text{Mn}_3\text{O}_4$ CS nanoparticles. However, since the synthesis, which was carried out under inner atmosphere, was opened to air at relatively high temperature, i.e. 180 °C, the nanoparticles form a manganese-iron mixed $\text{Mn}_x\text{Fe}_{3-x}\text{O}_4|\text{Fe}_x\text{Mn}_{3-x}\text{O}_4$ CS structure with a graded interface. The new phases formed by the ion interdiffusion maintain their crystallographic and magnetic structures, i.e., soft-FiM cubic spinel and hard-FiM tetragonal spinel for the core and shell, respectively. TEM images reveal highly monodisperse CS nanoparticles with an increase of overall size compared with Fe_3O_4 seed. Importantly, the size increase in both CS nanoparticles with respect to their corresponding seeds is the same, 1.2 nm, implying the growth of 0.6 nm manganese oxide shell. FFT analysis of the HR-TEM images confirms the presence of the crystallographic planes of both tetragonal (manganese oxide) and cubic spinel (iron oxide) structures. Further, XRD analysis of the CS nanoparticles show the presence of cubic and tetragonal phases in the CS system. Rietveld refinement of the cubic spinel phase discloses an increment of the cation occupancy from the seeds to the CS nanoparticles, which can be ascribed to the possible manganese diffusion from the shell to the core. The tetragonal diffraction peaks are rather small and their Rietveld refinement does not result in meaningful values. To get further insight, EELS analysis was performed to obtain the local relative elemental concentration, i.e. manganese, iron and oxygen. EELS data show three clear differentiated regions i) iron-rich oxide core with small quantity of manganese ions, ii) graded manganese-iron oxide interphase and iii) manganese-rich shell with a low amount of iron ions. The simulated data could be referred as a $\text{Mn}_{0.75}\text{Fe}_{2.25}\text{O}_4$ 8 nm core, $\text{Fe}_{0.75}\text{Mn}_{2.25}\text{O}_4$ 0.6 nm outer shell and a graded interface with an increase/decrease of manganese/iron ions from the core to shell. XAS and XMCD structural analyses show the presence of an extra concentration of Fe^{2+} and Mn^{2+} ions in the iron and manganese L_3 edges, respectively. This feature can be explained by the formation of $\text{Mn}_x\text{Fe}_{3-x}\text{O}_4$ and $\text{Fe}_x\text{Mn}_{3-x}\text{O}_4$ phases. The temperature dependence of the magnetization for the CS nanoparticles displays two magnetic transitions, ascribed to the T_C at 40 K of the hard-FiM shell and T_B for the soft-FiM core. Hysteresis loop present small coercivities and exchange bias demonstrating, thus, the strong exchange coupling between both layers. In addition M_S values for the CS with larger core size, i.e., initial bigger Fe_3O_4 seeds, present larger values than the smaller CS nanoparticles as expected from the larger amount of the high M_S soft phase. XMCD was used to obtain elemental specific hysteresis loops at the iron and manganese edges. The similarity between both loops corroborates the good exchange coupling between the layers. Although both XMCD loops show a similar behavior, the manganese loop present larger saturation fields and slightly larger coercivities than the iron one loops. These features reveal the hard-FiM behavior is taken by the manganese-based phase in spite of the soft-FiM for iron-based phase. The coupling between the core and shell is further investigated by analyzing first order reversal curves (FORC). The FORC switching field distributions (FORC-SFDs) present clear asymmetries related to the hard-FM|soft-FM character of the system. Finally a Monte Carlo simulations have been carried on in two different approaches i) soft-FiM|hard-FiM CS structure with a sharp interface and ii) with a graded interface. Both simulations confirm the strong exchange coupling of the system; however, the graded anisotropy case, with a smoother approach to saturation, seems to fit better our experimental results.



Cite this: DOI: 10.1039/c2nr30986f

www.rsc.org/nanoscale

PAPER

Strongly exchange coupled inverse ferrimagnetic soft/hard, $\text{Mn}_x\text{Fe}_{3-x}\text{O}_4/\text{Fe}_x\text{Mn}_{3-x}\text{O}_4$, core/shell heterostructured nanoparticles†A. López-Ortega,^a M. Estrader,^{*ab} G. Salazar-Alvarez,^b S. Estradé,^{cd} I. V. Golosovsky,^e R. K. Dumas,^f D. J. Keavney,^g M. Vasilakaki,^h K. N. Trohidou,^h J. Sort,^{ij} F. Peiró,^c S. Suriñach,^j M. D. Baró^j and J. Nogués^{ai}

Received 24th April 2012, Accepted 13th June 2012

DOI: 10.1039/c2nr30986f

Inverted soft/hard, in contrast to conventional hard/soft, bi-magnetic core/shell nanoparticles of $\text{Mn}_x\text{Fe}_{3-x}\text{O}_4/\text{Fe}_x\text{Mn}_{3-x}\text{O}_4$ with two different core sizes (7.5 and 11.5 nm) and fixed shell thickness (~ 0.6 nm) have been synthesized. The structural characterization suggests that the particles have an interface with a graded composition. The magnetic characterization confirms the inverted soft/hard structure and evidences a strong exchange coupling between the core and the shell. Moreover, larger soft core sizes exhibit smaller coercivities and loop shifts, but larger blocking temperatures, as expected from spring-magnet or graded anisotropy structures. The results indicate that, similar to thin film systems, the magnetic properties of soft/hard core/shell nanoparticles can be fine tuned to match specific applications.

1. Introduction

Core/shell (CS) nanoparticles are an efficient way to construct multicomponent systems that combine the distinct properties of the diverse constituents in a single structure.¹ Importantly, the advantage of multicomponent nanostructures lies not only in their multifunctionality, but also in the possibility to improve and tune the single-phase properties using the interactions between the different components. Moreover, the recent advances in wet chemistry synthesis have allowed an

unprecedented control of the structural parameters (*e.g.*, size, shape and composition) of the particles which leads to the possibility to fine tune the different functionalities of these multiphase systems.^{2–4} In the search for materials suitable for permanent magnets, biomedical applications, sensing applications, and future magnetic recording media, bi-magnetic CS nanoparticles, where both core and shell are magnetic materials, are attracting a great deal of interest, particularly since an inherent exchange bias can be used to overcome the superparamagnetic limit.⁵ In this context, standard and “inverse” bi-magnetic CS systems involving antiferromagnetic (AFM) and ferromagnetic (FM) phases structured as FM/AFM or AFM/FM have been extensively studied in the recent years.^{6–14} Interestingly, the so-called “exchange-spring” magnets,¹⁵ where hard and soft magnetic phases are exchange coupled, have been the focus of renewed effort in thin film systems for recording applications,¹⁶ although less attention has been paid to the case of nanoparticles.¹⁷ These bi-component materials can exhibit the desirable properties of both phases, *i.e.* large coercivities and large magnetization arising from the hard and soft phases, respectively.¹⁵ Hard–soft nanocomposites such as FePt–Fe₃Pt,¹⁸ NdFeB–FeCo,^{19,20} NdFeB–Fe,^{21,22} FePt–Fe₃O₄ (ref. 23 and 24) and FePt–CoFe₂O₄ (ref. 25) heterodimers have been prepared by mechanical milling,^{19–21} self-assembly processes¹⁸ or wet-chemistry.^{22–25} However, the limited intimate contact between both phases in heterodimer systems and the reduced homogeneity in the case of nanocomposites and self-assembly processes make these materials non-ideally suited to accomplish strong exchange coupling and enhanced properties. In this regard, core/shell nanoparticles, where the interface contact is maximized, would be more adequate. Hard/soft core/shell nanoparticles composed

^aCIN2(ICN-CSIC) and Universitat Autònoma de Barcelona, Catalan Institute of Nanotechnology, Campus de la UAB, 08193 Bellaterra (Barcelona), Spain. E-mail: martaestrader@gmail.com

^bDepartment of Materials and Environmental Chemistry, Stockholm University, 10691 Stockholm, Sweden

^cLENS-MIND-IN2UB, Departament d'Electrònica, Universitat de Barcelona, Martí i Franquès 1, E-08028 Barcelona, Spain

^dTEM-MAT, SCT, Universitat de Barcelona, Barcelona, Spain

^eSt Petersburg Nuclear Physics Institute, Gatchina, 188300 St Petersburg, Russia

^fDepartment of Physics, University of Gothenburg, 41296 Gothenburg, Sweden

^gAdvanced Photon Source, Argonne National Laboratory, Argonne, Illinois 60439, USA

^hInstitute of Materials Science, NCSR “Demokritos”, 153 10 Aghia Paraskevi, Attiki, Greece

ⁱInstitució Catalana de Recerca i Estudis Avançats (ICREA), Barcelona, Spain

^jDepartament de Física, Universitat Autònoma de Barcelona, 08193 Bellaterra, Spain

† Electronic supplementary information (ESI) available: Simulated elemental quantification at a given core/shell structure, XAS and XMCD spectra of CS2 nanoparticles and hysteresis loops after FC and ZFC for both CS1 and CS2 samples. See DOI: 10.1039/c2nr30986f

of FePt/Fe₃O₄,^{24,26–30} Fe/Fe₃O₄,^{31,32} CoFe₂O₄/MFe₂O₄ (M = Zn, Mn, Fe)³³ and Sm(Co_{1–x}Fe_x)/Fe₃O₄ (ref. 34) have shown, in some cases, an enhanced energy product of the bi-component system over the hard single phase.^{25,32,35} On the other hand, “inverse” soft/hard core/shell configurations have been less studied, and only a few examples, FePt/CoFe₂O₄,³⁰ MFe₂O₄/CoFe₂O₄ (M = Zn, Mn, Fe)³³ and γ -Fe₂O₃/CoFe₂O₄,³⁶ have been reported. There are a number of issues that are well known from thin film studies on spring-magnets that have not been addressed in nanoparticles. Amongst these are the strong dependence of the properties on the thickness of the two constituents³⁷ and the enhancement of the properties by intermixed interfaces³⁵ or graded anisotropy (*i.e.*, where the anisotropy changes *continuously* from hard to soft).³⁸

Herein we present an exhaustive structural and magnetic study of inverted soft/hard core/shell nanoparticles composed of Mn_xFe_{3–x}O₄/Fe_xMn_{3–x}O₄ with two different core sizes (7.5 and 11.5 nm) and a fixed shell thickness (~0.6 nm) obtained by seeded growth of manganese oxide using different Fe₃O₄ nanoparticles as seeds. The smooth hysteresis loops obtained from magnetometry and the compelling similarity between the element resolved loops obtained by soft X-ray magnetic circular dichroism indicate a strong core/shell exchange coupling. Furthermore, we show that the magnetic properties, *e.g.*, saturation magnetization, coercivity, loop shift or blocking temperature, are easily controlled by adjusting the size of the soft core.

2. Experimental

2.1. Synthesis

Unless stated, all starting materials were purchased from Sigma-Aldrich and used without further purification. The CS nanoparticles were synthesized following an earlier reported procedure where, in two steps, pre-made Fe₃O₄ nanoparticles were used as seeds to subsequently grow a Mn₃O₄ layer.³⁹ Firstly, Fe₃O₄ seeds were prepared following a similar method to that developed by Park *et al.*⁴⁰ in which a given amount of iron (III) oleate and 1 mmol of oleic acid were added into 36 mL of 1-octadecene. The mixture was heated under magnetic stirring, with a heating rate of 3 °C min⁻¹, up to 320 °C and kept for 30 min. The slurry was removed from the heating source and allowed to cool down to room temperature. Depending on the surfactant-to-metal molar ratio, [S]/[M], different particle sizes were obtained. Two [S]/[M] ratios were studied: [S]/[M] = 0.6 (*seed1* – large particles) and [S]/[M] = 0.3 (*seed2* – small particles).

Subsequently, the heterogeneous growth of the manganese oxide layer was carried out at the surface of the two different seeds following a slightly modified literature process by adding 42 mg of initial seeds in a solution containing 0.6 mmol of manganese (II) acetylacetonate, 0.6 mmol of 1,2-hexadecanediol, 0.3 mmol of oleylamine, 0.3 mmol of oleic acid and 40 mL of dibenzyl ether.³⁹ The slurry was mechanically stirred and heated, under an Ar controlled atmosphere, with a heating rate of 10 °C min⁻¹, to 200 °C and kept for 1 h. The flask was removed from the heating source and cooled down in Ar to 180 °C. The solution was then exposed to air and allowed to cool to room

temperature. Two different CS particles were obtained based on two seeds, *i.e.* CS1 (from the large seed1) and CS2 (from the small seed2). Both the Fe₃O₄ seeds and the CS nanoparticles were washed by several cycles of coagulation with ethanol, centrifugation at 2000 × *g*, disposal of supernatant solution and re-dispersion in hexane.

2.2. Characterization

Transmission electron microscopy. TEM images were obtained using a Jeol JEM-2010 microscope with a LaB₆ filament and a Jeol-JEM-2010F microscope with a field-emission gun operated at 200 kV. The nanoparticles were dispersed in hexane and then placed dropwise onto a holey carbon supported grid. The particle size of the different samples and its standard deviation were obtained by calculating the average number by manually measuring the equivalent diameters of >200 particles from TEM micrographs.

X-ray diffraction. XRD patterns were collected using a Panalytical X'Pert Pro diffractometer with Cu K α radiation. The measurements were carried out in a range of 10–100 2 θ in steps of 0.012° and collection time of 300 s. All diffraction patterns were analyzed using the FullProf code.⁴¹ Note that a simple fitting of the diffraction patterns by the Rietveld method using an isotropic approximation gives rise to unsatisfactory results due to non-uniform size effects. In these cases the numerical computation of the scattering intensity on the Debye formula was used.⁴² The diffraction profiles were satisfactorily described by implementing an artificial shape (platelet-like) for the shell component. Finally note that the diffraction signal from the shell is exceedingly weak to reliably refine the sizes and stoichiometry.

Electron energy loss spectroscopy. EEL spectra were acquired every 0.5 nm along the diameter of the nanoparticles at an energy range containing the O K, Mn L_{2,3} and Fe L_{2,3} edges, with an energy resolution of 0.8 eV. Mn/O and Fe/O quantifications were carried out using the Gatan Digital Micrograph commercial software. Importantly, data obtained for different particles of the CS1 sample showed no relevant differences.

X-ray absorption spectroscopy and X-ray magnetic circular dichroism. XAS and XMCD measurements were performed on dried CS nanoparticles spread onto carbon tape at the 4-ID-C beamline of the Advance Photon Source of the Argonne National Laboratory. Both XAS and XMCD spectra were recorded at the Fe and Mn L_{2,3} edges using total electron yield (TEY) mode at 10 K in a magnetic field of 50 kOe after field cooling (FC) from 300 K under an applied field of 50 kOe. The element resolved XMCD hysteresis loops, for the Fe and Mn L₃ edges, were acquired by recording the field dependence of the XMCD signals at the energies corresponding to the three main peaks of the Fe-edge (*i.e.*, 707.6, 708.7, 709.3 eV) and for the main energy of the Mn edge (640.1 eV). The XMCD signal was normalized by the area of the XAS spectra after correcting for the background. Note that since the Fe edge loops at the different energies were analogous only the one at *E* = 709.3 eV is used in the discussion.

Magnetic measurements. The magnetic properties of the nanoparticles were measured on tightly packed powdered samples using a superconducting quantum interference device (SQUID, Quantum Design) magnetometer with a 70 kOe maximum field. The magnetization *versus* temperature measurements were performed in zero field cooled (ZFC) and field cooled (FC) conditions in 50 Oe. After FC in 20 kOe from 300 K to 10 K, hysteresis loops were measured at different constant temperatures. Moreover, hysteresis loops were also measured at 10 K after ZFC from 300 K.

In addition to standard major loop measurements, a first-order reversal curve (FORC)^{43–46} analysis was conducted using the following procedure. After positive saturation the applied field is reduced to a given reversal field, H_R . From this reversal field the magnetization is then measured back towards positive saturation, thereby tracing out a single FORC. This process is repeated for a series of decreasing reversal fields, thus filling the interior of the major hysteresis loop, which can be seen as the outer boundary of the family of FORCs. The FORC distribution is then defined as a mixed second order derivative of the normalized magnetization:

$$\rho(H, H_R) \equiv -\frac{1}{2} \frac{\partial^2 M(H, H_R)/M_S}{\partial H \partial H_R}, \quad (1)$$

which is then plotted against (H, H_R) coordinates on a contour map. For a given reversal field, H_R , the magnetization is measured for increasing applied fields, H , and therefore $H \geq H_R$ by design. Following the measurement procedure the FORC distribution is read in a “top-down” fashion and from left to right for a particular reversal field. The FORC distribution provides a useful “fingerprint” of the reversal mechanism by mapping out, in (H, H_R) coordinates, only the *irreversible* switching processes. It is often useful to have a one-dimensional visualization of the irreversibility by projecting the FORC distribution onto the H_R -axis. This is equivalent to an integration over the applied field H :

$$\int \frac{\partial^2 M(H, H_R)}{\partial H \partial H_R} dH = \frac{\partial M(H_R)}{\partial H_R}, \quad (2)$$

and is termed a FORC-switching field distribution (FORC-SFD).

Monte Carlo simulations. Monte Carlo simulations were carried out considering a single spherical nanoparticle of radius R , expressed in lattice spacings, on a simple cubic lattice, with FiM order. The nanoparticle consists of a soft core (either 10.7 or 16.7 lattice spacings) and a hard shell of thickness equal to 3 lattice spacings. The outer layer of one lattice spacing is considered to be the surface of the nanoparticle. We use atomic-scale modeling where the spins in the particle interact with nearest neighbors Heisenberg exchange interaction, and at each crystal site they experience a uniaxial anisotropy. We consider the size of the atomic spins in the two sublattices of the FiM particle equal to 1 and 3/2, respectively, for both the core and the shell. The energy of the system includes the exchange interaction between the spins in the nanoparticle and the single-site anisotropy energy terms. In the presence of an external magnetic field, the total energy of the system is:

$$\begin{aligned} \mathcal{H} = & -J_{\text{core}} \sum_{i,j \in \text{core}} \vec{S}_i \cdot \vec{S}_j - J_{\text{IF}} \sum_{i \in \text{core}, j \in \text{shell}} \vec{S}_i \cdot \vec{S}_j - J_{\text{shell}} \sum_{i,j \in \text{shell}} \vec{S}_i \cdot \vec{S}_j \\ & - K_{\text{core}} \sum_{i \in \text{core}} (\vec{S}_i \cdot \hat{e}_i)^2 - K_{\text{IF}} \sum_{i \in \text{IF}} (\vec{S}_i \cdot \hat{e}_i)^2 - K_{\text{shell}} \sum_{i \in \text{shell}} (\vec{S}_i \cdot \hat{e}_i)^2 \\ & - K_{\text{srf}} \sum_{i \in \text{srf}} (\vec{S}_i \cdot \hat{e}_i)^2 - \vec{H} \cdot \sum_i \vec{S}_i. \end{aligned} \quad (3)$$

Here S_i and \hat{e}_i are the atomic spin and the unit vector in the direction of the easy axis at site i . The first three terms give the Heisenberg nearest neighbor exchange interaction between the spins in the core, in the shell and at the interface. We set exchange coupling as $J_{\text{core}} = -0.01J$ in the core, where J is defined as a dimensionless ferromagnetic exchange coupling constant taken as $J = 1$, $J_{\text{IF}} = 4 \times J_{\text{core}}$ at the interface and smaller in the shell ($J_{\text{shell}} = 0.5 \times J_{\text{core}}$) to account for its lower transition temperature. The following four terms are the anisotropy energies of the core, the interface, the shell and the surface, respectively. The anisotropy is assumed uniaxial and directed along the z -axis in the core, the shell and at the interface and random at the surface. The last term is the Zeeman energy. The anisotropies in the conventional core/shell structure are taken as $K_{\text{core}} = 0.01J$, $K_{\text{IF}} = 0.03J$, $K_{\text{shell}} = 0.08J$ and $K_{\text{srf}} = 0.6J$, respectively.

Importantly, to account for the chemical gradients, we also considered the case of graded anisotropy, similar to thin film systems.^{38,47} For such structures, the anisotropy energy term of the core or the shell is split into different layers. For example, we have considered that the inner core K_{core} is maintained constant at $0.01J$, while as the layers get closer to the interface the anisotropy gradually increases as 0.02, 0.03, 0.04, 0.05 and 0.06 J (for the top 5 layers in the core) and 0.07 and 0.08 J for the shell and finally we maintain $K_{\text{srf}} = 0.6J$.

To take into consideration the random distribution of easy axis directions with respect to the applied fields present experimentally, we have calculated hysteresis loops for different angles between the easy axis and the applied field direction. The results for the magnetization are averaged as:

$$\langle M \rangle = \frac{1}{4\pi} \int_0^{2\pi} d\varphi \int_0^\pi d\theta M(\theta) \cos \theta = \frac{1}{2} \int_0^\pi d\theta M(\theta) \cos \theta \quad (4)$$

Note that the different parameters are given with respect to J , *i.e.*, the field H is given in units of $J \text{ g}^{-1} \mu_B^{-1}$, the temperature T in units $J k_B^{-1}$ and the anisotropy coupling constants K in units of J . The magnetization M is normalized to the saturation magnetization, M_S .

The Monte Carlo simulations are performed using the Metropolis algorithm⁴⁸ where the microstructure and the temperature are explicitly included. We perform our calculations of the hysteresis loops at a low temperature after a field cooling procedure at a constant rate for a cooling field of $H_{\text{FC}} = 0.4 J \text{ g}^{-1} \mu_B^{-1}$, which is in the same field range as the one used experimentally.

3. Results and discussion

3.1. Structural and morphological characterization

Fig. 1 shows the transmission electron microscopy (TEM) images of the Fe_3O_4 seeds (Fig. 1a and b for samples seed1 and seed2,

respectively) and the CS nanoparticles (Fig. 1c and d for samples CS1 and CS2, respectively). Particle size histograms of both the seeds and the CS nanoparticles are depicted in Fig. 1e and f corresponding to samples seed1–CS1 and seed2–CS2, respectively. As can be seen, all histograms are well fitted by a Gaussian distribution, showing a unique size population, with a narrowly distributed diameter (deviation <10%). After the growth of the Mn oxide layer, the diameter of the CS nanoparticles becomes 8.6(0.6) (CS2) and 12.6(1.0) (CS1) compared to the initial 7.5(0.6) nm (seed2) and 11.5(0.9) nm (seed1), respectively. Importantly, upon comparing the sizes of the seeds and CS nanoparticles, there is a clear shift of 1.1 nm to larger diameters both for CS1 and CS2 samples, indicating that a Mn oxide shell of roughly 0.6 nm thickness is indeed grown on top of the seeds. Moreover, the similarity between the thicknesses of the two shells suggests that the seed-growth procedure does not depend strongly on the initial seed size.

High resolution TEM (HR-TEM) images of seed2, CS1 and CS2 and their respective fast Fourier transform (FFT) are shown in Fig. 2. The FFT analysis obtained from the HR-TEM images of the CS samples (Fig. 2e and f) confirms the presence of a new phase in contrast to the data of the seeds which display a purely cubic structure (Fig. 2d). In both CS samples two sets of different

diffraction spots attributed to an iron oxide cubic spinel phase [(111)_c $d = 0.481$ nm, (220)_c $d = 0.290$ nm, (311)_c $d = 0.248$ nm and (331)_c $d = 0.180$ nm (JCPDS card no. 82-1533)] and a manganese oxide tetragonal spinel phase [(200)_t $d = 0.288$ nm, (211)_t $d = 0.248$ nm, (004)_t $d = 0.237$ nm and (204)_t $d = 0.183$ nm (JCPDS card no. 24-0734)] can be observed. Remarkably, while the tetragonal (200)_t, (211)_t and (204)_t diffraction planes overlap with the cubic (220)_c, (311)_c and (331)_c ones, the plane (004)_t (highlighted by arrows in Fig. 2e and f) belongs only to a tetragonal spinel phase.

The analysis of the XRD patterns corresponding to the iron oxide seeds and the CS nanoparticles (Fig. 3) revealed that the sizes of the seeds are similar to the corresponding core sizes of the CS nanoparticles (see Table 1). Moreover, these values are consistent with those obtained from TEM analysis. Interestingly, the refinement of the site occupancies shows that both the core and the seeds have a near stoichiometric spinel Fe₃O₄ composition. However, there are small differences in the occupancy of the seeds, *i.e.*, (Fe_{0.82(1)})[Fe_{0.90(1)}]₂O₄ and the CS particles, *i.e.*, (M_{0.90(1)})[M_{0.96(1)}]₂O₄ (M = Fe and Mn) which imply that probably some Mn ions have diffused into the core during the synthesis of the CS particles. Note that it is not possible to distinguish between iron and manganese ions using X-rays, hence it is difficult to give a more quantitative account of the manganese diffusion. A comparison of the refined cell parameters for the core with the reported values for the Mn₃O₄–Fe₃O₄ system⁴⁹ indicates that the core can incorporate up to 50% of Mn atoms. Concerning the shell, the comparison of the obtained cell parameters with the literature values⁴⁹ unambiguously evidences that in sample CS1 about 10% of manganese ions of the Mn₃O₄ shell are substituted by iron ions, while maintaining the Mn₃O₄ tetragonal structure.

In order to gain further insight into the structure of the CS particles, the local electron energy loss spectra (EELS) were analyzed by evaluating the M–L_{2,3} onset and the M/O ratio (M = Mn and Fe) to obtain the distributions of the different ions across the particles, see Fig. 4. The EELS analysis reveals the presence of two clearly differentiated regions in the particle, *i.e.*, a core and a shell, the former being iron rich and the latter one manganese rich. However, remarkably, both iron and manganese ions were found across the whole particle (Fig. 4e). Bearing in mind these results, together with the XRD and FFT studies where the existence of a tetragonal spinel phase was confirmed, different CS structures (*i.e.*, sizes and compositions) were simulated to match the observed metal distribution. The best correspondence was found for a MnFe₂O₄(10.2 nm)/FeMn₂O₄(1.2 nm) CS structure, as schematically shown in Fig. 4b, with an iron rich core and a manganese rich shell. Interestingly, using compositional gradients throughout the particles (rather than fixed core/shell structures) *e.g.*, Mn_{0.75}Fe_{2.25}O₄(8 nm)/Fe_{1.75}Mn_{1.25}O₄(0.6 nm) shell 1/Fe_{1.5}Mn_{1.5}O₄(0.6 nm) shell 2/Fe_{0.75}Mn_{2.25}O₄(0.6 nm) shell 3, leads to a further improvement of the agreement between the simulated and experimental results (see Fig. S1 in the ESI†). It is known that mixed spinel phases can preserve their initial crystal symmetry before reaching a critical doping value, for instance MnFe₂O₄ (*Fd3m*) and FeMn₂O₄ (*I41/amd*) would keep the cubic and tetragonal structure of Fe₃O₄ and Mn₃O₄, respectively.⁴⁹ The results indicate that an interdiffusion of iron and manganese

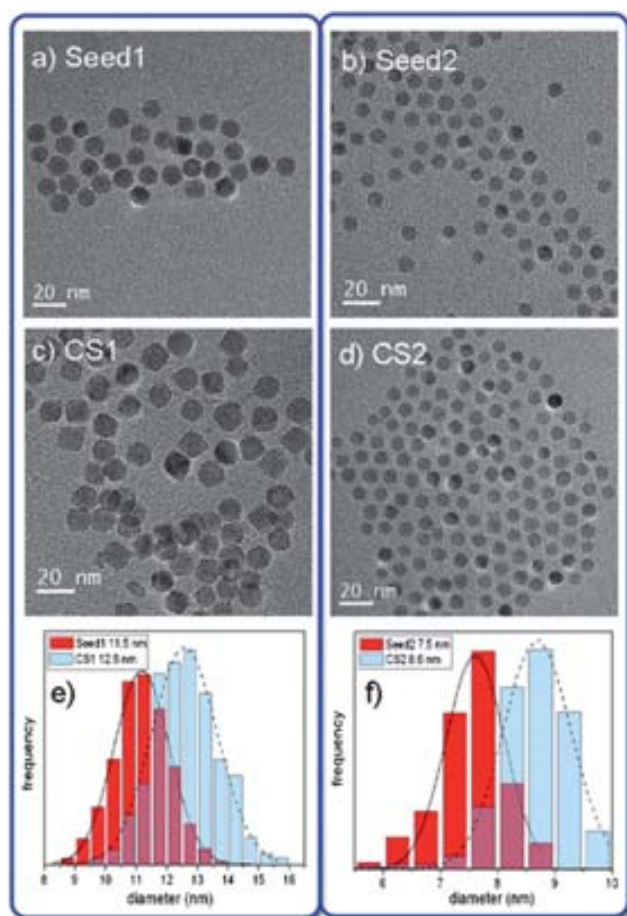


Fig. 1 TEM images of iron oxide seed particles, (a) seed1 and (b) seed2 and of the corresponding CS nanoparticles, (c) CS1 and (d) CS2. Histograms of the different nanoparticles, (e) seed1–CS1 and (f) seed2–CS2.

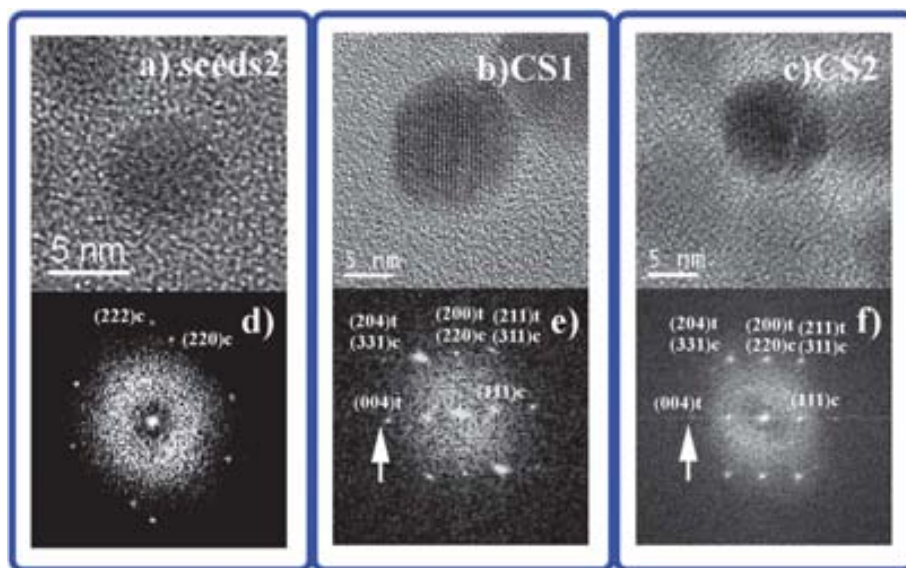


Fig. 2 HR-TEM images of (a) seed2, (b) CS1 and (c) CS2 nanoparticles together with their respective FFT analysis, (d–f). The diffraction spots in FFT images for cubic and tetragonal structures are marked with c and t, respectively. The pure tetragonal spots are highlighted by arrows.

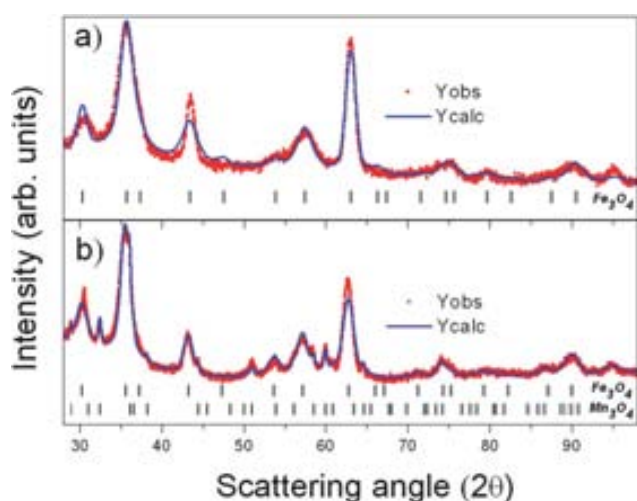


Fig. 3 Profile analysis of the X-ray diffraction patterns from seed1 (a) and the CS1 nanoparticles (b). The observed profile (in red) and the calculated (in blue) are both shown in the graphs. The vertical bars mark the position of Bragg reflections as indicated.

Table 1 Unit cell parameters and sizes (both in Å) for the different seeds and CS nanoparticles. The figure in parenthesis corresponds to the standard deviation in the last digit

| Sample | Core Fe ₃ O ₄ | | Shell Mn ₃ O ₄ | |
|--------|-------------------------------------|-------|--------------------------------------|----------|
| | <i>a</i> | Size | <i>a</i> | <i>c</i> |
| CS1 | 8.3801(6) | 93(1) | 5.767(1) | 9.414(2) |
| Seed1 | 8.3501(5) | 91(2) | | |
| CS2 | 8.3803(5) | 73(1) | 5.775(1) | 9.432(2) |
| Seed2 | 8.343(1) | 68(3) | | |

ions between core and shell has taken place leading to mixed Fe–Mn spinel CS particles.⁵⁰ The ion diffusion and the concomitant change in the composition of the CS nanoparticles

can be attributed to a soft annealing while exposing the slurry to air at 180 °C. Note that the nanoparticles in sample CS2 displayed a rather poor signal-to-noise ratio since, given the small size of CS2 nanoparticles, the signal at the Fe- and Mn-edges was rather weak compared to the carbon signal arising from the organic surfactants and thus the EEL Spectra for CS2 were not analysed.

Additional evidence for the graded composition of the CS particles was obtained by using X-ray absorption spectroscopy (XAS) and X-ray magnetic circular dichroism (XMCD). Importantly, the total electron yield (TEY) mode depends on the probing depth (λ_x), which for soft X-rays can be taken to be of the order of 10 nm for most metal oxides.⁵¹ Assuming such λ_x and that the nanoparticles are composed of, approximately, 85%–MnFe₂O₄/15%–FeMn₂O₄, the spectra should be understood as a convolution of the signal from the shell and the core. Fig. 5 shows an example of XAS and XMCD spectra obtained at Fe and Mn L_{2,3} edges for sample CS1. From the theoretical XAS spectra of Fe²⁺ ions in octahedral and Fe³⁺ ions in octahedral and tetrahedral environments, the peak *I*₁ in Fig. 5b can be associated to the presence of Fe²⁺ in Oh positions while peak *I*₂ correlates to Fe³⁺ ions located in Oh and Td environments.⁵² By analyzing the ratio of the different peak intensities, *I*₁/*I*₂, it is possible to obtain qualitative information about the cation concentration in each oxide phase.⁵³ Given the structure of Fe₃O₄, (Fe³⁺)[Fe³⁺Fe²⁺]₂O₄, and γ -Fe₂O₃, (Fe³⁺)[Fe³⁺_{5/3}□_{1/3}]₂O₃ one would expect *I*₁/*I*₂ ratios of 0.53 and 0.19 for Fe₃O₄ and γ -Fe₂O₃, respectively.⁵¹ The experimental *I*₁/*I*₂ value for both samples CS1 and CS2 is 0.4. This implies that the samples have an intermediate composition between γ -Fe₂O₃ and Fe₃O₄. Therefore, the presence of a MnFe₂O₄ structure, (Fe³⁺)[Fe³⁺Mn²⁺]₂O₄,^{52,54} without Fe²⁺ ions in octahedral positions, would fit adequately in this scenario in agreement with the EELS results (particularly assuming that due to the thin shell with small iron content most of the XAS iron signal arises from the core). On the other hand the XAS spectrum at the Mn L_{2,3} edge (Fig. 5a) resembles that of pure tetragonal

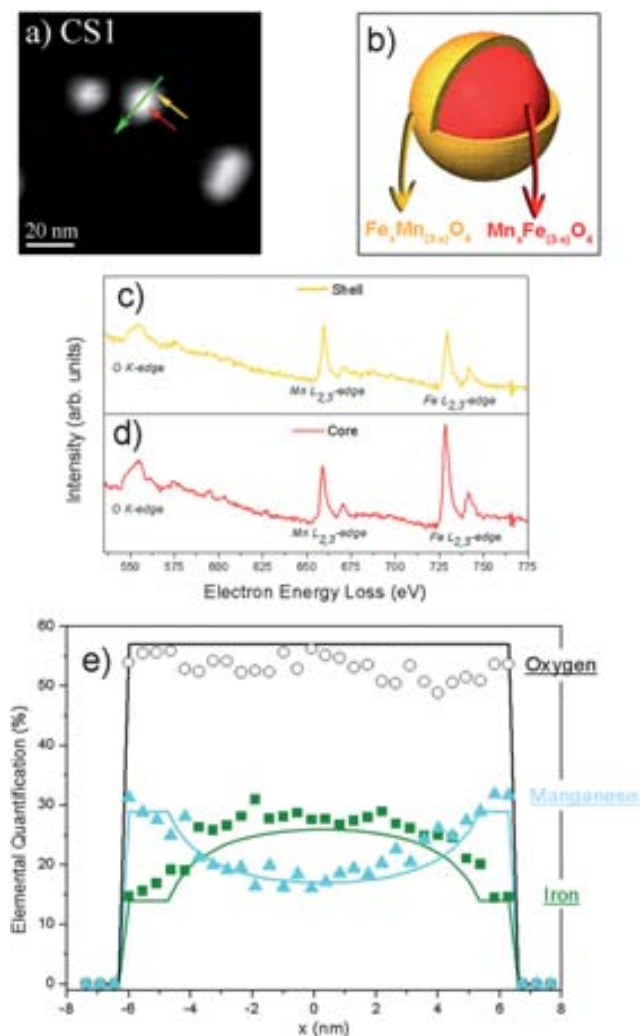


Fig. 4 (a) High-angle annular dark field (HAADF) image of CS1 nanoparticles, where the approximate positions where the local spectra were obtained are shown by a green arrow. (b) Schematic representation of the CS nanoparticles simulated from the EELS analysis. (c) and (d) show EELS spectra for the shell and core, respectively, as indicated by yellow and red arrows, respectively, in (a). (e) Elemental quantification along the particle diameter for Fe (squares), Mn (triangles) and O (circles). The solid lines represent the simulated elemental profile for a particle with a MnFe_2O_4 (10.2 nm) core/ FeMn_2O_4 (1.2 nm) shell structure.

Mn_3O_4 , $(\text{Mn}^{2+})[\text{Mn}^{3+}]_2\text{O}_4$.⁵⁵ However, it has a lower intensity ratio, $I_1/I_2 = 0.7$, than expected for Mn_3O_4 , *i.e.*, $I_1/I_2 = 0.87$, but larger than the corresponding one for MnFe_2O_4 , $I_1/I_2 = 0.5$.⁵⁴ Hence, the Mn L_{2,3} signal can be understood as a mixed signal arising both from the shell, close to a tetragonal FeMn_2O_4 phase, and the core, with a cubic MnFe_2O_4 structure.

Concerning the XMCD spectra, the signal of the iron edge (Fig. 5d) is somewhat consistent with those of pure cubic spinel iron oxides (Fe_3O_4 and $\gamma\text{-Fe}_2\text{O}_3$) spectra,⁵³ although some small deviations attributed to the presence of the mixed MnFe_2O_4 oxide can be observed. Concretely, the different intensity peak ratios of the first two peaks of the iron XMCD signal with respect to pure iron oxides can be interpreted in the same way as the XAS analysis regarding the concentration of Fe^{2+} ions in octahedral positions.^{54,56} In contrast, the spectrum at the manganese

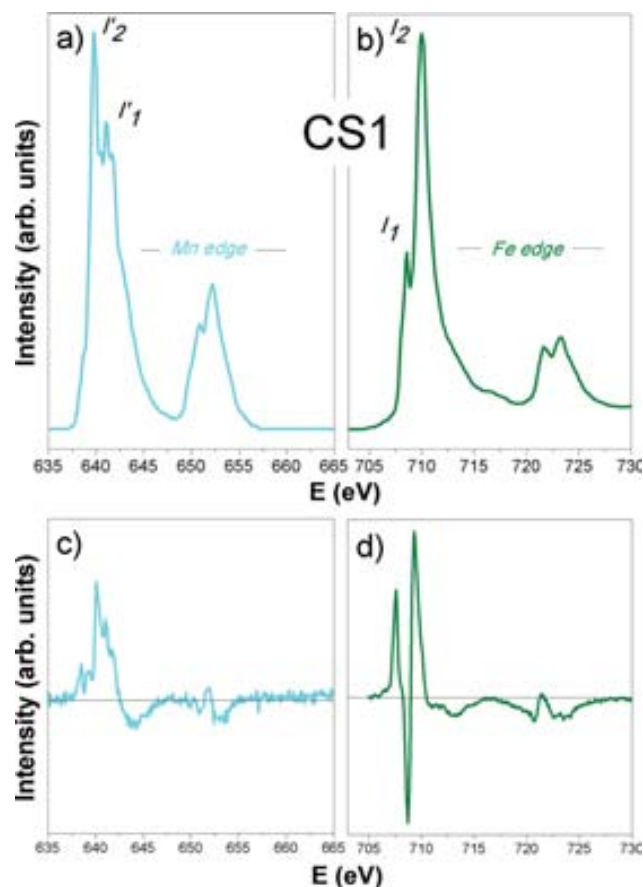


Fig. 5 (Top) XAS and (bottom) XMCD spectra at the (left) Mn and (right) Fe edges of CS1 nanoparticles.

edge (Fig. 5c) cannot be associated to any single phase and can be clearly ascribed to a mixed XMCD signal, *e.g.*, arising from tetragonal FeMn_2O_4 and cubic MnFe_2O_4 oxide structures.⁵⁵ Note that the lack of XMCD studies at the Mn L_{2,3} edge on pure FeMn_2O_4 (in bulk or nanoparticle form) makes a more detailed analysis rather complex. Similar results were found for CS2 nanoparticles, both for the XAS and XMCD analysis, see Fig. S2†.

3.2. Magnetic properties

Fig. 6a shows the ZFC/FC magnetization curves for the CS1 and CS2 nanoparticles. Although at high temperatures both samples exhibit the characteristics of superparamagnetic systems⁵⁷ with blocking temperatures, $T_{B,1}^{\text{CS1}} = 205$ K and $T_{B,1}^{\text{CS2}} = 115$ K, both systems exhibit a second transition at $T_{B,2} \sim 40$ K. However, the features at $T_{B,2}$ are more evident for CS2. Moreover, as can be seen in Fig. 6b, the low temperature (10 K) hysteresis loops show that the saturation magnetization, M_S , for CS1 ($M_S^{\text{CS1}} = 48$ emu g^{-1}) is higher than that for CS2 ($M_S^{\text{CS2}} = 40$ emu g^{-1}). Upon enlarging it becomes clear that the loops are rather smooth, *i.e.*, no kinks – typical of two phase systems¹⁵ can be observed, Fig. 6b. Interestingly, both samples exhibit a loop shift in the field axis, H_E (*i.e.*, exchange bias), with respect to the zero field cooled loop (Fig. S3†), and moderate coercivities, H_C ,⁶ that vanish around 50–60 K, both parameters being larger for CS2 (Fig. 7).

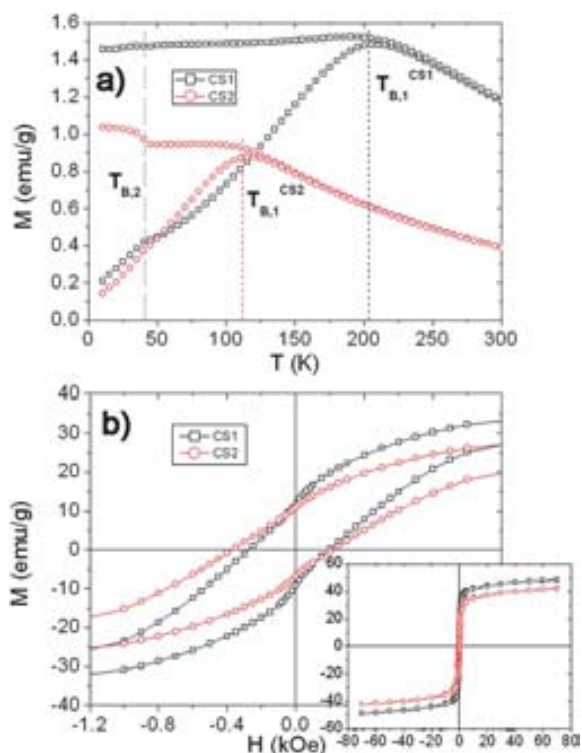


Fig. 6 (a) Temperature dependence of the field cooled (FC) and zero field cooled (ZFC) magnetizations and (b) an enlarged view at low field of the hysteresis loops at 10 K for CS1 and CS2 nanoparticles. The inset shows the hysteresis loops in the full field range.

These results are consistent with the proposed $\text{Mn}_x\text{Fe}_{3-x}\text{O}_4/\text{Fe}_x\text{Mn}_{3-x}\text{O}_4$ core/shell structure. Concerning the different T_B , the high temperature ones ($T_{B,1}$) could be related to the cubic ferrimagnetic (FiM) $\text{Mn}_x\text{Fe}_{3-x}\text{O}_4$ phase that constitutes the core of the nanoparticle, while the low temperature one ($T_{B,2}$) to the tetragonal FiM $\text{Fe}_x\text{Mn}_{3-x}\text{O}_4$ phase forming the shell. Thus, the lower $T_{B,1}$ for CS2 can be easily explained by its smaller core volume since $T_B = KV/25 k_B$,⁵⁷ (where K is the magnetic anisotropy, V the volume and k_B the Boltzmann constant). In fact, assuming that the anisotropies remain the same in both cores, the ratio $T_{B,1}^{\text{CS2}}/T_{B,1}^{\text{CS1}}$ leads to a volume ratio in rough concordance with the initial seed sizes. In principle, similar effects should occur for $T_{B,2}$ since, although the shell thickness is the same for both systems, the core sizes vary and the corresponding shell volumes should be different. The origin of this $T_{B,2}$ is probably two-fold. First, FeMn_2O_4 is known to have a very strong temperature dependence of K , with a sharp increase in K around 50–60 K.^{58,59} Thus, when K reaches a certain threshold the system becomes blocked. Moreover, since the $\text{Fe}_x\text{Mn}_{3-x}\text{O}_4$ shell phase exhibits a tetragonal structure with a non-stoichiometric structure, probably close to that of Mn_3O_4 (as hinted from the XRD lattice parameters and the EELS graded composition simulation), a magnetic behaviour similar to that of Mn_3O_4 could be expected. In this sense, the second temperature transition present in both samples, $T_{B,2} \sim 40$ K, would be consistent with the $T_C = 40$ K of bulk Mn_3O_4 , as expected from the strong dependence of T_C on the Mn content for Mn-rich $\text{Fe}_x\text{Mn}_{3-x}\text{O}_4$.^{49,60,61} Similarly, the larger M_S

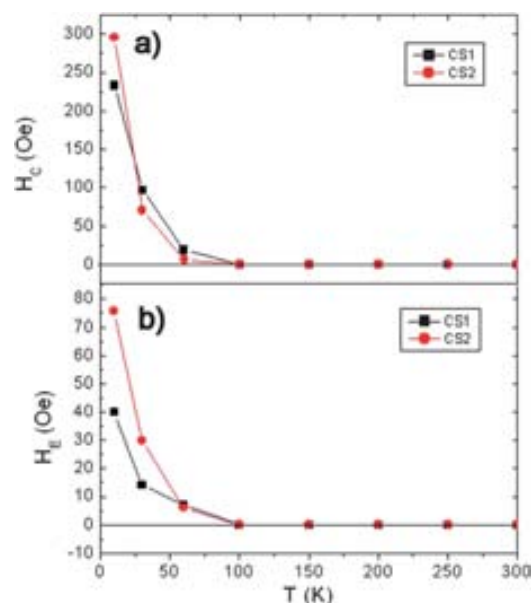


Fig. 7 Temperature dependence of (a) the coercivity, H_C , and (b) the loop shift, H_E , for CS1 and CS2 nanoparticles. The lines are guides to the eye.

exhibited by CS1 is consistent with its larger core, since the relative contribution of the shell (with a smaller M_S than that of the core⁶²) should be smaller for larger particles. This core/shell volume ratio also explains the more prominent features at $T_{B,2}$ shown by CS2.

Concerning the presence of exchange bias and moderate coercivities, although these effects are expected for an exchange coupled antiferromagnetic AFM/FM systems, they can also be found in coupled soft FiM (or FM) and hard FiM (or FM).⁶ In the current core/shell nanoparticles, assuming the composition of the shell is in the range $\text{Mn}_3\text{O}_4\text{--FeMn}_2\text{O}_4$, at 10 K the anisotropy would be expected to be about $|K_{\text{shell}}| \sim 5 \times 10^5$ to 1×10^6 erg cm^{-3} .^{58,63,64} In contrast, if the core composition is in the range $\text{Fe}_3\text{O}_4\text{--MnFe}_2\text{O}_4$, the corresponding anisotropy would be $|K_{\text{core}}| \sim 2 \times 10^5$ erg cm^{-3} .^{58,65} Consequently, our core/shell particles can be considered as an ‘inverted’ soft/hard system, although the difference in $K_{\text{shell}} - K_{\text{core}}$ may not be as large as in some of the typical hard/soft spring-magnet systems.¹⁵

In AFM/FM thin film systems it is well established that H_C and H_E are inversely proportional to the thickness (size) of the FM phase. Thereby, by drawing an analogy, in soft/hard systems it is accepted that $H_C, H_E \propto 1/\text{size}_{(\text{soft-FM})}$. Thus, the smaller H_E and H_C for CS1 arise from the larger diameter of its core. Finally, the temperature dependence of H_C and H_E is controlled by the phase with lowest T_B , *i.e.*, the hard shell phase, in analogy with most of the standard AFM/FM systems.⁶ Interestingly, the coercivity of both CS particles is relatively small compared with that expected for $\text{Mn}_3\text{O}_4\text{--FeMn}_2\text{O}_4$ (forming the shell).¹² In analogy with thin film systems, this implies that the soft core and the hard shell are strongly exchange coupled as expected from their small size (smaller than the domain wall width) and their similar anisotropies.^{15,37} This leads to smooth loops with increased M_S and reduced H_C , with respect to the pure hard Mn_3O_4 phase.

To gain further insight into the core/shell structure of the nanoparticles, we acquired element-specific XMCD hysteresis loops at the iron and manganese edges (shown in Fig. 8). Although the overall shape of the XMCD hysteresis loops at both edges is rather similar, their approach to saturation shows clear differences. Namely, the loop taken at the iron edge saturates at considerably lower fields than the loop corresponding to manganese (see Fig. 8 for CS1). Remarkably, H_C of both elements is similar for both samples. However, while for CS1 $H_C(\text{Mn})$ and $H_C(\text{Fe})$ are roughly the same, within the error, for CS2 $H_C(\text{Mn})$ is slightly larger than $H_C(\text{Fe})$ (see inset in Fig. 8). These results are in concordance with the magnetometry hysteresis loops where CS2, with proportionally more Mn, exhibits both an enhanced H_C and larger saturation field than those of CS1. The element resolved loops allow us to assign these features to the presence of a magnetically harder manganese-based phase. Given that, nominally, the iron and the manganese hysteresis loops should mainly correspond to the core and the shell, respectively, the element specific hysteresis loops confirm the inverse soft/hard core/shell structure of the nanoparticles. Importantly, the similarities between the Fe and Mn contributions to the hysteresis loops imply again a strong coupling between the core and the shell. However, the concomitant overlap of diverse contributions in the XMCD spectra (due to simultaneous interdiffusion of iron and manganese ions between the core and the shell) makes a quantitative analysis rather complex.

The coupling between the core and shell is further investigated by analyzing the first order reversal curves (FORC). The measured family of FORC curves is shown in Fig. 9a and b for samples CS1 and CS2, respectively. The major loop, seen as the outer boundary of the FORCs, shows the expected exchange bias. The resultant FORC distributions, shown as insets in Fig. 9a and b, are both broad single peaks, consistent with prior nanoparticle FORC distributions.⁴⁴ The broadness of the peaks can be attributed to distributions in size, anisotropy easy axis direction and strength, and exchange coupling. The FORC switching field distributions (FORC-SFDs), plotted in Fig. 9c, show a clear asymmetry for both the CS1 and CS2 samples, where the initial rapid onset of reversal ($H_R \sim +500$ Oe) is

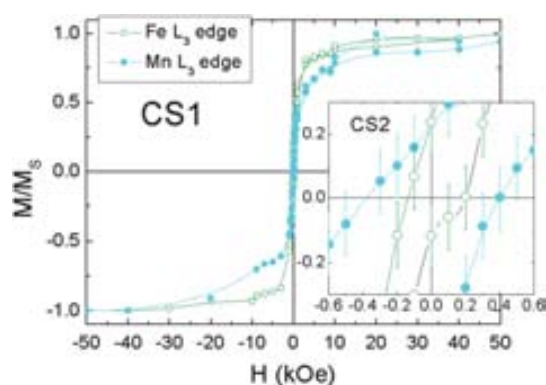


Fig. 8 Element resolved XMCD hysteresis loop at the iron edge (709.3 eV – open symbols) and manganese edge (640.1 eV – filled symbols) for sample CS1. The inset shows an enlargement of the hysteresis loops for sample CS2. The lines are guides to the eye.

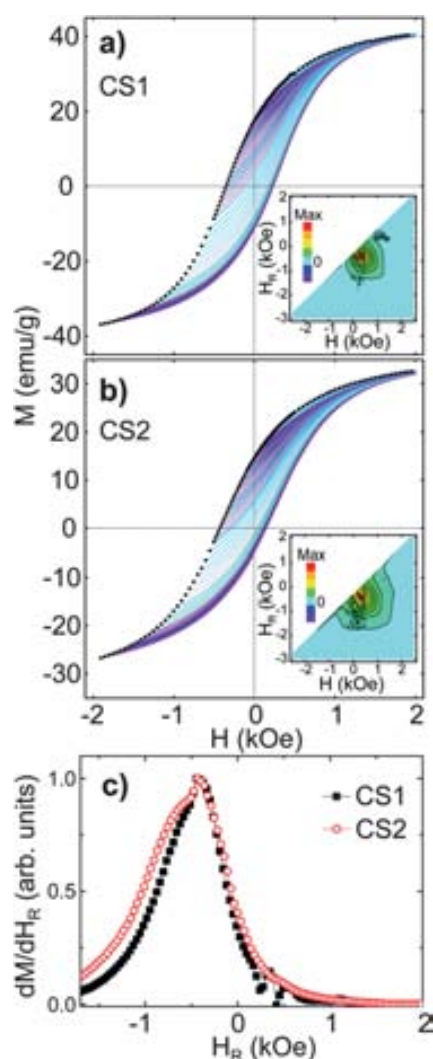


Fig. 9 Families of FORCs, whose starting points are represented by black dots, for samples (a) CS1 and (b) CS2 with the corresponding FORC distributions plotted in (H, H_R) coordinates shown as insets. The resultant FORC-SFDs are shown in (c).

followed by a more gradual and extended switching tail towards negative H_R values. Similar asymmetric FORC-SFDs have been observed in hard/soft and graded anisotropy composite films^{38b,45,46} where the extended hump can be attributed to the more negative H_R needed to switch the high anisotropy components. Note that single phase nanoparticles similar to the core (*i.e.*, without shell) exhibit symmetric peaks in the FORC-SFD. Interestingly, sample CS2 approaches negative saturation more gradually than CS1, suggesting a more dominant hard phase component, which is also consistent with the larger exchange bias and coercivity observed in this sample at 10 K.

The hysteresis loops were simulated by using Monte Carlo based on a (a) conventional core/shell model (*i.e.*, a single value for the interface anisotropy; Fig. 10a) a graded anisotropy model (Fig. 10b). As can be seen in the figures, both approaches capture the main features of the experimental loops. For example, the smaller nanoparticles exhibit larger H_C and H_E than the bigger ones. Similarly, in the moderate field range the small particles have a broader loop both in the experimental and

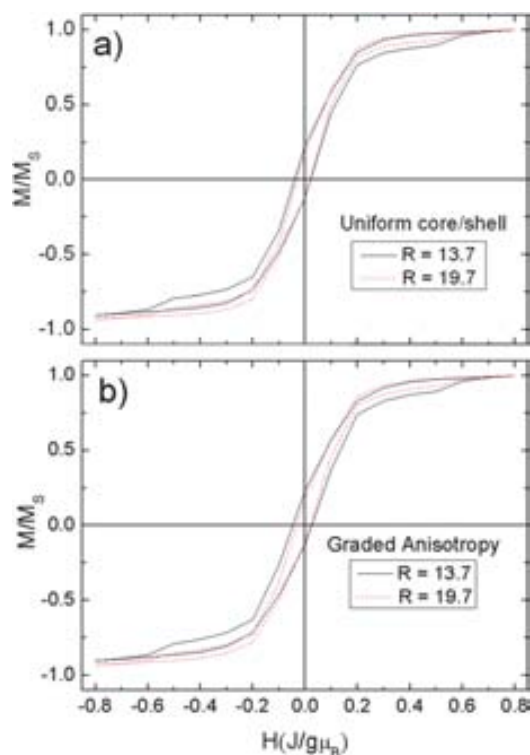


Fig. 10 Simulated hysteresis loops for the $R = 13.7$ and 19.7 lattice spacings nanoparticles using a (a) uniform core/shell and (b) graded anisotropy models of the nanoparticles.

simulated loops. Moreover, the calculations clearly show that the high field features are dominated by the shell, as hinted by the XMCD results. Most importantly, the ratio of core/shell anisotropies needed to properly simulate the experimental loops is in concordance with the core/shell anisotropy ratio of the phases deduced from the structural characterization. Hence, the Monte Carlo simulations confirm the strongly exchange coupled inverse soft/hard core/shell structure of the nanoparticles. Finally, comparing the simulation of the conventional core/shell structure and the graded anisotropy, although both models give rise to similar overall results, the latter model gives a somewhat smoother approach to saturation, similar to what is observed experimentally. Thus, the simulations might hint at a possible graded anisotropy character to the nanoparticles.

4. Conclusions

Core/shell nanoparticles with a narrow size distribution have been synthesized using a seeded growth procedure. Two CS nanoparticles with different core size and equal shell thickness have been presented. Interestingly, in both cases an iron and manganese ion interdiffusion has been found, leading to an inverse soft/hard ferrimagnetic $\text{Mn}_x\text{Fe}_{3-x}\text{O}_4/\text{Fe}_x\text{Mn}_{3-x}\text{O}_4$ core/shell structure, as opposed to the conventional hard/soft systems. The particles display a strong exchange coupling between the soft core and hard shell as expected from the core and shell dimensions. The coupling also results in a loop shift along the field axis and a coercivity increase, which are more pronounced for the samples with smaller core size. Thus, the fine control of the

magnetic properties by the soft/hard coupling could render novel types of core/shell nanoparticles suitable for applications such as permanent magnets or in magnetic shielding.

Acknowledgements

This work is supported by the 2009-SGR-1292 and 2009-SGR-35 projects of the Generalitat de Catalunya, by the MAT2010-20616-C02, MAT2011-27380-C02-01, MAT2010-16407 and CSD2009-00013 projects of the Spanish Ministry of Science and Innovation (MICINN), the ONDA project (no. FP7-PEOPLE-2009-IRSES-247518) of the European Union and the Russian grants RFBR-10-02-00576 and MESRF-16.518.11.7034. The authors thank P. Gambardella and J. J. Kavich for useful discussions. I. V. G. thanks the Generalitat de Catalunya for his sabbatical fellowship (2010 PIV 00096). M. D. B. was partially supported by an ICREA Academia award. Use of the Advanced Photon Source was supported by the U.S. Department of Energy, Office of Science, Office of Basic Energy Sciences, under Contract DE-AC02-06CH11357.

References

- 1 W. Schärfl, *Nanoscale*, 2010, **2**, 829.
- 2 H. Zeng and S. Sun, *Adv. Funct. Mater.*, 2008, **18**, 391.
- 3 R. Costi, A. E. Saunders and U. Banin, *Angew. Chem., Int. Ed.*, 2010, **49**, 4878.
- 4 L. Carbone and P. D. Cozzoli, *Nano Today*, 2010, **5**, 449.
- 5 V. Skumryev, S. Stoyanov, Y. Zhang, G. Hadjipanayis, D. Givord and J. Nogués, *Nature*, 2003, **423**, 850.
- 6 J. Nogués, J. Sort, V. Langlais, V. Skumryev, S. Suriñach, J. S. Muñoz and M. D. Baró, *Phys. Rep.*, 2005, **422**, 65.
- 7 O. Iglesias, A. Labarta and X. Batlle, *J. Nanosci. Nanotechnol.*, 2008, **8**, 2761.
- 8 W. Liu, W. Zhong and Y. W. Du, *J. Nanosci. Nanotechnol.*, 2008, **8**, 2781.
- 9 I. S. Lee, N. Lee, J. Park, B. H. Kim, Y. W. Yi, T. K. Kim, I. H. Lee, S. R. Paik and T. Hyeon, *J. Am. Chem. Soc.*, 2006, **128**, 10658.
- 10 O. Masala and R. Seshadri, *J. Am. Chem. Soc.*, 2005, **127**, 9354.
- 11 D. W. Kavich, J. H. Dickerson, S. V. Mahajan, S. A. Hasan and J.-H. Park, *Phys. Rev. B: Condens. Matter Mater. Phys.*, 2008, **78**, 174414.
- 12 G. Salazar-Alvarez, J. Sort, S. Suriñach, M. D. Baró and J. Nogués, *J. Am. Chem. Soc.*, 2007, **129**, 9102.
- 13 I. V. Golosovsky, G. Salazar-Alvarez, A. López-Ortega, M. González, J. Sort, M. Estrader, S. Suriñach, M. D. Baró and J. Nogués, *Phys. Rev. Lett.*, 2009, **102**, 247201.
- 14 A. López-Ortega, D. Tobia, E. Winkler, I. V. Golosovsky, G. Salazar-Alvarez, S. Estradé, M. Estrader, J. Sort, M. A. González, S. Suriñach, J. Arbiol, F. Peiró, R. D. Zysler, M. D. Baró and J. Nogués, *J. Am. Chem. Soc.*, 2010, **132**, 9398.
- 15 E. E. Fullerton, J. S. Jiang and S. D. Bader, *J. Magn. Magn. Mater.*, 1999, **200**, 392.
- 16 R. H. Victora and X. Shen, *IEEE Trans. Magn.*, 2005, **41**, 537.
- 17 N. A. Frey, S. Peng, K. Cheng and S. Sun, *Chem. Soc. Rev.*, 2009, **38**, 2532.
- 18 H. Zeng, J. Li, J. P. Liu, Z. L. Wang and S. Sun, *Nature*, 2002, **420**, 395.
- 19 C. W. Kim, Y. H. Kim, H. G. Cha and Y. S. Kang, *Mol. Cryst. Liq. Cryst.*, 2007, **464**, 583.
- 20 C. W. Kim, Y. H. Kim, H. G. Cha, J. C. Kim and Y. S. Kang, *Mol. Cryst. Liq. Cryst.*, 2007, **472**, 545.
- 21 C. W. Kim, Y. H. Kim, D. K. Lee, I. C. Jeong, H. W. Kwon and Y. S. Kang, *Solid State Phenom.*, 2007, **119**, 147.
- 22 D. K. Lee, H. G. Cha, Y. H. Kim, C. W. Kim, E. S. Ji and Y. S. Kang, *J. Nanosci. Nanotechnol.*, 2009, **9**, 4453.
- 23 A. Figuerola, A. Fiore, R. D. Corato, A. Falqui, C. Giannini, E. Micotti, A. Lascialfari, M. Corti, R. Cingolani, T. Pellegrino, P. D. Cozzoli and L. Manna, *J. Am. Chem. Soc.*, 2008, **130**, 1477.

- 24 V. Nandwana, G. S. Chaubey, K. Yano, C.-B. Rong and J. P. Liu, *J. Appl. Phys.*, 2009, **105**, 014303.
- 25 G. S. Chaubey, V. Nandwana, N. Poudyal, C.-B. Rong and J. P. Liu, *Chem. Mater.*, 2008, **20**, 475.
- 26 H. Zeng, J. Li, Z. L. Wang, J. P. Liu and S. Sun, *Nano Lett.*, 2004, **4**, 187.
- 27 J. Kim, C. Rong, Y. Lee, J. P. Liu and S. Sun, *Chem. Mater.*, 2008, **20**, 7242.
- 28 L. C. Varanda, M. Imaizumi, F. J. Santos and M. Jafellicci, Jr, *IEEE Trans. Magn.*, 2008, **44**, 4448.
- 29 C. Liu, X. Wu, T. Klemmer, N. Shukla and D. Weller, *Chem. Mater.*, 2005, **17**, 620.
- 30 H. Zeng, S. Sun, J. Li, Z. L. Wang and J. P. Liu, *Appl. Phys. Lett.*, 2004, **85**, 792.
- 31 Q. K. Ong and A. Wei, *Phys. Rev. B: Condens. Matter Mater. Phys.*, 2009, **80**, 134418.
- 32 C. Wang, D. R. Baer, J. E. Amonette, M. H. Engelhard, J. Antony and Y. Qiang, *J. Am. Chem. Soc.*, 2009, **131**, 8824.
- 33 (a) O. Masala, D. Hoffman, N. Sundaran, K. Page, T. Proffen, G. Lawes and R. Seshadri, *Solid State Sci.*, 2006, **8**, 1015; (b) J.-H. Lee, J.-T. Jang, J.-S. Choi, S.-H. Moon, S.-H. Noh, J.-W. Kim, J.-G. Kim, I.-S. Kim, K.-I. Park and J. Cheon, *Nat. Nanotechnol.*, 2011, **6**, 418; (c) J. Cheon, J.-I. Park, J.-S. Choi, Y.-W. Jun, S. Kim, M. G. Kim, Y.-M. Kim and Y. J. Kim, *Proc. Natl. Acad. Sci. U. S. A.*, 2006, **103**, 3023.
- 34 J. H. Hong, W. S. Kim, J. I. Lee and N. H. Hur, *Solid State Commun.*, 2007, **141**, 541.
- 35 J. S. Jiang, J. E. Pearson, Z. Y. Liu, B. Kabius, S. Trasobares, D. J. Miller and S. D. Bader, *J. Appl. Phys.*, 2005, **97**, 10K311.
- 36 G. Salazar-Alvarez, J. Sort, A. Uheida, M. Muhammad, S. Suriñach, M. D. Baró and J. Nogués, *J. Mater. Chem.*, 2007, **17**, 322.
- 37 A. J. Zambano, H. Oguchi, I. Takeuchi, Y. Choi, J. S. Jiang, J. P. Liu, S. E. Loftland, D. Josell and L. A. Bendersky, *Phys. Rev. B: Condens. Matter Mater. Phys.*, 2007, **75**, 144429.
- 38 (a) C. L. Zha, R. K. Dumas, Y. Y. Fang, V. Bonanni, J. Nogués and J. Åkerman, *Appl. Phys. Lett.*, 2010, **97**, 182504; (b) V. Bonanni, Y. Y. Fang, R. K. Dumas, C. L. Zha, S. Bonetti, J. Nogués and J. Åkerman, *Appl. Phys. Lett.*, 2010, **97**, 202501.
- 39 G. Salazar-Alvarez, H. Lidbaum, A. López-Ortega, M. Estrader, K. Leifer, J. Sort, S. Suriñach, M. D. Baró and J. Nogués, *J. Am. Chem. Soc.*, 2011, **133**, 16738.
- 40 J. Park, K. An, Y. Hwang, J. G. Park, H. J. Noh, J. Y. Kim, J. H. Park, N. M. Hwang and T. Hyeon, *Nat. Mater.*, 2004, **3**, 891.
- 41 (a) H. M. Rietveld, *Acta Crystallogr.*, 1966, **20**, 508; (b) J. Rodriguez-Carvajal, *Phys. B*, 1993, **192**, 55.
- 42 (a) K. R. Beyerlein, J. Solla-Gullón, E. Herrero, E. Garnier, F. Pailloux, M. Leoni, P. Scardi, R. L. Snyder, A. Aldaz and J. M. Feliu, *Mater. Sci. Eng., A*, 2010, **528**, 83; (b) I. V. Golosovsky, I. Mirebeau, E. Elkaim, D. A. Kurdyukov and Y. A. Kumzerov, *Eur. Phys. J. B*, 2005, **47**, 55.
- 43 C. R. Pike, A. P. Roberts and K. L. Verosub, *J. Appl. Phys.*, 1999, **85**, 6660.
- 44 (a) S.-J. Cho, A. M. Shahin, G. L. Long, J. E. Davies, K. Liu, F. Grandjean and S. M. Kauzlarich, *Chem. Mater.*, 2006, **18**, 960; (b) M. T. Rahman, R. K. Dumas, N. Eibagi, N. N. Shams, Y.-C. Wu, K. Liu and C. H. Lai, *Appl. Phys. Lett.*, 2009, **94**, 042507; (c) N. Sakuma, T. Ohshima, T. Shoji, Y. Suzuki, R. Sato, A. Wachi, A. Kato, Y. Kawai, A. Manabe and T. Teranishi, *ACS Nano*, 2011, **5**, 2806.
- 45 J. E. Davies, O. Hellwig, E. E. Fullerton, J. S. Jiang, S. D. Bader, G. T. Zimanyi and K. Liu, *Appl. Phys. Lett.*, 2005, **86**, 262503.
- 46 R. K. Dumas, C. L. Zha, Y. Y. Fang, V. Bonanni, J. W. Lau, J. Nogués and J. Åkerman, *IEEE Trans. Magn.*, 2011, **47**, 1580.
- 47 D. Suess, *Appl. Phys. Lett.*, 2006, **89**, 113105.
- 48 K. Binder, in *Applications of Monte Carlo Methods in Statistical Physics*, Springer, Berlin, 1984.
- 49 V. Baron, J. Gutzmer, H. Rundlöf and R. Tellegren, *Am. Mineral.*, 1998, **83**, 786.
- 50 (a) P. Franke and R. Dieckman, *Solid State Ionics*, 1989, **817**, 32; (b) H. Meher, in *Diffusion in Solids, Fundamentals, Methods, Materials, Diffusion-Controlled Processes*, Springer-Verlag, Berlin, 2007.
- 51 M. Abbate, J. B. Goedkoop, F. De Groot, M. Grioni, J. C. Fuggle, S. Hofmann, H. Petersen and M. Sacchi, *Surf. Interface Anal.*, 1992, **18**, 65.
- 52 H. J. Lee, G. Kim, D. H. Kim, J.-S. Kang, C. L. Zhang, S. W. Cheong, J. H. Shim, S. Lee, H. Lee, J.-Y. Kim, B. H. Kim and B. I. Min, *J. Phys.: Condens. Matter*, 2008, **20**, 295203.
- 53 E. Pellegrin, M. Hagelstein, S. Doyle, H. O. Moser, J. Fuchs, D. Vollath, S. Schuppler, M. A. James, S. S. Saxena, L. Niesen, O. Rogojanu, G. A. Sawatzky, C. Ferrero, M. Borowski, O. Tjernberg and N. B. Brookes, *Phys. Status Solidi B*, 1999, **215**, 797.
- 54 C. L. Chen, Electronic and Magnetic Properties of Transition Metal Ferrites and Superlattice Studied by X-ray Absorption Spectroscopy, PhD thesis, Tamkang University, Tamsui, Taiwan, 2005.
- 55 V. Bayer, R. Podloucky, C. Franchini, F. Allegretti, B. Xu, G. Parteder, M. G. Ramsey, S. Surnev and F. P. Netzer, *Phys. Rev. B: Condens. Matter Mater. Phys.*, 2007, **76**, 165428.
- 56 V. Pool, M. Klem, C. Jolley, E. A. Arenholz, T. Douglas, M. Young and Y. U. Idzerda, *J. Appl. Phys.*, 2010, **107**, 09B517.
- 57 M. Knobel, W. C. L. Nunes, M. Socolovsky, E. De Biasi, J. M. Vargas and J. C. Denardin, *J. Nanosci. Nanotechnol.*, 2008, **8**, 2836.
- 58 W. Palmer, *J. Appl. Phys.*, 1962, **33**, 1201.
- 59 B. Boucher, R. Buhl and M. Perrin, *J. Appl. Phys.*, 1969, **40**, 1126.
- 60 R. Gerber, Z. Šimša and M. Vicher, *Czech. J. Phys.*, 1963, **16**, 913.
- 61 T. Battault, R. Legros and A. Rousset, *J. Eur. Ceram. Soc.*, 1995, **15**, 1141.
- 62 A. H. Eschenfelder, *J. Appl. Phys.*, 1958, **29**, 378.
- 63 K. Dwight and N. Menyuk, *Phys. Rev.*, 1960, **119**, 1470.
- 64 J. Kub, V. Brabers, P. Novák, R. Gemperle and J. Šimšová, *J. Magn. Mater.*, 2000, **217**, 19.
- 65 K. Abe, Y. Miyamoto and S. Chikazumi, *J. Phys. Soc. Jpn.*, 1976, **41**, 1894.

Electronic supplementary information

**Strongly exchange coupled inverse
ferrimagnetic soft|hard, $Mn_xFe_{3-x}O_4|Fe_xMn_{3-x}O_4$, core|shell
heterostructured nanoparticles**

Alberto López-Ortega,^a Marta Estrader,^{*a,b} German Salazar-Alvarez,^b Sònia Estradé,^{c,d} Igor V. Golosovsky,^c Randy K. Dumas,^f David J. Keavney,^g Marianna Vasilakaki,^h Kalliopi N. Trohidou,^h Jordi Sort,^{ij} Francesca Peiró,^c Santiago Suriñach,^j Maria.Dolors Baró^j and Josep Nogués^{a,i}

^aCIN2(ICN-CSIC) and Universitat Autònoma de Barcelona, Catalan Institute of Nanotechnology, Campus de la UAB, 08193 Bellaterra (Barcelona), Spain

^bDepartment of Materials and Environmental Chemistry, Stockholm University, 10691 Stockholm, Sweden

^cLENS-MIND-IN2UB, Departament d'Electrònica, Universitat de Barcelona, Martí i Franquès 1, E-08028 Barcelona, Spain

^dTEM-MAT, SCT, Universitat de Barcelona, Barcelona, Spain

^eSt. Petersburg Nuclear Physics Institute, 188300 Gatchina, St. Petersburg, Russia

^fDepartment of Physics, University of Gothenburg, 41296 Gothenburg, Sweden

^gAdvanced Photon Source, Argonne National Laboratory, Argonne, Illinois 60439, United States

^hInstitute of Materials Science, NCSR "Demokritos", 153 10 Aghia Paraskevi, Attiki, Greece

ⁱInstitució Catalana de Recerca i Estudis Avançats (ICREA), Barcelona, Spain

^jDepartament de Física, Universitat Autònoma de Barcelona, 08193 Bellaterra, Spain

Corresponding Author: *E-mail: martaestrader@gmail.com

EELS Analysis:

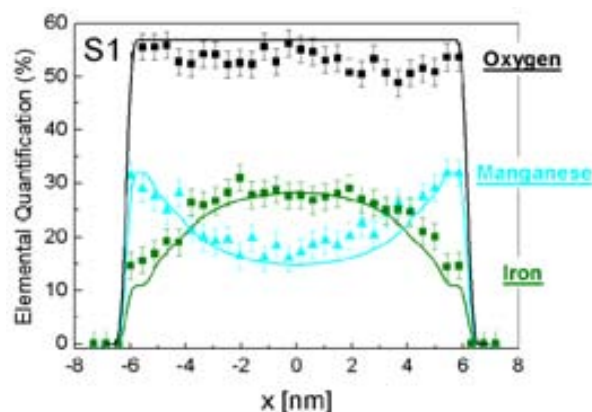


Fig. S1 Expected elemental quantification along the particle diameter for Fe (squares), Mn (triangles) and O (circles). The solid lines represent the simulated profile for a particle with a graded $\text{Mn}_{0.75}\text{Fe}_{2.25}\text{O}_4$ (8 nm) | $\text{Fe}_{1.75}\text{Mn}_{1.25}\text{O}_4$ (0.6 nm) shell 1 | 0.6 nm $\text{Fe}_{1.5}\text{Mn}_{1.5}\text{O}_4$ (0.6 nm) shell 2 | $\text{Fe}_{0.75}\text{Mn}_{2.25}\text{O}_4$ (0.6 nm) shell 3 structure.

XAS and XMCD measurements:

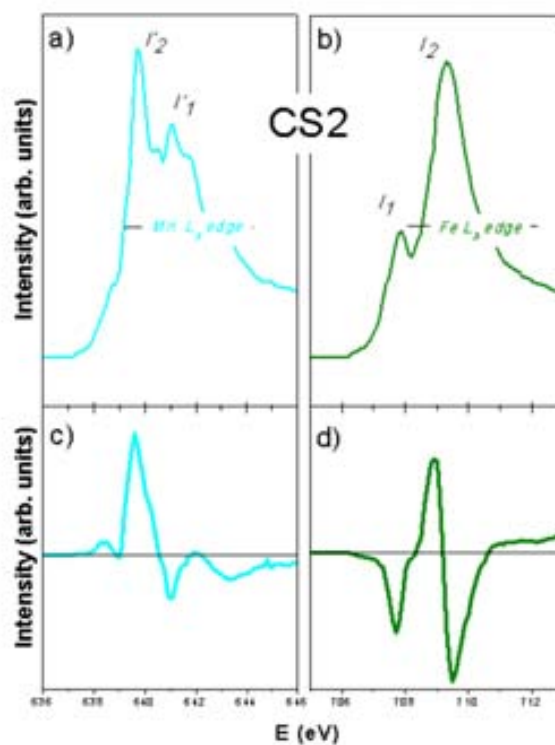


Fig. S2 (top) XAS and (bottom) XMCD spectra at the (left) Mn and (right) Fe edges of CS2 nanoparticles.

Magnetometry measurements:

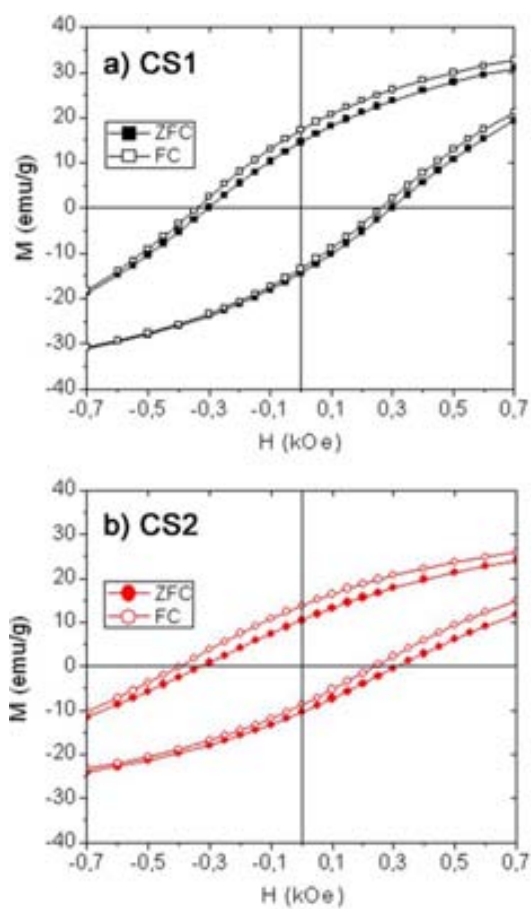


Fig. S3 Enlarged view at low fields of the FC and ZFC hysteresis loops, at 10 K, for (a) CS1 and (b) CS2 nanoparticles.



Chapter 7

Conclusions

In this thesis the synthesis and the structural and magnetic characterization of two different types of poly-magnetic nanoparticles in a core|shell (CS) and onion-like architectures has been presented. Firstly, the doubly inverted system composed by core-MnO|shell-Mn₃O₄ (γ -Mn₂O₃) nanoparticles, where the core and the shell display an AFM and a FiM behavior, respectively, has been discussed. MnO|Mn₃O₄ (γ -Mn₂O₃) system, differs structurally and magnetically from previous literature CS systems since the core is the AFM, instead of shell, and because the Néel temperature of the AFM is higher than the Curie temperature of the FiM. The other system presented is based on the synthesis of heterostructured CS and onion-like nanoparticles derived from two different materials, i.e. iron and manganese oxides. Interestingly, in this case the synthesis of fully magnetic onion-like particles has been demonstrated for the first time. Moreover, our study on hard|soft FiM CS nanoparticles, in contrast to conventional soft|hard, is one of the few studies of this morphology in the literature.

All the nanoparticles have been synthesized using the thermal decomposition of organometallic precursors, i.e., iron oleate and manganese acetylacetonate. Thermal decomposition has been chosen as synthetic route due to the high degree of control on the final size, shape and crystallographic structure of the phases composing the nanoparticles. The syntheses have been performed by controlling the reaction atmosphere and the synthetic parameters, such as decomposition temperature, digestion time, precursor concentration, solvent and surfactant type and precursor/surfactant ratio. For example, MnO|Mn₃O₄ CS nanoparticles have been obtained by the passivation of a pre-made MnO nanoparticles. This approach allows controlling the final thickness of the shell. In order to obtain different initial MnO core sizes without varying the monodispersity, decomposition temperature, digestion time and surfactant/precursor concentration ratios were carefully adjusted. Similarly, FeO|Fe₃O₄ CS nanoparticles have been obtained by the controlled passivation of FeO nanoparticles.

The heterostructured CS and onion-like nanoparticles have been obtained following the seed-mediate growth approach, where manganese oxide is grown on seeds nanoparticles composed of either FeO|Fe₃O₄ CS nanoparticles or pure Fe₃O₄ single-phase nanoparticles. FeO|Fe₃O₄ two-component (CS) seed nanoparticles were used to create the three and four-components onion-like nanoparticles, i.e. FeO|Fe₃O₄|Mn₃O₄ and FeO|Fe₃O₄|MnO|Mn₃O₄, respectively. On the other hand fully oxidized Fe₃O₄ seed nanoparticles were employed to deposit a manganese thin shell and force the manganese-iron interdiffusion to form the final Mn_xFe_{3-x}O₄|Fe_xMn_{3-x}O₄ CS nanoparticle with a graded interface.

The structural characterization of the different systems has been carried out using many different techniques. Transmission electron microscopy (TEM) images have been used to assess the sizes and particle size distributions. High resolution-TEM images and electron energy loss spectra (EELS) analysis allowed to elucidate the structural composition and element distribution inside of the nanoparticles. X-ray and neutron diffraction and synchrotron X-ray absorption, XAS, were used to structurally confirm the phases forming the systems and to obtain their structural parameters (oxidation state, cell parameter, volume ratios, occupancies,...). The magnetic characterization was mainly performed using magnetometric techniques. Magnetization and susceptibility vs. temperature were used to distinguish

the magnetic transitions present in the systems. Hysteresis loops provided the saturation magnetization, coercivity and exchange bias, which gives information of the magnetic character of the phases (i.e., AFM, FiM, soft or hard). A more detailed analysis of the hysteresis loops, FORC analysis, provided the switching behavior of the coupling between different magnetic layers. In addition, neutron diffraction allows us to distinguish the magnetic phases composing the system and to extract their magnetic parameters (e.g., atomic moment of the atoms, magnetic domain size, or magnetic transitions). XMCD has been a useful tool to study separately the magnetic response of the different elements of the system. Finally, ESR spectra have been used to magnetically and structurally characterize the sample. The paramagnetic resonance is strongly dependent of the resonant ion and its magnetic environment giving information on magnetic transitions and the exchange or anisotropy field in coupled systems.

Concerning the MnO|Mn₃O₄ (γ -Mn₂O₃) system, it was demonstrated that the composition passivation shell depends on the nanoparticle size, with the larger nanoparticles presenting mainly Mn₃O₄. However, when the size diminishes, the density of defects increases and as a consequence γ -Mn₂O₃ is the more stable shell phase. Besides, small AFM MnO cores can induce a magnetic proximity effect to the FiM γ -Mn₂O₃ shell to maintain their magnetic order well above their Curie temperature, T_C , and up to T_N of the shell. Moreover, surface effects in the MnO core have been shown to lead to an increase of the Néel temperature of the AFM.

For the system based on the manganese oxide deposition onto iron oxide seed nanoparticles we have shown, structurally and magnetically, the feasibility to synthesize complex multilayered nanoparticles using surface passivation combined with seed growth. Moreover, the results reveal that the manganese oxide grows epitaxially on the (111) planes of (111) truncated faces of the cubic FeO|Fe₃O₄ or Fe₃O₄ seeds. Finally, the soft-FiM|hard-FiM CS Mn_xFe_{3-x}O₄|Fe_xMn_{3-x}O₄ nanoparticle have been shown to display a strong exchange coupling leading a magnetically single phase-like switching.

The results show that iron and manganese oxides allow the synthesis of complex nanoparticles in CS or onion-like architectures with a good control over the morphological parameters. Moreover, the exchange coupling between the dissimilar magnetic phases in the studied CS or onion-like nanoparticles demonstrate that not only the magnetic characteristics of the diverse phases but also their coupling can be used to fine tune the magnetic properties of the final poly-magnetic nanoparticles.

Future work

In this thesis the ability to synthesize CS or onion-like nanoparticles based in the combination of different magnetic layers has been clearly demonstrated. In fact, the control of the synthetic parameters allows us to create well defined core sizes and shell thickness with high reproducibility. However, in some cases we have only showed a few sizes. From the basic point of view, in order to have a more complete understanding of the role played by dimensionality in CS structures (core size and shell thickness) a more systematic study of, for example, soft-FM|hard-FM CS structures can be one of the future works. Moreover, we have only used iron and manganese oxides. Thus, it would be interesting to extend our synthetic studies to other types of materials exhibiting other magnetic properties (e.g., saturation magnetization or anisotropies), particularly with transition temperatures above room temperatures.

Having in mind the current crisis in permanent magnet materials it would be appealing to try to create novel permanent magnets. Nowadays the use of rare-earth (RE) and precious metals (PM) are crucial in fabrication; however, the prices have increased exponentially due to poor availability of these materials. Interestingly, the capability to synthesize new hard-FM metastable phases at the nanoscale opens new avenues for state-of-the-art permanent magnets. Moreover, the study of exchange coupled core|shell conventional, hard|soft, or inverse, soft|hard, exchange coupled permanent magnets is still at its infancy and their properties are far from being optimized. Thus, systematic studies of are needed to obtain high performance magnets.

Finally, in this thesis we have studied the combination of two or more magnetic materials. However, core|shell nanoparticles can be designed to have many different combined functionalities for diverse applications in fields like biomedicine, catalysis or magnetic shielding. Thus, the extension of our

synthetic routes for other application is also an attractive extension of the research presented in the thesis.



Bibliography

- [1] M. Ratner and D. Ratner, *Nanotechnology: A Gentle Introduction to the Next Big Idea*. Prentice Hall, November 2002.
- [2] N. Taniguchi, "On the basic concept of nanotechnology," in *Proceeding of International Conference on Production Engineering*, vol. 2, pp. 18–23, 1974.
- [3] G. Binnig, H. Rohrer, C. Gerber, and E. Weibel, "Surface studies by scanning tunneling microscopy," *Physical Review Letters*, vol. 49, pp. 57–61, 1982.
- [4] R. F. Curl and R. E. Smalley, "Probing C60," *Science*, vol. 242, pp. 1017–1022, 1988.
- [5] C. Lock, "Small wonders," *Nature*, vol. 467, pp. 18–21, 2010.
- [6] <http://www.nano.gov/>.
- [7] V. Markel and T. George, *Optics of Nanostructured Materials*. Willey, 2000.
- [8] H. S. Nalwa, *Magnetic Nanostructures*. American Scientific Publishers, 2002.
- [9] S. Scott, C. Crudden, and C. Jones, *Nanostructured Catalysts*. Springer, 2003.
- [10] S. Zhang, D. M. Marini, W. Hwang, and S. Santoso, "Design of nanostructured biological materials through self-assembly of peptides and proteins," *Current Opinion in Chemical Biology*, vol. 6, pp. 865–871, 2002.
- [11] R. Coombs, *Nanotechnology in Medicine (Guide Historique)*. Routledge, 2011.
- [12] A. Gusev and A. Rempel, *Nanocrystalline Materials*. Cambridge International Science, 2004.
- [13] C. P. Bean and J. D. Livingston, "Superparamagnetism," *Journal of Applied Physics*, vol. 30, pp. S120–S129, 1959.
- [14] M. Knobel, W. Nunes, L. Socolovsky, E. De Biasi, J. Vargas, and J. Denardin, "Superparamagnetism and other magnetic features in granular materials: A review on ideal and real systems," *Journal of Nanoscience and Nanotechnology*, vol. 8, pp. 2836–2857, 2008.
- [15] G. Cao and Y. Wang, *Nanostructures and nanomaterials: synthesis, properties, and applications*. World Scientific series in nanoscience and nanotechnology, World Scientific, 2010.
- [16] E. Roduner, "Size matters: why nanomaterials are different," *Chemical Society Reviews*, vol. 35, pp. 583–592, 2006.
- [17] M. Baraton, *Synthesis, functionalization and surface treatment of nanoparticles*. American Scientific Publishers, 2003.
- [18] M. Niederberger and G. Garnweitner, "Organic reaction pathways in the nonaqueous synthesis of metal oxide nanoparticles," *Chemistry A European Journal*, vol. 12, pp. 7282–7302, 2006.

-
- [19] T. S. Ahmadi, Z. L. Wang, T. C. Green, A. Henglein, and M. A. El-Sayed, "Shape-controlled synthesis of colloidal platinum nanoparticles," *Science*, vol. 272, pp. 1924–1925, 1996.
- [20] M. Chen, J. P. Liu, and S. Sun, "One-step synthesis of FePt nanoparticles with tunable size," *Journal of the American Chemical Society*, vol. 126, pp. 8394–8395, 2004.
- [21] M. Willard, L. Kurihara, E. Carpenter, S. Calvin, and V. Harris, "Chemically prepared magnetic nanoparticles," *International Materials Review*, vol. 49, pp. 125–170, 2004.
- [22] H. Cui, Y. Feng, W. Ren, T. Zeng, H. Lv, and Y. Pan, "Strategies of Large Scale Synthesis of Monodisperse Nanoparticles," *Recent Patents on Nanotechnology*, vol. 3, pp. 32–41, 2009.
- [23] J. Park, J. Joo, S. G. Kwon, Y. Jang, and T. Hyeon, "Synthesis of monodisperse spherical nanocrystals," *Angewandte Chemie International Edition*, vol. 46, pp. 4630–4660, 2007.
- [24] R. Nagarajan and T. A. Hatton, eds., *Nanoparticles: Synthesis, Stabilization, Passivation, and Functionalization*. Washington, DC: American Chemical Society, 2008.
- [25] P. Cozzoli, *Advanced Wet-Chemical Synthetic Approaches to Inorganic Nanostructures*. Transworld Research Network, 2008.
- [26] J. Lv, L. Qiu, and B. Qu, "Controlled growth of three morphological structures of magnesium hydroxide nanoparticles by wet precipitation method," *Journal of Crystal Growth*, vol. 267, pp. 676–684, 2004.
- [27] E. Auzans, D. Zins, E. Blums, and R. Massart, "Synthesis and properties of Mn-Zn ferrite ferrofluids," *Journal of Materials Science*, vol. 34, pp. 1253–1260, 1999.
- [28] P. Ayyub, A. Maitra, and D. O. Shah, "Microstructure of the CTAB-butanol-octane-water microemulsion system - effect of dissolved salts," *Journal of the Chemical Society-Faraday Transactions*, vol. 89, pp. 3585–3589, 1993.
- [29] G. N. Glavee, K. J. Klabunde, C. M. Sorensen, and G. C. Hadjipanayis, "Chemistry of borohydride reduction of iron(II) and iron(III) ions in aqueous and nonaqueous media. Formation of nanoscale Fe, FeB, and Fe₂B powders," *Inorganic Chemistry*, vol. 34, pp. 28–35, 1995.
- [30] C. Black, C. Murray, R. Sandstrom, and S. Sun, "Spin-dependent tunneling in self-assembled cobalt-nanocrystal superlattices," *Science*, vol. 290, pp. 1131–1134, 2000.
- [31] A. Bianco, G. Gusmano, R. Montanari, G. Montesperelli, and E. Traversa, "Preparation of Ni-Co metal powders by co-reduction of Ni(II) and Co(II) hydroxides for magnetoresistive sensors," *Materials Letters*, vol. 19, pp. 263–268, 1994.
- [32] Q.-T. Bui, Q. Pankhurst, and K. Zulqarnain, "Inter-particle interactions in biocompatible magnetic fluids," *IEEE Transactions on Magnetism*, vol. 34, pp. 2117–2119, 1998.
- [33] E. Carpenter, C. Sangregorio, and C. O'Connor, "Synthesis of antiferromagnetic macromolecular particles," *Molecular Crystals and Liquid Crystals Science and Technology- Section A: Molecular Crystals and Liquid Crystals*, vol. 334, pp. 641–649, 1999.
- [34] J. Zhuang, Q. Peng, and Y. Li, "A general strategy for nanocrystal synthesis," *Nature*, vol. 437, pp. 121–124, 2005.
- [35] G. H. Mohamed Saeed, S. Radiman, S. S. Gasaymeh, H. N. Lim, and N. M. Huang, "Mild hydrothermal synthesis of Ni-Cu nanoparticles," *Journal of Nanomaterials*, p. 184137, 2010.
- [36] D. Chen and R. Xu, "Hydrothermal synthesis and characterization of nanocrystalline Fe₃O₄ powders," *Materials Research Bulletin*, vol. 33, pp. 1015–1021, 1998.

-
- [37] J. Chen, K. Lee, C. Sorensen, K. Klabunde, and G. Hadjipanayis, "Magnetic-properties of microemulsion synthesized cobalt fine particles," *Journal of Applied Physics*, vol. 75, pp. 5876–5878, 1994.
- [38] Q. Chen, A. J. Rondinone, B. C. Chakoumakos, and Z. J. Zhang, "Synthesis of superparamagnetic MgFe_2O_4 nanoparticles by coprecipitation," *Journal of Magnetism and Magnetic Materials*, vol. 194, pp. 1–7, 1999.
- [39] R. Jagannathan, G. Irvin, T. Blanton, and S. Jagannathan, "Organic nanoparticles: Preparation, self-assembly, and properties," *Advanced Functional Materials*, vol. 16, pp. 747–753, 2006.
- [40] V. F. Puentes, K. M. Krishnan, and A. P. Alivisatos, "Colloidal nanocrystal shape and size control: The case of cobalt," *Science*, vol. 291, pp. 2115–2117, 2001.
- [41] T. Hyeon, S. S. Lee, J. Park, Y. Chung, and H. B. Na, "Synthesis of highly crystalline and monodisperse maghemite nanocrystallites without a size-selection process," *Journal of the American Chemical Society*, vol. 123, pp. 12798–12801, 2001.
- [42] D. Caruntu, Y. Remond, N. Chou, M. Jun, G. Caruntu, J. He, G. Goloverda, C. O'Connor, and V. Kolesnichenko, "Reactivity of 3d transition metal cations in diethylene glycol solutions. Synthesis of transition metal ferrites with the structure of discrete nanoparticles complexed with long-chain carboxylate anions," *Inorganic Chemistry*, vol. 41, pp. 6137–6146, 2002.
- [43] C. B. Murray, D. J. Norris, and M. G. Bawendi, "Synthesis and characterization of nearly monodisperse CdE (E = sulfur, selenium, tellurium) semiconductor nanocrystallites," *Journal of the American Chemical Society*, vol. 115, pp. 8706–8715, 1993.
- [44] V. Salgueirino-Maceira, L. Liz-Marzan, and M. Farle, "Water-based ferrofluids from $\text{Fe}_x\text{Pt}_{1-x}$ nanoparticles synthesized in organic media," *Langmuir*, vol. 20, pp. 6946–6950, 2004.
- [45] Z. Guo, L. Henry, V. Palshin, and E. Podlaha, "Synthesis of poly(methyl methacrylate) stabilized colloidal zero-valence metallic nanoparticles," *Journal of Materials Chemistry*, vol. 16, pp. 1772–1777, 2006.
- [46] S. Thimmaiah, M. Rajamathi, N. Singh, P. Bera, F. Meldrum, N. Chandrasekhar, and R. Seshadri, "A solvothermal route to capped nanoparticles of $\gamma\text{-Fe}_2\text{O}_3$ and CoFe_2O_4 ," *Journal of Materials Chemistry*, vol. 11, pp. 3215–3221, 2001.
- [47] N. Egorov, L. Eremin, V. Usov, and A. Larionov, "Preparation of lead sulfide nanoparticles in the photolysis of aqueous solutions of lead thiosulfate complex," *High Energy Chemistry*, vol. 41, pp. 251–254, 2007.
- [48] J. Park, K. An, Y. Hwang, J. Park, H. Noh, J. Kim, N. Park, and T. Hyeon, "Ultra-large-scale syntheses of monodisperse nanocrystals," *Nature Materials*, vol. 3, pp. 891–895, 2004.
- [49] T. Yamamoto, Y. Wada, H. Yin, T. Sakata, H. Mori, and S. Yanagida, "Microwave-driven polyol method for preparation of TiO_2 nanocrystallites," *Chemistry Letters*, pp. 964–965, 2002.
- [50] Y. Lee, J. Lee, C. Bae, J.-G. Park, H.-J. Noh, J.-H. Park, and T. Hyeon, "Large-scale synthesis of uniform and crystalline magnetite nanoparticles using reverse micelles as nanoreactors under reflux conditions," *Advanced Functional Materials*, vol. 15, pp. 503–509, 2005.
- [51] Y. Lu, Y. Yin, B. T. Mayers, and Y. Xia, "Modifying the surface properties of superparamagnetic iron oxide nanoparticles through a sol-gel approach," *Nano Letters*, vol. 2, pp. 183–186, 2002.
- [52] S. Acosta, R. Corriu, D. Leclercq, P. H. Mutin, and A. Vioux, "Novel non-hydrolytic sol-gel route to metal oxides," *Journal of Sol-Gel Science and Technology*, vol. 2, pp. 25–28, 1994.

-
- [53] A. Vioux, "Nonhydrolytic sol-gel routes to oxides," *Chemistry of Materials*, vol. 9, pp. 2292–2299, 1997.
- [54] F. Dumestre, B. Chaudret, C. Amiens, P. Renaud, and P. Fejes, "Superlattices of iron nanocubes synthesized from $\text{Fe}[\text{N}(\text{SiMe}_3)_2]_2$," *Science*, vol. 303, pp. 821–823, 2004.
- [55] C. Feldmann, "Polyol-mediated synthesis of nanoscale functional materials," *Solid State Science*, vol. 7, pp. 868–873, 2005.
- [56] T. Bala, C. Sankar, M. Baidakova, V. Osipov, T. Enoki, P. Joy, B. Prasad, and M. Sastry, "Cobalt and magnesium ferrite nanoparticles: Preparation using liquid foams as templates and their magnetic characteristics," *Langmuir*, vol. 21, pp. 10638–10643, 2005.
- [57] S. Mörup, D. E. Madsen, C. Frandsen, C. R. H. Bahl, and M. F. Hansen, "Experimental and theoretical studies of nanoparticles of antiferromagnetic materials," *Journal of Physics-Condensed Matter*, vol. 19, 2007.
- [58] M. H. Rashid, M. Raula, and T. K. Mandal, "Polymer assisted synthesis of chain-like cobalt-nickel alloy nanostructures: Magnetically recoverable and reusable catalysts with high activities," *Journal of Materials Chemistry*, vol. 21, pp. 4904–4917, 2011.
- [59] P. Zhang and T. K. Sham, "X-ray studies of the structure and electronic behavior of alkanethiolate-capped Gold nanoparticles: The interplay of size and surface effects," *Physical Review Letters*, vol. 90, p. 245502, 2003.
- [60] R. Elghanian, J. J. Storhoff, R. C. Mucic, R. L. Letsinger, and C. A. Mirkin, "Selective colorimetric detection of polynucleotides based on the distance-dependent optical properties of Gold nanoparticles," *Science*, vol. 277, pp. 1078–1081, 1997.
- [61] K. J. J. Mayrhofer, B. B. Blizanac, M. Arenz, V. R. Stamenkovic, P. N. Ross, and N. M. Markovic, "The impact of geometric and surface electronic properties of Pt-catalysts on the particle size effect in electrocatalysis," *The Journal of Physical Chemistry B*, vol. 109, pp. 14433–14440, 2005.
- [62] F. Hou, W. Wang, and H. Guo, "Effect of the dispersibility of ZrO_2 nanoparticles in Ni- ZrO_2 electroplated nanocomposite coatings on the mechanical properties of nanocomposite coatings," *Applied Surface Science*, vol. 252, pp. 3812–3817, 2006.
- [63] V. A. Sinani, D. S. Koktysh, B.-G. Yun, R. L. Matts, T. C. Pappas, M. Motamedi, S. N. Thomas, and N. A. Kotov, "Collagen coating promotes biocompatibility of semiconductor nanoparticles in stratified lbl films," *Nano Letters*, vol. 3, pp. 1177–1182, 2003.
- [64] "Surface modification of superparamagnetic magnetite nanoparticles and their intracellular uptake," *Biomaterials*, vol. 23, pp. 1553–1561, 2002.
- [65] O. Salata, "Applications of nanoparticles in biology and medicine," *Journal of Nanobiotechnology*, vol. 2, p. 3, 2004.
- [66] A. Solanki, J. Kim, and K.-B. Lee, "Nanotechnology for regenerative medicine: nanomaterials for stem cell imaging," *Nanomedicine*, vol. 3, pp. 567–578, 2008.
- [67] J. Gao, H. Gu, and B. Xu, "Multifunctional magnetic nanoparticles: Design, synthesis, and biomedical applications," *Accounts of Chemical Research*, vol. 42, pp. 1097–1107, 2009.
- [68] D. Wang, H. L. Xin, Y. Yu, H. Wang, E. Rus, D. A. Muller, and H. D. Abrun a, "Pt-decorated PdCo@Pd/C core-shell nanoparticles with enhanced stability and electrocatalytic activity for the oxygen reduction reaction," *Journal of the American Chemical Society*, vol. 132, pp. 17664–17666, 2010.

-
- [69] H. L. Xin, J. A. Mundy, Z. Liu, R. Cabezas, R. Hovden, L. F. Kourkoutis, J. Zhang, N. P. Subramanian, R. Makharia, F. T. Wagner, and D. A. Muller, "Atomic-resolution spectroscopic imaging of ensembles of nanocatalyst particles across the life of a fuel cell," *Nano Letters*, vol. 12, pp. 490–497, 2012.
- [70] "Surface modification of superparamagnetic magnetite nanoparticles and their intracellular uptake," *Biomaterials*, vol. 23, pp. 1553–1561, 2002.
- [71] Z. Liu, Y. Qi, and C. Lu, "High efficient ultraviolet photocatalytic activity of BiFeO₃ nanoparticles synthesized by a chemical coprecipitation process," *Journal of Materials Science: Materials in Electronics*, vol. 21, pp. 380–384, 2010.
- [72] A. Murugadoss, P. Goswami, A. Paul, and A. Chattopadhyay, "green chitosan bound silver nanoparticles for selective C-C bond formation via in situ iodination of phenols," *Journal of Molecular Catalysis A: Chemical*, vol. 304, pp. 153–158, 2009.
- [73] B. C. Ranu, K. Chattopadhyay, L. Adak, A. Saha, S. Bhadra, R. Dey, and D. Saha, "Cheminform abstract: Metal nanoparticles as efficient catalysts for organic reactions," *ChemInform*, vol. 41, 2010.
- [74] K. C. Krogman, T. Druffel, and M. K. Sunkara, "Anti-reflective optical coatings incorporating nanoparticles," *Nanotechnology*, vol. 16, p. S338, 2005.
- [75] H. Chen, X. Kou, Z. Yang, W. Ni, and J. Wang, "Shape- and size- dependent refractive index sensitivity of gold nanoparticles," *Langmuir*, vol. 24, pp. 5233–5237, 2008.
- [76] P. K. Jain, K. S. Lee, I. H. El-Sayed, and M. A. El-Sayed, "Calculated absorption and scattering properties of gold nanoparticles of different size, shape, and composition: Applications in biological imaging and biomedicine," *The Journal of Physical Chemistry B*, vol. 110, pp. 7238–7248, 2006.
- [77] A. D. McFarland and R. P. Van Duyne, "Single silver nanoparticles as real-time optical sensors with zeptomole sensitivity," *Nano Letters*, vol. 3, pp. 1057–1062, 2003.
- [78] J. N. Anker, W. P. Hall, O. Lyandres, N. C. Shah, J. Zhao, and R. P. Van Duyne, "Biosensing with plasmonic nanosensors," *Nature Materials*, vol. 7, pp. 442–453, 2008.
- [79] G. Reiss and A. Hutten, "Magnetic nanoparticles: Applications beyond data storage," *Nature Materials*, vol. 4, pp. 725–726, 2005.
- [80] N. A. Frey and S. Sun, *Inorganic Nanoparticles: Synthesis, Applications, and Perspectives*, ch. Magnetic nanoparticle for information storage applications, pp. 33–68. Boca Raton, FL : CRC Press, 2010.
- [81] I. S. Lee, N. Lee, J. Park, B. H. Kim, Y.-W. Yi, T. Kim, T. K. Kim, I. H. Lee, S. R. Paik, and T. Hyeon, "Ni/NiO core/shell nanoparticles for selective binding and magnetic separation of histidine-tagged proteins," *Journal of the American Chemical Society*, vol. 128, pp. 10658–10659, 2006.
- [82] J. B. Haun, T.-J. Yoon, H. Lee, and R. Weissleder, "Magnetic nanoparticle biosensors," *Wiley Interdisciplinary Reviews: Nanomedicine and Nanobiotechnology*, vol. 2, pp. 291–304, 2010.
- [83] H. Lee, T.-J. Yoon, and R. Weissleder, "Ultrasensitive detection of bacteria using core-shell nanoparticles and an NMR-filter system," *Angewandte Chemie International Edition*, vol. 48, pp. 5657–5660, 2009.
- [84] T.-J. Yoon, H. Lee, H. Shao, and R. Weissleder, "Highly magnetic core-shell nanoparticles with a unique magnetization mechanism," *Angewandte Chemie International Edition*, vol. 50, pp. 4663–4666, 2011.

-
- [85] R. A. Taylor, P. E. Phelan, T. P. Otanicar, C. A. Walker, M. Nguyen, S. Trimble, and R. Prasher, "Applicability of nanofluids in high flux solar collectors," *Journal of Renewable and Sustainable Energy*, vol. 3, p. 023104, 2011.
- [86] E. C. Nsofor, "Recent patents on nanofluids (nanoparticles in liquids) heat transfer," *Recent Patents on Mechanical Engineering*, vol. I, pp. 190–197, 2008.
- [87] L. Shi, D. S. Shang, Y. S. Chen, J. Wang, J. R. Sun, and B. G. Shen, "Improved resistance switching in ZnO-based devices decorated with Ag nanoparticles," *Journal of Physics D: Applied Physics*, vol. 44, p. 455305, 2011.
- [88] F. Marciano, L. Bonetti, R. Pessoa, J. Marcuzzo, M. Massi, L. Santos, and V. Trava-Airoldi, "The improvement of DLC film lifetime using silver nanoparticles for use on space devices," *Diamond and Related Materials*, vol. 17, pp. 1674–1679, 2008.
- [89] J. J. Adams, E. B. Duoss, T. F. Malkowski, M. J. Motala, B. Y. Ahn, R. G. Nuzzo, J. T. Bernhard, and J. A. Lewis, "Conformal printing of electrically small antennas on three-dimensional surfaces," *Advanced Materials*, vol. 23, pp. 1335–1340, 2011.
- [90] J. H. Fendler, "Chemical self-assembly for electronic applications," *Chemistry of Materials*, vol. 13, pp. 3196–3210, 2001.
- [91] J. E. Millstone, D. F. J. Kavulak, C. H. Woo, T. W. Holcombe, E. J. Westling, A. L. Briseno, M. F. Toney, and J. M. J. Fréchet, "Synthesis, properties, and electronic applications of size-controlled poly(3-hexylthiophene) nanoparticles," *Langmuir*, vol. 26, pp. 13056–13061, 2010.
- [92] "<http://ecadigitallibrary.com/detail.php?cid=9&pid=195&keywords=&pg=>."
- [93] C. D. Wessells, R. A. Huggins, and Y. Cui, "Copper hexacyanoferrate battery electrodes with long cycle life and high power," *Nature Communications*, vol. 2, p. 550, 2011.
- [94] H.-S. Kim, H. Lee, K.-S. Han, J.-H. Kim, M.-S. Song, M.-S. Park, J.-Y. Lee, and J.-K. Kang, "Hydrogen storage in ni nanoparticle-dispersed multiwalled carbon nanotubes," *The Journal of Physical Chemistry B*, vol. 109, pp. 8983–8986, 2005.
- [95] B. Bogdanovic, M. Felderhoff, S. Kaskel, A. Pommerin, K. Schlichte, and F. Schüth, "Improved hydrogen storage properties of ti-doped sodium alanate using titanium nanoparticles as doping agents," *Advanced Materials*, vol. 15, pp. 1012–1015, 2003.
- [96] X. Chen, B. Jia, J. K. Saha, B. Cai, N. Stokes, Q. Qiao, Y. Wang, Z. Shi, and M. Gu, "Broadband enhancement in thin-film amorphous silicon solar cells enabled by nucleated silver nanoparticles," *Nano Letters*, vol. 12, pp. 2187–2192, 2012.
- [97] A. Morrish and I. M. Society, *The physical principles of magnetism*. IEEE Press Classic Reissue, IEEE Press, 1965.
- [98] D. L. Leslie-Pelecky and R. D. Rieke, "Magnetic properties of nanostructured materials," *Chemistry of Materials*, vol. 8, pp. 1770–1783, 1996.
- [99] X. Batlle and A. Labarta, "Finite-size effects in fine particles: magnetic and transport properties," *Journal of Physics D: Applied Physics*, vol. 35, p. R15, 2002.
- [100] R. H. Kodama and A. E. Berkowitz, "Atomic-scale magnetic modeling of oxide nanoparticles," *Physical Review B*, vol. 59, pp. 6321–6336, 1999.
- [101] E. De Biasi, R. D. Zysler, C. A. Ramos, H. Romero, and D. Fiorani, "Surface anisotropy and surface-core interaction in Co-Ni-B and FeNiB dispersed amorphous nanoparticles," *Physical Review B*, vol. 71, p. 104408, 2005.

-
- [102] H. Kachkachi, M. Nogués, E. Tronc, and D. Garanin, “Finite-size versus surface effects in nanoparticles,” *Journal of Magnetism and Magnetic Materials*, vol. 221, pp. 158–163, 2000.
- [103] M. Knobel, W. Nunes, A. Brandl, J. Vargas, L. Socolovsky, and D. Zanchet, “Interaction effects in magnetic granular systems,” *Physica B: Condensed Matter*, vol. 354, pp. 80–87, 2004.
- [104] J. Dormann, D. Fiorani, and E. Tronc, “On the models for interparticle interactions in nanoparticle assemblies: comparison with experimental results,” *Journal of Magnetism and Magnetic Materials*, vol. 202, pp. 251–267, 1999.
- [105] M. Khan, “Magnetic fluid and nanoparticle applications to nanotechnology,” *Journal of Nanoparticle Research*, vol. 3, pp. 71–73, 2001.
- [106] W. Zapka, L. Belova, K. V. Rao, and V. W., “Application of inkjet technology for the deposition of magnetic nanoparticles to form micron-scale structures,” *IEE Proceedings: Science, Measurement and Technology*, vol. 150, pp. 252–256, 2003.
- [107] “Magnetic nanostructures as amplifiers of transverse fields in magnetic resonance,” *Solid State Nuclear Magnetic Resonance*, vol. 28, pp. 91–105, 2005.
- [108] M. Arruebo, R. Fernández-Pacheco, M. R. Ibarra, and J. Santamaría, “Magnetic nanoparticles for drug delivery,” *Nano Today*, vol. 2, pp. 22–32, 2007.
- [109] J.-H. Lee, J.-t. Jang, J.-s. Choi, S. H. Moon, S.-h. Noh, J.-w. Kim, J.-G. Kim, I.-S. Kim, K. I. Park, and J. Cheon, “Exchange-coupled magnetic nanoparticles for efficient heat induction,” *Nature Nanotechnology*, vol. 6, pp. 418–422, 2011.
- [110] H. Zeng, J. Li, J. P. Liu, Z. L. Wang, and S. Sun, “Exchange-coupled nanocomposite magnets by nanoparticle self-assembly,” *Nature*, vol. 420, pp. 395–398, 2002.
- [111] B. D. Cullity and C. D. Graham, *Introduction to Magnetic Materials*. New Jersey, USA: Wiley, John & Sons, 2008.
- [112] S. Chikazumi, *Physics of Magnetism*. Malabar, USA: Robert E. Krieger Publishing Company, 1st ed., 1964.
- [113] L. Néel, “Antiferromagnetism and ferrimagnetism,” *Proceedings of the Physical Society. Section A*, vol. 65, p. 869, 1952.
- [114] A. Hubert and R. Schäfer, *Magnetic domains: the analysis of magnetic microstructures*. Springer, 1998.
- [115] G. C. Papaefthymiou, “Nanoparticle magnetism,” *Nano Today*, vol. 4, pp. 438–447, 2009.
- [116] D. Peddis, C. Cannas, A. Musinu, and G. Piccaluga, “Magnetism in nanoparticles: Beyond the effect of particle size,” *Chemistry A European Journal*, vol. 15, pp. 7822–7829, 2009.
- [117] J. L. Dormann, D. Fiorani, and E. Tronc, *Advances in Chemical Physics*, ch. Magnetic Relaxation in Fine-Particle Systems, pp. 283–494. John Wiley & Sons, Inc., 2007.
- [118] E. C. Stoner and E. P. Wohlfarth, “A mechanism of magnetic hysteresis in heterogeneous alloys,” *Philosophical Transactions of the Royal Society of London. Series A, Mathematical and Physical Sciences*, vol. 240, pp. 599–642, 1948.
- [119] B. Sohn, R. Cohen, and G. Papaefthymiou, “Magnetic properties of iron oxide nanoclusters within microdomains of block copolymers,” *Journal of Magnetism and Magnetic Materials*, vol. 182, pp. 216–224, 1998.

-
- [120] M. Popovici, M. Gich, A. Roig, L. Casas, E. Molins, C. Savii, D. Becherescu, J. Sort, S. Suriñach, J. S. Muñoz, M. D. Baró, and J. Nogués, “Ultraporous single phase iron oxide-silica nanostructured aerogels from ferrous precursors,” *Langmuir*, vol. 20, pp. 1425–1429, 2004.
- [121] J. Koch and R. Sabirianov, “Finite size effects in shell nanoparticles,” *Journal of Magnetism and Magnetic Materials*, vol. 321, pp. 1137–1141, 2009.
- [122] D. A. Dimitrov and G. M. Wysin, “Effects of surface anisotropy on hysteresis in fine magnetic particles,” *Physical Review B*, vol. 50, pp. 3077–3084, 1994.
- [123] G. Salazar-Alvarez, J. Qin, V. Speleák, I. Bergmann, M. Vasilakaki, K. N. Trohidou, J. D. Ardisson, W. A. A. Macedo, M. Mikhaylova, M. Muhammed, M. D. Baró, and J. Nogués, “Cubic versus spherical magnetic nanoparticles: The role of surface anisotropy,” *Journal of the American Chemical Society*, vol. 130, pp. 13234–13239, 2008.
- [124] D. Li, Z. Han, J. G. Zheng, X. L. Wang, D. Y. Geng, J. Li, and Z. D. Zhang, “Spin canting and spin-flop transition in antiferromagnetic Cr_2O_3 nanocrystals,” *Journal of Applied Physics*, vol. 106, p. 053913, 2009.
- [125] X. Batlle, X. Obradors, M. Medarde, J. Rodríguez-Carvajal, M. Pernet, and M. Vallet-Regí, “Surface spin canting in $\text{BaFe}_{12}\text{O}_{19}$ fine particles,” *Journal of Magnetism and Magnetic Materials*, vol. 124, pp. 228–238, 1993.
- [126] C. Serna, F. Böker, and S. M. “Spin frustration in maghemite nanoparticles,” *Solid State Communications*, vol. 118, pp. 437–440, 2001.
- [127] E. Winkler, R. D. Zysler, M. V. Mansilla, and D. Fiorani, “Surface anisotropy effects in nio nanoparticles,” *Physical Review B*, vol. 72, p. 132409, 2005.
- [128] R. H. Kodama, S. A. Makhlof, and A. E. Berkowitz, “Finite size effects in antiferromagnetic nio nanoparticles,” *Physical Review Letters*, vol. 79, pp. 1393–1396, 1997.
- [129] R. H. Kodama, A. E. Berkowitz, E. J. McNiff, Jr., and S. Foner, “Surface spin disorder in NiFe_2O_4 nanoparticles,” *Physical Review Letters*, vol. 77, pp. 394–397, 1996.
- [130] B. Martínez, X. Obradors, L. Balcells, A. Rouanet, and C. Monty, “Low temperature surface spin-glass transition in $\gamma\text{-Fe}_2\text{O}_3$ nanoparticles,” *Physical Review Letters*, vol. 80, pp. 181–184, 1998.
- [131] T. J. Daou, J.-M. Greneche, S.-J. Lee, S. Lee, C. Lefevre, S. Bégin-Colin, and G. Pourroy, “Spin canting of maghemite studied by NMR and in-field Mössbauer spectrometry,” *The Journal of Physical Chemistry C*, vol. 114, pp. 8794–8799, 2010.
- [132] J. Mazo-Zuluaga, J. Restrepo, F. Muñoz, and J. Mejía-López, “Surface anisotropy, hysteretic, and magnetic properties of magnetite nanoparticles: A simulation study,” *Journal of Applied Physics*, vol. 105, p. 123907, 2009.
- [133] X. H. Huang, J. F. Ding, G. Q. Zhang, Y. Hou, Y. P. Yao, and X. G. Li, “Size-dependent exchange bias in $\text{La}_{0.25}\text{Ca}_{0.75}\text{MnO}_3$ nanoparticles,” *Physical Review B*, vol. 78, p. 224408, 2008.
- [134] D. Tobia, E. Winkler, R. D. Zysler, M. Granada, and H. E. Troiani, “Size dependence of the magnetic properties of antiferromagnetic Cr_2O_3 nanoparticles,” *Physical Review B*, vol. 78, p. 104412, 2008.
- [135] F. Liu, M. R. Press, S. N. Khanna, and P. Jena, “Magnetism and local order: *Ab initio* tight-binding theory,” *Physical Review B*, vol. 39, pp. 6914–6924, 1989.

-
- [136] R. Bhowmik and R. Ranganathan, "Enhancement of surface magnetization in antiferromagnetic nanoparticles," *Solid State Communications*, vol. 141, pp. 365–368, 2007.
- [137] M. Ghosh, K. Biswas, A. Sundaresan, and C. N. R. Rao, "MnO and NiO nanoparticles: synthesis and magnetic properties," *Journal of Materials Chemistry*, vol. 16, pp. 106–111, 2006.
- [138] J. Wesselinowa, "Size and anisotropy effects on magnetic properties of antiferromagnetic nanoparticles," *Journal of Magnetism and Magnetic Materials*, vol. 322, pp. 234–237, 2010.
- [139] J. L. Dormann, L. Bessais, and D. Fiorani, "A dynamic study of small interacting particles: superparamagnetic model and spin-glass laws," *Journal of Physics C: Solid State Physics*, vol. 21, p. 2015, 1988.
- [140] W. Luo, S. R. Nagel, T. F. Rosenbaum, and R. E. Rosensweig, "Dipole interactions with random anisotropy in a frozen ferrofluid," *Physical Review Letters*, vol. 67, pp. 2721–2724, 1991.
- [141] S. Mörup and E. Tronc, "Superparamagnetic relaxation of weakly interacting particles," *Physical Review Letters*, vol. 72, pp. 3278–3281, 1994.
- [142] Y. Sun, M. B. Salamon, K. Garnier, and R. S. Averback, "Memory effects in an interacting magnetic nanoparticle system," *Physical Review Letters*, vol. 91, p. 167206, 2003.
- [143] M. Sasaki, P. E. Jönsson, H. Takayama, and P. Nordblad, "Comment on memory effects in an interacting magnetic nanoparticle system," *Physical Review Letters*, vol. 93, p. 139701, 2004.
- [144] M. F. Hansen, P. E. Jönsson, P. Nordblad, and P. Svedlindh, "Critical dynamics of an interacting magnetic nanoparticle system," *Journal of Physics: Condensed Matter*, vol. 14, p. 4901, 2002.
- [145] W. Kleemann, O. Petracic, C. Binek, G. N. Kakazei, Y. G. Pogorelov, J. B. Sousa, S. Cardoso, and P. P. Freitas, "Interacting ferromagnetic nanoparticles in discontinuous $\text{Co}_{80}\text{Fe}_{20}\text{Al}_2\text{O}_3$ multilayers: From superspin glass to reentrant superferromagnetism," *Physical Review B*, vol. 63, p. 134423, 2001.
- [146] S. Shtrikman and E. Wohlfarth, "The theory of the Vogel-Fulcher law of spin glasses," *Physics Letters A*, vol. 85, pp. 467–470, 1981.
- [147] C. Djurberg, P. Svedlindh, P. Nordblad, M. F. Hansen, F. Bødker, and S. Mörup, "Dynamics of an interacting particle system: Evidence of critical slowing down," *Physical Review Letters*, vol. 79, pp. 5154–5157, 1997.
- [148] K. Hiroi, K. Komatsu, and T. Sato, "Superspin glass originating from dipolar interaction with controlled interparticle distance among $\gamma\text{-Fe}_2\text{O}_3$ nanoparticles with silica shells," *Physical Review B*, vol. 83, p. 224423, 2011.
- [149] D. Kechrakos and K. N. Trohidou, "Magnetic properties of dipolar interacting single-domain particles," *Physical Review B*, vol. 58, pp. 12169–12177, 1998.
- [150] K. Trohidou and M. Vasilakaki, "Magnetic behaviour of core/shell nanoparticle assemblies: Interparticle interactions effects," *Acta Physica Polonica A*, vol. 117, p. 374, 2010.
- [151] S. Gangopadhyay, G. Hadjipanayis, C. Sorensen, and K. Klabunde, "Effect of particle size and surface chemistry on the interactions among fine metallic particles," *IEEE Transactions on Magnetism*, vol. 29, pp. 2619–2621, 1993.
- [152] A. Lyberatos and E. Wohlfarth, "A monte carlo simulation of the dependence of the coercive force of a fine particle assembly on the volume packing factor," *Journal of Magnetism and Magnetic Materials*, vol. 59, pp. L1–L4, 1986.

-
- [153] D. Kechrakos, K. Trohidou, and M. Vasilakaki, "Magnetic properties of dense nanoparticle arrays with core/shell morphology," *Journal of Magnetism and Magnetic Materials*, vol. 316, pp. e291–e294, 2007.
- [154] S. Bader, "Preface to the viewpoint set on: nanostructured permanent magnets," *Scripta Materialia*, vol. 47, pp. 527–529, 2002.
- [155] J. E. Gould, "Permanent magnet applications," *IEEE Transactions on Magnetics*, vol. MAG5, p. 812, 1969.
- [156] M. Leonowicz, "Nanocrystalline permanent magnets with enhanced properties," *Acta Polonica A*, vol. 102, pp. 35–43, 2002.
- [157] E. Kneller and R. Hawig, "The exchange-spring magnet: a new material principle for permanent magnets," *IEEE Transactions on Magnetics*, vol. 27, 1991.
- [158] R. Skomski and J. M. D. Coey, "Giant energy product in nanostructured two-phase magnets," *Physical Review B*, vol. 48, pp. 15812–15816, 1993.
- [159] E. E. Fullerton, J. Jiang, and S. Bader, "Hard/soft magnetic heterostructures: model exchange-spring magnets," *Journal of Magnetism and Magnetic Materials*, vol. 200, pp. 392–404, 1999.
- [160] R. Victora and X. Shen, "Composite media for perpendicular magnetic recording," *IEEE Transactions on Magnetics*, vol. 41, pp. 537–542, 2005.
- [161] Z. J. Guo, J. S. Jiang, J. E. Pearson, S. D. Bader, and J. P. Liu, "Exchange-coupled Sm-Co/Nd-Co nanomagnets: correlation between soft phase anisotropy and exchange field," *Applied Physics Letters*, vol. 81, pp. 2029–2031, 2002.
- [162] T. Leineweber and H. Kronmüller, "Micromagnetic examination of exchange coupled ferromagnetic nanolayers," *Journal of Magnetism and Magnetic Materials*, vol. 176, pp. 145–154, 1997.
- [163] A. J. Zambano, H. Oguchi, I. Takeuchi, Y. Choi, J. S. Jiang, J. P. Liu, S. E. Lofland, D. Josell, and L. A. Bendersky, "Dependence of exchange coupling interaction on micromagnetic constants in hard/soft magnetic bilayer systems," *Physical Review B*, vol. 75, p. 144429, 2007.
- [164] N. A. Frey, S. Peng, K. Cheng, and S. Sun, "Magnetic nanoparticles: synthesis, functionalization, and applications in bioimaging and magnetic energy storage," *Chemical Society Reviews*, vol. 38, pp. 2532–2542, 2009.
- [165] R. Skomski, Y. Liu, J. E. Shield, G. C. Hadjipanayis, and D. J. Sellmyer, "Permanent magnetism of dense-packed nanostructures," *Journal of Applied Physics*, vol. 107, p. 09A739, 2010.
- [166] G. C. Hadjipanayis, "Nanophase hard magnets," *Journal of Magnetism and Magnetic Materials*, vol. 200, pp. 373–391, 1999.
- [167] E. Goto, N. Hayashi, T. Miyashita, and K. Nakagawa, "Magnetization and switching characteristics of composite thin magnetic films," *Journal of Applied Physics*, vol. 36, pp. 2951–2958, 1965.
- [168] W. Rave and K. Ramstack, "Micromagnetic calculation of the grain size dependence of remanence and coercivity in nanocrystalline permanent magnets," *Journal of Magnetism and Magnetic Materials*, vol. 171, pp. 69–82, 1997.
- [169] R. Sabirianov and S. Jaswal, "Magnetic properties of hard/soft composites: $\text{SmCo}_5/\text{Co}_{1-x}\text{Fe}_x$," *Physical Review B - Condensed Matter and Materials Physics*, vol. 58, pp. 12071–12074, 1998.
- [170] J. S. Jiang, S. D. Bader, H. Kaper, G. K. Leaf, R. D. Shull, A. J. Shapiro, V. S. Gornakov, V. I. Nikitenko, C. L. Platt, A. E. Berkowitz, S. David, and E. E. Fullerton, "Rotational hysteresis of exchange-spring magnets," *Journal of Physics D: Applied Physics*, vol. 35, p. 2339, 2002.

-
- [171] W. H. Meiklejohn and C. P. Bean, "New magnetic anisotropy," *Physics Review*, vol. 102, pp. 1413–1414, 1956.
- [172] J. Nogués and I. K. Schuller, "Exchange bias," *Journal of Magnetism and Magnetic Materials*, vol. 192, pp. 203–232, 1999.
- [173] J. Nogués, J. Sort, V. Langlais, V. Skumryev, S. Suriñach, J. Muñoz, and M. Baró, "Exchange bias in nanostructures," *Physics Reports*, vol. 422, pp. 65–117, 2005.
- [174] E. Wohlfarth and K. Buschow, *Handbook of magnetic materials*. Handbook of Magnetic Materials, North-Holland Pub. Co., 2003.
- [175] M. Kiwi, "Exchange bias theory," *Journal of Magnetism and Magnetic Materials*, vol. 234, pp. 584–595, 2001.
- [176] K. Takano, R. H. Kodama, A. E. Berkowitz, W. Cao, and G. Thomas, "Interfacial uncompensated antiferromagnetic spins: Role in unidirectional anisotropy in polycrystalline $\text{Ni}_{81}\text{Fe}_{19}/\text{CoO}$ bilayers," *Physical Review Letters*, vol. 79, pp. 1130–1133, 1997.
- [177] H. Ohldag, A. Scholl, F. Nolting, E. Arenholz, S. Maat, A. T. Young, M. Carey, and J. Stöhr, "Correlation between exchange bias and pinned interfacial spins," *Physical Review Letters*, vol. 91, p. 017203, 2003.
- [178] S. Brück, G. Schütz, E. Goering, X. Ji, and K. M. Krishnan, "Uncompensated moments in the MnPd/Fe exchange bias system," *Physical Review Letters*, vol. 101, p. 126402, 2008.
- [179] J. Camarero, Y. Pennec, J. Vogel, S. Pizzini, M. Cartier, F. Fettar, F. Ernult, A. Tagliaferri, N. B. Brookes, and B. Dieny, "Field dependent exchange coupling in NiO/Co bilayers," *Physical Review B*, vol. 67, p. 020413, 2003.
- [180] M. R. Fitzsimmons, B. J. Kirby, S. Roy, Z.-P. Li, I. V. Roshchin, S. K. Sinha, and I. K. Schuller, "Pinned magnetization in the antiferromagnet and ferromagnet of an exchange bias system," *Physical Review B*, vol. 75, p. 214412, 2007.
- [181] W. H. Meiklejohn and C. P. Bean, "New magnetic anisotropy," *Physics Review*, vol. 105, pp. 904–913, 1957.
- [182] 1328-1335, "Exchange anisotropy-A review," *Journal of Applied Physics*, vol. 33, pp. 1328–1335, 1962.
- [183] D. Paccard, C. Schlenker, O. Massenet, R. Montmory, and A. Yelon, "A new property of ferromagnetic-antiferromagnetic coupling," *Physica Status Solidi (B)*, vol. 16, pp. 301–311, 1966.
- [184] J. W. Cai, K. Liu, and C. L. Chien, "Exchange coupling in the paramagnetic state," *Physical Review B*, vol. 60, pp. 72–75, 1999.
- [185] X. W. Wu and C. L. Chien, "Exchange coupling in ferromagnet/antiferromagnet bilayers with comparable T_C and T_N ," *Physical Review Letters*, vol. 81, pp. 2795–2798, 1998.
- [186] M. G. Blamire, M. Ali, C.-W. Leung, C. H. Marrows, and B. J. Hickey, "Exchange bias and blocking temperature in Co/FeMn/CuNi trilayers," *Physical Review Letters*, vol. 98, p. 217202, 2007.
- [187] K. D. Sossmeier, L. G. Pereira, J. E. Schmidt, and J. Geshev, "Exchange bias in a ferromagnet/antiferromagnet system with $T_c \ll T_n$," *Journal of Applied Physics*, vol. 109, p. 083938, 2011.
- [188] K. Wang, W. Tan, and X. He, "Biomedical applications based on core-shell nanoparticles," in *IEEE-EMBS 2005. 27th Annual International Conference of the Engineering in Medicine and Biology Society*, pp. 717–719, 2005.

-
- [189] S. Alayoglu, A. U. Nilekar, M. Mavrikakis, and B. Eichhorn, "Ru-Pt core-shell nanoparticles for preferential oxidation of carbon monoxide in hydrogen," *Nature Materials*, vol. 7, pp. 333–338, 2008.
- [190] F. Wang, R. Deng, J. Wang, Q. Wang, Y. Han, H. Zhu, X. Chen, and X. Liu, "Tuning upconversion through energy migration in core-shell nanoparticles," *Nature Materials*, vol. 10, pp. 968–973, 2011.
- [191] H. Zeng and S. Sun, "Syntheses, properties, and potential applications of multicomponent magnetic nanoparticles," *Advanced Functional Materials*, vol. 18, pp. 391–400, 2008.
- [192] S. Kudera, L. Carbone, E. Carlino, R. Cingolani, P. D. Cozzoli, and L. Manna, "Synthesis routes for the growth of complex nanostructures," *Physica E: Low-dimensional Systems and Nanostructures*, vol. 37, pp. 128–133, 2007.
- [193] M. R. Buck, J. F. Bondi, and R. E. Schaak, "A total-synthesis framework for the construction of high-order colloidal hybrid nanoparticles," *Nature Chemistry*, vol. 4, pp. 37–44, 2012.
- [194] A. Ito, F. Matsuoka, H. Honda, and T. Kobayashi, "Heat shock protein 70 gene therapy combined with hyperthermia using magnetic nanoparticles," *Cancer Gene Therapy*, vol. 10, pp. 918–925, 2003.
- [195] N. Nitin, L. E. W. LaConte, O. Zurkiya, X. Hu, and G. Bao, "Functionalization and peptide-based delivery of magnetic nanoparticles as an intracellular MRI contrast agent," *Journal of Biological Inorganic Chemistry*, vol. 9, pp. 706–712, 2004.
- [196] Z. Liu, Y. Liu, H. Yang, Y. Yang, G. Shen, and R. Yu, "A phenol biosensor based on immobilizing tyrosinase to modified core-shell magnetic nanoparticles supported at a carbon paste electrode," *Analytica Chimica Acta*, vol. 533, pp. 3–9, 2005.
- [197] Y. Zhang, G.-M. Zeng, L. Tang, D.-L. Huang, X.-Y. Jiang, and Y.-N. Chen, "A hydroquinone biosensor using modified core-shell magnetic nanoparticles supported on carbon paste electrode," *Biosensors and Bioelectronics*, vol. 22, pp. 2121–2126, 2007.
- [198] D. J. Irvine, "Drug delivery: One nanoparticle, one kill," *Nature Materials*, vol. 10, pp. 342–343, 2011.
- [199] J. Wu, G. Wang, D. Jin, J. Yuan, Y. Guan, and J. Piper, "Luminescent europium nanoparticles with a wide excitation range from uv to visible light for biolabeling and time-gated luminescence bioimaging," *Chemical Communications*, pp. 365–367, 2008.
- [200] M. Green, H. Harwood, C. Barrowman, P. Rahman, A. Eggeman, F. Festry, P. Dobson, and T. Ng, "A facile route to cdte nanoparticles and their use in bio-labelling," *Journal of Materials Chemistry*, vol. 17, pp. 1989–1994, 2007.
- [201] S. Sao-Joao, S. Giorgio, J. M. Penisson, C. Chapon, S. Bourgeois, and C. Henry, "Structure and deformations of Pd-Ni core-shell nanoparticles," *The Journal of Physical Chemistry B*, vol. 109, pp. 342–347, 2005.
- [202] W. Tang and G. Henkelman, "Charge redistribution in core-shell nanoparticles to promote oxygen reduction," *The Journal of Chemical Physics*, vol. 130, p. 194504, 2009.
- [203] P. Reiss, M. Protière, and L. Li, "Core/shell semiconductor nanocrystals," *Small*, vol. 5, pp. 154–168, 2009.
- [204] A. Imhof, "Preparation and characterization of titania-coated polystyrene spheres and hollow titania shells," *Langmuir*, vol. 17, pp. 3579–3585, 2001.

-
- [205] M. Ocana, W. P. Hsu, and E. Matijevic, "Preparation and properties of uniform-coated colloidal particles. titania on zinc oxide," *Langmuir*, vol. 7, pp. 2911–2916, 1991.
- [206] S. Sun and H. Zeng, "Size-controlled synthesis of magnetite nanoparticles," *Journal of the American Chemical Society*, vol. 124, pp. 8204–8205, 2002.
- [207] S. Sun, H. Zeng, D. B. Robinson, S. Raoux, P. M. Rice, S. X. Wang, and G. Li, "Monodisperse MFe_2O_4 ($M = Fe, Co, Mn$) nanoparticles," *Journal of the American Chemical Society*, vol. 126, pp. 273–279, 2004.
- [208] G. Salazar-Alvarez, H. Lidbaum, A. López-Ortega, M. Estrader, K. Leifer, J. Sort, S. Suriñach, M. D. Baró, and J. Nogués, "Two-, Three-, and Four-component magnetic multilayer onion nanoparticles based on Iron Oxides and Manganese Oxides," *Journal of the American Chemical Society*, vol. 133, pp. 16738–16741, 2011.
- [209] M. Okaniwa, "Synthesis of poly(tetrafluoroethylene)/poly(butadiene) core-shell particles and their graft copolymerization," *Journal of Applied Polymer Science*, vol. 68, pp. 185–190, 1998.
- [210] H. Zou, S. Wu, and J. Shen, "Polymer/silica nanocomposites: Preparation, characterization, properties, and applications," *Chemical Reviews*, vol. 108, pp. 3893–3957, 2008.
- [211] G. Hota, S. Jain, and K. C. Khilar, "Synthesis of CdS-Ag₂S core-shell/composite nanoparticles using AOT/n-heptane/water microemulsions," *Colloids and Surfaces A: Physicochemical and Engineering Aspects*, vol. 232, pp. 119–127, 2004.
- [212] M. Y. Han, W. Huang, C. H. Chew, L. M. Gan, X. J. Zhang, and W. Ji, "Large nonlinear absorption in coated Ag₂S/CdS nanoparticles by inverse microemulsion," *The Journal of Physical Chemistry B*, vol. 102, pp. 1884–1887, 1998.
- [213] J. H. Son, H. Y. Park, D. P. Kang, and D. S. Bae, "Synthesis and characterization of Ag/Pd doped SiO₂ nanoparticles by a reverse micelle and sol-gel processing," *Colloids and Surfaces A: Physicochemical and Engineering Aspects*, vol. 313-314, pp. 105–107, 2008.
- [214] D.-S. Bae, S.-W. Park, K.-S. Han, and J. Adair, "Synthesis of ag/sio₂ nanosize particles by reverse micelle and sol-gel processing," *Metals and Materials International*, vol. 7, pp. 399–402, 2001.
- [215] S. Srivastava and N. A. Kotov, "Composite layer-by-layer (lbl) assembly with inorganic nanoparticles and nanowires," *Accounts of Chemical Research*, vol. 41, pp. 1831–1841, 2008.
- [216] D. B. Shenoy, A. A. Antipov, G. B. Sukhorukov, and H. Mahwald, "Layer-by-layer engineering of biocompatible, decomposable core-shell structures," *Biomacromolecules*, vol. 4, pp. 265–272, 2003.
- [217] S. Banerjee, S. Roy, J. Chen, and D. Chakravorty, "Magnetic properties of oxide-coated iron nanoparticles synthesized by electrodeposition," *Journal of Magnetism and Magnetic Materials*, vol. 219, pp. 45–52, 2000.
- [218] C. Gu, H. Xu, M. Park, and C. Shannon, "Synthesis of metal-semiconductor core-shell nanoparticles using electrochemical surface-limited reactions," *Langmuir*, vol. 25, pp. 410–414, 2009.
- [219] S. Gangopadhyay, G. C. Hadjipanayis, C. M. Sorensen, and K. J. Klabunde, "Exchange anisotropy in oxide passivated Co fine particles," *Journal of Applied Physics*, vol. 73, pp. 6964–6966, 1993.
- [220] J. B. Tracy, D. N. Weiss, D. P. Dinega, and M. G. Bawendi, "Exchange biasing and magnetic properties of partially and fully oxidized colloidal cobalt nanoparticles," *Physical Review B*, vol. 72, p. 064404, 2005.
- [221] J. B. Tracy and M. G. Bawendi, "Defects in CoO in oxidized cobalt nanoparticles dominate exchange biasing and exhibit anomalous magnetic properties," *Physical Review B*, vol. 74, p. 184434, 2006.

-
- [222] K. Simeonidis, C. Martinez-Boubeta, O. Iglesias, A. Cabot, M. Angelakeris, S. Mourdikoudis, I. Tsiaoussis, A. Delimitis, C. Dendrinos-Samara, and O. Kalogirou, "Morphology influence on nanoscale magnetism of Co nanoparticles: Experimental and theoretical aspects of exchange bias," *Physical Review B*, vol. 84, p. 144430, 2011.
- [223] G. Salazar-Alvarez, J. Sort, A. Uheida, M. Muhammed, S. Surinach, M. D. Baro, and J. Nogues, "Reversible post-synthesis tuning of the superparamagnetic blocking temperature of γ -Fe₂O₃ nanoparticles by adsorption and desorption of Co(II) ions," *Journal of Materials Chemistry*, vol. 17, pp. 322–328, 2007.
- [224] V. Skumryev, S. Stoyanov, Y. Zhang, G. Hadjipanayis, D. Givord, and J. Nogués, "Beating the superparamagnetic limit with exchange bias," *Nature*, vol. 423, pp. 850–853, 2003.
- [225] J. Nogués, V. Skumryev, J. Sort, S. Stoyanov, and D. Givord, "Shell-driven magnetic stability in core-shell nanoparticles," *Physical Review Letters*, vol. 97, p. 157203, 2006.
- [226] H. Zeng, J. Li, Z. L. Wang, J. P. Liu, and S. Sun, "Bimagnetic core/shell FePt/Fe₃O₄ nanoparticles," *Nano Letters*, vol. 4, pp. 187–190, 2004.
- [227] G. S. Chaubey, V. Nandwana, N. Poudyal, C.-b. Rong, and J. P. Liu, "Synthesis and characterization of bimagnetic bricklike nanoparticles," *Chemistry of Materials*, vol. 20, pp. 475–478, 2008.
- [228] B. Lu, H. Huang, X. L. Dong, X. F. Zhang, J. P. Lei, J. P. Sun, and C. Dong, "Influence of alloy components on electromagnetic characteristics of core/shell-type Fe-Ni nanoparticles," *Journal of Applied Physics*, vol. 104, p. 114313, 2008.
- [229] L. Xi, Z. Wang, Y. Zuo, and X. Shi, "The enhanced microwave absorption property of CoFe₂O₄ nanoparticles coated with a Co₃Fe₇-Co nanoshell by thermal reduction," *Nanotechnology*, vol. 22, p. 045707, 2011.
- [230] A. H. Habib, C. L. Ondeck, P. Chaudhary, M. R. Bockstaller, and M. E. McHenry, "Evaluation of iron-cobalt/ferrite core-shell nanoparticles for cancer thermotherapy," *Journal of Applied Physics*, vol. 103, p. 07A307, 2008.
- [231] P. Z. Si, D. Li, J. W. Lee, C. J. Choi, Z. D. Zhang, D. Y. Geng, and E. Brück, "Unconventional exchange bias in oxide-coated manganese nanoparticles," *Applied Physics Letters*, vol. 87, p. 133122, 2005.
- [232] I. S. Lee, N. Lee, J. Park, B. H. Kim, Y.-W. Yi, T. Kim, T. K. Kim, I. H. Lee, S. R. Paik, and T. Hyeon, "Ni/NiO core/shell nanoparticles for selective binding and magnetic separation of histidine-tagged proteins," *Journal of the American Chemical Society*, vol. 128, pp. 10658–10659, 2006.
- [233] A. C. Johnston-Peck, J. Wang, and J. B. Tracy, "Synthesis and structural and magnetic characterization of Ni(core)/NiO(shell) nanoparticles," *ACS Nano*, vol. 3, pp. 1077–1084, 2009.
- [234] R. K. Zheng, G. H. Wen, K. K. Fung, and X. X. Zhang, "Training effect of exchange bias in γ -Fe₂O₃ coated Fe nanoparticles," *Physical Review B*, vol. 69, p. 214431, 2004.
- [235] C. Luna, M. del Puerto Morales, C. J. Serna, and M. Vázquez, "Exchange anisotropy in Co₈₀Ni₂₀/oxide nanoparticles," *Nanotechnology*, vol. 15, p. S293, 2004.
- [236] C.-M. Hsu, H.-M. Lin, K.-R. Tsai, and P.-Y. Lee, "HRTEM analysis and magnetic properties study of surface oxidizing and nitriding of nanocrystalline particles," *MRS Proceedings*, vol. 351, p. 227, 1994.

-
- [237] J. H. Greiner, I. M. Croll, and M. Sulich, "Ferromagnetic-antiferromagnetic interaction in Fe-FeS," *Journal of Applied Physics*, vol. 31, pp. 2316–2317, 1960.
- [238] R. Cornell and U. Schwertmann, *The Iron Oxides: Structure, Properties, Reactions, Occurrences and Uses*. John Wiley & Sons, 2007.
- [239] R. K. Zheng, H. Liu, Y. Wang, and X. X. Zhang, "Cr₂O₃ surface layer and exchange bias in an acicular CrO₂ particle," vol. 84, pp. 702–704, 2004.
- [240] F. X. Redl, C. T. Black, G. C. Papaefthymiou, R. L. Sandstrom, M. Yin, H. Zeng, C. B. Murray, and S. P. O'Brien, "Magnetic, electronic, and structural characterization of nonstoichiometric iron oxides at the nanoscale," *Journal of the American Chemical Society*, vol. 126, pp. 14583–14599, 2004.
- [241] D. W. Kavich, J. H. Dickerson, S. V. Mahajan, S. A. Hasan, and J.-H. Park, "Exchange bias of singly inverted FeO/Fe₃O₄ core-shell nanocrystals," *Physical Review B*, vol. 78, p. 174414, 2008.
- [242] C. J. Bae, Y. Hwang, J. Park, K. An, Y. Lee, J. Lee, T. Hyeon, and J.-G. Park, "Inter-particle and interfacial interaction of magnetic nanoparticles," *Journal of Magnetism and Magnetic Materials*, vol. 310, pp. e806–e808, 2007.
- [243] G. Salazar-Alvarez, J. Sort, S. Suriñach, M. D. Baró, and J. Nogués, "Synthesis and size-dependent exchange bias in inverted core-shell MnO-Mn₃O₄ nanoparticles," *Journal of the American Chemical Society*, vol. 129, p. 9102, 2007.
- [244] A. E. Berkowitz, G. F. Rodriguez, J. I. Hong, K. An, T. Hyeon, N. Agarwal, D. J. Smith, and E. E. Fullerton, "Antiferromagnetic MnO nanoparticles with ferrimagnetic Mn₃O₄ shells: Doubly inverted core-shell system," *Physics Review B*, vol. 77, p. 024403, 2008.
- [245] A. E. Berkowitz, G. F. Rodriguez, J. I. Hong, K. An, T. Hyeon, N. Agarwal, D. J. Smith, and E. E. Fullerton, "Monodispersed MnO nanoparticles with epitaxial Mn₃O₄ shells," *Journal of Physics D: Applied Physics*, vol. 41, p. 134007, 2008.
- [246] A. López-Ortega, D. Tobia, E. Winkler, I. V. Golosovsky, G. Salazar-Alvarez, S. Estrade, M. Estrader, J. Sort, M. A. González, S. Suriñach, J. Arbiol, F. Peiró, R. D. Zysler, M. D. Baró, and J. Nogués, "Size-dependent passivation shell and magnetic properties in antiferromagnetic/ferrimagnetic core/shell MnO nanoparticles," *Journal of the American Chemical Society*, vol. 132, pp. 9398–9407, 2010.
- [247] J. De Toro, J. Andrés, J. González, J. Riveiro, M. Estrader, A. López-Ortega, I. Tsiaoussis, N. Frangis, and J. Nogués, "Role of the oxygen partial pressure in the formation of composite Co-CoO nanoparticles by reactive aggregation," *Journal of Nanoparticle Research*, vol. 13, pp. 4583–4590, 2011.
- [248] X. Liu, B. Gu, W. Zhong, H. Jiang, and Y. Du, "Ferromagnetic/antiferromagnetic exchange coupling in SrFe₁₂O₁₉/CoO composites," *Applied Physics A: Materials Science & Processing*, vol. 77, pp. 673–676, 2003.
- [249] O. Masala and R. Seshadri, "Spinel Ferrite/MnO core/shell nanoparticles: Chemical synthesis of all-oxide exchange biased architectures," *Journal of the American Chemical Society*, vol. 127, pp. 9354–9355, 2005.
- [250] R. D. Rutledge, W. H. Morris, M. S. Wellons, Z. Gai, J. Shen, J. Bentley, J. E. Wittig, and C. M. Lukehart, "Formation of FePt nanoparticles having high coercivity," *Journal of the American Chemical Society*, vol. 128, pp. 14210–14211, 2006.
- [251] B. K. Yun, Y. S. Koo, and J. H. Jung, "Exchange bias in Cr₂O₃/Fe₃O₄ core/shell nanoparticles," *Journal of Magnetism*, vol. 14, pp. 147–149, 2009.

-
- [252] H. Zeng, J. Li, J. P. Liu, Z. L. Wang, and S. Sun, "Exchange-coupled nanocomposite magnets by nanoparticle self-assembly," *Nature*, vol. 420, pp. 395–398, 2002.
- [253] V. Nandwana, G. S. Chaubey, K. Yano, C. Bing Rong, and J. P. Liu, "Bimagnetic nanoparticles with enhanced exchange coupling and energy products," *Journal of Applied Physics*, vol. 105, p. 014303, 2009.
- [254] J. Kim, C. Rong, Y. Lee, J. P. Liu, and S. Sun, "From core/shell structured FePt/Fe₃O₄/MgO to ferromagnetic FePt nanoparticles," *Chemistry of Materials*, vol. 20, pp. 7242–7245, 2008.
- [255] L. Varanda, M. Imaizumi, F. Santos, and M. Jafelicci, "Iron oxide versus FePt/FeO: Improved magnetic properties of core/shell nanoparticles for biomedical applications," *IEEE Transactions on Magnetics*, vol. 44, pp. 4448–4451, 2008.
- [256] A. Figuerola, A. Fiore, R. Di Corato, A. Falqui, C. Giannini, E. Micotti, A. Lascialfari, M. Corti, R. Cingolani, T. Pellegrino, P. D. Cozzoli, and L. Manna, "One-pot synthesis and characterization of size-controlled bimagnetic FePt-Iron oxide heterodimer nanocrystals," *Journal of the American Chemical Society*, vol. 130, pp. 1477–1487, 2008.
- [257] C. W. Kim, Y. H. Kim, H. G. Cha, and Y. S. Kang, "Exchange-coupling effect of Nd₂Fe₁₄B/FeCo nanocomposite by colloidal method," *Molecular Crystals and Liquid Crystals*, vol. 464, pp. 1/[583]–7/[589], 2007.
- [258] C. W. Kim, Y. H. Kim, H. G. Cha, J. C. Kim, and Y. S. Kang, "A study on the exchange-coupling effect of Nd₂Fe₁₄B/CoFe forming core/shell shape," *Molecular Crystals and Liquid Crystals*, vol. 472, pp. 155/[545]–160/[550], 2007.
- [259] J. H. Hong, W. S. Kim, J. I. Lee, and N. H. Hur, "Exchange coupled magnetic nanocomposites of Sm(Co_{1-x}Fe_x)₅/Fe₃O₄ with core/shell structure," *Solid State Communications*, vol. 141, pp. 541–544, 2007.
- [260] Q. K. Ong, A. Wei, and X.-M. Lin, "Exchange bias in Fe/Fe₃O₄ core-shell magnetic nanoparticles mediated by frozen interfacial spins," *Physics Review B*, vol. 80, p. 134418, 2009.
- [261] C. Wang, D. R. Baer, J. E. Amonette, M. H. Engelhard, J. Antony, and Y. Qiang, "Morphology and electronic structure of the oxide shell on the surface of iron nanoparticles," *Journal of the American Chemical Society*, vol. 131, pp. 8824–8832, 2009.
- [262] O. Masala, D. Hoffman, N. Sundaram, K. Page, T. Proffen, G. Lawes, and R. Seshadri, "Preparation of magnetic spinel ferrite core/shell nanoparticles: Soft ferrites on hard ferrites and vice versa," *Solid State Sciences*, vol. 8, pp. 1015–1022, 2006.
- [263] J.-H. Lee, J.-T. Jang, J.-S. Choi, S. H. Moon, S.-h. Noh, J.-W. Kim, J.-G. Kim, I.-S. Kim, K. I. Park, and J. Cheon, "Exchange-coupled magnetic nanoparticles for efficient heat induction," *Nature Nanotechnology*, vol. 6, pp. 418–422, 2011.
- [264] A. López-Ortega, M. Estrader, G. Salazar-Alvarez, S. Estradé, I. V. Golosovsky, R. K. Dumas, D. J. Keavney, M. Vasilakaki, K. N. Trohidou, J. Sort, F. Peiró, S. Suriñach, M. D. Baró, and J. Nogués, "Strongly exchange coupled inverse ferrimagnetic soft|hard, Mn_xFe_{3-x}O₄|Fe_xMn_{3-x}O₄, core|shell heterostructured nanoparticles," *Nanoscale*, p. DOI:10.1039/C2NR30986F, 2012.
- [265] H. Zeng, S. Sun, J. Li, Z. L. Wang, and J. P. Liu, "Tailoring magnetic properties of core/shell nanoparticles," *Applied Physics Letters*, vol. 85, pp. 792–794, 2004.
- [266] P. Goodhew, F. Humphreys, and R. Beanland, *Electron microscopy and analysis*. Taylor & Francis, 2001.
- [267] Z. Wang, *Characterization of nanophase materials*. Wiley-VCH, 2000.

-
- [268] B. Fultz and J. Howe, *Transmission electron microscopy and diffractometry of materials*. Advanced Texts in Physics, Springer, 2007.
- [269] “<http://www.jeol.com/>.”
- [270] “<http://www.gatan.com/>.”
- [271] H. Kurata and C. Colliex, “Electron-energy-loss core-edge structures in manganese oxides,” *Physics Review B*, vol. 48, pp. 2102–2108, 1993.
- [272] R. Egerton, *Electron energy-loss spectroscopy in the electron microscope*. Language of science, Plenum Press, 1996.
- [273] S. Estradé, J. Arbiol, F. Peiró, L. Abad, V. Laukhin, L. Balcells, and B. Martínez, “Cationic diffusion in $\text{La}_{2/3}\text{Ca}_{1/3}\text{MnO}_3$ thin films grown on LaAlO_3 (001) substrates,” *Applied Physics Letters*, vol. 91, p. 252503, 2007.
- [274] S. Estradé, J. Arbiol, F. Peiró, I. C. Infante, F. Sánchez, J. Fontcuberta, F. de la Peña, M. Walls, and C. Colliex, “Cationic and charge segregation in $\text{La}_{2/3}\text{Ca}_{1/3}\text{MnO}_3$ thin films grown on (001) and (110) SrTiO_3 ,” *Applied Physics Letters*, vol. 93, p. 112505, 2008.
- [275] S. Estradé, J. M. Rebled, J. Arbiol, F. Peiró, I. C. Infante, G. Herranz, F. Sánchez, J. Fontcuberta, R. Córdoba, B. G. Mendis, and A. L. Bleloch, “Effects of thickness on the cation segregation in epitaxial (001) and (110) $\text{La}_{2/3}\text{Ca}_{1/3}\text{MnO}_3$ thin films,” *Applied Physics Letters*, vol. 95, p. 072507, 2009.
- [276] B. Cullity and S. Stock, *Elements of x-ray diffraction*. Pearson education, Prentice Hall, 2001.
- [277] G. Will, *Powder diffraction: the Rietveld method and the two-stage method to determine and refine crystal structures from powder diffraction data*. Springer, 2006.
- [278] V. Pecharsky and P. Zavalij, *Fundamentals of powder diffraction and structural characterization of materials*. Recent Results in Cancer Research, Springer, 2009.
- [279] J. Rodriguez-Carvajal, “Recent advances in magnetic structure determination by neutron powder diffraction,” *Physica B*, vol. 192, pp. 55–69, 1993.
- [280] “<http://www.ill.eu/sites/fullprof/>,”
- [281] “<http://www.ing.unitn.it/maud/>,”
- [282] S. Petrick Casagrande and R. Castillo Blanco, “Método de rietveld para el estudio de estructuras cristalinas,” *Revista de la Facultad de Ciencias, Universidad Nacional de Ingeniería, Lima-Peru*, vol. 2, pp. 1–5, 2004.
- [283] “<http://www.nist.gov/srm/>.”
- [284] T. Chatterji, *Neutron scattering from magnetic materials*. Elsevier, 2006.
- [285] J. B. Parise, “Introduction to neutron properties and applications,” *Reviews in Mineralogy and Geochemistry*, vol. 63, pp. 1–25, 2006.
- [286] E. Prince, “International tables for crystallography,” *International Union of Crystallography*, vol. Volume C: Mathematical, physical and chemical tables, pp. 444–454, 2006.
- [287] T. C. Hansen, P. F. Henry, H. E. Fischer, J. Torregrossa, and P. Convert, “The D20 instrument at the ill: a versatile high-intensity two-axis neutron diffractometer,” *Measurement Science and Technology*, vol. 19, p. 034001, 2008.

-
- [288] <http://www.ill.eu/>
- [289] “[http://www.qdusa.com/.](http://www.qdusa.com/)”
- [290] B. Josephson, “Possible new effects in superconductive tunnelling,” *Physics Letters*, vol. 1, pp. 251–253, 1962.
- [291] M. Hanson, C. Johansson, M. S. Pedersen, and S. Mörup, “The influence of particle size and interactions on the magnetization and susceptibility of nanometre-size particles,” *Journal of Physics: Condensed Matter*, vol. 7, p. 9269, 1995.
- [292] I. D. Mayergoyz, “Mathematical models of hysteresis,” *Physical Review Letters*, vol. 56, pp. 1518–1521, 1986.
- [293] C. R. Pike, A. P. Roberts, and K. L. Verosub, “Characterizing interactions in fine magnetic particle systems using first order reversal curves,” *Journal of Applied Physics*, vol. 85, pp. 6660–6667, 1999.
- [294] “[http://www.bruker-biospin.com/epr-products.html.](http://www.bruker-biospin.com/epr-products.html)”
- [295] D. Koningsberger and R. Prins, *X-ray absorption: principles, applications, techniques of EXAFS, SEXAFS, and XANES*. Chemical analysis, Wiley, 1988.
- [296] M. Abbate, J. B. Goedkoop, F. M. F. de Groot, M. Grioni, J. C. Fuggle, S. Hofmann, H. Petersen, and M. Sacchi, “Probing depth of soft x-ray absorption spectroscopy measured in total-electron-yield mode,” *Surface and Interface Analysis*, vol. 18, pp. 65–69, 1992.
- [297] “[http://www.esrf.eu/usersandscience/experiments/electstructmagn/id08.](http://www.esrf.eu/usersandscience/experiments/electstructmagn/id08)”
- [298] “[http://aps.anl.gov/.](http://aps.anl.gov/)”
- [299] “[http://www.psi.ch/sls/sim/sim.](http://www.psi.ch/sls/sim/sim)”
- [300] G. Schütz, W. Wagner, W. Wilhelm, P. Kienle, R. Zeller, R. Frahm, and G. Materlik, “Absorption of circularly polarized x rays in iron,” *Physics Review Letters*, vol. 58, pp. 737–740, 1987.
- [301] J. Stöhr and Y. Wu, *New Directions in Research with Third-Generation Soft X-Ray Synchrotron Radiation Sources*. Kluwer Academic Publishers, Netherlands, 1994.
- [302] J. Stöhr, “X-ray magnetic circular dichroism spectroscopy of transition metal thin films,” *Journal of Electron Spectroscopy and Related Phenomena*, vol. 75, pp. 253 – 272, 1995.
- [303] K. Trohidou and M. Vasilakaki, *Applications of Monte Carlo Method in Science and Engineering*. InTech, February 2011.
- [304] N. Metropolis, A. W. Rosenbluth, M. N. Rosenbluth, A. H. Teller, and E. Teller, “Equation of state calculations by fast computing machines,” *The Journal of Chemical Physics*, vol. 21, pp. 1087–1092, 1953.
- [305] T. Sugimoto, *Monodispersed Particles*. Elsevier B.V., 2001.
- [306] V. K. LaMer and R. H. Dinegar, “Theory, production and mechanism of formation of monodispersed hydrosols,” *Journal of the American Chemical Society*, vol. 72, pp. 4847–4854, 1950.
- [307] I. Lifshitz and V. Slyozov, “The kinetics of precipitation from supersaturated solid solutions,” *Journal of Physics and Chemistry of Solids*, vol. 19, pp. 35–50, 1961.
- [308] A. Gomez Roca, *Preparacion de nanopartículas magnéticas uniformes y de alta cristalinidad para biomedicina*. PhD thesis, Instituto de Ciencia de Materiales de Madrid, CSIC, and Universidad Complutense de Madrid, febrero 2009.

-
- [309] H. Reiss, "The growth of uniform colloidal dispersions," *The Journal of Chemical Physics*, vol. 19, pp. 482–487, 1951.
- [310] X. Peng, J. Wickham, and A. P. Alivisatos, "Kinetics of II-VI and III-V colloidal semiconductor nanocrystal growth:focusing of size distributions," *Journal of the American Chemical Society*, vol. 120, pp. 5343–5344, 1998.
- [311] W. Bu, Z. Chen, F. Chen, and J. Shi, "Oleic acid/oleylamine cooperative-controlled crystallization mechanism for monodisperse tetragonal bipyramid NaLa(MoO₄)₂ nanocrystals," *The Journal of Physical Chemistry C*, vol. 113, pp. 12176–12185, 2009.
- [312] L. M. Bronstein, X. Huang, J. Retrum, A. Schmucker, M. Pink, B. D. Stein, and B. Dragnea, "Influence of iron oleate complex structure on iron oxide nanoparticle formation," *Chemistry of Materials*, vol. 19, pp. 3624–3632, 2007.
- [313] C.-J. Chen, R.-K. Chiang, H.-Y. Lai, and C.-R. Lin, "Characterization of monodisperse wustite nanoparticles following partial oxidation," *The Journal of Physical Chemistry C*, vol. 114, pp. 4258–4263, 2010.
- [314] R. Boistelle and J. Astier, "Crystallization mechanisms in solution," *Journal of Crystal Growth*, vol. 90, pp. 14–30, 1988.
- [315] M. V. Kovalenko, M. I. Bodnarchuk, R. T. Lechner, G. Hesser, F. Schäffler, and W. Heiss, "Fatty acid salts as stabilizers in size- and shape-controlled nanocrystal synthesis:the case of inverse spinel iron oxide," *Journal of the American Chemical Society*, vol. 129, pp. 6352–6353, 2007.

